IMAGE PROCESSING OF OPTICAL COHERENCE TOMOGRAPHY FOR IMAGE GUIDED DENTAL DRILLING

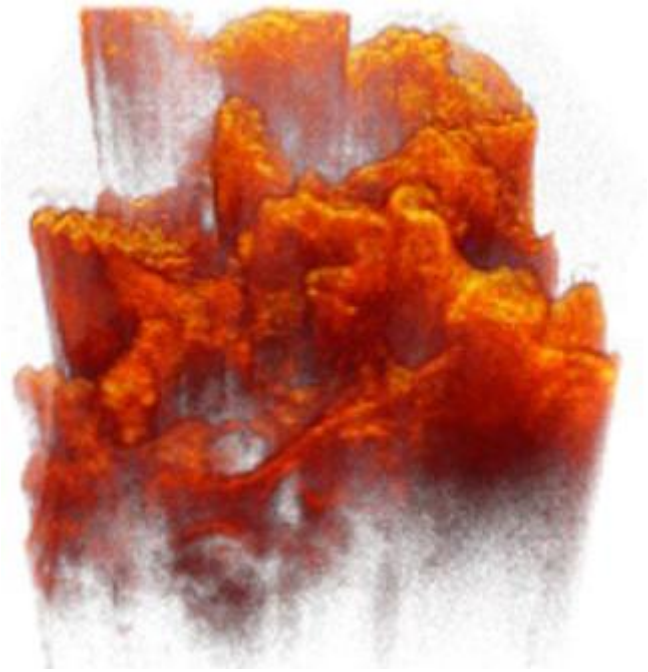

Author:	Xiaojun Zha
Student Number:	1532146
Supervisor:	Ir. A.J. Loeve
Date:	Dec. 19, 2011

Committee Members:

1. Prof. Dr. J. Dankelman

2. Prof. Dr. P.J. French

3. Ir. A.J.Loeve

Day of the defense: December.19, 2011

M.Sc. Thesis

IMAGE PROCESSING OF OPTICAL COHERENCE TOMOGRAPHY FOR IMAGE GUIDED DENTAL DRILLING

DELFT UNIVERSITY OF TECHNOLOGY

FACULTY OF MECHANICAL ENGINEERING

BIOMECHANICAL ENGINEERING

Written By
Xiaojun Zha (1532146)

Supervised By
Arjo Loeve

IMAGE PROCESSING OF OPTICAL COHERENCE TOMOGRAPHY FOR IMAGE GUIDED DENTAL DRILLING

Thesis

submitted in partial fulfillment of the requirements for the degree of

MASTER OF SCIENCE

in

BIOMEDICAL ENGINEERING

By

Xiaojun Zha

This work was performed in:

Department of Biomedical Engineering
Faculty of Mechanical, Maritime and Materials Engineering
Delft University of Technology

ABSTRACT

In the past two decades, dental implants have been an essential component of the public health. However, lack of a reliable and safe dental surgery imaging modality remains a major problem. Optical coherence tomography (OCT) is an interferometic optical imaging modality that is somewhat similar to B-mode ultrasound but utilizes infrared light instead of sound waves. It can provide optical biopsy at a very high resolution and in real time. The compact fiber-optic components of OCT make it easy to integrate into dental drill bit to provide the dentists with real-time image feedback about the anatomical structure in the vicinity of the drill bit. This research focuses on the image processing for such a concept designing OCT integrated dental drilling system. Various image processing methods are applied to the OCT images with the intention of finding out the suitable solutions for speckle noise reduction, image reconstruction and dental tissues segmentation.

OCT imaging system obtains the cross sectional structure of samples by measuring the back reflected light. The coherent detection makes the OCT images are always subject to speckle noise. The existence of speckle noise limits the interpretation of OCT images. In this study, various speckle reduction digital filters are applied to the images obtained from OCT during high speed rotation. Our results indicate that the adaptive Wiener filter is particularly suitable for our specific application. It is a time–saving method that not only significantly suppresses speckle noise but also preserves image edges.

The study also concerns the image restoration due to the non-uniform rotational scanning. One modified method based on the cross correlation between successive A-scans is posted and studied. The assembled images indicate our algorithm is capable of reconstructing the manually-scanned images with an acceptable assemble accuracy.

In tissue segmentation, the porous structure of the trabecular bones enables us to discriminate different them from cortical bones. However, due to the intensity decay along the depth direction, the way for image automatic segmentation is still a major problem need to be solved in future research.

To test and verify our algorithms, the experiments are conducted to both real animal jawbones and silicone elastomer-based optical tissue phantoms. This proof-of-concept study shows that OCT is able to probe dental tissues in rotational scanning. The results from both samples are highly in accord with each other. This conclusion suggests that our optical phantom is a good jawbone substitute. The durable, easy-to-make phantoms can significantly reduce the cost of future researches.

Key words:

dental implants, optical coherence tomography, speckle noise, digital filter, image quality analysis, image reconstruction, optical phantom, jawbone, tissues recognition

.

ACKNOWLEDGEMENT

First of all, I would like to give my special thanks to my parents. They gave me their unconditional support and love during my years of study and through all this long work. They encouraged me and made this work possible.

I would like to express the deepest appreciation to my direct supervisor Ir. A.J. Loeve for his time, understanding, tolerance and patience. His abundant help and suggestions made me grow in my thesis. I would not be able to finish this thesis without his special guidance. And I also would like to thank my former advisor Dr. D. H. B. Wicaksono, who introduced me to this research and gave me courage to complete this thesis.

My gratitude also goes to Dr. D J. Faber, Dr. D. M. de Bruin and Ir. P van Horssen at the Academic Medical Center at the University of Amsterdam. Thank you for giving me the opportunity to do my internship at their department and use their imaging systems. Their prolific and fruitful discussions helped me in this research. I consider it an honor to work with them.

I am indebted to my Prof. Dr. J. Dankelman and Prof. Dr. P. J. French for giving me the opportunity to work in their research group and for accepting being the members of the committee. I wish to thank P. Trimp for his help throughout this research. In addition, I am deeply indebted to all the people who helped me in my research.

Finally, I also would like to thank Dr. F. Mosch for his professional advises on dental implant.

CONTENTS

LIST OF FIGURES

LIST OF TABLES

LIST OF SYMBOLS

Parameter	Symbol
Intensity of the interference light	I_0
Electromagnetic field of light from reference arm	E_R
Electromagnetic field of light from sample arm	E_S
Optical path length of the reference arm	L_R
Optical path length of the sample arm	L_S
Optical path length between reference arm and sample arm	ΔL
Center wavelength of the incident light	λ_0
Field amplitude spectrum of the light	$s(\omega)$
Light frequency	ω
Time variation	t
Wave number	k
Light split ratio of fiber coupler to reference arm and sample arm	$T_R : T_S$
Electromagnetic field of light from source	E_{in}
Electromagnetic field of interference light	E_{out}
Light reflectivity	γ
Frequency response function	$H(\omega)$
Accumulated phase difference due to optical path length difference	$\phi(\Delta z)$
Modulus-squared average	$\langle\ \rangle$
Light speed	c
Group refractive index of air	n_{air}
Refraction index of medium	n_{med}
Inverse Fourier transform	FT^{-1}
Spectrum of light	$I(\omega)$
Maximal imaging depth in Z direction	z_{max}
Number of detectors in CCD detector array	N
Average refractive index of probing sample	n_{ave}
Imaging depth where signal-to-noise ratio is reduced to half	Δz_{-3dB}
Spectral resolution of spectral meter	$\delta_r k$
Coherence length of light source	l_c
Full width at half maximum	FWHM
Spectral width of the light source	$\Delta\lambda$
OCT axial resolution	r_z
OCT lateral resolution	r_l
Focal length of lens	F
Spot sizes of the beam on the objective lens	D
The Numerical aperture of the lens	$N.A.$
The depth of field	b
Angular spread of the Gaussian light	θ_S

Noise equivalent current	NEC
Electron charge constant	q_e
Photodetector response	S
Light source output power	P_0
Photodetector quantum efficiency	η
Planck constant	h
Center frequency of light	υ_0
Effective optical line width	$\Delta\nu_{eff}$
Signal-to-noise ratio	SNR
Variance of total noise	σ^2_{noise}
Electrical signal bandwidth	B
Light absorption coefficient in medium	μ_a
Light scattering coefficient in medium	μ_s
Light reduced scattering coefficient in medium	μ'_s
Anisotropic factor of light scattering in medium	g
Penetration depth of a certain reflected light	z
Ideal Intensity of the back scattered light from sample at depth z	$\bar{I}(z)$
Observed intensity of the back scattered light from sample at depth z	$I(z)$
Signal-independent random variable	f
Angle between the drill bit rotation axis and the output light path	α
Distance from the drill bit rotation axis and the fiber opening	d
Instantaneous rotational speed of drill bit in RPM	n
OCT sampling ratio	ζ
Image size	(M, N)
Sub-image size	(m, n)
Local mean	μ
Local variance	σ^2
Variance of background noise	σ^2_{bg}
Unfiltered image pixel value (with noise)	I
Filtered image pixel value (noise reduced)	$\hat{I}$
All ones matrix	O
Convolution operation	$*$
Weight coefficient of pixel $I(i,j)$	$W(i,j)$
Variance coefficient	C_u
Variance coefficient	C_i
Variance coefficient	C_{max}
Equivalent number of looks	L
Damping coefficient of filters	K
Mean of the entire image	μ_I
Variance of the entire image	σ^2_I
Gamma distribution	Γ
Peak Signal-to-Noise Ratio	PSNR
Signal-to-Mean Square Error	$\mathrm{S/MSE}$
Root Mean Square Error	RMSE

Structure Similarity Index	SSIM
Edge preserve factor	EPF
Contrast-to-Noise Ratio	CNR
Equivalent Number of Looks	ENL
Weight for image quality assessment	w
Edge detected image	ΔI
Maximum possible pixel value in image	I_{MAX}
Image convoluted with circular-symmetric Gaussian weighted filter	I'
A-scan lines interpolation ratio	i
Number of A-scan extracted in a single lateral resolution volume	n_{ascan}
Number of pixels between two uncorrelated pixels	n_{interval}
Downsampling threshold	ρ
A-scan redundancy ratio	ARR
Distortion ratio	DR
High speed rotational optical coherence tomography	$\mathrm{HSR\text{-}OCT}$

OCT SCANNING DIRECTION

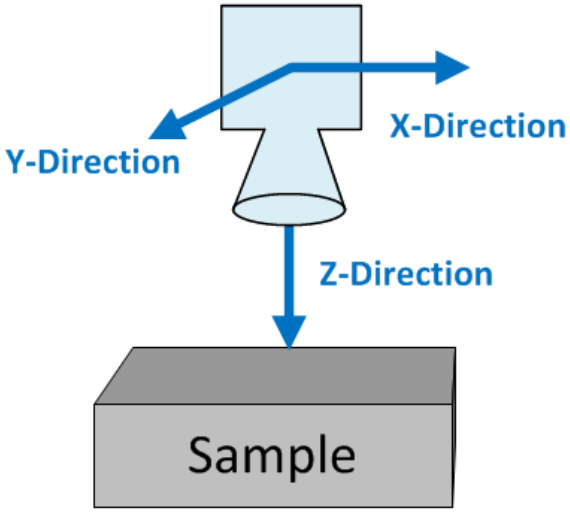

X direction (lateral scanning)	x
Y direction (lateral scanning)	y
Z direction (depth scanning)	z

CHAPTER 1

INTRODUCTION

1.1 Missing Tooth and Associated Problems

We lose our teeth as we age or by accident. Missing tooth has become one of the most common diseases that plague people life. The reasons of tooth loss can be categorized into two types, congenital and acquired. The congenital loss is caused by mistakes in genes (genic mutation) or decay. Study found that in USA, tooth missing is a very common developmental problem in children. And as a rule, one permanent tooth will be absent once its counterpart primary tooth is missing. For adult, the permanent teeth may lose due to surprising ways, including tooth decay, periodontal diseases, diabetes, drugs, smoking, accident, etc. Based on data from American National Center for Health Statistics, the average 20 to 39-year-old is missing 1 tooth, the average 40 to 59-year-old 3.5 teeth, and those aged 60 and over are missing 8 teeth [1].

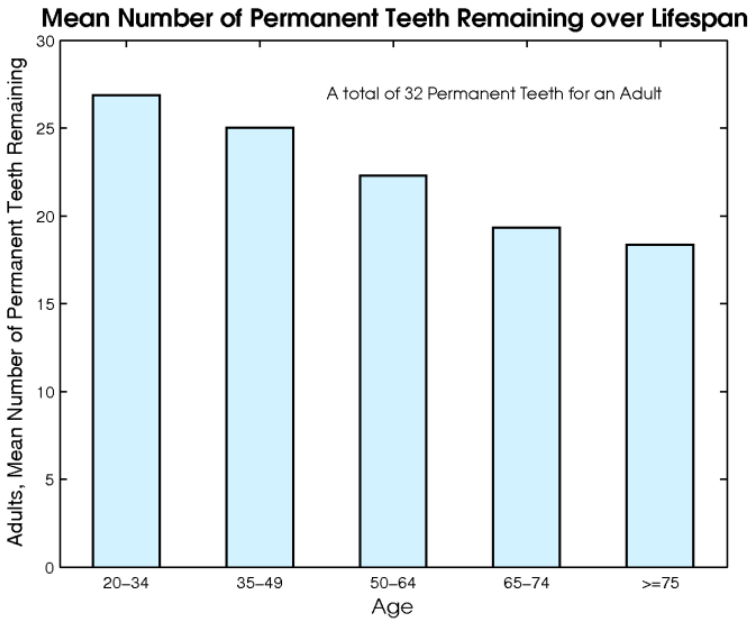

Figure 1. Tooth loss over lifespan for Americans (Adapted from reference [2])

Tooth loss can cause lots of problems. Tooth pain or sensitivity can occur immediately after tooth missing. Patients also feel inconvenience of eating and speech. They may feel lack of confidence of smiling and talking. In the long term, tooth missing can lead to teeth shift (the remaining teeth shift in with the purpose to fill in the gap left after tooth missing) and bone loss. Tooth missing can weaken the structure of the overall jaw, causing additional tooth loss. In addition, aesthetic problem will arise. Patient's face will begin to look prematurely aged since lack of tooth's or facial bone's support.

1.2 Dental Implant

Thanks to the rapid development of dental technologies, various dental treatments are offered to and improve oral health. Among them, dental implant/replacement is considered as the most effective and durable treatment that is widely used to replace one or more missing teeth since it offers more advantages than other traditional methods, like denture and bridgework. In additional to the remarkable success rate (over 90% in general), the implanted artificial tooth provides a natural looking that feels like your own tooth. And since the dental implant is integrated into the jawbone, there is no harm to the adjacent teeth, the patients have no need to worry about the bone loss and gum recession that often accompany the denture and bridgework [3].

1.2.1 Dental Implant Procedures

Before the dental implant surgery, there will be several meetings between the patient and the patient's dentist to discuss your options. The dentist will take a complete dental history and a thorough oral examination as well as some x-ray / CT images to determine whether the patient is a good candidate for the dental implant. For the good candidate, the dentist will assess the surrounding tooth and the jaw area. For the patients who have no sufficient bone for the implant, bone from own body will be grafted to create a better environment for the implant. This is known as onlay grafting.

The implantation of the dental implant involves two main steps and is preformed over a period of, normally, three to six months depends on the type of the missing tooth and the patient's oral condition.

First, the dentist needs to place the implant into the bone. In this surgery, the dentist will cut and open the gum to expose the bone where the implant is about to be placed. Next, a small diameter pilot hole is drilled in the bone. During this drilling, dentist need to stop few times to make sure the hole is prepared at the right place with right angle. Then the plot hold will be widened by some large drill bits until the hold matches the requirement. Once the implant is placed correctly, the gum tissue is positioned back and is sutured. The surgical operation is performed under local anesthesia.

Following this is a healing period. The bone begins to fuse with the implant once it is placed. This is known as osseointegration. The procedure usually lasts three months for the lower jaw and six months for the upper jaw.

After the healing period, a small surgery takes at the gum to expose the top of the implant. The dentist will screw down the titanium abutment into the implant. About four to six weeks later, the final permanent artificial tooth will be attached to the abutment once the gum tissue has matured and is well attached.

1.2.2 Dental Implant Failures

Although the dental replacement offers so many conveniences and benefits, there are still lots of questions associated with these surgeries because of the inherent limitation of the current dental imaging system. The images they provided are offline. During the dental surgery, there is no available

solution that can provide real time image. But during the surgery, the dentists are total blinded by the drill bit. The dentist cannot visualize the jawbone structure close to the drill bit. The drill bit may damage the nerve bundle and blood vessels in deeper part of jawbone. In literature survey, it was found that neurosensory disturbances occur for 7% of all placed implants/total teeth replacements [4, 5] and temporary sensory disturbances of the gingival tissues (32% to 45%) or tongue (11% to 16%) occur in patients reporting altered sensation after mandibular implant surgery [6]. For the ultimate goal of dental implant improvement, a dental drill system with integrated Optical coherence tomography (OCT) imaging system for real-time image feedback is under busy development at Delft University of Technology (TUD). The OCT is somewhat similar to ultrasound imaging system, but it uses infrared light instead of sound wave. The OCT system is compact and easy to integrate with many medical instruments and provides optical biopsy (the illumination of tissue by selected light and analysis of light returning from the tissue) at a very high resolution. The integration of the OCT allows monitoring the jawbone structure in the close vicinity of the drill bit in real time. The dentists can stop the drill bit before it get too close to the nerves or blood vessels.

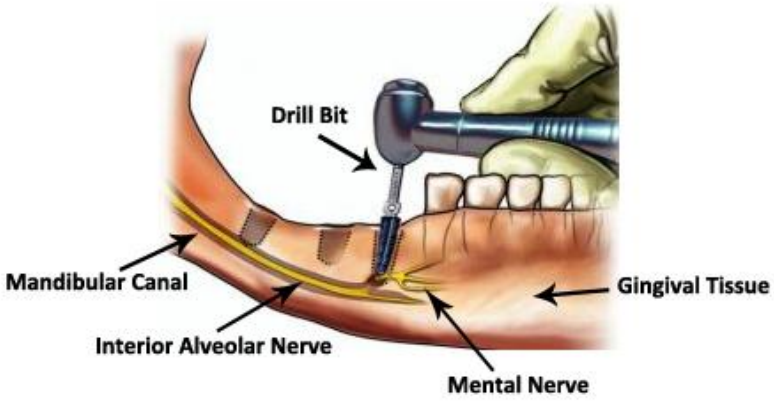

Figure 2. Mental nerve injury during dental implant surgery (reprinted with the permission from [7]). Interior alveolar nerve and mental nerve, which are plotted in yellow color, are located inside and protected by the mandibular canal (brown colored shell). During the dental drilling, the mental nerve is easily damaged by the drill bit because of the sight-blocking and lack of feedback.

1.3 Motivations and Objectives

As mention in subsection 1.2.2, some most common dental problems and side effects are caused because of the damage to the jaw structure and the inferior alveolar nerve or blood vessels. Dental implants are highly depended on the experience of the dentist. The highly-trained dentist must carefully plan the dental surgery to minimize the potential risks.

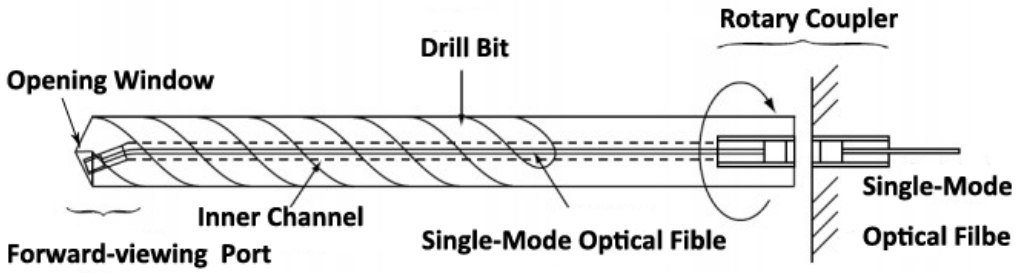

Figure 3. OCT optical fiber implanted drill bit, reprinted from reference [8]

In order to help the dentists to improve the implant success ratio and reduce patients' pain, at TUD, a new dental drill system (shown in Figure 3 above) is under development to offer real time image feedback to the dentist during the drilling procedure to prevent damage to the nerves and blood vessels.

As shown in Figure 3, the embedded optical fiber has a small opening window at the tip of the drill bit. During drilling, the light emitted from the single-mode optical fiber illuminates the tissues in the vicinity of the drill bit. To our best knowledge, it is the first time that to acquire OCT images in such a way (high rotational speed). The OCT images are subject to speckle noise. The high-speed rotation changes the speckle noise pattern and could degrade the acquired OCT images quality. Thus, to get a better understanding of the effect of the drilling speed on image quality, finding a proper method to suppress the inherent speckle noise, reconstruct image distortion due to rotational scanning and to find a way of tissue segmentation become vital requirements for the new dental drill system design. In this master project, these requirements will be studied, analyzed and discussed. Results and conclusions will be presented at the end of this report.

Another object of this master project is to find out a cheap material for future researches. Jawbone is biological tissue. The optical properties change due to degradation which can result in different experimental results. Besides, the acquisition and storage of jawbone also increase the cost of research. To solve the sample problem, one common way widely applied in OCT community is to use tissue phantoms [9]. In this research, silicone elastomer-based optical phantoms will be created and tested. The results from both animal jawbone and optical phantoms will be analyzed and compared to check the feasibility of using silicone elastomer-based phantom as a substitute for real tissues.

1.4 Thesis Organization

In this dissertation, Chapter 2 provides background knowledge about optical coherence tomography (OCT) and human jaw structure. The noise sources of an OCT system will be discussed.

In Chapter 3, the experimental setup used for the entire research is presented. The optical phantom modeling method of human jaw structure is introduced.

In Chapter 4, some commonly used speckle noise reduction algorithms and image quality assessments methods for OCT image enhancement will be studied. A modified cross correlation methods image reconstruction approach will be introduced and discussed in this chapter as well.

In Chapter 5, the OCT images obtained from the optical phantoms are presented. The speckle noise suppression method introduced in Chapter 4 will be evaluated with the intention of finding the suitable

despeckle filter for the high speed rotational OCT system. The feasibility of the modified cross correlation based image reconstruction method posted in Chapter 4 will also be checked with the obtained OCT images.

In Chapter 6, experiments are introduced to a pig's jaw to verify the results from the optical phantoms. The results from the real tissues will be analyzed and compared with that from optical phantom with the purpose of obtaining a proper method for optical phantom modeling for future work. The OCT dental tissue segmentation method for the high rotational application will be mentioned as well.

In Chapter 7, conclusions of this master project. Recommendations for future research will also be discussed.

CHAPTER 2

BACKGROUND KNOWLEDGE

2.1 Introduction

The OCT is a type of geometrical optical tomography that can acquire micrometer-scale resolution and three-dimensional images from biological tissues in vivo. The measurements of the cross sectional structure information depend on the backscattering or back reflection from the probing sample. The development of OCT provides the researchers one approach to observe tissue functional information, including oxygenation, perfusion, blood content, tissue viability and chemical characterization of malformations [9].

This chapter mainly supplies the jawbone anatomy and the relevant theory behind OCT system. In section 2.2, the anatomical structure of human jawbone as well as it optical properties will be carefully studied. The principles behind of OCT as well as general issues in OCT system designing are introduced and discussed in section 2.3. The noises sources, the inherent speckle noise in particular, are discussed and analyzed in section 2.4.

2.2 Human Jaw Anatomy

As mentioned earlier in chapter 1, in dental implant surgery, lots of the patients are suffered by pain or implant failures because of neurovascular bundle injuries during the implant surgeries. To avoid the injuries, the structure of human jaw must be carefully studied.

2.2.1 Jaw Structure

Human jaw is an opposable articulated structure that contains two main parts, mandible and maxilla. The mandible locates at the lower part and is moveable. Teeth grown in these two bones are used to grasp, manipulate and reproduce natural chew. Tooth is one of the hardest tissues of human beings. The hard material of tooth is composed of calcium, phosphorus, and other mineral salts. The tooth is surrounded and supported by the periodontium. A tooth consists of four main parts, from outside to inside, they are enamel, dentin, cementum and pulp. The tooth root goes into the deeper part of the jaw. At the end of the root, there is an apical foramen used to connect the blood vessels and nerves. The blood vessels supply the nutrients and oxygen to the tooth; whereas the nerves provide sensation.

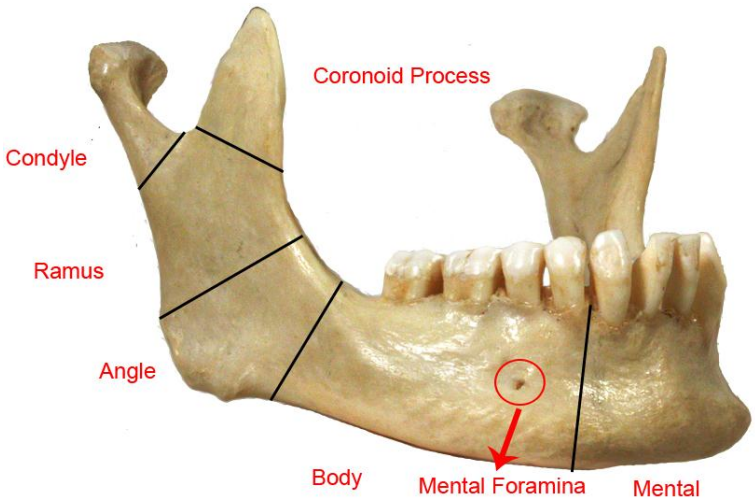

Figure 4. Mandible structure (reprinted from reference [10]). The inferior alveolar nerve is contains within the mandibular canal in the mandible to provide sensation to different dental tissues. The mandible canal is not labeled in this image.

In the mandible, there is a canal that gives passages to the neurovascular bundle, including the inferior alveolar nerve (IAN), inferior alveolar artery and inferior alveolar vein that are wrapped in a soft membrane. On the internal surface of the ramus, the neurovascular bundle enters into the mandible and passes through the mandibular canal. In the canal, IAN gives off some small gingival and dental nerves to the mandibular teeth. And at about the level of the mandibular 2nd premolars, IAN again branches out a new trunk of nerves, mental nerve. The mental nerve emerges and exits the mandibular canal through the mental foramen. The mental nerve supplies the sensation to the chin, premolars and low lip and associated gingival as well. The rest of IAN (mandibular incisive nerve) continues passes through the mandibular incisive as to supply sensation to the mandibular canines and incisors.

To avoid the neurovascular bundle damage and achieve a successful dental implant, a safety margin must be preserved. In reference [11], the recommended "safety zone" is 2 mm between the neurovascular bundle and the implant. And for some people who have anterior loops of the mental nerve mesial to the mental foramen, a safe guideline of 4 mm from the most anterior point of the mental foramen is recommended [12]. However, it is reported that the anatomical aspects (position, shape and size) of the mandibular canal and mental foramen are unreliable and possess many variations, including individual, gender, race and age.

In the conventional radiographs, the soft tissues are not observed directly since the soft tissues have a very lower electron density (X-ray attenuation) compared to the jawbone (Figure 5). As alternatives, some strategies are posted to help to locate the position of nerves. For example, the mental foramen is a strategically important landmark when performing the surgical procedures in the foramen area procedures [11]. However, this approach is imperfect enough because of the uncertainty of the mandibular canal and mental foramen. The inferior alveolar neurovascular bundle exists in different locations and possesses many variations [13]. Differences of the shape, location, size and even number of the mental foramen are found. The variations are induced by individual, gender, age and race [11, 14, 15]. The clear visibility of the mental foramen is only 49% in radiographs and 64% in panoramic radiographs.

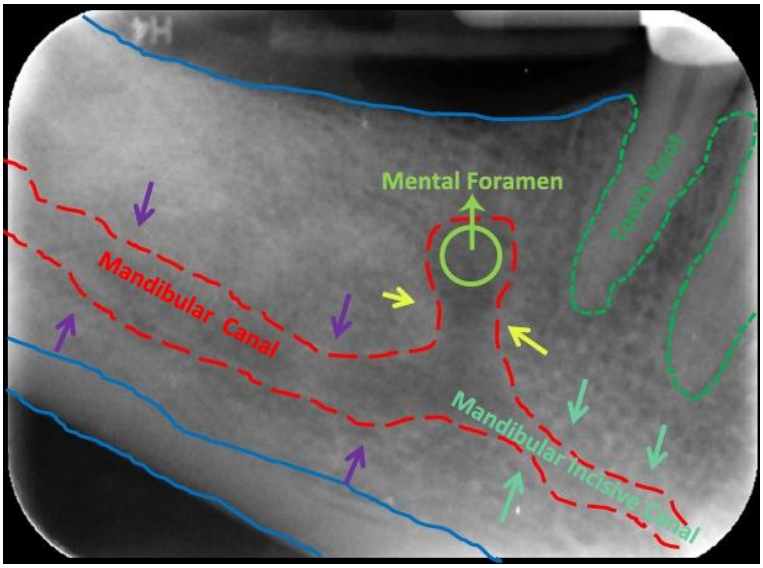

Figure 5. An X-ray image from human mandible. The red dash line outlines the position and the sharp of the mandibular canal (indicated by purple arrows) and the mandibular incisive canal (indicated by coral green arrows). The light green circle denotes the position of the mental foramen. Image reprinted from reference [16]

In addition, radiographs also have some shortages that make troubles to the dentists and implantologists. In our interview with Dr. Florian Mosch, he mentioned some implant failures were caused because of the lack of bone width information in x-ray images. In the surgeries, the drill bit can break through the jaw and hit the soft tissues nearby, if the drill bit is placed with a wrong angle or the patients whose jawbones are too narrow.

2.2.2 Dental Tissues' Optical properties

B. Colston et al. [17] first introduced OCT into dental diagnostic. OCT is the only imaging modality that can provide the structure both of the dental hard tissues and soft tissues. Compared to dental X-ray imaging system, the OCT can provide images with resolution 10 times higher than X-ray images; whereas the imaging depth of OCT (1300 nm, 15 mW) in dental hard tissues (enamel and dentine) and soft tissues are about 1.5 mm and 3 mm, respectively [17]. Light can penetrate deeper in hard tissue because than they contain less collagen than that in dental soft tissues

The researches on optical properties of human mandible are rare. One close reference [18] is by A.N. Bashkatov et al. in 2006. They measured optical properties from ten skull bones (including temporal bone, parietal and temporoparitetal bone) in vitro with light wavelength from 800 nm to 2000 nm. Their results are presented in the Figure 6 below.

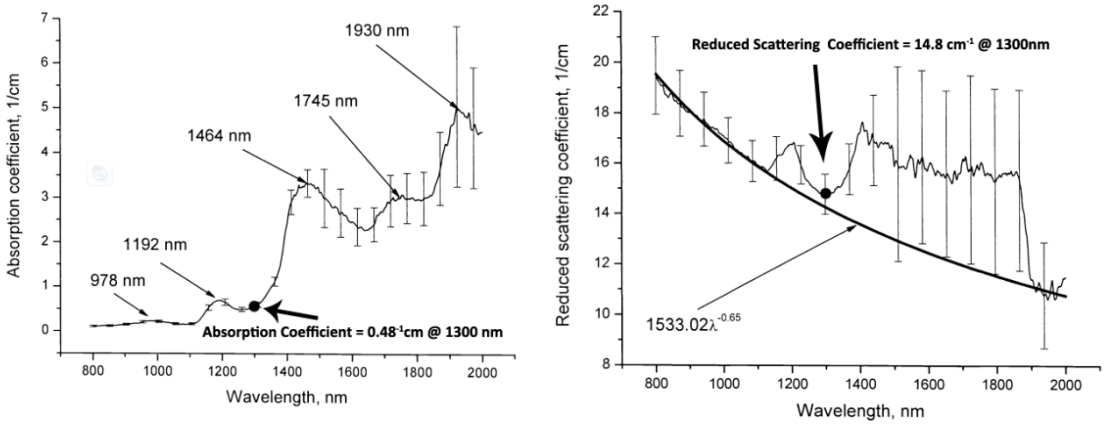

A. Wavelength VS. absorption coefficient

B. The wavelength VS. reduced scattering coefficient

Figure 6. The wavelength dependence of the optical properties of human cranial bone in vitro (reprinted from [18])

2.3 Optical Coherence Tomography

Optical coherence tomography (OCT) is a novel biomedical imaging modality that is based on low coherence interferometry. OCT works similar to ultrasound imaging system but utilizes the spatial and temporal coherence properties of optical waves backscattered from material or biological tissues [19]. As a new imaging system, OCT has widely been used in various fields of medicine and biology since it provides a noninvasive, nondestructive, ultra high resolution images. The axial resolution of OCT images usually locates in the range from 1 μm to 15 μm (discussed in more detail in section 2.3.3) that is one to two orders of magnitude higher that of other conventional medical modalities [20]. OCT can measure and acquire biological tissues or organs internal microstructure without contact or invasive. With all these unique features, OCT becomes an important image tool in various fields of medicine and biology.

OCT constructs images by measuring the back-scattering or back-reflected light from the illuminated samples. Light penetration depth is highly limited by the optical properties of the probing sample (absorption coefficient and scattering coefficient, discussed in subsection 2.4.2.1). Unfortunately, most biological tissues have high light scattering coefficients. Therefore, OCT can only provide sub-surface images with imaging depth 2-3 mm.

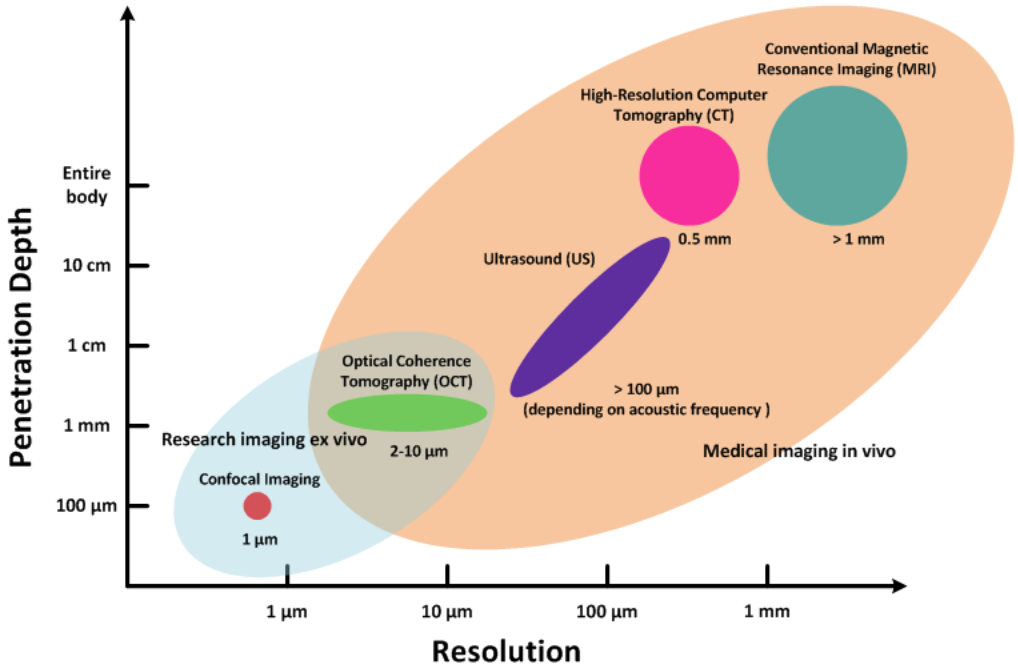

Figure 7. Comparison of OCT resolution and imaging depth with other medical imaging modalities. The axial resolution of OCT can vary from 1 µm to 15 µm depending on the optical source and numeral aperture of lens. In most biological tissues, the penetration depth is limited to 2-3 mm due to the high light scattering properties of the tissues. The confocal imaging has the same problem as OCT, its imaging depth is only few hundreds micrometers in most tissues. High frequency ultrasound can capture better resolution images but the penetration depth is shorter than low frequency ultrasound. CT and MRI can create images of nearly the entire body but the resolution is insufficient compared to the former imaging modalities. (Image adapted from [20, 21])

The outstanding abilities of OCT have attracted the attention of engineers and scientists working in the photonics field. OCT technologies have been rapidly developed in the last two decades, and there is a great shift in the method of OCT imaging. In general, there are three kinds of OCT: time-domain OCT (TD-OCT), spectral domain (or Fourier domain) OCT (SD-OCT) and swept source OCT (SS-OCT). In some papers, SS-OCT is referred to as optical frequency domain imaging (OFDI). The last two OCTs are also categorized as frequency domain OCT (FD-OCT).

2.3.1 Time Domain OCT

The TD-OCT is the traditional OCT technology that is in fact a reflectometry [22]. Figure 8 shows the schematic of a conventional TD-OCT system. In such system, a high power Gaussian spectrum superluminescent diode (SLD) is typically employed to generate the incentive light. The discontinuous light (light pulse) from optical source propagates through a single-mode optical fiber (to avoid light dispersion) and splits into two parts (typically 50/50) at the optical-coupler (also known as beam splitter). The two separated light beams then are guided into two arms, reference arm and sample arm, pass optical collimators and illuminate the objects ahead. The light reflected and back scattered will be collected by the lenses again and propagate along the fiber optics. These two reflected beams combine together inside the optical-coupler again. The resultant interference fringe will appear at the

interferometer output when the time delay of the two arms (optical path length difference) are equal but not when they are sufficiently mismatched [22]. The interferometric light lightens the photodetector followed by the single mode fiber. The light reflected from sample arm is weak, and the frequency of light is so high that hard to detect by electrical device directly. To solve this problem, the optical heterodyne detection is applied. In heterodyne detection, the photodetector measures the envelope (envelope signal is comprised by tracking the peaks values of high frequency signal and pretending that they are connected. The envelop signal is shown in Figure 8) magnitude of the interferometric light instead of measuring the magnitude of the interferometric signal (shown in Figure 8). The frequency of the envelope (envelope signal in Figure 8) is much lower than the light frequency. That's to say, the heterodyne detection can down shifted the signal from the optical band to an electronically tractable frequency range. In this way, OCT can obtain both a high axial resolution and a high sensitivity to light. In photodetector the measured light signal is converted to electrical signal. The digitalized signal from analog-to-digital coder is then post-processed into A-scan (depth-resolved reflectivity profile of the sample at focal point). The two-dimensional cross-sectional images are comprised by multiple successive A-scans obtained from a certain sample.

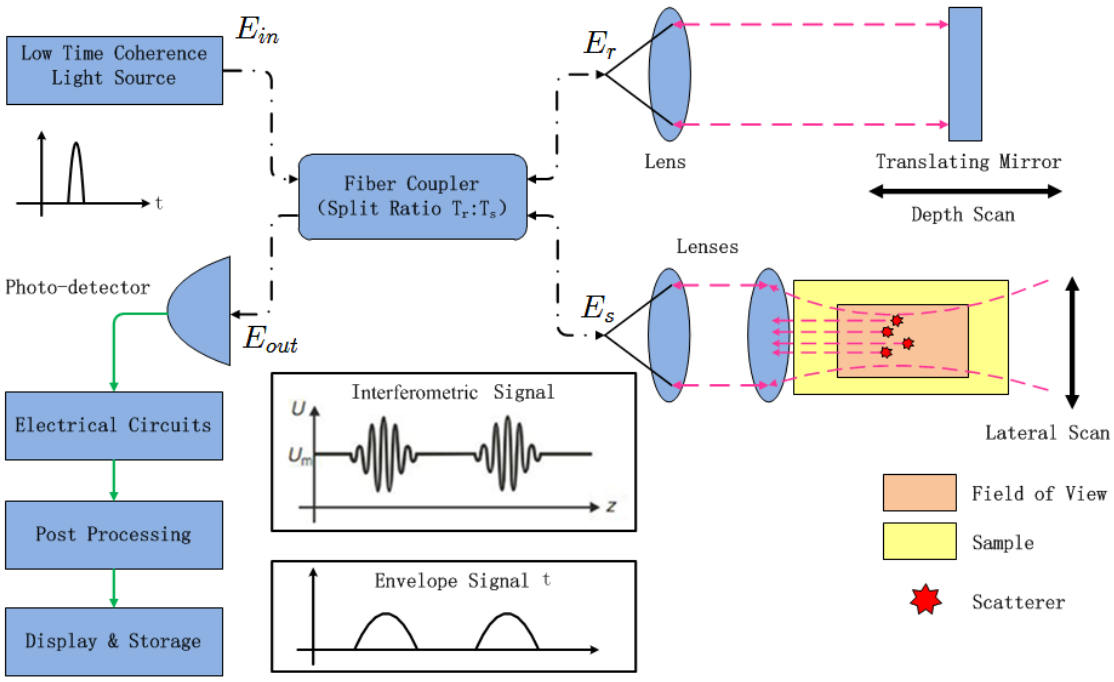

Figure 8. Schematic representation of a fiber based TD-OCT system. The combined coherence light from the fiber coupler is detected by a single photodetector. The envelope of the interference fringe is recorded by the detector and generates electrical signal. This signal is encoded and post processed for display and storage. The black dot-dash lines represent the optical fibers. The pink dash-lines depict the light paths in the free space. The green solid lines are the electrical lines.

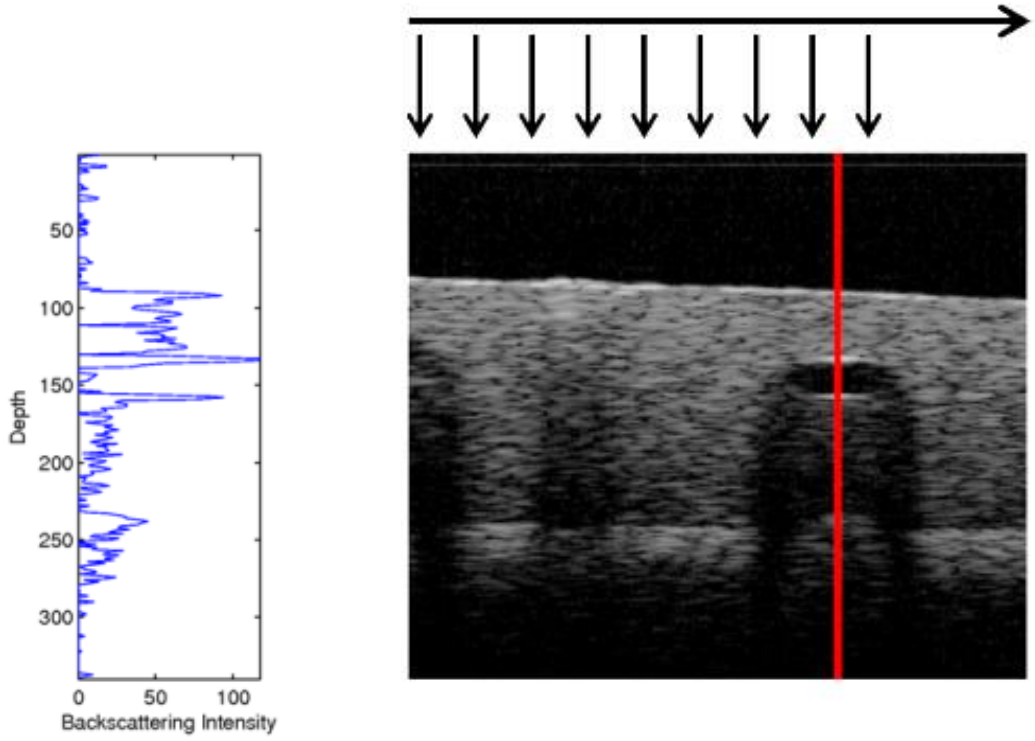

A. Backscattering intensity along depth direction

B. 2D OCT image

Figure 9. 2D OCT image generation. The 2D cross-sectional image (B), which contains much of successive A-scans (A), is constructed by performing lateral scanning over the interested sample.

The A-scan profile, or the sample structure along the depth direction is acquired by measuring the intensity of the interference light and "time of flight" of the light directly. In physics, the intensity of interference light of two coherence lights is described as:

$$I_0(t) \propto \frac{1}{4}\,|E_R|^2 + \frac{1}{4}\,|E_S|^2 + \frac{1}{2}E_S\,E_R\,\cos 2\frac{2\pi}{\lambda_0}\Delta L \tag{2.1}$$

In which: I_0 is the intensity of the interference light;

E_R is the electromagnetic field of light beam reflected from reference arm;

E_S is the electromagnetic field of light beam reflected from sample of interest;

ΔL is the path length difference of two lights defined as $\Delta L = |L_S - L_R|$;

L_R is the optical path length of reference arm (mm);

L_S is the optical path length of sample arm (mm);

λ_0 is the center wavelength of the light (nm).

The generated interference signal oscillates as a function of optical path length difference. The bright fringe only appears when the path length difference locates within the coherence length of the light source.

The photodetector is a square law intensity detection device. The light intensity it recorded is

proportional to the time average over the electromagnetic field multiplied by its complex conjugate Here, the electromagnetic field of the light is defined as a complex exponential formation [23]:

$$E(\omega, t) = s(\omega)\exp[-i(\omega t + k\Delta z)] \tag{2.2}$$

In which: $s(\omega)$ is the spectral amplitude of the light;

ω is the frequency;

t is the time variation;

k is the wave number defined as $k = \frac{2\pi}{\lambda_0}$;

Δz is the distance that accounts for phase accumulated throughout the interferometer.

Assuming the split ratio of the fiber coupler is $T_r : T_s$ $(T_r + T_s = 1)$. $E_{in}, E_{out}, E_s, E_r$ present the electromagnetic field of light in input arm, output arm, sample arm and reference arm respectively. For simplicity, the reflector in the reference arm is ideal who has a reflectivity equals 1 ($\gamma_s = \gamma_r = 1$). $H(\omega)$ is frequency domain response function describes the overall reflection from all structure distributed in the depth direction of the sample. Therefore, the electromagnetic fields of each port of the interferometer can be list as:

$$E_{in}(\omega, t) = s(\omega)e^{-i\omega t} \tag{2.3}$$

$$E_r(\omega, t, \Delta z) = (T_r T_s)^{1/2} E_{in}(\omega, t)e^{-i\phi(\Delta z)} \tag{2.4}$$

$$E_s(\omega, t) = (T_r T_s)^{1/2} E_{in}(\omega, t)H(\omega) \tag{2.5}$$

$$E_{out}(\omega, t, \Delta z) = E_r(\omega, t) + E_s(\omega, t, \Delta z) \tag{2.6}$$

Where $\phi(\Delta z)$ is the phase accumulated in translating the reference mirror by a geometric distance $\Delta z = \Delta t c / n_{air}$.

$$\phi(\Delta z) = \frac{2\omega n_{air}\Delta z}{c} \tag{2.7}$$

In which Δt is the corresponding optical time of flight difference;

c is light speed in air;

n_{air} is the group refractive index of air.

The factor 2 represents the round-trip of the light in reference arm. The optical path change is always twice the displacement of the translating mirror.

At the photodetector, the light intensity is the modulus-squared average of the electromagnetic field of the interference light [23, 24] given as:

$$\begin{aligned} I(\omega, \Delta z) &= \langle E_{out}(\omega, t, \Delta z) E^*_{out}(\omega, t, \Delta z)\rangle \\ &= \lim_{T\to\infty} \frac{1}{2T}\int_{-T}^{T} E_{out}(\omega, t, \Delta z) E^*_{out}(\omega, t, \Delta z) dt \end{aligned} \tag{2.8}$$

In which: $\langle\ \rangle$ denotes the temporal averaging;

$*$ denotes the complex conjugate of the corresponding field, for example, E_{out} and

E^*_{out} is a pair of complex numbers, both having the same real part, but with imaginary parts of equal magnitude and opposite signs.

By substituting Equation (2.6) into Equation (2.8), the interference light can be presented as:

$$I(\omega, \Delta z) = \langle E_s E_s^* \rangle + \langle E_r E_r^* \rangle + \langle E_r E_s^* \rangle + \langle E_s E_r^* \rangle \tag{2.9}$$

The first two terms denote the auto-correlation (self-interference) of the light. The last two terms are the cross-correlation of the lights from two different arms. Since the interference information is contained in the real part of the cross-correlation functions [20]. Then Equation (2.9) can be reduced to:

$$I(\omega, \Delta z) = \langle E_s E_s^* \rangle + \langle E_r E_r^* \rangle + 2\Re\{\langle E_s E_r^* \rangle\} \tag{2.10}$$

By substituting Equations (2.4) & (2.5) into Equation (2.10), we can obtain the frequency and path length depended light intensity as :

$$I(\omega, \Delta z) = T_r T_s S(\omega) \left|H(\omega)\right|^2 + T_r T_s S(\omega) + 2T_r T_s \Re\{S(\omega) H(\omega) e^{-i\phi(\Delta z}\} \tag{2.11}$$

Where $S(\omega) = \left|s(\omega)\right|^2$ is the intensity spectrum. This equation tells us that the internal structure of the sample can be obtained from both measurement in the time domain and frequency domain (refer to subsection 2.3.2).

For simplicity, assuming the light is split identically (use an ideal 50:50 optical coupler which $T_r = T_s = 0.5$) and neglect the power loss. Thus, the cross spectrum density becomes the spectrum of the light. Rewrite Equation (2.11) we have the interference signal obtained in each axial scan is given as:

$$\begin{aligned} I(\Delta z) = &\frac{1}{4} \int_{-\infty}^{\infty} S(\omega)(\left|H(\omega)\right|^2 + 1) d\omega \\ &+ \frac{1}{2} \Re\{ \int_{-\infty}^{\infty} H(\omega) S(\omega) \cos\{\phi(\Delta z)\} d\omega \} \end{aligned} \tag{2.12}$$

The first term describes the intensity only from the self-interference and the second is only contributed from the cross-interference.

The TD-OCT constructs sample internal structure by measuring the strength of the coherence light (Equation (2.12)) while recording the displacement of the translating mirror.

The TD-OCT acquires sample depth structure by rapidly translation the reflect mirror inside the reference arm. This mechanical movement limits the TD-OCT performance. In addition to the resolution, for any OCT imaging systems, imaging depth and sample rate are also important for system design. But for TD-OCT, these two features are hard to satisfy simultaneously. High imaging depth means low sampling frequency. The motion of the probing sample can create motion artificial and blur obtained images; however, a high sample rate but short imaging depth sometimes cannot meet the requirements of the clinical diagnosis. Another problem with TD-OCT is SNR drop-off. The SNR of OCT images degrades dramatically when the imaging depth is larger than 1mm ($z > 1\ mm$). Although this SNR drop-off can be compensated by using the a powerful light source with higher output, for some applications, especially the ophthalmic imaging, the incident optical power cannot be increased beyond the American National Standards Institute (ANSI Z1361) limit [20].

2.3.2 Frequency Domain OCT

Luckily, the development of frequency domain OCT (FD-OCT) have addressed this problem and have attracted attention from the worldwide OCT community. FD-OCT is another important implementation of OCT and was first proposed by Fercher et al. in 1995 [25] for ophthalmic research.c

In the FD-OCT system, instead of obtaining the depth profile of the sample by scanning the reference arm length, the resultant coherence light from the interferometer is analyzed with a spectrometer. The entire depth profile of the sample is simultaneously obtained by applying inverse Fourier transform to the measured spectrum of the interferometer. The absence of the mechanical movement in reference arm significantly improves the acquisition speed. Another advantage of FD-OCT is sensitivity. FD-OCT measures optical energy rather than optical power. The measured noise is lower than TD-OCT. It is reported, the average sensitivity of FD-OCT is commonly 20 dB higher than TD-OCT [26].

FD-OCT is based on spectral interferometery. From Equation (2.11), since the reference scanning is no longer performed, $\Delta z = 0$. Equation (2.12) is simplified to:

$$I(\Delta z) = \frac{1}{4} S(\omega)\{H(\omega) + 1\}^2 \tag{2.13}$$

That's to say, the sample response can be obtained by dividing the output intensity spectrum (n (2.13) by the measured source spectrum. The depth information can be obtained by converting the intensity spectrum $I(\omega)$ to time domain interference fringe pattern $I(t)$ via inverse Fourier transform (FT^{-1}).

$$I(t) = FT^{-1}\{I(\omega)\} \tag{2.14}$$

The FD-OCT has two distinct realizations: the spectral domain OCT (SD-OCT) and swept source OCT (SS-OCT).

In spectral domain OCT (Figure 10.A), the moveable reference mirror is replaced with a fixed reference mirror, the coherent light from the beam splitter illuminate the diffraction grating spectrometer. The frequency of the interference fringes as a function of the source spectrum encodes the optical path length difference. A larger fringe frequency results from a larger path length difference [27]. The formed spectral distribution of the light is recorded by a line CCD (charge-coupled device) or CMOS (complementary-symmetry metal–oxide–semiconductor) detectors array. The different detectors on the detector strip correspond to different frequencies of the interference light. The different frequencies of the interference light contain the cross sectional information at different depth. In medical, this interference fringe which contains both frequency and phase information is represented in K-space (K-space is an extended Fourier space). The scatters' depths are analyzed by calculating the Fourier-transform of the recorded data. In additional to the sensitivity and imaging depth, the stationary scanning mechanism greatly increases the sample rate, and reduces the influence of the movement from the imaged samples. And the A-lines acquisition speed is only limited by the speed of detectors array frame transfer rate and the computer calculation time to perform the inverse Fourier transform of the detectors acquired raw data into A-scan information.

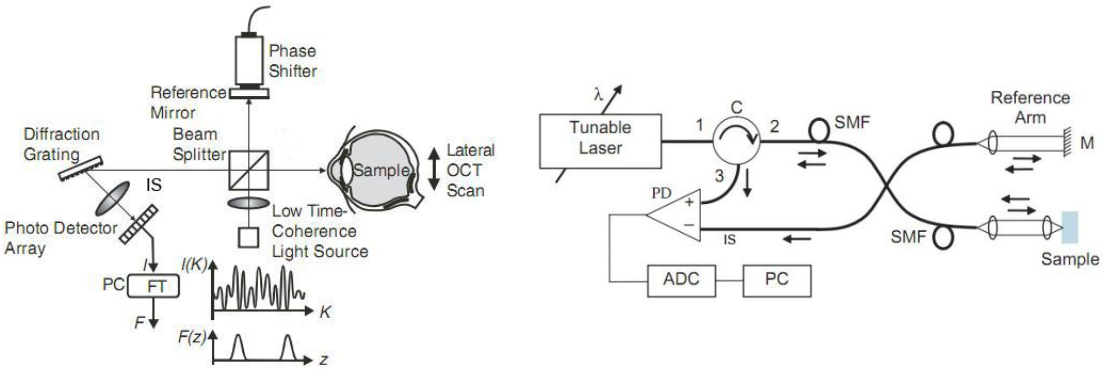

A. Spectral domain OCT B. Swept soure OCT

Figure 10. Schematic representation of two FD-OCT systems (reprinted with the permission from [28]).IS: Interference signal; FT: Fourier transform; PC: personal computer; K: K-space information; Z: depth (Z) profile; PD`: photodetector; ADC: analog-to-digital coder; SMF: single mode fiber; C: circulator; M: mirror. In B, the SS-OCT employs the heterodyne detection with purpose of achieving a high sensitivity and SNR.

The imaging depth of the SD-OCT is highly depended on the number of the detector (N) in the line CCD array. Since in a real SD-OCT system, the maximal imaging depth is linear to N and inverse proportional to the average refractive index (n_{ave}) of the probing sample.

$$z_{max} = \frac{1}{4n_{ave}} \frac{\lambda_0^2}{\Delta\lambda} N \tag{2.15}$$

The swept source OCT (Figure 10.B), also called optical frequency domain image (OFDI) in some documents, is another variation of frequency domain OCT that has recently attracted considerable attention. SS-OCT tries to combine both the advantages of the TD-OCT and SD-OCT by encoding the spectral information in time. SS-OCT employs a different light source. It rapidly sweeps a narrow linewidth laser through a wide optical bandwidth. The benefit from this narrow band source is an increase in SNR since the drop-off due to finite wavelength resolution in SD-OCT no longer exists. For a SD-OCT, the SNR is not the same through the whole depth scan range because of the fixed reference mirror. The SNR decreases as the path length difference between reference and sample arms increases , usually an overall decrease of approximately 20 dB over the whole axial depth [29]. This SNR-drop results from optical resolution limits of the spectrometer, finite pixel width, aliasing at high spatial frequencies, and inter-pixel cross-talk in the spectrometer [30]. The -3dB drop-off point in depth direction is defined by Equation (2.8) [31]:

$$\Delta z_{-3dB} = \frac{2\ln 2}{\delta_r k} \tag{2.16}$$

In which:

Δz_{-3dB} is the imaging depth (z direction) where the image SNR is reduced to half (-3dB);

$\delta_r k$ is the spectral resolution (resolving power) of the FD-OCT system which is defined as $\delta_r k = \frac{\lambda_0}{\Delta\lambda}$, λ_0 is the center wavelength of the incident light, $\Delta\lambda$ is the spectrum width.

The short coherence light, with a much narrower beam width, from SS-OCT lowers the wavenumber so that the SNR drop-off can be neglected. Another advantage of the SS-OCT is its detector. For a simple SS-OCT system, a low cost, high speed photodetector is enough and the spectrometer and line CCD camera are not required. For the more, the balanced detection, as same as that used in TD-OCT, can also be applied to improve the images' SNR. The sample frequency and axial resolution of SS-OCT systems are fully determined by the tunable light source. A wider optical wavelength sweep range gives a fine axial resolution and a faster sweep rate leads to a rapider scanning frequency [29].

2.3.3 OCT General Performance

OCT is designed based on measurement of the back-scattered light. The general performances of an OCT system are heavily determined by the light source and the optical properties of the investigated tissue.

The most common light sources used for OCT systems are superluminescent diode (SLD) The SLD is an edge-emitting semiconductor light source based on superluminecence that has the advantages of both the laser diode and the light emitting diode (LED). SLD can offer high-power, low coherence and broadband spectrum infrared light as the requirements of OCT.

In the OCT community, the light with a Gaussian spectrum is preferred and well established since two reasons [20]. First, the Fourier transform of a Gaussian spectrum remains a Gaussian function. There are no side-lobes (Figure 11.A) in the interference fringe envelope. The second arises from the consideration of the blindness. For a non-Gaussian spectrum, its tail of axial point spread function is usually sufficient broad that a weak reflection place next to a strong reflection can be obstructed (Figure 11.B). But for a Gaussian spectrum, its tails decay exponentially with the squared path length mismatch that he blind area is minimized to some extent.

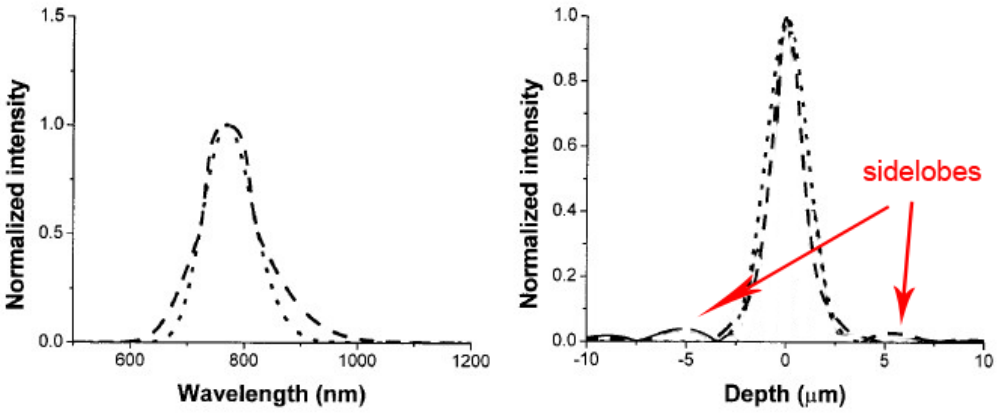

A. Sidelobes of coherence light using a non-Gaussian light source. In the left picture are two different light sources: the dashed curve is the spectrum of a non-Gaussian light, dotted curve represents soectrum of a Gaussian light. These two lights have the same full width at half maximam (FWHM, for Gaussian-type light, it equals the bandwidth of the light). In right are the plots of the resultant interference fringes of these two light beams. The sidelobes appear when the non-Gaussian light source is applied (dashed line). Reprinted from [32].

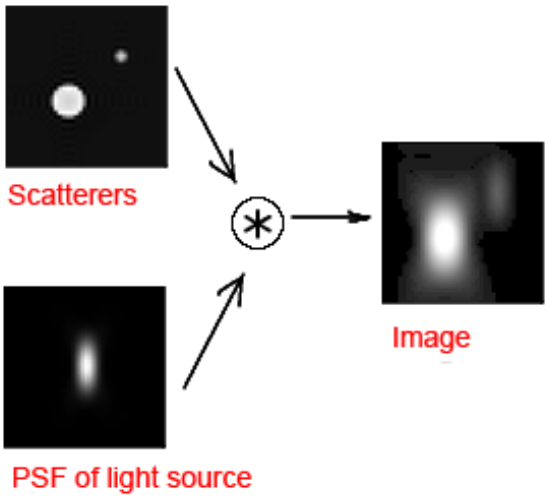

B. Blindness of beads when using a non-Gaussian light source. At the upper left, two scatterers (big and small) are shown. The lower left is the point spread function of the light source. Its axial direction is relatively broad compared to lateral direction. The large right image shows the observed image. Thus, we can imagine that if the small objects were located right above the big one, the two spots in the right image will be superpositioned. The weak reflection from the small object is covered by the large one. Reprinted from [32].

Figure 11. Comparisons of Gaussian and non-Gaussian light sources

One important specification of an OCT system is axial resolution who directly determines the sensitivity and diagnostic capability of an OCT system. In OCT community, the axial resolution is generally defined as half the source coherence length l_c. For a source with a Gaussian spectral distribution, the coherence length equals the full width at half maximum (FWHM) of the source since the detected interference signal of the OCT system is the electric field autocorrelation of the light source.

$$r_z = \frac{l_c}{2} = \frac{FWHM}{2} = \frac{2\ln(2)}{\pi}\,\frac{\lambda_0^2}{\Delta\lambda} \tag{2.17}$$

Where $\Delta\lambda$ is the bandwidth of the light spectrum.

In clinical research, OCT with high depth resolution is appreciated since it enables a superior observation of physics activities or pathological changes of biological samples. Equation (2.17) tells us that the OCT axial resolution can be improved by increasing the light source spectral bandwidth. However, in practical, it is unrealistic. As is well known, light refraction index depends on the wavelength. For the non-monochromatic light, the different frequencies waves propagate at different speed in the sample and lead to different “time of flight”. This time difference introduces additional

phase to the Fourier components. The unbalanced dispersions from two arms will cause OCT images' distortion. For the high resolution OCT, the dispersion becomes a critical factor that degrades the axial resolution and imaging depth. In addition, the dispersion will also lower the OCT image contrast. For high resolution OCT, the dispersion must be compensated by software or hardware before image reconstruction. Besides, it is reported that to use a light with center wavelength near 1 μm can significantly reduce the dispersion in biological tissues [33].

Another important resolution of OCT is lateral resolution. For an assumed Gaussian profile, the lateral resolution is equal to the size of the focal spot and is simply governed by Rayleigh length of OCT probe focal lens (illustrated in Figure 12). Typically, the lateral resolution r_l is inverse proportional to the lens' numerical aperture.

$$r_l = \frac{4\lambda_0}{\pi}\frac{F}{D} \approx \frac{2\lambda_0}{\pi \cdot \mathrm{N.A.}} \tag{2.18}$$

Where $\mathrm{N.A.}$ is the numerical aperture of the OCT scan lens, F is the focal length of the lens and D is the spot diameter of beam on the objective lens.

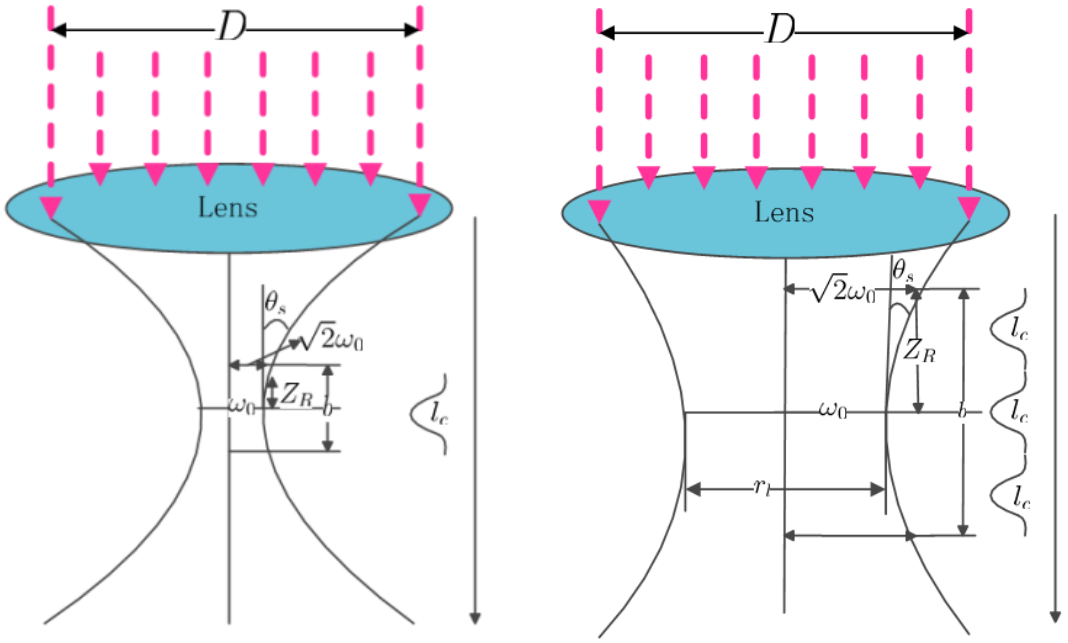

A. Focal lens with high numerical aperture B. Focal lens with low numerical aperture

Figure 12. Focal lenses with different numerical apertures. θ_S denotes the angular spread of the Gaussian beam. l_c is the coherence length of the incident light. The relation between numerical aperture $\mathrm{N.A.}$ and θ_S is given as $N.A = n_{\mathrm{med}} \times \sin\theta_S \approx D/2F$ in which n_{med} is the index of refraction of the medium; Z_R is the Rayleigh length which represents the distance along the propagation direction of a beam from its waist ω_0 (the minimum width value of the beam spot) to the place where the area of the cross section is doubled; b is the depth of field.

Although fine lateral resolution can be archived by applying a large numerical aperture lens in, it also produces decrease in the depth of field (the range of distances in object space for which object points are imaged with acceptable sharpness, b,shown in Figure 12 above) of OCT. The length of axial depth of field of OCT is twice the Rayleigh length and it is also related to the depth of field.

$$b = 2Z_R = \frac{\pi \cdot r_l^2}{\lambda_0} \tag{2.19}$$

By substituting Equation (2.18) to Equation (2.19), the relation between depth of field and numerical aperture is:

$$b = \frac{4\lambda_0}{\pi \cdot \text{N.A.}^2} \tag{2.20}$$

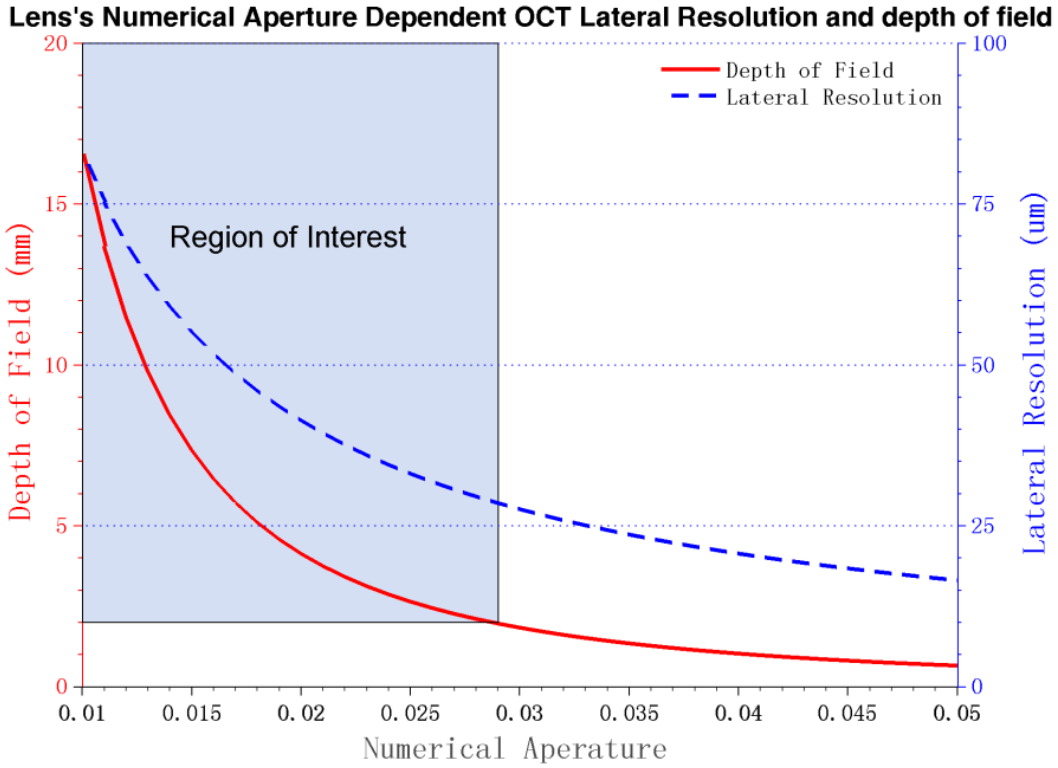

Figure 13. Lens's numerical aperture dependent OCT lateral resolution and depth of field. The calculations are based on Gaussian spectrum light with center wavelength of 1300 nm. Depth of focus indicates the range of distance in the object space for which the probed object can be imaged with an acceptable sharpness.

Figure 13 above illustrates the influence of lens' numerical aperture on OCT's lateral resolution and depth of field. The dramatic decrease of depth of field offsets the improvement of lateral resolution as a means of increasing numerical aperture, since the depth of field is inversely proportional to the square of lens' numerical aperture. Thus, to choose a proper objective lens for FD-OCT has become too important for FD-OCT system designing, since FD-OCT acquires entire A-scan profile simultaneously. To maintain the sharpness of image with a sufficient imaging depth, it is necessary to sacrifice the physical transverse resolution. According to 2 mm safety zone for dental implant, the applied objective lens of our designing OCT image guided dental drill system should have a numerical aperture not larger than 0.03, assuming 1300 nm Gaussian spectrum.

In addition to the depth limitation, a high N.A. lens also meets the problem of spherical aberration causing by the refractive index mismatch. Dispersion of the sample light also increases significantly with N.A..

Since OCT always has a much better physical axial resolution that one order of magnitude higher than its physical lateral resolution. To display illuminated object properly, conventionally, the images can be compensated in lateral direction by means of, for example, interpolation.

2.4 OCT Noises

As a medical imaging tool, high signal-to-noise ratio (SNR) is intuitively expected for the obtained OCT images. However, as other imaging systems, the presence of various noises contaminates OCT images. The noises degrade the image quality, lower the image contrast, blur the edge features and cover the useful diagnosis information. To understand the source of these noises is important for OCT system design and OCT image processing. In this subsection, the origin of noises in the OCT system will be studied.

In a real OCT system, the existing noises can be categorized into two types. The noises arise from any optical-, electrical- or optoelectronic-component in the system. The other is the inherent speckle noise originates from OCT signal acquisition method.

2.4.1 System Noise

In an OCT system, the primary system noises include thermal noise, shot noise, excess noise, relative intensity noise [20, 34]. They must be properly processed to improve OCT signal-to-noise ratio (SNR).

In some papers, the thermal noise is referred to as receiver noise [35, 36],and it is not related to the power of the light from reference arm [34]. The thermal noise originates from the energy exchange between the environment and the light receiver (photodetector or CCD array). The shot noise arises from current fluctuations. The charge emitted by the optical detector is random and discrete [20]. The shot noise follows the Poisson distribution when light power is small. When increasing the light power, the shot noise increases too and its distribution can be considered as normal distribution. The excess noise is due to the multiplication process at a gain M in the detector and is determined by detector's quantum efficiency limit. The above three noises are co-related and depend on the powers of light from OCT two arms.

	TD-OCT	**FD-OCT**
$\sigma^2_{thermal}$	$\mathrm{NEC}^2 B$	$\sigma^2_{read}+\sigma^2_{dark}$
σ^2_{shot}	$2q_e S P_0(T_s\gamma_s+T_r\gamma_r)B$	$\frac{\rho\eta\tau}{h\nu_0}\frac{P_0}{N}(T_s\gamma_s+T_r\gamma_r)$
σ^2_{excess}	$\frac{(1+\Pi^2)}{\Delta\nu_{eff}}S^2\cdot P_0^2(T_s\gamma_s+T_r\gamma_r)B$	$\frac{1+\Pi^2}{2}\left(\frac{\rho\eta}{h\nu_0}\right)^2\tau\cdot\frac{P_0^2}{N^2}(T_s\gamma_s+T_r\gamma_r)^2\frac{N}{\Delta\nu_{eff}}$

Table 1. The theoretical variances of system noises for TD-OCT and FD-OCT system. NEC is the noise equivalent current in $pa/\sqrt{Hz}$; B is the electronic bandwidth; q_e is the electron charge; $S=\eta q_e/h\nu_0$ detector response; P_0 is the output power of the light source; η is the detector quantum

efficiency;h is the Planck constant; v_0 is the center frequency of the light; Π is the degree of the polarization; $\Delta\nu_{eff}$ is the effective optical line width defined by $\Delta v_{eff} = \left[\int P(v)dv\right]^2 / \int P^2(v)dv$. (adapted from [35])

The system SNR for OCT is defined as [20]:

$$SNR = \frac{P_{signal}}{\sigma^2_{noise}} \tag{2.21}$$

In which σ^2_{noise} is the variance of the system overall noise.

Biological tissues are infrared light in transparent, the light reflected from biological sample is weak. The power of interference signal is dominated by the reflection from reference arm. In Equation (2.21), the SNR is inverse proportional to the power of the interference light ($P_{out} = T_S P_S + T_R P_R$). The split ratio for the fiber coupler must be carefully to keep the OCT system has high sensitivity (SNR). In reference [37], it suggested to keep the detection sensitivity (obtained from Equation (2.21)) of greater than 105 dB to provide sufficient penetration depth for accurate diagnosis and quantitative evaluation of tissue properties.

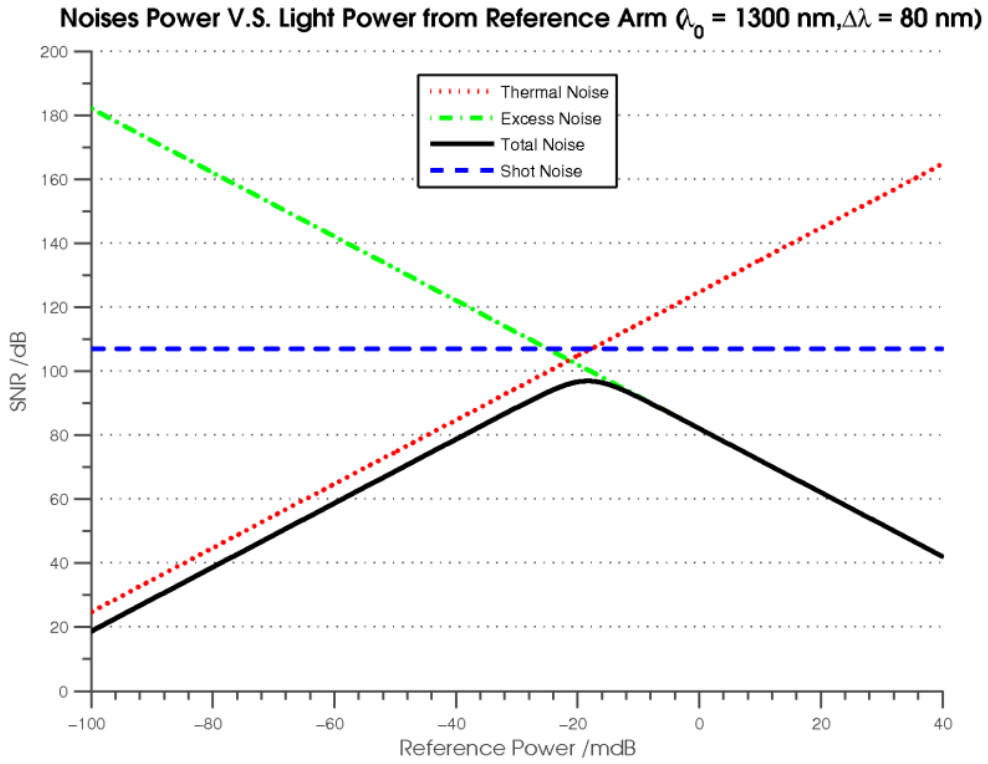

Figure 14. Theoretical sensitivity of a TD-OCT system. Light profiles are: center wavelength 1300nm, spectrum width 80 nm and polarization is 1. The reflected light power from sample arm is assumed to 1 mW. The reflectivity of the reference arm is 1. Bandwidth of electrical signal $\overline{I}(z)$ is 100 KHz, quantum efficiency f is 0.65. The OCT system operates at the room temperature. Please note, the related intensity noise is neglected in this simulation.

In Figure 14, the theoretical SNR of a TD-OCT is simulated. It clearly demonstrates that the TD-OCT has the best SNR when the shot noise is the dominate noise. Summarizing, to optimize system

sensitivity, the OCT must work under the shot noise limit [20, 35].

The relative intensity noise generates (RIN) due to the instability of the output power of the light source. For OCT, the RIN includes any noise source whose power spectral density scales linearly with the mean photocurrent power. Besides the fluctuations of light output power, the mechanical movement of the reflector in the reference arm (for TD-OCT only) also results in RIN [20]. RIN is a common mode noise that can be suppressed by balanced detection to some extent.

In addition, in an OCT system, some other electronics noises are presented. But in practical, the electronica circuit and components are always carefully designed and chosen, their noise level is much smaller than that of the noises mentioned previously. There are generally neglected.

2.4.2 Speckle Noise

The word “coherence” in optical coherence tomography indicates that this new imaging modality relies on interferometry technique by measuring the back-scattering light from the interested samples. However the “coherence” gives rise to speckle [19], which degrades the OCT image contrast, blurs the locations of boundaries between regions. Image processing is difficult in noisy image since noise changes image spatial and temporal features. Therefore, the source of speckle noise in OCT must be carefully studied.

2.4.2.1 Tissue optical properties

Before going into speckle straightforward, another issue must be figured out: what is happening when sample is probing. As mentioned earlier, the heterodyne detection is applied in OCT system since the light from the probing sample is rather weak compared to reflection from reference arm. The light power degradation is caused due to the interactivities between the light and the illuminated tissues.

In OCT, the light attenuation is mainly determined by both absorption and scattering. In physics, these two phenomena can be explained by quantum electrodynamics. In nature, any substance is comprised of discrete electric charges. When the material is illuminated, the electrical charges are excited and set into oscillatory motion by the electric field.

The absorption happens when the frequency of the electric field equals or near equals the nature frequency of the electric charges. Electric field energy from incident light is transferred to the charges. The resonance occurs and the amplitude of the vibration of the charges is greatly increased. The accelerated chargers impact with one another and lose its energy [38]. Most of the lose energy is dissipated as heat in the absorbing material. The absorption coefficient varies with the light wavelength depending on the tissue composition.

Different to light absorption, the light scattering happens when the incident light frequency is not corresponding to the natural frequency. The charger is excited and forced to vibrate at the frequency of the incident electric field. The magnitude of the motion is relatively small since the charger is bounded by a force. The charger emits light when it decays from a higher energy level to a lower energy level. Since the vibration magnitude of the charger is small, the amplitude of the resultant light is much

smaller than that of incident light [38]. The re-emitted light normally has the same frequency as that of the exciting light that the scattered light can be thought of as the propagation direction of incident light is redirected when it encounters a scatterer. Light scattering has two theoretical frameworks:

- Rayleigh scattering: the wavelength of the incident light is much longer compared to the diameter of the scatterer (also known as scattering center). The intensity of Rayleigh scattering highly depends on the wavelength and the diameter of the scatterer and increases rapidly as the ratio of the diameter to wavelength increases;
- Mie scattering: In Mie theory there is no size limitations. It can be used to calculate light scattering from a large scatterer. Mie theory is widely used to describe scattered light from biological tissues since the sizes of scatterers (such as hemoglobin, melanin [39], collagen, tubules [40] and organelles [41]) in biological tissues are quite larger compared to light wavelength. The Mie scattering in living tissue is discussed in reference [41].

The absorption and scattering properties of a material are quantitatively characterize ass absorption coefficient (μ_a) and scattering coefficient (μ_s). They are determined by wavelength of the incident light and the optical characteristics of the biological tissue. In OCT, the light wavelength usually used locates in the range from 600 nm to 1300 nm (the so-called "therapeutic window"). In this certain range, the absorption coefficient μ_a in most tissue is less than the scattering coefficient μ_s by two to three orders of magnitude. The absorption coefficient becomes appreciable when the wavelength of the light approaching 1900 - 2000 nm due to water absorption [20].

Another common property referred in many papers is the reduced scattering coefficient. This value (μ_s') is a lumped property incorporating the scattering coefficient μ_s and the anisotropy factor g [42]:

$$\mu_s' = \mu_s \times (1 - g) \tag{2.22}$$

The anisotropic factor g as a function of the cosine of the scattering angle θ measures the degree of anisotropic in scattering. For back scattering light, g is commonly default to 0.9 since this value is typical for the biological tissues in the near infrared spectral range [18].

2.2.2.2 Source of Speckle Noise

As mentioned earlier, OCT constructs samples internal structure by means of measuring the spatial and temporal coherence of back-scattering light from sample using heterodyne detection. The measurement technique is the essential of OCT but also leads to speckle noise, which is inherent to OCT imaging system.

Speckle noise is a stochastic, deterministic interference pattern in an image formed with coherent radiation of a medium containing many sub-resolution scatterers [43]. And it has no obvious relation with the texture of the rough surface where the back scatter comes from. The speckle noise pattern of an given OCT image can be affected by lots of factors, including the size and temporal coherence of the light source, motion of the object, the aperture of the photodetector, phase aberration of the propagating light, and light multiple scattering in the samples (shown in Figure 15) [19].

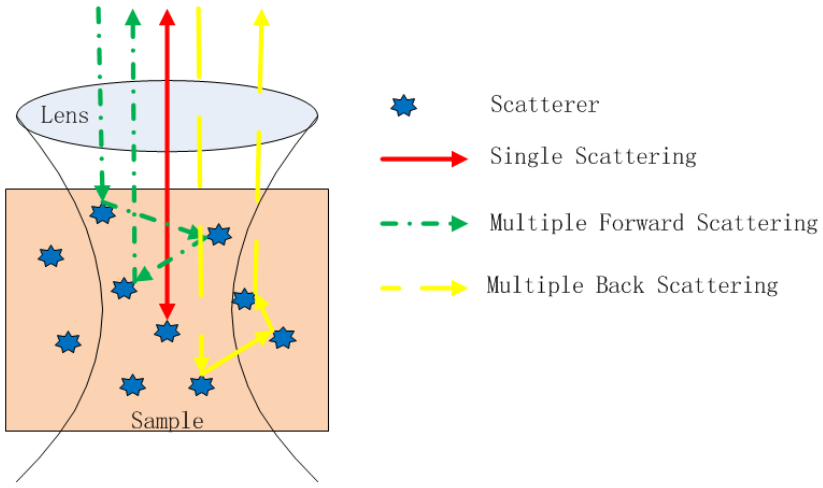

Figure 15. Illustration of light scattering in sample. The blue stars represent the scatterers in an imaged sample. The red solid arrows show the optical path of the single scattering, in which the light only interacts with one scatter. The green dash-dot and yellow dashed arrows show two examples of multiple scattering.

The observed scattered light from sample path is contributed by three main terms: the single-scattering contribution, the multiple scattering contribution (Figure 15) and the cross relation (refers to the coherent mixing of the unscattered and the multiple scattered light) [19, 44]. The multiple scattering is abundant in OCT images and is considered as a type of speckle noise since it reduces the correspondence between the local density of scatterers and the intensity variations in OCT images [19].

To eliminate the effect of the signal-degrade speckle, many analytical models are created including the most advanced Monte Carlo radiation transport model and the extended Huygens–Fresnel model. However, for simplicity, the most common model used is based on Beer-Lambert law [45]. In this model, only the single-scattering is taken into account. Similar to the ultrasound imaging system, the measured light strength is proportional to an exponential decay (with time):

$$\bar{I}(z) = I_0 \exp(-2\mu_s z) \tag{2.23}$$

In which: $\bar{I}(z)$ is the intensity of back scattered light from depth z;

z is the penetration depth of the reflected light.

The inherent speckle noise in the OCT image can be modeled as the multiplicative random noise [45]. For a single pixel in the OCT image, the noise corrupted pixel can be described as:

$$I(z) = f \times \bar{I}(z) \tag{2.24}$$

In which: $I(z)$ donates the observed value of the pixel at depth z;

$\bar{I}(z)$ is the ideal pixel value without noise corruption at depth z;

f is the signal-independent random variable whose probability density function (PDF) depends on the image type. Usually, a widely adopted assumption of speckle's PDF is it

follows an exponential distribution $p_u(z) = \begin{cases} \exp(-z) & z \geqslant 0 \\ 0 & \text{otherwise} \end{cases}$ [45].

Equation (2.24) shows that the speckle noise is highly depend on the local image intensity. We can conclude that, in an image, "*a brighter area will be more corrupted than a low-intensity area"*[45]. This is consistence with the statistical properties of speckle mentioned in reference [19] that *"the appearance of speckle noise has no obvious dependence on depth".* The observed speckle noise is primarily contributed by the multi-scattering.

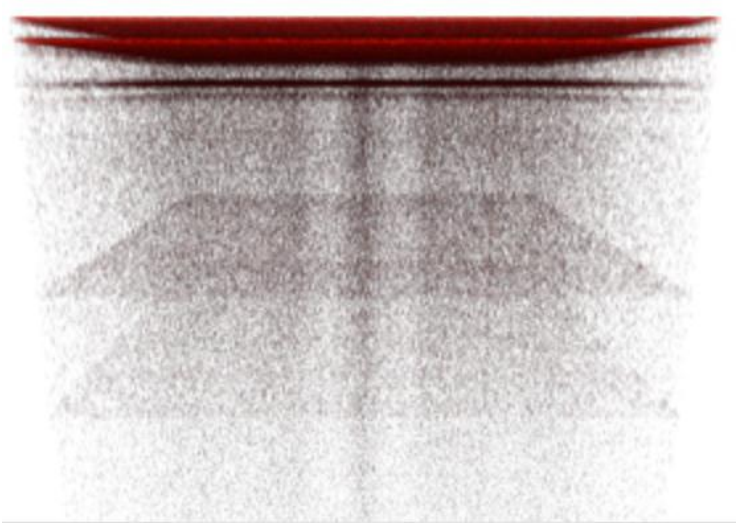

Figure 16. Illustration of speckle noise. An infrared view card (VISUALIZE™, Applied Scintillation, Harlow, UK) is illuminated by SS-OCT. The bright spots, especially at the deeper part, result from the multiply scattering which changes optical path length significantly. The overall depth of the image is about 3.5 mm. The image is contrast enhanced for well display.

Speckle introduced by the sample volume plays a dual role in OCT images: noise source and microstructure information carrier. The signal-carrying speckles originate from the large scatterers in the sample volume; whereas the signal-degrading speckles come from light scattered by small scatterers outside the sample volume and accidentally interfere with reference light. A proper designed optical scanner can reduce the signal-degrading speckle to some extent. But, the remaining is hard to discriminate since they show same amplitude as the signal-carrying [19]. In the chapter 3, the influence of the speckle noise on OCT images will be continually discussed.

2.5 Short Conclusion

In this chapter, the principles behind OCT have been studied. There are various factors that affect the obtained OCT images including the light source type, light spectrum, light coherence length, the configuration of the focal lens and in our case, the drilling speed of the drill bit. To the best of our knowledge, in our research, the OCT is first used in high speed rotational application. Which type of OCT system is our best choice? Does the drilling speed of the drill bit influence the OCT images' quality? If yes, to how extent it will affect? OCT images are subject to speckle noise. How will the

speckle noise influence an OCT image with large image depth? Can we reconstruct such OCT image from raw data properly? Can we...? All these questions need more researches.

Based on the anatomy of human jawbone studied at the beginning of this chapter, we conclude that the SS-OCT is recommended for our future OCT integrated dental drill system., This choice is determined based on four reasons, although the SS-OCT is much expensive than a conventional TD-OCT or SD-OCT:

First, the SS-OCT provides a much higher sensitivity at the deep part. A High SNR image is appreciated for clinical diagnostic. For TD-OCT, image quality decreases dramatically as the imaging depth increases. Although the SD-OCT sensitivity performance is better than TD-OCT, the finite wavelength resolution leads to a sufficient SNR drop-off at the deeper part, which can be eliminates by the advanced swept light source in SS-OCT.

Second is decided based on the acquisition speed of each OCT system. The SS-OCT uses spectral analysis or advanced optical source technology. As a consequence, the reference mirror is fixed. The absence of mechanical reference scanning greatly improves SS-OCT's A-scan acquisition speed. The most advanced SS-OCT system can offer 100,000 A-scans per second which is three or four orders of magnitude than a conventional TD-OCT. By contrast, the reciprocating movement in TD-OCT limits it performance. A longer scanning results in a low acquisition speed. In dental implant surgery, the dental drill usually operates at a relative high speed compared to TD-OCT A-scan rate. The TD-OCT is unable to provide sufficient A-scan rate. Thus, lots of structure information is lost due to under sampling.

Third, for safety issues, in dental implant, at least 2 mm safety zone must be preserved between the neurovascular bundle and the dental implant. That's to say, in our designing system, the imaging depth of the OCT system must be at least 2 mm long. Currently, only SS-OCT systems are satisfied with this requirement. This is because TD-OCT and SD-OCT can only provide a good sensitivity image depth of 1 mm and 1.5 mm, respectively.

Four, a high A-scan acquisition rate can reduces the motion-induced artificial caused by dental drilling.

Besides, a powerful light source for the designing OCT maybe required. Because, in subsection 2.2.2, we found the bone tissues possess high light scattering property that probably limits the OCT imaging depth. This will be discussed in section 0.

CHAPTER 3

MATERIALS AND EXPERIMENT SETUP

3.1 Introduction

In this master project, silicone elastomer-based optical phantoms and pig jawbone are used in OCT test. This chapter begins by introducing the tissue phantoms. The optical properties, structure as well as the protocols for preparation of the optical phantoms are introduced in more detail in section 3.2. The animal tissue used in experiment is presented in section 3.3. The experiment setup for OCT images acquisition will be shown in Section 3.4.

3.2 Optical phantom

3.2.1 Material Choice

In OCT community, optical phantoms have become widely used in current research including imaging research, measurement techniques and data analysis algorithms [9]. The optical phantoms occupy the properties of reliable, robust and reproducible.

Several types of tissue-like phantoms to simulate the optical behaves and characteristics of tissues have been described and studied more in detail in reference [9, 46-50].

The most popular robust phantoms are solid. The host materials of such phantoms can be rubbers, plastics, wax, silicone, polyester, polyurethane or epoxy resin. These solid phantoms are long term optical stability and greater shaping flexible. The optical properties of them are controlled by the concentration of mixed absorber and scatterer. The solid phantoms usually have low absorption coefficients but relatively high scattering coefficients. The scattering objects usually limited to aluminum oxide (Al_2O_3), titanium dioxide (TiO_2) and silicon dioxide (SiO_2), polyester, polystyrene or latex microspheres. The type of the scatter agent also determines the choice of the host material. One limitation of the solid phantoms is that these phantoms are not suitable for the condition in which the detector or optical fiber have to be moved below the surface of the phantom.

Therefore, some kinds of liquid phantoms are purposed as an alternative. Some researchers have used milk as the scattering component. But the optical properties of milk are not stable, since they vary with the type of the milk. In current, the most popular materials are fat emulsions, including the intralipid and nutrilipid, which are widely used in hospital as an intravenous nutrient. The lipid suspensions are cheap and non-toxic. The inter-/intra- experiment optical properties of lipid-based liquid phantoms are fairly easy to control by adjusting lipid concentration. The major problems of the lipid are they are food substances that are made from soybean oil. They are not easy to story and transport after creating. The optical properties of them always change over time.

For all kinds of phantoms, their scattering and absorption properties are the most important design factors that need to be carefully controlled [9, 51].

In this research, we adopted the silicone based optical phantom with titanium dioxide scattering objects since this type of phantom has advantages list as below:

- Easy to make and fulfill many of the criteria for an "ideal phantoms" [9];
- Controllable optical properties (scattering coefficient, absorption coefficient) [9];
- Controllable thickness and structure (wavy, flat [9]and channeled structure);
- Durable, all phantoms are stable over 6 months [9];
- Linear relation between the scattering coefficient and added scattering particles weight percentage ($w\% < 1\%$) [9];
- Have nearly same mechanical properties as most biological tissues [51].

But this phantom also encounters some limitations that can generalize to other solid phantoms:

- Not suitable for simulating all the tissues since tissues often possess structural inhomogeneity [9] and we can hardly make a inhomogeneous phantom;
- A short range of scattering coefficient, since we are unable to make homogeneous phantoms containing scatterer with weight percentage $w\% > 1\%$ [9];
- The densities of the different phantoms are nearly same;
- Too much incident light power loss due to the reflection at the surface of the silicone

3.2.2 Phantom Design

In this experiment, only the scattering coefficient is taken into account since it plays a leading role in the light attenuation inside the tissue [52, 53]. The oral tissues usually have larger scattering coefficients that are two to three orders of magnitude higher than the absorption coefficients (Table 2). As mentioned in reference [9], the scattering coefficient of the optical phantoms is included by adding dioxide Titanium (TiO_2) particles (refractive index 2.49, anatase form, Sigma Aldrich, Saint Louis, Missouri) into the silicone (refractive index 1.41, Sylgard® 184 Silicone Elastomer Dow Corning)followed the relations listed as follows [9]:

$$\mu_s = 21.56 \times w\% - 0.11 \tag{3.1}$$

In which:

μ_s is the scattering coefficient of the tissue (unit in mm^{-1})

$w\%$ is the weight percentage of the added TiO_2 particles;

Since the Equation (3.1) is obtained with a standard Time-Domain OCT operating at 850 nm, for our experience, Equation (3.2) [54] is included to calculate the scattering coefficients for 1300nm light.

$$(\mu_s)_{\lambda_2} = (\frac{\lambda_1}{\lambda_2})^{SP}(\mu_s)_{\lambda_1} \tag{3.2}$$

In which:

SP is the scattering power that determines how strong the scattering coefficient changes with the wavelength of the incidence infrared light. The value of SP is decided by the average diameter of the scatterers. Large scatterers have a low SP.In our case SP equals 1.9 (from 850 nm to 1300 nm) for our phantoms [9];

λ_1, λ_2 are the wavelengths of two different light ($\lambda_1 < \lambda_2$), in Equation (3.2), $\lambda_1 = 850\ nm$ and $\lambda_2 = 1300\ nm$

The scattering coefficient of live tissue varies widely depending on the type of the tissue. the low scattering tissues usually have scattering coefficients few orders of magnitude less than the high scattering tissues [53]. Therefore the controllable scattering coefficient of the optical phantoms cannot cover all desired ranges of scattering coefficients that found in dental tissues [9], since we cannot make a homogenous phantom when the weight percentage ($w\%$) of the included TiO2 particles in the silicone is over 1%, and also because the relation between the dioxide titanium and silicone shown in Equation (3.1) is no longer linear. Because of the two factors mentioned above, in the phantom preparation, only three different dental tissues, tooth enamel, blood and alveolar bone, are simulated. The values of scattering coefficients of these tissues are based on references [18, 52, 53] in order to match the optical properties of real dental tissues as close as possible. The scattering coefficients and TiO_2 concentrations of phantoms are shown in Table 2.

Simulated tissue	**Absorption coefficient @ 1300 nm (cm^{-1})**	**Scattering coefficient @ 1300 nm (cm^{-1})**	**Scattering coefficient @ 850 nm (cm^{-1})**	**Concentration of TiO_2 (%)**	**Weight of TiO_2 (g)**	**Weight of curing agent/silicone (g)**
Enamel [52]*	0.1	6	13.45	0.0675	0.4049	5.9595/54
Alveolar Bone[18]	0.48	148	331.79	1.5440	0.9264	5.0736/55
Blood [53]*	2.84	38.4	86.09	0.4044	0.2426	5.7573/54

Table 2: Optical properties for optical phantoms. The reduced scattering coefficients of enamel and blood listed above are not for the light source centered at 1300 nm exactly. The 0.6 for enamel and 3.84 for human whole blood (HbO_2 Hct = 0.41) are measured from light at wavelength of 1054 nm and 960 nm, respectively.

Please note, in Table 2, the weight percentage of TiO_2 inside simulated alveolar bone is higher than 1%. Although this value infringed upon the rule of Equation (3.1) and the resulting liquid silicone may be inhomogeneous, we still made and used this phantom based two reasons: first, the jawbone is the

position where the drill bit working at, and second is the scattering coefficient of jawbone is no too large that we can still use Equation (3.1) to estimate the ratio between silicone and TiO_2 inclusion. Thus, the actual scattering of that phantom layer (used to simulate the alveolar bone) is probably not 14.8 cm^{-1} exactly.

3.2.3 Protocols for the Optical Phantoms Preparation

The silicone (Sylgard® 184) is a two-part (silicone and curing agent) silicone that is supplied as flowable liquid that cures to a flexible elastomer. The silicone mixture is able to cure at either room temperature (48 hours) or high temperature to shorten the curing time [55]. The advantage of this liquid silicone is that it can be mixed with any absorbers and scatterers. The flexibility of liquid mixture enables us to construct any shape of complex phantoms as we like.

The phantoms are manufactured fully according to the procedures mentioned in reference [9]. This preparation contains six steps in brief.

1. The TiO_2 particles are forced to mix with the curing agent by using a tissue homogenizer / glass rod;
2. The mixture is placed in a 30 KHz ultrasound bath to break the residual TiO_2 clusters for 30 min;
3. The declustered mixture is mixed with the Sylgard 184 liquid silicone with a weight ratio of 1:9 and then carefully stirred using a mixer;
4. The vacuum pump is used to degas the remaining air bubbles inside the mixture;
5. To form the desired phantom layers, the mixture is placed between two glass plates. The thickness is controlled by using different spacers with different thicknesses;
6. The phantoms are placed in an air oven at 60 ℃ for 6 hours.

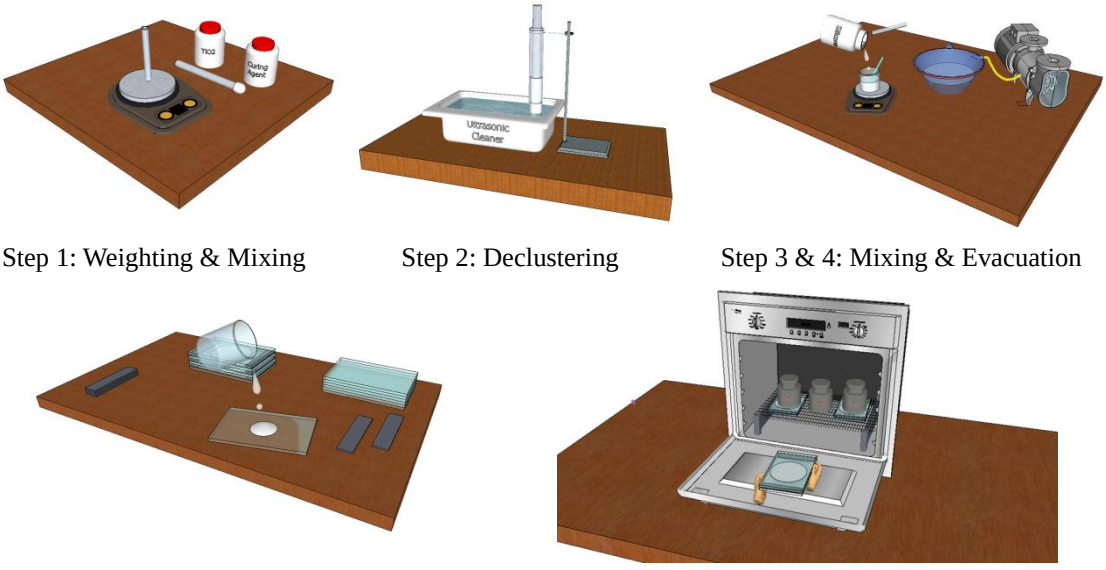

Step 1: Weighting & Mixing | Step 2: Declustering | Step 3 & 4: Mixing & Evacuation

Step 5: Molding | Step 6: Curing at high temperature

Figure 17: Phantoms preparation

The cured thin layers are removed from the glasses using alcohol and cut to any shapes as we want. In our test, three kinds of phantoms (shown in Figure 18) have been made, multilayered phantoms, channeled phantoms and multilayered sponge-like phantoms. All these phantoms are protected by a PVC cylinder (the blue shell in Figure 18) outside since the artificial samples maybe expand at high revolutions per minute (RPM) due to the centrifugal force when placed on the rotary stage.

Each multilayered phantom has five layers. From top to bottom, they are named as: Enamel – Alveolar Bone – Blood – Alveolar Bone – Base. The first layers have the optical scattering properties as mentioned in Figure 18 above. The transparent silicone base supports the upper four TiO_2 included layers. The electrostatic forces keep the different layers together and the residual air bubbles between the layers are removed by placing the phantoms inside an air vacuum chamber. We prepared five such phantoms and two of them are used for experiment:

Phantom:	**Thickness (unit in μm, from top to bottom):**			
	Enamel	Alveolar bone	blood	Alveolar bone
1	240	246	240	246
2	117	131	92	125

Table 3. The thickness for the multi-layered phantoms' layers. In the phantom making, the thickness of each layer is controlled by the inserted spacers between two glasses. But due to some reasons, like the smoothness of the glass plate, the weights putting on the glass plates during curing, etc., the actual thickness of the phantom layer is not the same as that of the spacers. The thicknesses of phantom layers in the Table 3 above are measured with OCT before experiment.

The thicknesses of the different silicone layers are the actual values that measured by the SS-OCT.

For the channeled phantoms, copper wires or terylene surgical sutures are pre-placed in the liquid silicone before curing. The copper wires are removed after curing because the wire is light-tight, causing the area behind the top surface of the wire robe totally dark on the obtained OCT images. Thereby the created tubes are then filled with intralipid (20 weight %, Fresenius-Kabi). The optical properties of the intralipid depend on its contraction. Since lacks of optical properties of nerves and SP of blood and nerves, we use pure Fresenius-Kabi® intralipid (20 weight %) directly. Its attenuation and scattering coefficients are 5.2 mm^{-1} and 5.0 mm^{-1} at 1300 nm light, respectively [54].The scattering coefficient of the intralipid is not the same as that of the real blood vessels or nerve but the intralipid is a widely used in many optical measurements since it is a common tissue phantom used to provide different optical properties [13] and can be easily injected into the pre-made channels.

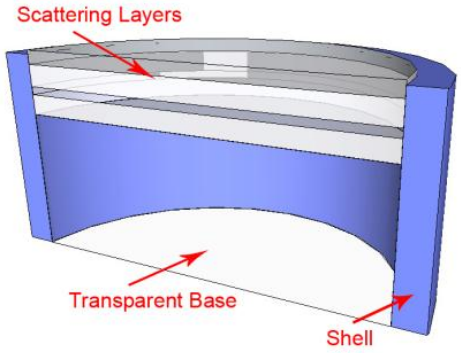

A. Multilayers phantom

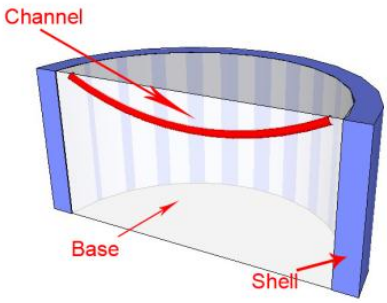

B. Channeled phantom

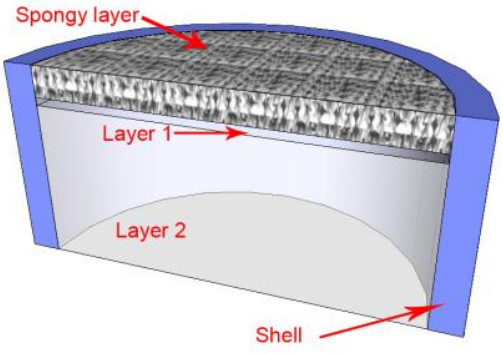

C. Multilayered sponge-like phantom

Figure 18: Cross-sectional view of the optical phantoms. In A, it shows the structure of the multilayered phantom. From top to bottom, the first four layers contain different weight percentages of TiO_2 that used to simulated different tissues, named as: Enamel, Alveolar Bone, Blood, and Alveolar Bone. The transparent base is the pure silicone Sylgard® 184 used to support the upper part. In B, the channeled phantom is used to simulate a mental nerve (red channel) inside the jawbone (white part). The red channel is prepared by implanting a copper wire in the liquid silicone and pulling it out after curing. The channel is filled with intralipid during experimental measurements. The adoptive scattering coefficient of the white base is much lower than that of the real jawbone tissue since jawbone is highly scattering medium with limited penetration depth. The infrared light cannot reach a deeper part inside the phantom such that the OCT cannot image the intralipid channel. In C, the multilayered sponge-like phantom consists of three layers, from top to bottom are: spongy layer, Alveolar bone and Blood. The scattering coefficient of spongy layer is the same as that of enamel. Thickness of the alveolar bone (layer 1) is 131 μm; whereas layer 2 has scattering coefficient 0.404 mm^{-1}. The blue PVC shell is used to protect the phantom since it maybe expand or even explode at high rotational speed due to centrifugal forces.

The scattering coefficient of the white base for the channeled phantom is lower than that of alveolar bone because a thin layer above the channel maybe deform or even breakup during pulling the wire out; whereas a thick layer with high scattering coefficient will block all light that we cannot see the channel from OCT images.

For multilayered sponge-like phantom, the spongy layer has the same scattering coefficient as the

enamel layer of in multilayer phantom. The thickness of this layer is about 1.5 mm measured by OCT. The pores were formed by heavily stirring the liquid mixture to involve more air bubbles. The cancellous mixture was cured at high temperature (125 ℃, 25 min) to prevent air bubbles burst. In OCT images, the average diameter of these air bubbles is about 200 μm. For small and well distributed air bubbles, a long time stirring is required. And the higher the concentration of the TiO_2 is, the more difficult to keep the shaped air bubbles. The thickness of the middle layer, the alveolar bone layer, has the average thickness of 131 μm. The reasons of using the low scattering spongy layer and thin alveolar layer are same, a high scattering layer or too thick layer will block most of the incident light so that the deeper part could not be imaged.

These phantoms are prepared with different purposes. The multilayered phantoms are used to test the effect of phantoms' thicknesses on image quality after denoising; the channeled phantom is made with the aim of understanding the relation between rotational speed and the visibility of channeled structure and anterior loop of the mental nerve in OCT images; whereas the third kind of phantom is structural similar to the jawbone. The porous layer is used to simulate the spongy bone; whereas the top and base solid layers are used to simulate the cortical bone and neurovascular bundle, respectively.

3.3 Animal Tissue

The pig jawbone used in this animal tissue study was acquired from the Erasmus Medical Centre. The jawbone was cleaned and stored in the refrigerator before testing to prevent degradation.

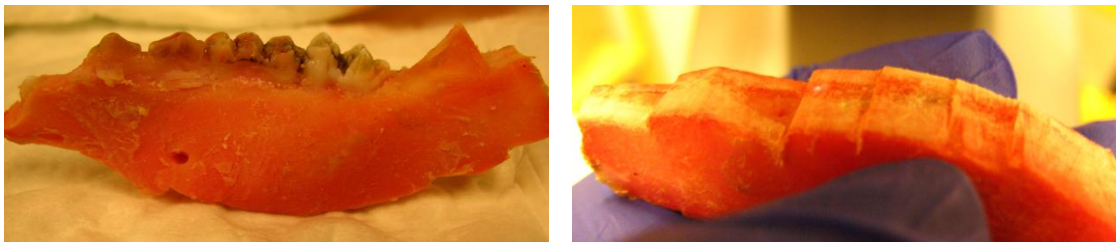

A. Side view B. Bottom view

Figure 19. Images for one piece of pig's lower anterior mandibular bone.

We choose the pig jawbone for our animal tissues experiment because it is low cost and very easy to obtain. In additional, the implantologist Dr. Florian Mosch we met also recommended us to use pig jawbones for our future research since they resemble human well very.

In dental implant, the transition between the cortical bone and trabecular bone is considered as the most important landmark to define the good region (trabecular bone) and bad region (mandibular canal or even the oral cavity) for dental implant. The same as other bones in body, the cortical makes up the outer layer of the trabecular bone. In the jawbone, the cortical bone also forms the outer shell around the neurovascular bundle. This means that the cortical bone is the last layer between the safe region and the dangerous region.

In order to measure the feasibility of OCT for tissues recognition, some wedge-shaped incisions have been made at the bottom of the mandibular bone to expose the trabecular bone and neurovascular bundle under the cover of a very thin layer of the cortical bone.

3.4 Experimental OCT setup

Since the OCT probe embedded in a dental drill bit is still under busy development, in this experiment, a similar experimental environment is adopted, called as HSR-OCT (high speed rational OCT) herein below for simplicity. A commercial high speed swept source OCT (HSL 2000, SS-OCT system, Santec®, Aichi, Japan) is employed for raw data gathering. The acquisition rate of the SS-OCT is up to 50,000 A-lines per second, and its axial and lateral resolutions are 10 μm and 5 μm (after interpolation), respectively, measured in air. The output power of the sample arm is 10 mW. The OCT probe is mounted on a stationary holder and one screw is inserted between the OCT probe and its holding arm (shown in Figure 20) to form a small angle ($\alpha \approx 3°$, Figure 20 B & C). In this way, the acquired images have nearly same distortion characteristics as the images we will get from real dental drill situation. A programmable high speed rotational stage (HR-3 high speed rotary stage, Newmark systems®, Rancho Santa Margarita, USA) is placed on the tray of the SS-OCT directly below the OCT sample probe. The rotation axis and the center of the fiber lens are along the same line. On top of the rotary stage, an aluminum platform (homemade) is pre-fixed for sample holding. The reflected light from the samples is collected by the OCT probe and analyzed and displayed by using Labview 8.5®.

The HSR-OCT setup is shown in Figure 20 below.

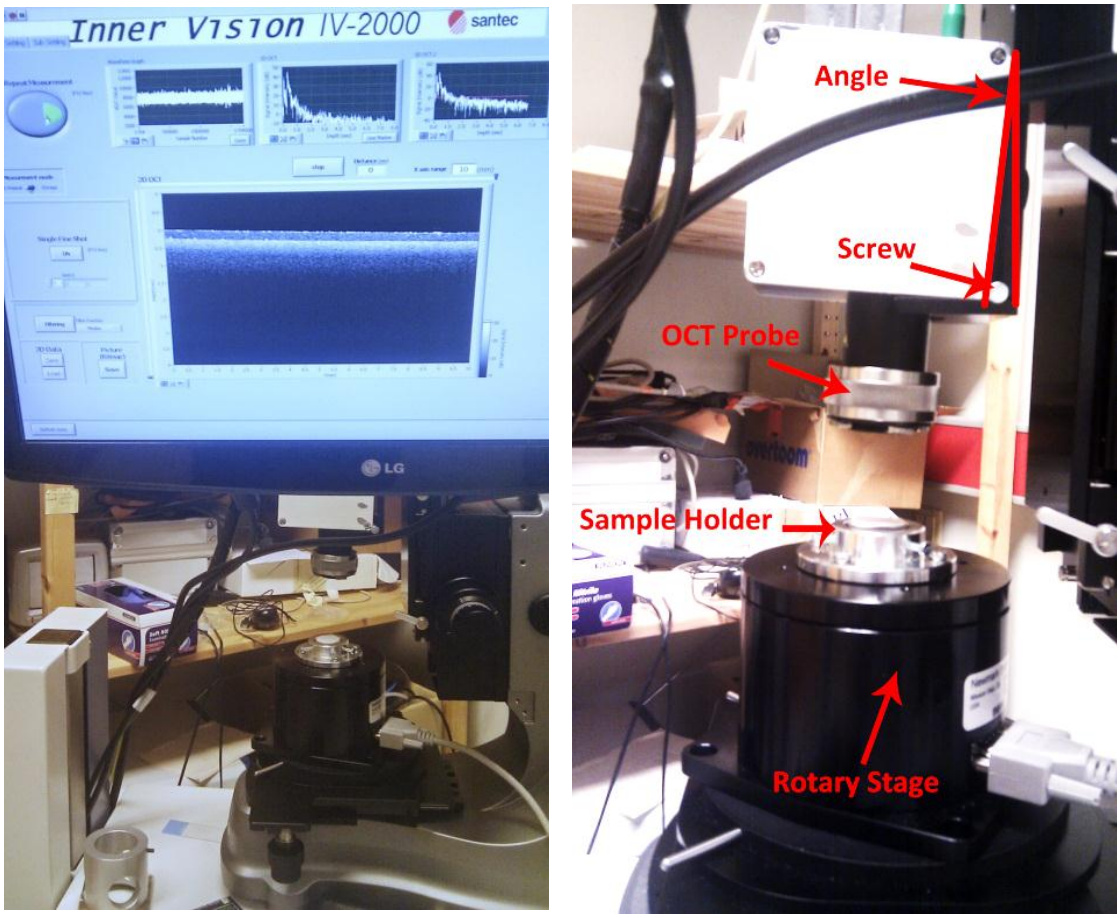

A. HSR-OCT setup

B. OCT probe and rotary stage

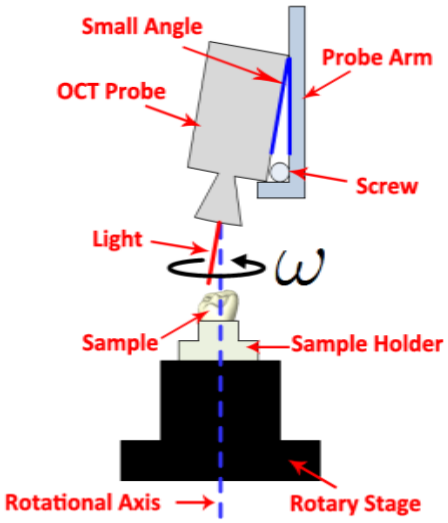

C. Schematic plot of experiment setup

Figure 20. Experiment stetup. A: the lower part shows the HSR-OCT fixture. The obtained signal is then processed by Labview® and displayed on the screen at the upper part of picture; B: Enlarged fixture part in A. The HR-3 programmable rotary stage is positioned on a platform under SS-OCT probe. A fixed aluminum sample holder is mounted on HR-3 to carry different samples. A screw is inserted between the OCT probe and the holding arm to form a small angle (marked by red lines in B), which is similar to that of our designing drill bit. Image C gives the schematic plot of our experiment setup.

CHAPTER 4

METHODS FOR OCT IMAGE PROCESSING

4.1 Introduction

As introduced in previous subsection 2.4.2, in optical coherence tomography (OCT), the inherence speckle noise arises due to the "coherence" detection. The speckle noise seriously degrades the obtained OCT image quality by lowering image contrast and blurring the edge features of the objects in the image. To improve OCT sensitivity, the speckle must be reduced.

The most used OCT speckle reduction technologies can be split into four main categories: polarization diversity, spatial compounding, frequency compounding and digital signal processing [19]. Since our OCT probe embedded dental drill system is still under busy development the first three techniques correspond to OCT system itself therefore, in this research, we only focus our attention solely on the digital filtering.

In this chapter, some commonly used speckle noise reduction algorithms are discussed. To our best knowledge, the sample probe is first embedded into a rotatable dental drill bit and acquires cross-sectional structure information at a high rotational speed. As a consequence, the performance of the speckle suppression methods may be affected and are quite different to usual. In order to objectively and quantitatively evaluate the speckle suppression abilities of different algorithms, some image quality assessment methods are employed and they are introduced and discussed in the following sections 4.3 and 4.4.

The rest parts of this chapter focus on the oversampled OCT image reconstruction. An adaptive cross-correlation coefficient based OCT image acquisition method is purposed in section 4.5. The advantages, disadvantages and limitations of this technique will be compared and discussed.

4.2 Over-sampled Image

In the past two decades, scientists and researchers have already done numerous experiments on OCT. Different digital filtering algorithms have been developed [56-61]. Their applicability on speckle noise reduction has been fully studied. So why in this research, we still need to compare the speckle reduction ability of different algorithms but not utilize the results from predecessors? Before stepping into the digital filtering, let's figure it out first.

In conventional OCT, to achieve a rapid lateral scanning to synchronize with the successive depth-resolved A-scans, one or two galvanometer-driven mirror(s) or lens(es) is(are) employed to change the angle of incident light on a stationary assembly of relay lenses [20]. Computer controls the motions of the swing mirrors to spread and change the incidence beam at high frequency (shown in Figure 21.A).

However, in our special case, the OCT sample arm is pre-embedded in the dental drill bit (Figure 3). The jaw internal structure in the vicinity of the drill bit is obtained via rotating the drill bit in the dental drilling surgery (Figure 1.B). The image acquisition speed of the HSR-OCT highly depends on the instantaneous rotational speed of the drill bit.

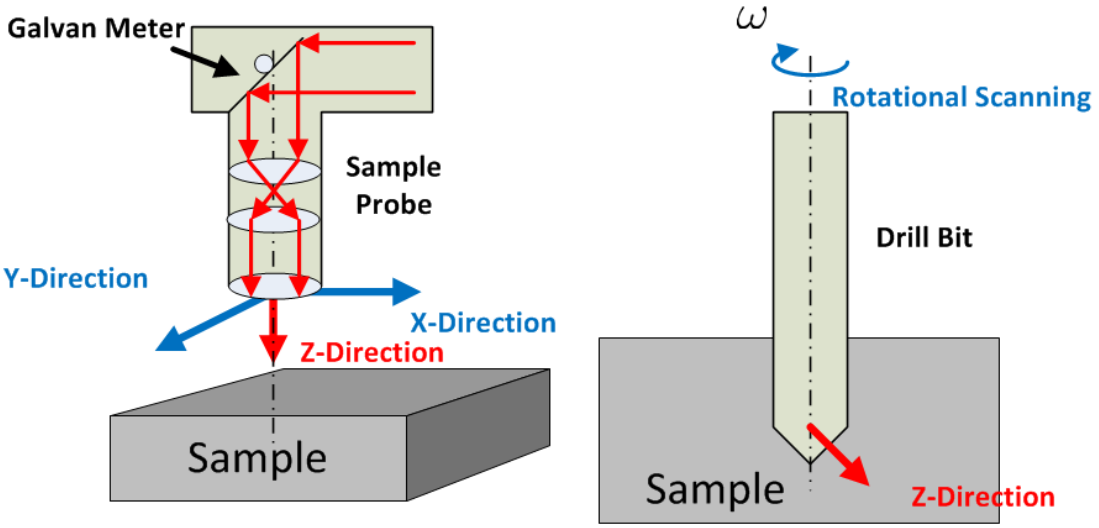

A. Conventional lateral scanning B. Rotational lateral scanning

Figure 21. Lateral scanning comparison between conventional OCT and HSR-OCT. In these two images above, the blue arrows indicate the scanning directions of the lateral scanning of two systems. The red arrows show the optical path of the incident infrared light which is also the directions of the Z-scanning direction.

In our designing dental drill bit, a channel is made at the center of the axial plane of the drill. Inside, a single-mode optical fiber is implanted (shown in Figure 22). The opening of fiber optics is covered by a Gradient Index (GRIN) lens, which is used to focus light about 2 mm ahead the opening in the free space and then to collect backscattered light.

A. Schematic of OCT fiber embedded drill bit B. A zoomed-in look of the drill bit tip

Figure 22. Schematic drawing of designing OCT probe implanted drill bit. The red line donates the path of the infrared light along the fiber optics. The opening of the fiber optics is located at the tip of the drill bit with a deviation 0.5 mm away from the rotational axis. The output window is covered by a GRIN lens used to focus the beam ahead the lens. In B, the drill bit tip is zoomed in and the mathematical symbols are represented. α is the angle between the output light path and rotation axis

of the drill bit. F is the focal length of the GRIN lens. d is the distance from the fiber opening to the rotation axis. d' is the distance between the focal spot and drill bit rotation axis.
First we define the A-scanning rate of OCT system is f_s Hz, the instantaneous rotational speed of the drill bit is n revolutions per minute (RPM). The geometry of the designing dental bit are: focal length of the GRIN lens is $F = 2\ mm$; the angle between output light and rotation axis of drill bit is $\alpha = 3°$, the distance between the rotation axis to fiber opening is $d = 0.5\ mm$.

Thus, given by the geometry, we can easily work out the distance from the focal point of the light to the center is:

$$d' = F \cdot \sin\alpha + d \tag{4.1}$$

The scanning length of the focal spot passes through in one second is defined as:

$$L_{scan} = \frac{2n\pi \cdot d'}{60} \tag{4.2}$$

For a normal OCT system, the lateral scanning distance in one second relies on the lateral resolution and A-scan line acquisition rate given as:

$$L_{OCT} = f_s \cdot r_l \tag{4.3}$$

Inspired by the references [56, 62], we define the sampling ratio (in reference [62], it is called as sampling rate) for our HSR-OCT as:

$$\zeta = \frac{L_{scan}}{L_{OCT}} = \frac{2n\pi \cdot d'}{f_s \cdot r_l} \tag{4.4}$$

Based on Nyquist-Shannon sampling theorem and value of ζ we categorizes OCT images into three types:

- Under-sampled image: $\zeta < 2$
- Critical-sampled image: based on Nyquist sampling theorem, the sampling rate should be at least twice the sampled frequency. Therefore, $\zeta = 2$ when the image is critical sampled, in which the OCT system acquires two A-scans in a conventional lateral resolution volume. ;
- Over-sampled image: $\zeta > 2$, within a traditional single resolution volume, more than two A-scans are acquired. For an optimal designed OCT system, the sampling ratio of the images must be kept above 2 to prevent signal aliasing after Fourier transformation.

In the experiment, we used a commercial swept source OCT [Santec® Aichi, Japan HSL 2000, 50 KHz A-scans per second, 10 μm axial resolution]. The lateral resolution of the SS-OCT is a little complicated. In air, the measured transverse resolution is 60 μm. From Equations (4.1) and (4.4) we can plot the rotational speed dependence sampling ratio as Figure 23 below:

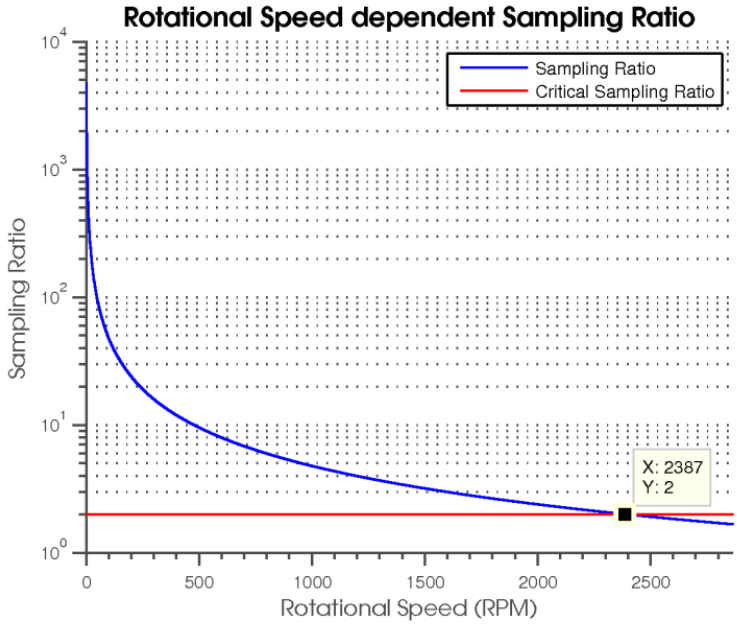

Figure 23. Rotational speed dependent sampling ratio ζ. The blue line indicates the instantaneous ζ at different RPM. The red line shows the critical sampling ratio which equals 2 (Nyquist sampling theorem). The Y-axis is presented in logarithmic scale.

Figure 23 shows the sampling ratio of the obtained SS-OCT images at different rotational speed. Assuming our designing system has the same optical properties as that we used in experiments, when the instantaneous rotational speed of the drill bit is approximately lower than about 2000 RPM, the images are always over-sampled.

As we known, in the dental implant surgery, the actual rotational speed of the drill bit relies on various unpredictable internal and external factors, including the hardness of the jaw, the applied force, the type of the drill bit, etc. It is difficult to keep drilling speed constant. The variability of the drill speed results in variability of the sampling ratio, and as a consequence, the variability of the cross-correlation between the adjacent A-scans. A lower speed drilling results in a higher cross-correlation. The sampling ratio, ζ, seriously decreases in the range from 1 rpm to 500 RPM and then reduces slightly. At 2,000 RPM, the ζ is only a quarter of the value at 500 RPM.The oversampled OCT images have two obvious benefits and are very important for our case: first, it increases the visibility of the small objects in transverse direction since OCT acquires more than one cross-correlated A-scans within a traditional single lateral resolution volume. FD-OCT can acquire an entire A-scan profile simultaneous. Thus, the optical components, the objective lens in particular, used in such systems (FD-OCT) must provide a relative large axial depth of field (b). Calculating from Equation (2.19) and Equation (2.20), we can find that the physical lateral resolutions of FD-OCT system are usually noticeable poor. The small objects cannot be clearly represented without oversampling or other display techniques; second, the overlapped information can be used to reconstruct image from the non-uniform drill motion. This will be continued discussed in section 4.5.

4.3 Speckle Noise Suppression

4.3.1 Sliding Window Technique

For our HSR-OCT, when scanning a single lateral resolution volume, the acquired successive A-scan lines should be nearly identical. However, any unfiltered OCT is subject to speckle noise, of course, ours is not an exception. This inherent noise changes the pattern of the uniform area and affects the future image reconstruction and clinical diagnosis. To eliminate the influence of the speckle noise, some digital image processing are applied with the purpose of finding a better speckle filter for our special HSR-OCT.

In this study, all the eight used speckle noise reduction algorithms are based on sliding window technique. They are known as: Mean filter, Median filter, adaptive Wiener filter [63], Kuwahara filter [64, 65], Symmetry Nearest Neighborhood (SNN) filter [66], Kuan filter [67], Enhanced Lee filter [68], and Gamma MAP filter [69]. All of these methods are proven that they can efficiently remove the speckle noise in the image while some of them smooth or blur the edge structure [56].

The sliding window algorithm is not a specific technology but a general technique that widely used in image filtering, object detection and object tracking. This method usually starts processing from the first pixel of the given image. A user predefined window with size $m \times n$ is centered at this pixel. The center pixel and its neighbors covered by the window are selected and calculated according to a given filtering operation. The center pixel's value is changed as the result of the operation. The window then moves to the rest pixel, pixel-by-pixel, and repeats the same filtering operation until it sliders over the entire image. The performance of the sliding window is influenced by the size of the sliding window and the filtering operation. Typically, this all sliding window based algorithms are computational expensive and require too much hardware resource, especially for high resolution images. But, fortunately, this technique is inherently high parallel. Our FPGA (Field Programmable Gate Array) can provide a fast and flexible solution for these applications and probably realize real time processing.

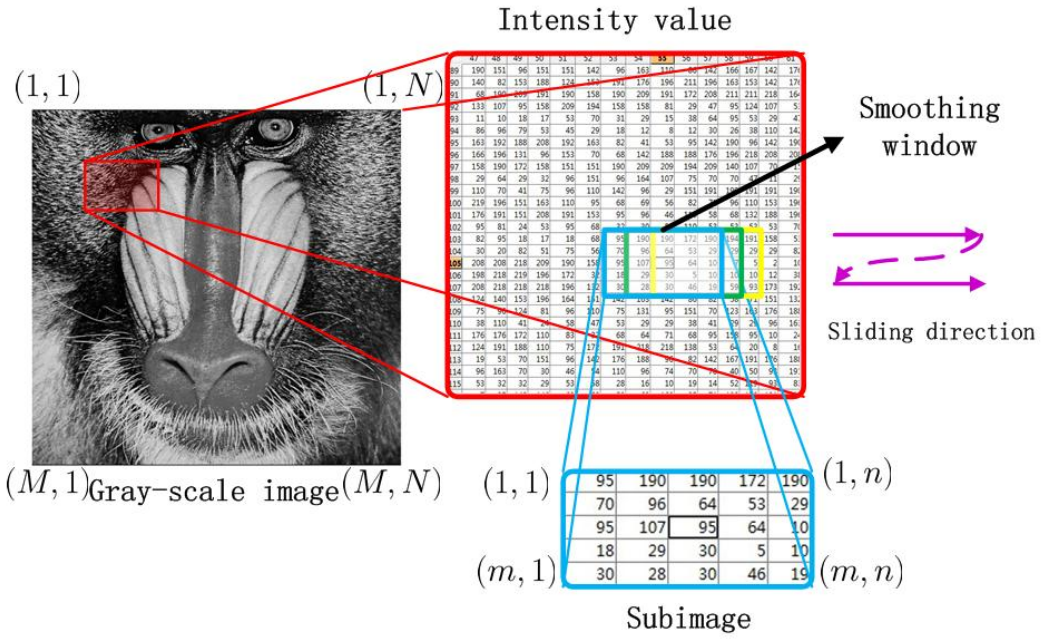

Figure 24: An example of sliding window based image processing. For an 8-bit gray-scale image ($M \times N$), the intensity of each pixel is represented by an integer from 0 and 255. The sliding window technique applies a $m \times n$ window in the raster. All pixels within the range of the sliding window are selected to perform a given filtering operation. The resultant value of the operation is put back and set as new intensity of the center pixel. After that, the window slides to the next pixel (direction is shown in purple lines).

4.3.2 Despeckle Filtering Algorithms

The mean filter (or average filter) perhaps is the simplest spatial linear filter design based on local-statistics. The idea of this filter is to replace each pixel value in the given image with the average value of the pixels in a specific region (covered by sliding window). The mean filter is a type of low-pass filter that usually used to reduce noise in images and smooth image intensity variation. When the mean filter spans one edge in the image, it will cause edge blurring. The denoising ability relies on the size of the sliding window. The smooth effect increases as the size of the window increases. However, the edge features will be very blurred. The most common used window is square window. Other shape of window can be applied but will produce different result.

The median filter is similar to the mean filter but is a non-linear filter that uses median value of the chosen pixels instead of average value. The median filter is more robust and often provides a better noise suppression since the outliers exist in the image (like pepper and salt noise) will not affect its output. And the median filter can preserve sharp edges to some extent since it does not create new unrealistic pixel value when it straddles an edge [70].

The symmetric nearest neighbor (SNN) filter uses both the spatial and gray value information of the image to be processed. In the subimages (parts of the original image extracted by a certain size of mask), the pairs of pixels located symmetrically opposite to the center pixel of the square smooth window are extracted. From each pair, the one that is closest to the center pixel is then used to compute

the output.

The rest despeckle filtering algorithms are designed based on local statistics (local mean and local variance) of the given image.

$$\mu = \frac{1}{mn} \sum_{(i,j)\in(m,n)} I(i,j) \tag{4.5}$$

$$\sigma^2 = \frac{1}{mn} \sum_{(i,j)\in(m,n)} I^2(i,j) - \mu^2 \tag{4.6}$$

In which: m, n are the dimensions of the sliding window;

$I(i,j)$ is the intensity of the pixel at location (i,j);

μ is the local mean, which is calculated from pixels within the sliding window;

σ^2 is the local variance calculated from pixels within the sliding window.

The Kuwahara filter posted in 1976 works on a window divided into four overlapping sub-windows (typically 5×5 size, Figure 25). The means and variances of these four subquardrants of the selected windowed selection are calculated and compared. The output value of the center pixel in the window is replaced by the mean of the subquadrant with the smallest variance.

a	a	ab	b	b
a	a	ab	b	b
ac	ac	abcd	bd	bd
c	c	cd	d	d
c	c	cd	d	d

Figure 25. Kuwahara filter's smoothing window

The adaptive wiener filter degrades the noise based on the local statistical feature. The mean (Equation (4.7)) and variance (Equation (4.8)) of the pixels within the sliding smoothing window are used to generate estimated pixel value (Equation (4.9)).

$$\hat{I}_{(i,j)} = \mu + \frac{\sigma^2 - \sigma_{bg}^2}{\sigma^2}(I_{(i,j)} - \mu) \tag{4.7}$$

Where $\hat{I}_(i,j)$ is the estimated value of the pixel in an ideal image. The σ_{bg}^2 is the variance of the background noise in the filter window which is estimated by Equation (4.8):

$$\sigma_{bg}^2 = \frac{1}{mn}[\frac{I^2 * O_{mn}}{mn} - (\frac{I * O_{mn}}{mn})^2] \tag{4.8}$$

In which: O is an all ones matrix which has the same dimension as the sliding window;

$*$ indicates convolution operation.

The Kuan filter, Enhanced Lee filter and Gamma MAP filter are also adaptive filters that perform noise suppression while preserving edge information. The difference is the applied different ways to get the weight coefficient.

To estimate the ideal image $\hat{I}$, Kuan describes the speckle reduction filter as the formation below:

$$\hat{I}(i,j) = I(i,j)W(i,j) + \overline{I}(i,j)(1 - W(i,j)) \tag{4.9}$$

In which: $W(i,j) = (1 - C_u^2/C_i^2)/(1 + C_u^2)$ is the weight coefficient;

$C_u = 1/\sqrt{L}$ and $C_i = \sigma/\mu$ are the variance coefficient;

$\overline{I}(i,j)$ is the average intensity value of the pixels in the filter window;

L is the equivalent number of looks which is calculated as $L = (\mu_I^2)/(\sigma_I^2)$, μ_I and σ_I^2 are the mean and variance of the unfiltered image, respectively.

The parameter number of look is used to describe the speckle noise variance in an image. To compare its value, I can estimate and control the amount of smoothing applied to the image by a certain filter. We measured the raw images obtained from our SS-OCT and find out that the average value of L for all SS-OCT images is around 0.5.

Lopes et al. improved the performance of Lee filter [71] and Kuan maximum a posteriori (MAP) filter [69] based on the principle of pixel segmentation. In the paper [71], he proposed to divide an image into three different areas: homogeneous area, heterogeneous and the area containing isolated point targets. This pixel segmentation is based on two thresholds C_u and C_{max}. In Lopes research, he found, in an L-look amplitude image, the lower threshold C_u, which is boundary between homogeneous area and heterogeneous area, has an observed coefficient of variation value $1/\sqrt{L}$. A litter difference between enhanced Lee filter and Gamma MAP filter is the upper threshold.

But it is hard to determine the value of C_{max} since it has connections with image parameters, including look number and spatial resolution [72]. The speckle noise has a high gradient as well as edges. The value of C_{max} must be well studied. In this work, C_{max} is default to $\sqrt{1 + 2/L}$ because former researchers found it is a good estimated value for likelihood ratio edge detection [72].

Thus to estimate a pixel's value by Enhanced Lee filter, the following equation is applied.

$$\hat{I}(i,j) = \begin{cases} \mu & \text{for } C_i \le C_u \\ I(i,j)W(i,j) + \overline{I}(i,j)(1 - W(i,j)) & \text{for } C_u < C_i < C_{max} \\ I(i,j) & \text{for } C_i \ge C_{max} \end{cases} \tag{4.10}$$

$$W(t) = \exp\left[-K(I(t) - C_u)/(C_{max} - I(t))\right] \tag{4.11}$$

In which: K is the damping coefficient;

$C_u = 1/\sqrt{L}$ and $C_{max} = \sqrt{1 + 2/L}$ are the variance coefficients

The damping coefficient K determines the smoothing ability of the filter. A larger K, ($K = 10$), results in a degradation of smoothing. In this experiment, corroding to reference [68], the K is set to 1, since it has a better ability to smooth out noise and preserves edge simultaneously. The Gamma MAP filter is also a maximum a posteriori (MAP) speckle reduction. A priori knowledge is required before applying it [68]. Researchers found that the scattered coherent wave by a surface has a Gamma

distributed cross section R [69], which is given as:

$$f(R) = (\frac{\beta}{< R >})^{\beta} \cdot \frac{1}{\Gamma_{(\beta)}} \cdot \exp(-\beta \frac{R}{< R >}) R^{\beta-1} \tag{4.12}$$

Where the $< R >$ equals the mean of the coherence signal intensity, Γ indicates the data follows Gamma distribution and $\beta = 1/C_R^2$;

To solve Equation (4.12), the only one real positive solution is:

$$\hat{R} = \frac{(\beta - L - 1)\bar{I}(i,j) + \sqrt{\bar{I}(i,j)^2(\beta - L - 1)^2 + 4\beta L \bar{I}(i,j)}}{2\beta} \tag{4.13}$$

At the condition $C_I^2 \leq 2C_u^2$ thus, Lopes got a different upper variable $C_{max} = \sqrt{2}C_u$. Therefore, with the Equation (4.12), Equation (4.13) and two thresholds, we can filter a speckle noise corrupted image pixelwisely with the Equation (4.14):

$$\hat{I}(i,j) = \begin{cases} \mu & \text{for } C_i \leq C_u \\ \frac{(\alpha - L - 1)\bar{I}(i,j) + \sqrt{\bar{I}(i,j)^2(\alpha - L - 1)^2 + 4\alpha L \bar{I}(i,j)}}{2\alpha} & \text{for } C_u < C_i < C_{max} \\ I(i,j) & \text{for } C_i \geq C_{max} \end{cases} \tag{4.14}$$

Where $C_u = 1/\sqrt{L}$, $C_{max} = \sqrt{2}C_u$ and $\alpha = \frac{1 + C_u^2}{C_i^2(t_0) - C_u^2}$. The output is an estimated value of the speckle noise free image.

4.4 Image Quality Assessments

A number of methods have been proposed in section 4.3 to address the problem of removing the speckle noise while preserving the edge features in the OCT images. However, which method gives a better result (tradeoff between speckle suppression and edge preservation) is still unknown. In order to get a better understanding of the performance of the above digital filters, in this research, several image quality assessment algorithms are employed and their result are compared in Chapters 4 & 5.

The most used metrics to evaluate noise suppression and despeckled image quality in OCT are the Signal-to-Noise Ratio (SNR), Peak Signal-to-Noise Ratio (PSNR), Signal-to-Mean Square Error (S/MSE), Root Mean Square Error (RMSE), Structure Similarity Index (SSIM), Edge preserve factor (EPF), Contrast-to-Noise Ratio (CNR), and Equivalent Number of Looks (ENL) [56, 59, 60, 73].

The definitions of these metrics are described in the Table 4 below.

	Metric	Definition		Papers
Global	SNR	$\text{SNR} = 10 \times \log_{10} \frac{\sum_{i=1}^{M}\sum_{j=1}^{N}(I_{(i,j)}^2 + \hat{I}_{(i,j)}^2)}{\sum_{i=1}^{M}\sum_{j=1}^{N}(I_{(i,j)} - \hat{I}_{(i,j)})^2}$	(4.15)	[56, 59, 73]

	RMSE	$$\text{RMSE} = \sqrt{\frac{1}{MN}\sum_{i=1}^{M}\sum_{j=1}^{N}(I_{(i,j)} - \hat{I}_{(i,j)})^2}$$	(4.16)	[73]
	S/MSE	$$\text{S/MSE} = 10 \times \log_{10} \frac{\sum_{i=1}^{M}\sum_{j=1}^{N} I_{(i,j)}}{\sum_{i=1}^{M}\sum_{j=1}^{N}(I_{(i,j)} - \hat{I}_{(i,j)})^2}$$	(4.17)	[56, 60]
	PSNR	$$\text{PSNR} = 10 \times \log_{10} \frac{I_{MAX}}{MSE}$$	(4.18)	[73]
	SSIM	$$\text{SSIM}_{i,j} = \frac{(2\mu_{I'_{(i,j)}}\mu_{\hat{I}'_{(i,j)}} + 6.5025) \times (2\sigma_{I'_{(i,j)}\hat{I}'_{(i,j)}} + 58.5225)}{(\mu^2_{I'_{(i,j)}} + \mu^2_{\hat{I}'_{(i,j)}} + 6.5025) \times (\sigma^2_{I'_{(i,j)}} + \sigma^2_{\hat{I}'_{(i,j)}} + 58.5225)}$$	(4.19)	[60, 73]
		$$\text{SSIM} = \frac{1}{MN}\sum_{i=1}^{M}\sum_{j=1}^{N} SSIM_{(i,j)}$$	(4.20)	
	EPF	$$\text{EPF} = \frac{\sum_{i=1}^{M}\sum_{j=1}^{N}(\Delta I_{(i,j)} - \mu_{\Delta I(i,j)})(\Delta \hat{I}_{(i,j)} - \mu_{\Delta \hat{I}_{(i,j)}})}{\sqrt{\sum_{i=1}^{M}\sum_{j=1}^{N}(\Delta I_{(i,j)} - \mu_{\Delta I(i,j)})(\Delta \hat{I}_{(i,j)} - \mu_{\Delta \hat{I}_{(i,j)}})}}$$	(4.21)	[60, 73]
Local metrics	CNR	$$\text{CNR}_m = 10 \times \log_{10}(\frac{\mu_I - \mu_b}{\sqrt{\sigma_I^2 + \sigma_b^2}})$$	(4.22)	[56, 59, 60]
		$$\text{CNR} = \frac{1}{M}\sum_{m=1}^{M} CNR_m$$	(4.23)	
	ENL	$$\text{ENL}_m = \frac{\mu_m^2}{\sigma_m^2}$$	(4.24)	[56, 59, 60]
		$$\text{ENL} = \frac{1}{M}\sum_{m=1}^{M} \text{ENL}_m$$	(4.25)	

Table 4: Definitions of image quality assessments. These global metrics compare the pixels' intensities between the $M \times N$ speckle noise corrupted image I and its despeckled outcome $\hat{I}$. In PSNR measurement, image's maximum possible pixel value I_{MAX} and image's mean square error (MSE) are taken into account. The SSIM score measures image quality based on structural similarity. Two compared images, original and denoised images, are convoluted with a 11×11 circular-symmetric Gaussian weighted filter ($\sigma^2 = 1.5$) to calculate local statistics parameters. The $\mu_{I'(i,j)}$, $\mu_{\hat{I}'(i,j)}$, $\sigma_{I'(i,j),\hat{I}'(i,j)}$ are the local means and variances matrixes of the corresponding images respectively. In Equation (4.21), $\Delta I, \Delta \hat{I}$ are the edge detected images using a standard high-pass 3×3 approximation of the Laplacian operator. $\mu_{\Delta I}, \mu_{\Delta \hat{I}}$ are the mean of images $\Delta I, \Delta \hat{I}$ respectively. For the last two metrics, μ_m, σ_m are the mean and standard deviation of the mth user selected region of interest (ROI) respectively. In CNR, μ_b and σ_b^2 are the mean and variance of the user defined background, respectively.

The SNR is a useful measure that compares the level of the desired signal to that of background noise

(speckle noise in this case). A higher SNR indicates less noise corruption and better denoising result. The PSNR is also used to qualify the noise reduction result in a denoised image. Typically, an acceptable image should have a PSNR greater than 25 dB. EPF shows the edge preservation after image smoothing. EPF is always close to unity if the edge information is preserved as much as possible.

The SSIM metric is designed based on comparing the local patterns of normalized pixels' intensities. For a natural image, its pixels are always highly related especially when they are spatially correlated. But for the most commonly used image quality assessments, they simply use linear or quasilinear operation (discussed in more detail in reference [74]), while the human visual system is a complicated nonlinear system. To solve this limitation, the SSIM score is designed to give a more direct way to assess the deblurred and compressed images' quality. The SSIM measurement compares the pixel luminance, contrast and the structure of the original and despeckled images by means of local statistics (local mean and local variance). In [74], the local statistics of two images are obtained by convoluting with a 11×11 symmetric Gaussian kernel. For an ideal denoising method, it suppresses noise without changing the image local features. Thus, its resulting SSIM is 1; whereas a bad similarity has a SSIM with -1 [73].

Different to the first six global metrics, the CNR and ENL are average values of the regions of interest (ROIs) user specified on the images. The CNR measures the contrast between the background and the foreground while the ENL indicate the smoothness of a speckle corrupted area that should have a homogenous feature [59]. To measure these two metrics, in reference [60], The values of the CNR and ENL all highly depend on the size of the ROIs. Due to this factor, in this research, all box ROIs are set to 10×10 for the just comparison (shown in Figure 26). The box dimension 10×10 was selected based on the thinnest phantom layer whose thickness is about 92 μm. The depth resolution of our SS-OCT is around 10 μm, that's to say in axial direction, this thinnest layer is approximately represented by 10 pixels. Thus, there are few or even no boundary straddle issues if ROIs were selected carefully. The numbers of the ROIs applied in these evaluations are inconsistent with the reference [59], ROIs is 7 (1 background + 6 foregrounds) for CNR and 6 (foregrounds) for the ENL. The output CNR and ENL are the average values over the ROIs in each images. Before measurement of these two metrics, the images are logarithmic transformed (Not for other metrics). Thereby, the multiplicative noise is converted to tractable additive noise.

The interested ROIs we selected are evenly distributed to the different homogeneous areas of the obtained OCT image. For example, Figure 26 has three visually identifiable different layers. To obtain its CNR score, we chose two ROIs (highlighted by green boxes) in each layer, and their position were randomly selected.

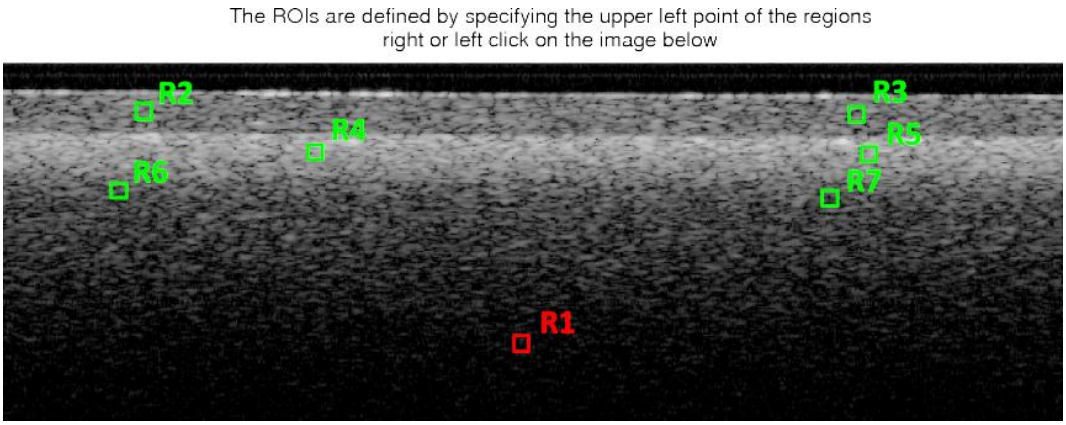

Figure 26. An example of region of interests (ROIs, highlighted by color) selection for OCT image's CNR evaluation. The box R7 (red) in the lower area was used to estimate the speckle noise level. The foregrounds (green box R1 to R6) were selected on the homogeneous regions. Image intensity has been adjusted.

As the author did in reference [56], to quantitatively judge the performance of each filter, we define an average figure of merit (FOM):

$$\mathrm{FOM} = \mathrm{SNR}_n + \mathrm{RMSE}_n + \mathrm{S/MSE}_n + \mathrm{PSNR}_n + w(\mathrm{SSIM}_n + \mathrm{EPF}_n + \mathrm{CNR}_n + \mathrm{ENL}_n) \tag{4.26}$$

Where n refers to the fact that the image quality score is normalized. For a certain quality metric, the best performed filter will give mark one. In OCT image speckle reduction, speckle noise suppression and edge feature retention are two primary issues, so that we give the last four metrics an extra weight w $(w = 2)$ to highlight their importance.

In addition, the CPU time of each filter to complete one processing also will be compared.

4.5 Image Reconstruction

As you may have noticed, the OCT images we may obtain from our dental drill system are distorted by lots of factors, including nonuniform rotation of the drill bit, the drill-induced vibration and the conical scan of the laser beam. The inherent distortion creates artifacts and severely affects the application result of OCT images. To avoid medical misdiagnosis, the distorted images must be compensated or corrected. To properly compensate the beam scanning distortion, the correction techniques used in ultrasound image or radar scanning can be applied in our system. For example, we can resample and display the raw data from Caresian coordinates to radial coordinates. The vibration artifacts can be reduced to some extent by using motion correction. Compared to the other factors, the nonuniform rotation (discussed previously in section 4.2) of drill bit constitutes a significant potential source of error in measurement of imaged object shape, area, and diameter. Thus, in the following part, we will concentrate only on oversampling-induced distortions.

Reference [62] purposed a novel OCT image acquisition technique for sensorless hand-held OCT application. They manually translate samples under a fixed spectral domain OCT slowly. The images they acquired are oversampled similar to ours. The non-uniform scan velocity induced motion artifacts are corrected by analyzing the Pearson correlation coefficients between consecutive A-scans. Figure 27

shows this representation of this algorithm. The method starts with selecting the first acquired A-scan as it reference. The cross-correlation coefficients between the reference A-scan and its following successive acquired A-scans are computed. When the computed cross correlation coefficient falls below a certain value (a user predefined threshold), this A-scan can be considered as acquired from next lateral resolution volume. This A-scan is selected to construct the downsampled image. The assembled A-scan is then set as the reference and program repeat until it iterated through all acquired A-scans.

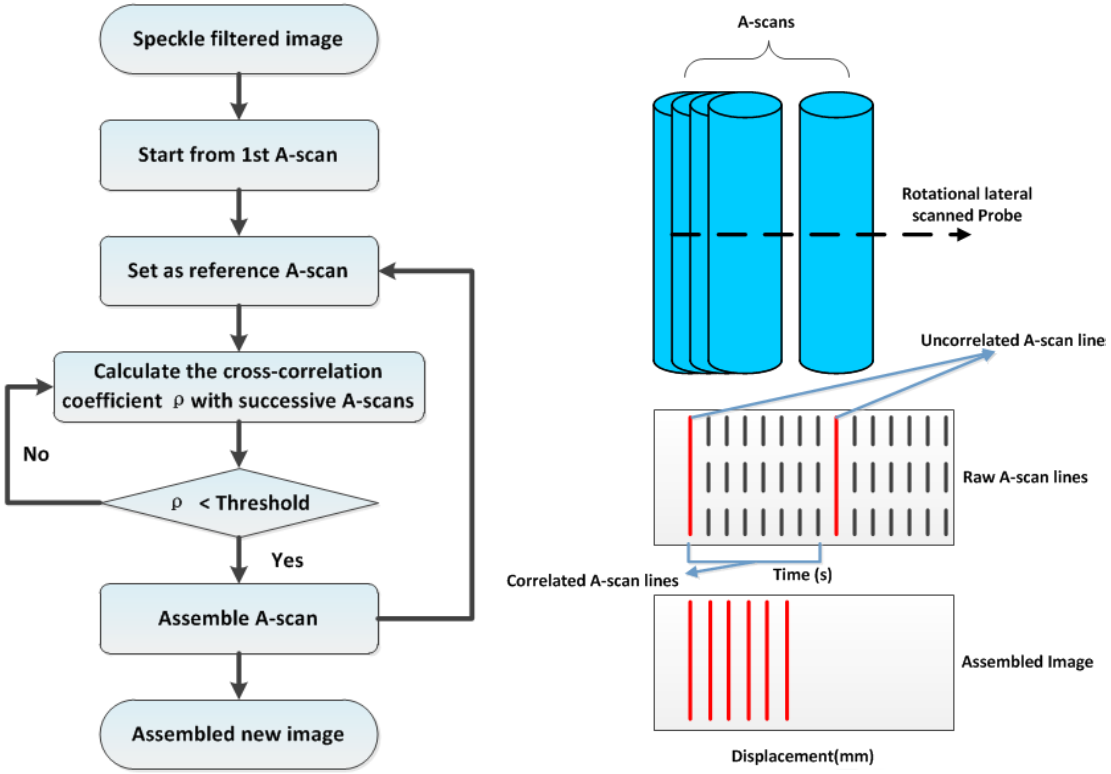

A. Flow chart of the motion-induced artifacts correction algorithm

B. Synchronization A-scans with the OCT rotational probe lateral displacement

Figure 27. Representation of the cross-correlation based OCT image motion correction algorithm. (Adapted from [62])

In Figure 28, the OCT images' decorrelation curves of different obtained from different rotational speeds obtained from silicone based optical phantom with titanium dioxide (TiO_2) power, shows the decorrelation curves of OCT images obtained at different rotational speed. The horizontal axis represents the lateral displacement between consecutive A-scans. The center A-scan line in each image is set as the reference. The horizontal line in Figure 28 indicates the distance between the sequential A-scans and the reference A-scan. The negative lateral displacement depicts the reference is compared with its previous A-scans. When RPM is zero, theoretically, the cross-correlation coefficient ρ should be equal "unity" at all displacement. However, in the speckle noise contaminated OCT images, the cross-correlation coefficient is always less than unity. For other rotational speeds, the decorrelation curves converge to a relative low cross correlation value when the lateral displacement is beyond the transverse resolution of the OCT system.

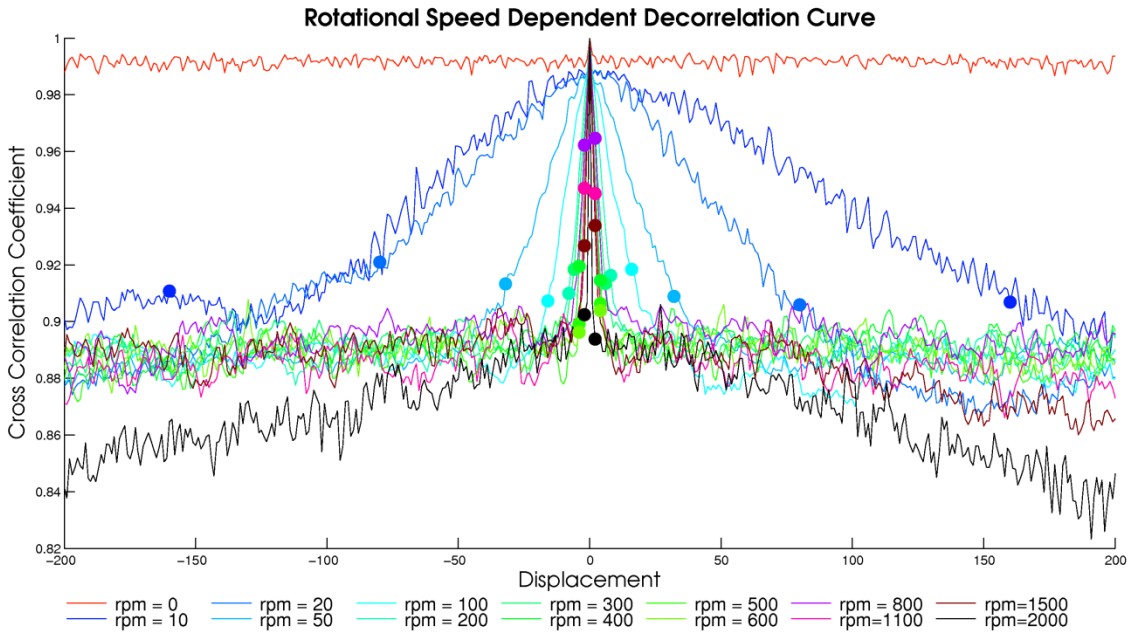

Figure 28. Rotational speed dependent decorrelation curves. Results were obtained from multilayered silicone based optical phantom. The center column in the OCT image is chosen as the reference A-scan. The closer to the reference line, the higher the cross-correlation coefficient would be. The small vibrations on the curves result from the speckle noise. The circles on the decorrelation curves indicate the position of the successive but uncorrelated A-scans (defined by Equation (4.29)). The unfiltered data were taken from a silicone based phantom with titanium dioxide (TiO_2) powder.

A big challenge of applying this approach in sensor-less OCT image reconstruction is the downsampling threshold selection. In reference [62], the author determined the threshold value by using a programmable motorized stage. The probing sample was moved along the lateral direction with known velocity. The downsampling threshold was selected from the decorrelation curve with a desired sampling ratio of the assembled image. And then the images were downsampled using the algorithm for the chosen sampling ratio. However, in our case, this novel method cannot be directly applied to our system. As mentioned in subsection 4.2 before, the instantaneous rotational speed can be influenced by lots of factors, but the lack of synchronization component or device in our drill system makes the measurement of the rotational speed unrealistic. Therefore, in our work, we modify this algorithm by using averaged uncorrelation coefficient defined by Equation (4.31).

Following the calculations in section 4.2, we already know that, in a conventional single lateral resolution volume, the number of A-scan lines the oversampled OCT will extract is:

$$n_{\text{ascan}} = i \cdot \zeta \tag{4.27}$$

Where the factor i denotes the A-scan lines interpolation ratio of the OCT system. Substituting Equation (4.4) into it, Equation (4.27) can be rewritten as:

$$n_{\text{ascan}} = i\frac{60 f_s \cdot l_r}{2n\pi \cdot d'} \tag{4.28}$$

In the following work, we noticed that, with our system configuration, the A-scans were interpolated with a relative lateral resolution about 5 μm (1001 pixels in 5 mm horizontal displacement, but the

system actual lateral resolution is 60 μm). Thus, in our case, i is approximately equal to 12 ($\frac{60}{(5000/1001)}$). In this way, we can predict the interval between two adjacent uncorrelated pixels is theoretical equal to:

$$n_{\text{interval}} = n_{\text{ascan}} - 1 \tag{4.29}$$

Therefore, we can estimate the threshold for adjacent uncorrelated A-scan lines separation by calculating the Pearson product-moment correlation coefficient of two continuous but uncorrelated A-scan lines with the interval given by Equation (4.29):

$$\rho_j = \frac{< (I_n - \mu_n)(I_{n+n_{\text{interval}}} - \mu_{n+n_{\text{interval}}}) >}{\sigma_n \sigma_{n+n_{\text{interval}}}} \tag{4.30}$$

In which:

<> depicts the expected value;

I_n is the intensity of anyone A-scan line in an image and its most neighbor uncorrelated A-scan has an intensity of $I_{n+n_{\text{interval}}}$;

$\mu_n, \mu_{n+n_{interval}}$ and $\sigma_n, \sigma_{n+n_{\text{interval}}}$ are the mean and standard deviations of the corresponding A-scans.

Then the downsampling threshold ρ shown in Figure 27.A for image downsampling can be obtained by averaging the Pearson product-moment correlation coefficients (shown in Figure 29) obtained at different rotational speeds:

$$\rho = \frac{1}{J} \sum_{j=1}^{J} \rho_j \tag{4.31}$$

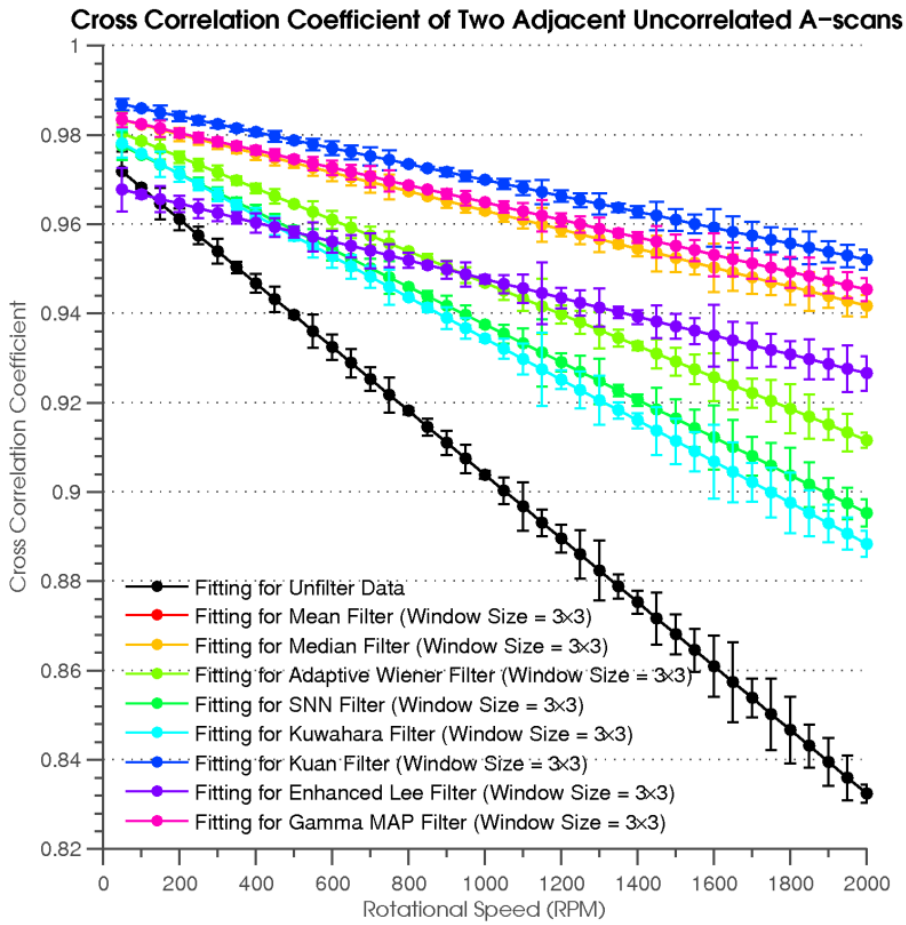

Figure 29. Cross correlation coefficients of two adjacent but uncorrelated A-scan lines at different rotational speeds. The errorbars depict the standard error of mean (SEM). In the plot, the fitting lines Mean filter and Kuan filter are overlapped.

Figure 29 presents the variation of the cross correlation coefficient of two successive uncorrelated A-scans. As the sampling ratio decreases, the cross correlation coefficients decrease no matter whether the images are filtered or not. This decrease is probably because the rotation-induced vibration from the rotary stage (see subsection 3.4 above). The vibration degrades the correspondence between two successive but uncorrelated A-scan. However, after denoising, the cross correlation coefficient is less sensitive to the rotational speed. And the error bars in Figure 29, depicting the standard error of mean (SEM) of the measurement, are also less than the unfiltered images. Therefore, we consider the image despeckling operation of the corrupted images not only improves the images visibility but also increases the image reconstruction accuracy of our approach. Of course, the cross correlation coefficient of two A-scan lines is affected by the types of digital filter and the size of the sliding window.

This downsampling threshold selection method is based on the decorrelation curve of a particular sample. Different samples have different homogeneities. This difference changes the speckle patterns and even the system noises (due to the change in reflection light power mentioned in subsection 2.4.1) in the OCT images and, of course, affects the cross correlation coefficients of the A-scan lines. Therefore, actively and adaptively modify the threshold value for image downsampling will significantly improve the reconstruction result. In reference [62], the author suggests to utilize real-time

tissue classification algorithms to adaptively adjust the threshold value. Besides, narrowing the range of rotational speed is another approach to improving the performance of this reconstruction algorithm.

This technique is insensitive to the direction of the displacement [62]. In dental drilling, the feed rate and vibration or jitter of the drill bit may bring some troubles to the image reconstruction, since they sufficiently degrade the cross correlation between the consecutive A-scans. To properly eliminate or remove these motion artifacts, some sophisticated motion estimation techniques can be combined with our algorithm to dynamically adjust the downsampling threshold for accurate reconstruction.

The performance of this technique for image reconstruction will be evaluated and discussed in the following chapters 5 and 6.

4.6 Short Conclusion

Different to other conventional OCT, in our application, the acquired OCT images are always oversampled. In this chapter, some common digital despeckle algorithms and image quality assessments have been studied. They will be applied to the oversampled OCT image to remove the natural speckle noise.

One question arises from the A-scan oversampling is image distortion. In dental surgery, the variation of drilling speed increases the difficult of image compensation and reconstruction. To address this problem, one adaptive decorrelation curve based method for rotational application is purposed in this chapter. This algorithm is designed based on image decorrelation curve. Its image reconstruction ability will be evaluated in the following chapters.

CHAPTER 5

RESULTS OF OPTICAL PHANTOMS TESTING

5.1 Introduction

This chapter mainly concentrates on the OCT image speckle noise reduction and image reconstruction. The qualities of images being processed by denoising programs, which were studied and discussed in chapter 4 before, are then compared objectively and quantitatively in section 5.3 in order to find the optimum filter for our design HSR-OCT system..

In section 5.4, we will conduct the adaptive cross correlation based OCT image reconstruction algorithm on the images despeckled by the filters we used in section 5.3. The results will be presented and discussed to verify the feasibility of this technique in our HSR-OCT application.

5.2 Image Preprocessing

It is worth mention that there are three pre-processing steps need to be done before denoising the raw data obtained from our SS-OCT:

First, similar to any high speed OCT system, our SS-OCT uses a frame grabber to buffer the depth-priority OCT images [20]. To use the data from the frame buffer of the frame grabber, the data have to be rotated 90 °clockwise (Figure 30).

Second, in inverse fast Fourier transform procedure, negative pixels may result from the fast inverse Fourier transform. We noticed in Santec® OCT 3D viewer, the negative pixels are usually neglected in image reconstruction and representation. Thus, in our experiment, the negative pixels were set to zero.

After that, all the raw data with size of 1019×1001 were cropped to 340×1001. No useful information loss is caused since light cannot penetrate to the deeper part (high reflection at the top layers) so that pixels of that region are total dark and carrier no structure information. The possible non-zero pixels in that area are due to the speckle noise or system noise. This shrinkage saves the storage space as well as greatly saves the computational time of post-processing.

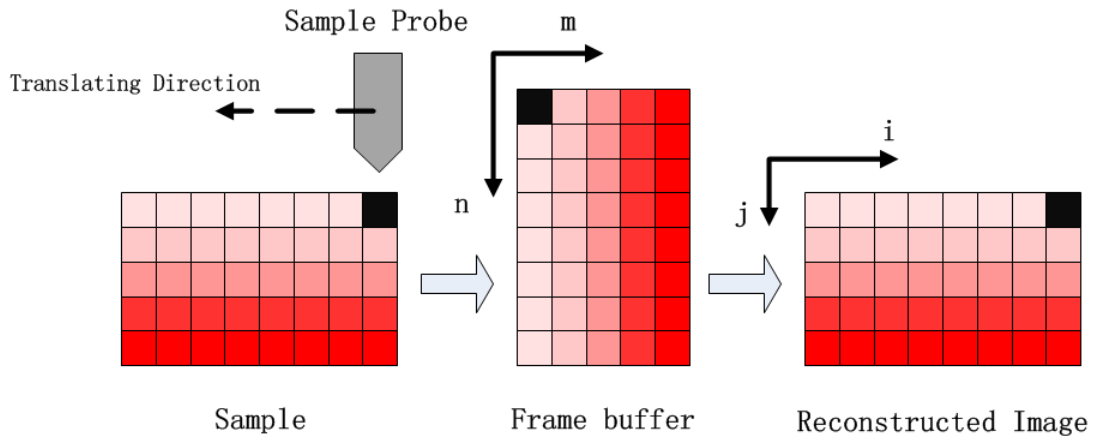

Figure 30. OCT image frame grabber. (Adapted from reference [20])

5.3 Despeckle Result and Discussion

The three different types of phantoms shown in Figure 18 were imaged in our experiment. And for the multilayered type, we prepared two with different thickness (Table 3). For each phantom, in image acquisition, the speed of the HR-3stage increased genteelly from 50 RPM to 2000 RPM, with an interval of 50 RPM. Images with obvious dispersion were discarded and retired until five prefect images (no dispersion and no mirrored image) were acquired at each RPM. Before increasing the speed, the position of the stage was reset to avoid the stage slide aside due to the rotation-induced vibration.

In this research, all the evaluations (noise reductions, image assessments and image reconstruction) are implemented in Matlab (version 2010b) on a 2.0 GHz Pentium Dual-core (T4200) personal laptop. And all the codes were optimized for Matlab with the intention of saving CPU time.

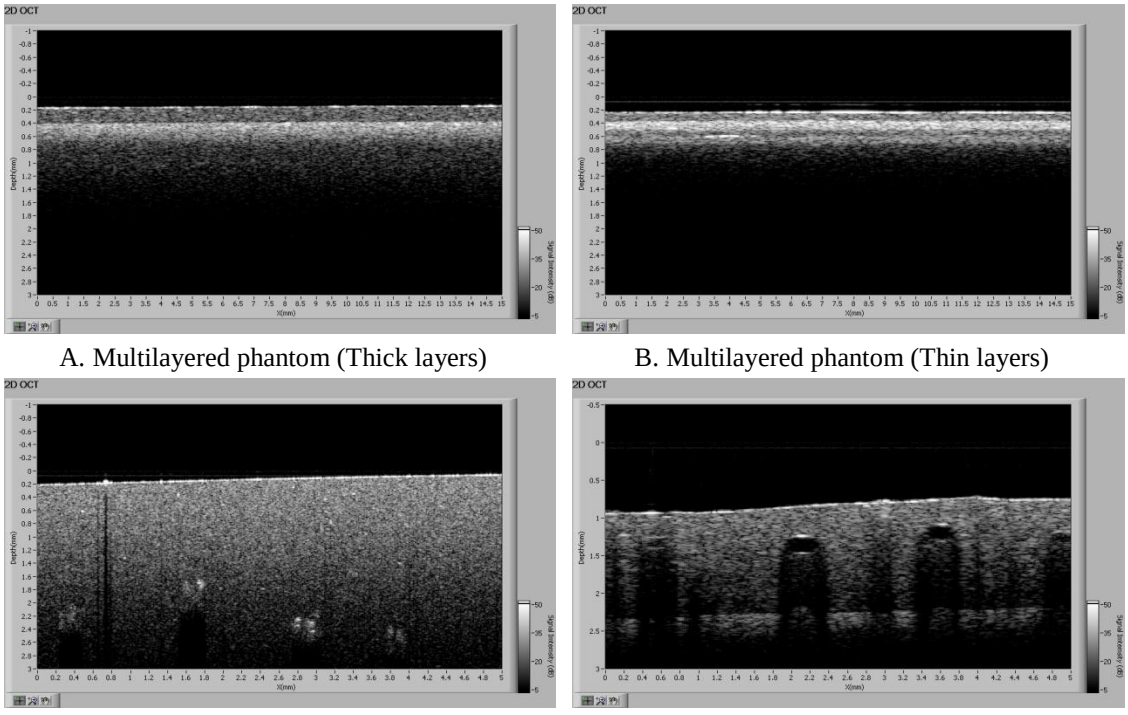

A. Multilayered phantom (Thick layers)

B. Multilayered phantom (Thin layers)

C. Multichanneled phantom

D. Multilayered spongy-like phantom

Figure 31. The unfiltered OCT images took from different phantom at instantaneous speed 350 RPM

5.3.1 Rotational Speed Dependent Image Quality

Two images in Figure 32 show the image metrics variations. When increasing the stage rotational speed, both CNR and ENL of the obtained images decrease due to the decline the OCT sampling ratio. When the stage rotates at a low speed, the obtained adjacent A-scans have a high correlation. The variation of the pixels' intensities of the high correlated A-scans is smaller than that from undersampled images. Therefore, the images obtained at low speed have a better micro-homogeneity feature.

From Figure 32, we can also conclude that, in our application, speckle noise is predominated by the imaging depth. The images extracted from thicker phantoms (Figure 31 C & D) have got bad ENL and CNR scores than that from thin phantoms (Figure 31 A & B), even acquired at a low speed. The ENL of the multilayered sponge-like phantom is slightly low than the multichanneled phantom since the base of the former one has a large scattering ability (Equation (2.24)).

Summarizing, the images we will get from our designing specific OCT must heavily contaminated by speckle noise due to many factors including high rotational speed, high scattering coefficient of biologic tissues, long imaging depth and maybe Mie scattering from coolant water. The speckle noise reduction is a critical issue that must be addressed first before any other image processing.

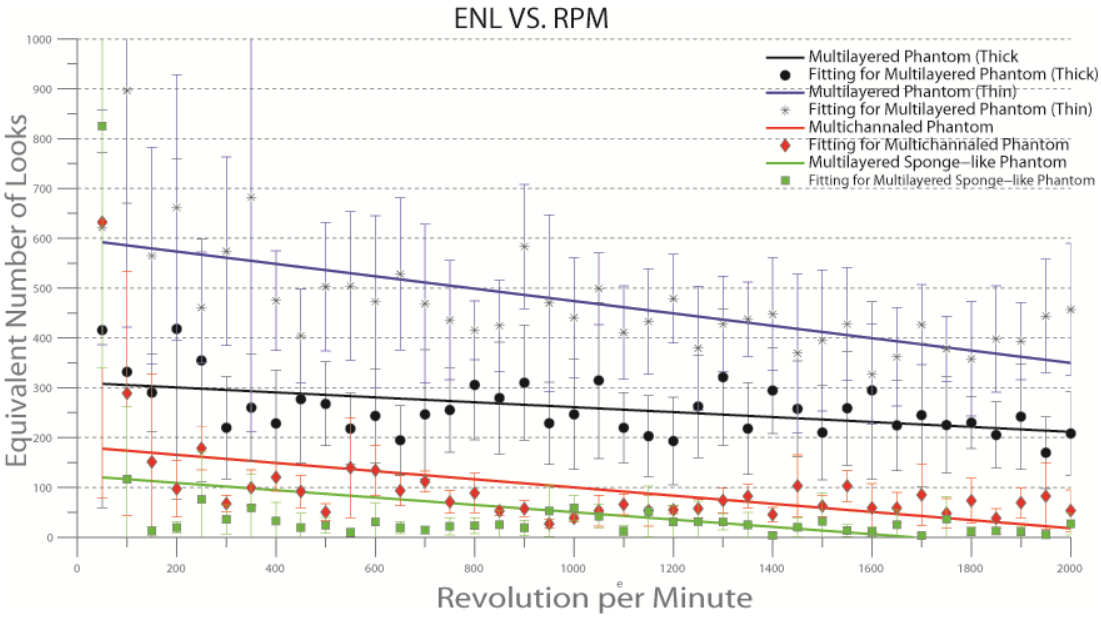

A. Plot of ENL VS. RPM

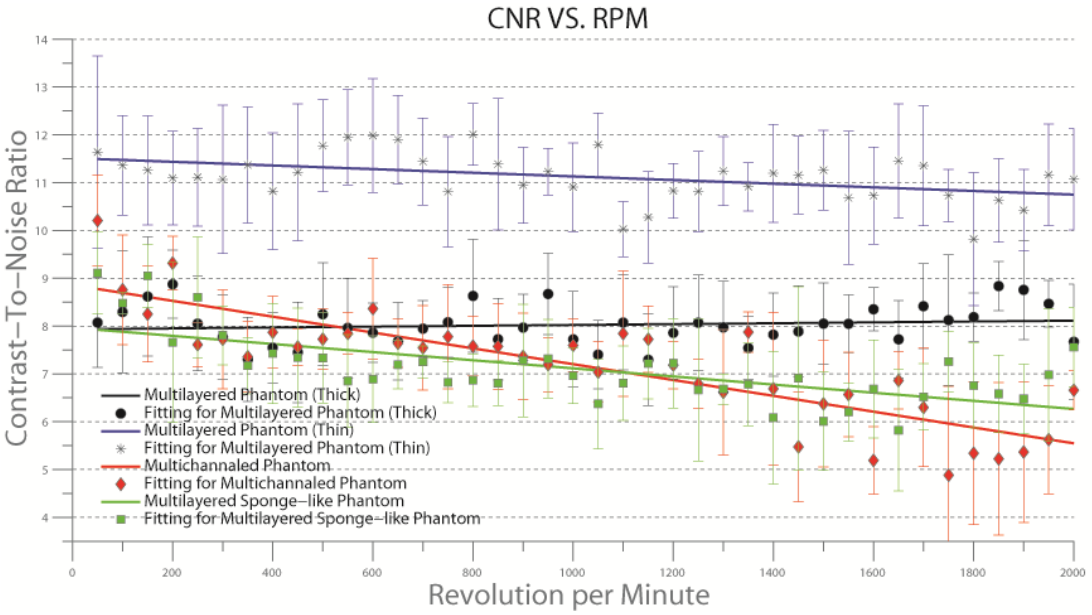

B. Plot of CNR VS. RPM

Figure 32: Effect of the rotation speed on the OCT image qualities. Solid lines show the linear fitting for the original data. The errorbars depict the standard error of mean (SEM).

5.3.2 Despeckle Performance of Different Digital Filters

We used the images from the multilayered sponge-like phantom (Figure 18.C) for the following test since they possess both the layered and the channeled structures in other phantoms. The scattering coefficient of the phantom layers are, from top to bottom, 6 cm^{-1} and 148 cm^{-1} respectively. And we used the traditional square odd sliding windows with sizes vary from 3 to 11. This range covers the most commonly used window sizes mentioned in references [9, 56, 62, 68, 73].

To quantitatively evaluate the performance of the 8 different digital filters directly, we choose an image which was taken at speed 350 RPM. At such circumstance, this image has a small sampling ratio ($\zeta \approx 10$). We selected the 248th column in the unfiltered image (Figure 33). The corresponding filtered images are presented in Appendix A, and the A-scans' profiles comparisons are plotted in the Figure 34.

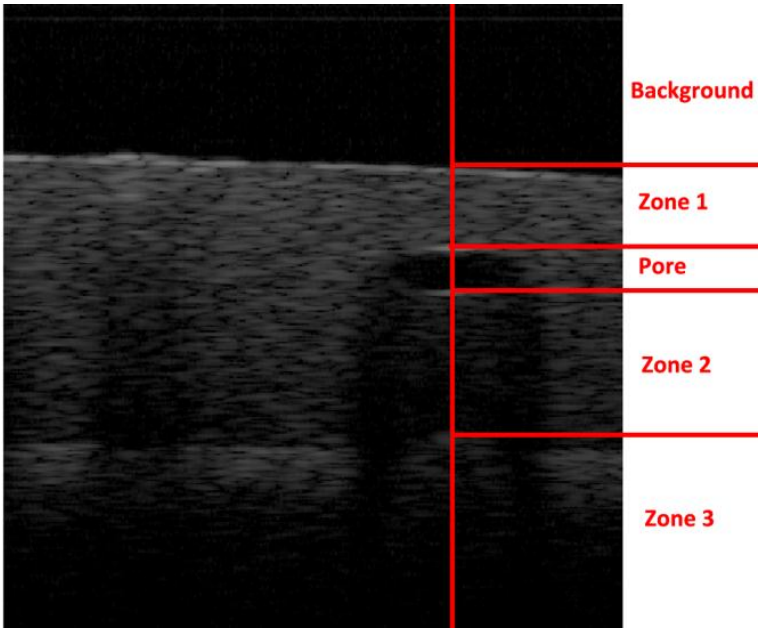

Figure 33. Unfiltered OCT image of the multilayered sponge-like phantom. The highlighted 248th column in the image is then analyzed in Figure 34. The image is cropped from original large image.

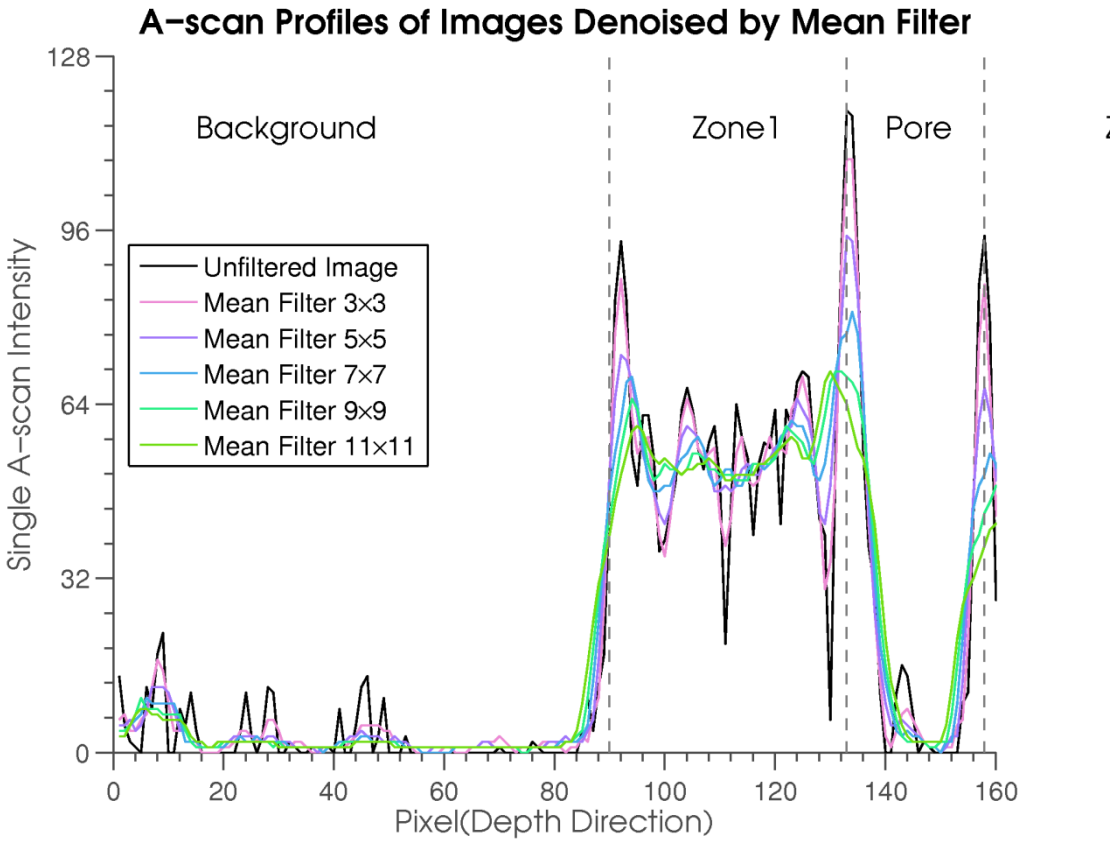

A. Despeckled by mean filter

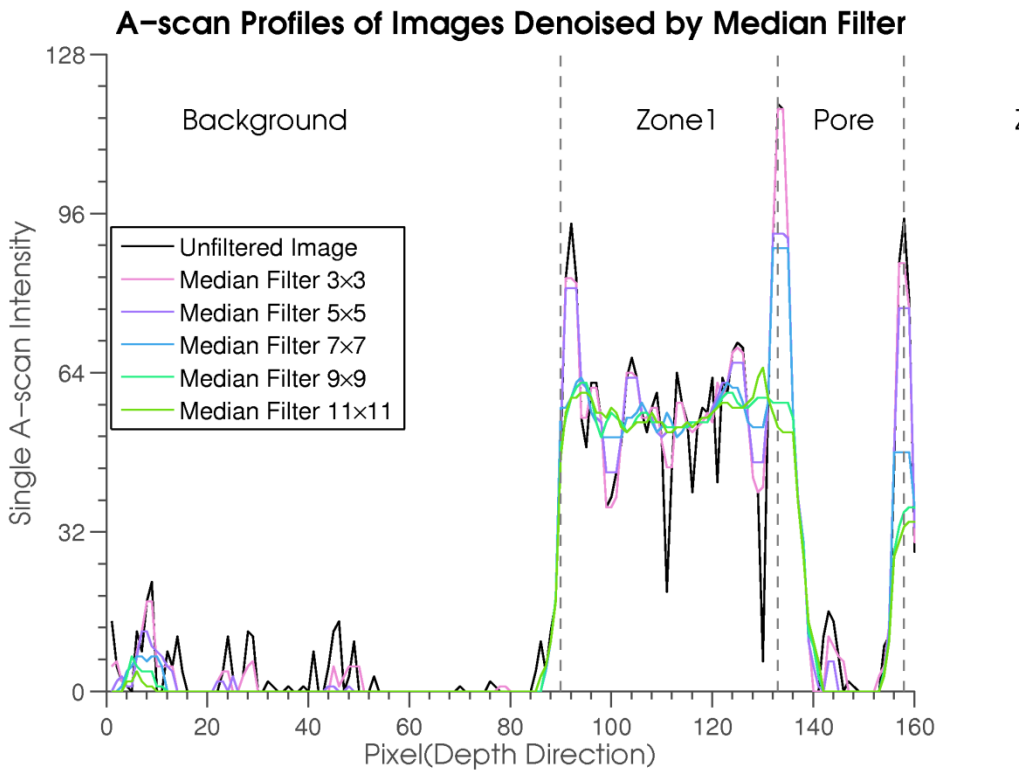

B. Despeckled by median filter

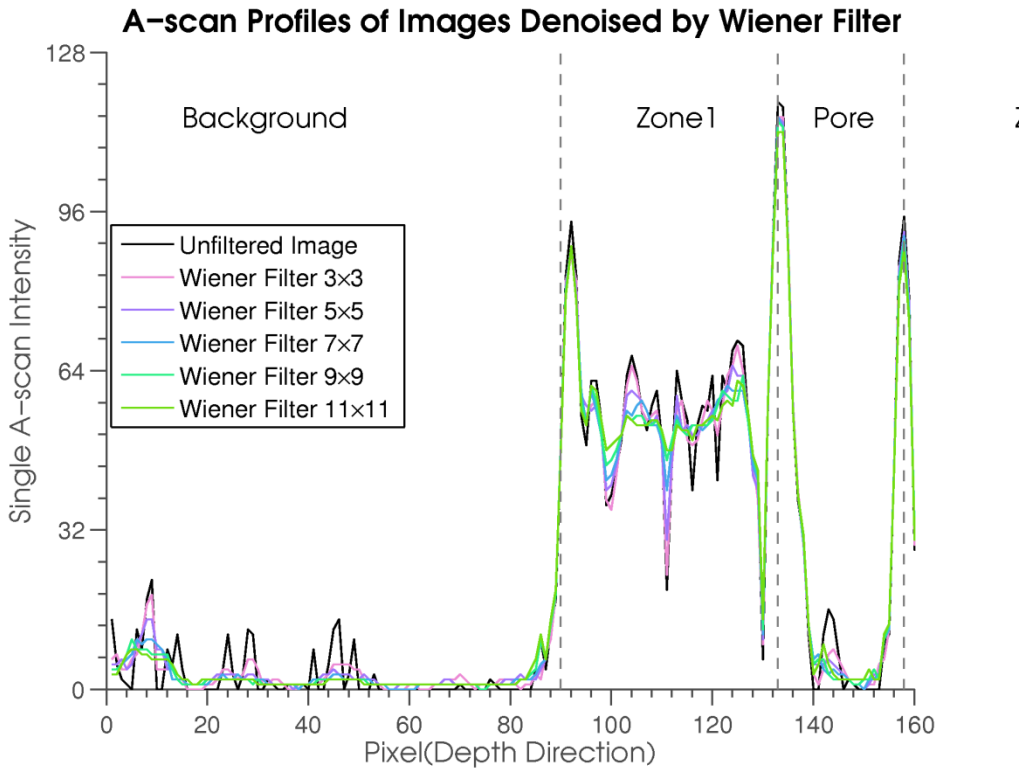

C. Despeckled by Wiener filter

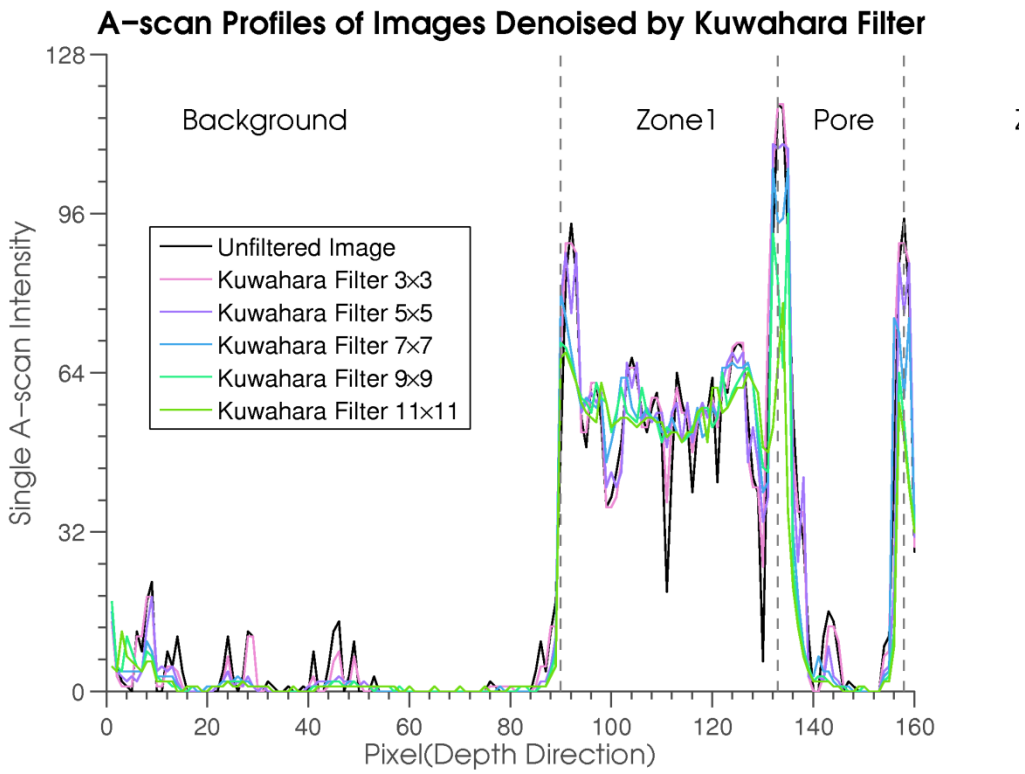

D. Despeckled by Kuwahara filter

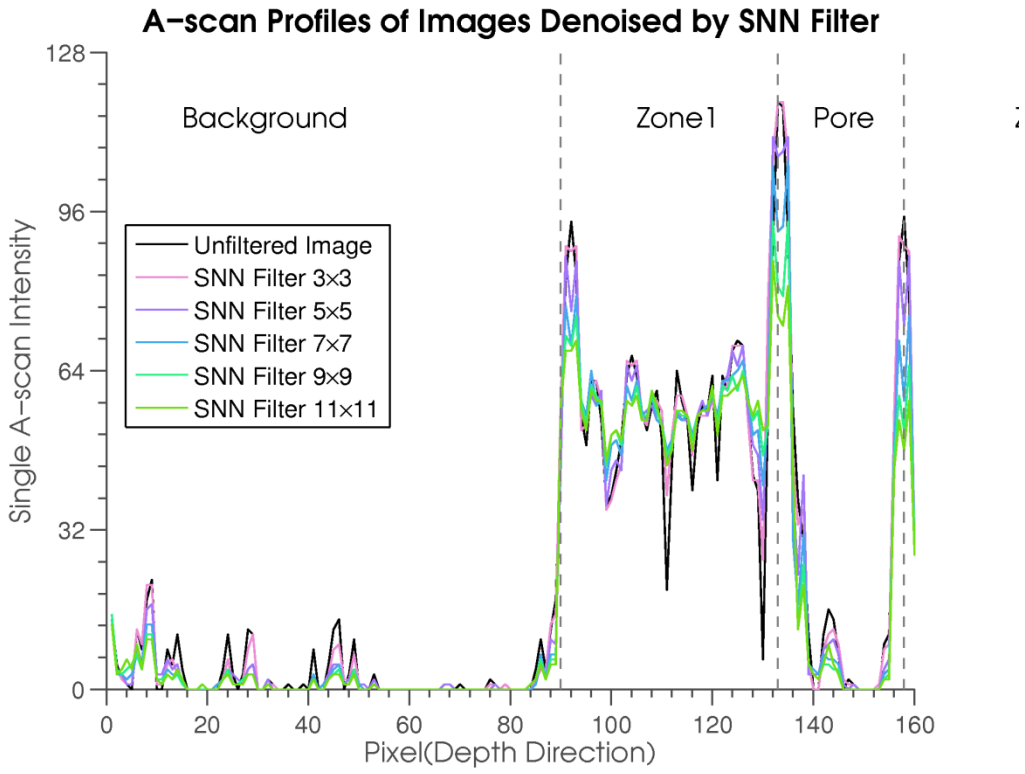

E. Despeckled by SNN filter

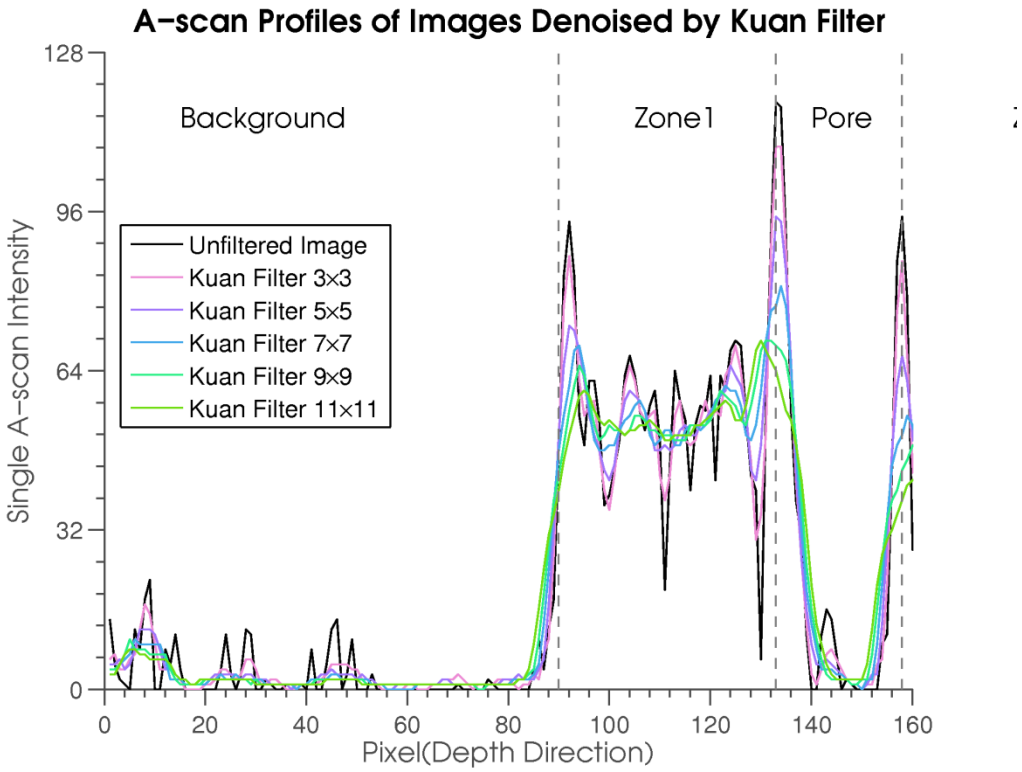

F. Despeckled by Kuan filter

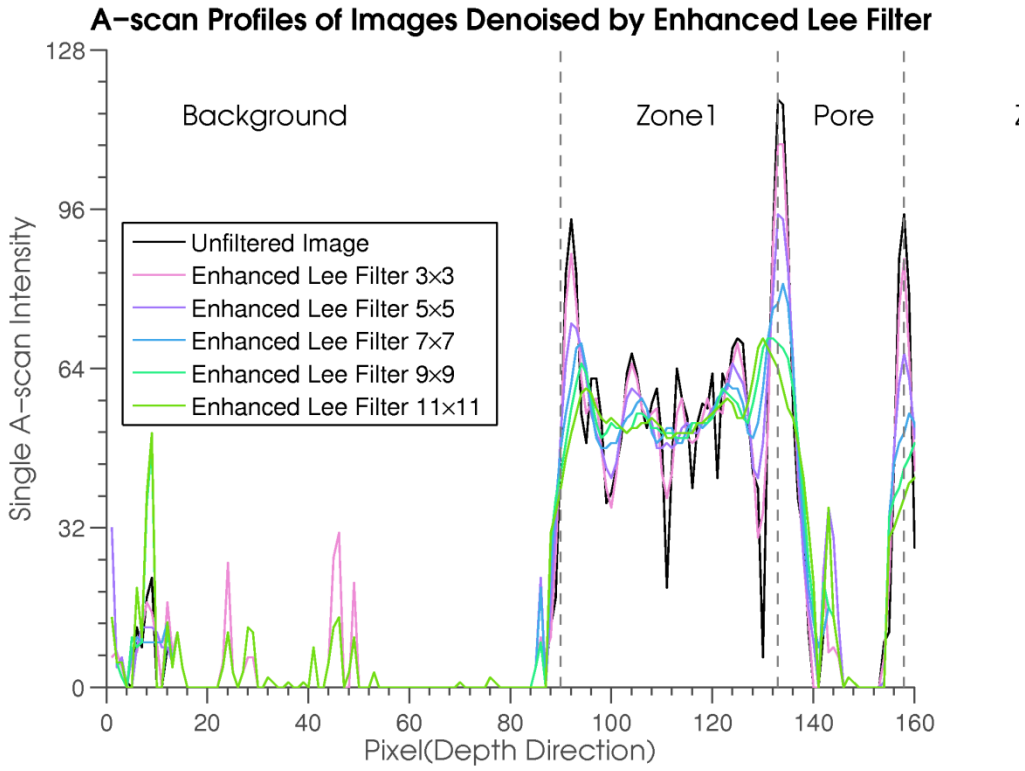

G. Despeckled by Enhanced Lee filter

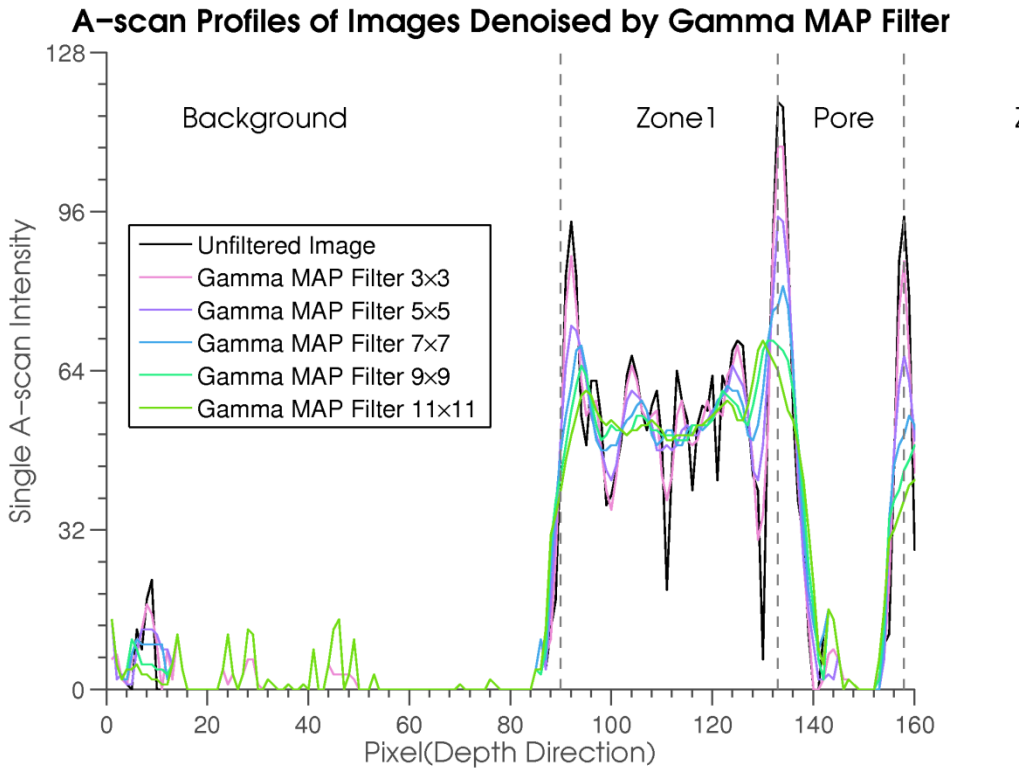

H. Despeckled by Gamma MAP filter

Figure 34. Comparison of despeckled A-scan profiles. The eight figures show A-scan profiles the denoise results of the multilayered sponge-like phantom (248th column in Figure 33, marking by red line). The y-axis represents the intensities value. The intensities change of the first 160 pixels along the depth direction is shown in x-axis, corresponding to an overall imaging depth of 1.6 mm.

Figure 34 compares the despeckle performance of the digital filters, grouping in filters. The first 90 pixels (background zone) along the X-axis correspond to the background area in front of the phantom. As we expected, the noises of the background above the phantom are eliminated by the first six filters. As the sliding window size grows, the degree of noise reduction becomes significantly. Especially for the median filter, the tiny ripples on the A-scan line nearly completely removed when the window size is 11×11. But it is important to note that, for the Enhanced Lee filter and Gamma MAP filter, the noises were emphasized. In the Figure 33, the noises (system noises or speckle noise from dust in air) are uniformly distributed. The last two filters despeckle based on image homogeneity. The algorithms' limitation makes them unable to distinguish and smooth homogeneous noise from background area (labeled as background in Figure 33). In Figure 34 G & H, the A-scan lines vary with the local noise intensity in background zone and sliding window size. The Enhanced Lee filtered images have larger noise pixels' values in background zone than those of Gamma MAP filter probably because they use different models.

At the pore region shown in Figure 34, all filtered OCT A-scan lines converge to zero as the sliding window size increases. But the median filter seems best suppress the speckle noise in the dark areas. It is consistent with the conclusion of the background area. In the zones 1 (labeled in Figure 33), the ripples on the A-scan profiles are smoothed out by digital filters with large window size as expected. However, the enhanced Lee filter is an exception to all filters we measured. When the sliding window size is larger than 7×7, the resultant filtered pixels will no longer be smoothed in some areas. The

inhomogeneity (or speckle noise) seems to be enlarged in such areas to some extent. In Appendix A, we can find some fake brighter spots in the enhanced Lee filter and Gamma MAP filter processed images.

To improve the denoising performance of Enhanced Lee filter and Gamma MAP filter in the background region, we may adopt angular compounding technique (a detectors array or a translation detector is placed in the back Fourier plane of the objective lens to receives light backscattered from the sample volume at different angles [19, 20], shown in Figure 35) before image post-processing as same as reference [56]. But this technique makes the system more complicated and, for the single detector case, light dispersion compensation is required [20].

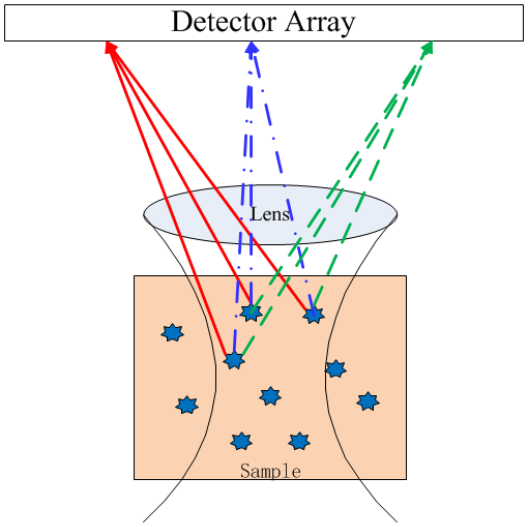

Figure 35. An example of angular compounding for speckle noise reduction. In this technique, a detector array is placed in the back Fourier plane of the objective lens to receive light backscattered from the sample volume at different angles. The absolute magnitudes of the signal measured by each detector is added and averaged to reduce the influence of speckle noise.

And in Figure 34, we can clearly see that, the A-scan profile reaches its local maximum at the interface between the air (background and pore) and the silicone due to the high surface reflection. This undesired incident power losses makes the imaging depth in silicone phantom shorter than usual. As expected, for all except adaptive Wiener filter, the peaks' value of the bright interface decreases as the smooth window size goes up. Thus, the adaptive Wiener filter performs quite well for preserving edges of high intensity.

5.3.3 Image Quality Assessment

Image quality metric	Abbreviation
Signal-to-noise ratio	SNR
Peak Signal-to-Noise Ratio	PSNR
Signal-to-Mean Square Error	S/MSE
Root Mean Square Error	RMSE
Structure Similarity Index	SSIM
Edge preserve factor	EPF
Contrast-to-Noise Ratio	CNR
Equivalent Number of Looks	ENL

Table 5. Abbreviations for image quality metrics (discussed in section 4.4)

In Appendix B. A, show that the speckle noise in images were significantly removed by the digital filters. The measured ENLs are quite sensitive to the choice of the sliding window size. Larger sliding window size always gives a better despeckle result. In our measurement, it seems the median filter gives the best despeckle results among all filters. When the window size is 11×11, the ENL of the despeckled images ENL is about 30 times than that of unfiltered images. Following by are Enhanced Lee filter, Gamma MAP filter, Kuan filter and mean filter, they have performed nearly same speckle suppression capability with our tested images. The ENL score of adaptive Wiener filtered images are not as high as reported in [56]. And its despcekle capability is less influenced by the window size growth. Besides, it is also found that the speckle suppression ability of each filter is also impacted by the rotational speed. From the observed results, we found, for a larger size of filter the ENL decreases much quicker than that of small filter as the RPM increases. For the median filter, in the entire speed range, the ENL has a promptly decrease of 1500 when the window size is 11×11; whereas the ENL drop of 3×3 median filter is only about 300.

In the terms CNR image quality metric, the median filter also outperforms other tested filters. An average leading CNR of about 2 were obtained for all measured window sizes. The interesting thing is, unlike to any other filters, the CNRs of median filtered images increase with increasing the drilling speed, this probably because the median filter uses the ranked original pixels with the window, no new unrealistic pixel values are generated according to the local statistics. The CNR improvements of enhanced Lee filter and Gamma MAP filter are relative small. Expanding sliding window size cannot significantly improve resultant image's CNR.

By increasing the sliding window size, the advantages of using digital filters for speckle suppression are more apparent. For the more speckle noise contaminated images, the large filter with larger smoothing window might give a better speckle suppression result. However, our experimental results show that, for all filters, there is an inverse relationship between the speckle noise reduction performance and edge / structure similarity preserve ability. The larger size of smooth window has less edge preservation capability as well as the structure similarity. To avoid the edge blurring, filter with small smooth window is sometimes recommended. Therefore, the optimal filter selection relies heavily on whether the speckle suppression or edge preservation is required.

We also note that in terms of edge preservation, Kuan filter, enhanced Lee filter and Gamma MAP filter perform not as well as reported in [73]. The obtained EPFs in we measurement are only half of the value posted in [73]. The enhanced Lee filter and the Gamma MAP filter perform more or less equally in terms of ENL, CNR, EPF and SSIM image metrics.

As expected, the image quality metrics (SNR, PSNR and S/MSE) decrease as the sliding window size grows. In terms of the SNR, images filtered by 3×3 mask have a 3 dB improvement dB at least. In Appendix B.F, we can clearly see that all PSNRs are above or around 30 dB, we can conclude that our filtered images have high fidelities, even in the worst-case scenario (mean filter with window size of 11×11). The adaptive Wiener filter performed the best in all of the last four image quality metrics (SNR, PSNR, S/MSE and RMSE). But it seems theses four metrics of the adaptive Wiener filter are more sensitive to the mask size growth and RPM speed increase. Under the circumstance of high rotational speed and large filtering mask size, Kuwahara filter and SNN filter offer can keep more reasonable image quality metrics.

To evaluate the effort of window size on speckle reduction and image quality, we also tried to enlarge the mask size (up to 31×31) of all the filters. No remarkable speckle noise reduction result has been achieved when the window size is larger than 11×11. Increasing window size will only lead to lose of more image features and waste computational resource.

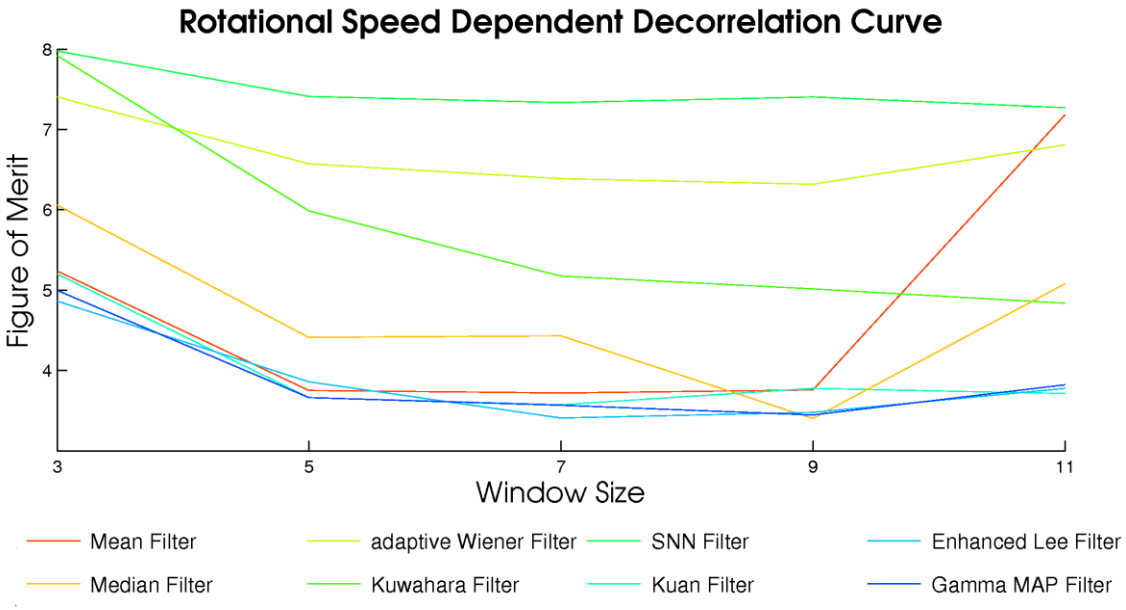

Figure 36. Summary of the digital filters performance based on Equation (4.26).

Based on Equation (4.26) in section Image Quality Assessments4.4, Figure 36 lists the figure of metrics (FOM) for different digital filters at different window size. The complete detailed comparison scores are list in Appendix C.

5.3.4 Comparison of Computational Complexity

Algorithm	CPU time (s)
Mean Filter	0.0265
Median Filter	0.0354
Wiener Filter	0.0613
Kuwahara Filter	42.0886
Symmetric Nearest Neighbor	23.9972
Kuan Filter	0.1052
Enhanced Lee Filter	0.1409
Gamma MAP Filter	0.1430

Table 6. The algorithm complexity of the digital filters. This table lists the CPU time required by each algorithm to complete a despeckle calculation session.

In Table 6, we compared the computational complexity of the digital filters by comparing the computer's CPU time required by each algorithm to complete a despeckle calculation session. The mean filter gives the fastest performance due to its simplest structure. Pixels with the sliding windows were only averaged. The median filter possesses the second place and takes a time a litter longer. The performance of Kuwahara filter and SNN filter are incapable of handing our data. Both two algorithms try to sweep the image pixel-by-pixel using for-loops. The repeated iterations slow the processing speed and take a long time, especially when the image size is large. To speed up the M-file performance in Matlab, we may compile the for-loops code into a MEX file and call them later in Matlab. GPU parallel computing is another option to shorten the denoising time. For the other four filters, they estimate and suppress speckle noise by calculating local statistical features, the mean and the variance of pixels within the sliding window in practical. These local features can be computed by convoluting the image with an all-ones matrix. The replacement using matrixing method greatly accelerates Matlab calculation speed, leading to order of magnitude improvements. The time consumption of the last three filter are about twice as many as that of Wiener filter since they use advanced multiplicative noise models to estimate local speckle variation, the resultant intensities are weighted rather than directly output. However, although we had tried our best knowledge to optimized our Matlab code for shortening time of computation, apparently, only mean and median filters satisfy the video rate (24 frames per second) image processing with my computer. To enable real time display, a powerful CPU or FPGA/DSP is appreciated.

In Matlab, we also found when the filtering mask size is relative small, the CUP computational time is nearly independent to window size. No significant changes have happened. The only drawback for large filtering window size is programmers took more system memory for calculation.

The CPU's time shown in Table 6 should therefore be considered preliminary estimates of the speed of algorithms.

5.3.5 Short Discussion

We summarize the FOM scores for all filters. And partly list the best FOM scores for each algorithm in Table 6. Comprehensively speaking, we conclude and recommend using adaptive Wiener filters to filter the oversampled, speckle noise contaminated OCT images. Such filters offer an optimal tradeoff between image quality and CPU time consumption. In our case, the adaptive Wiener filter with 3×3

mask size is sufficiently enough for images with relatively low speckle noise level. In case of image under high speckle noise contamination (low ENL and CNR), properly enlarge the filtering window size can improve the despeckle performance and image contrast as well.

The complete FOV scores comparison is given in Appendix C.

5.4 Oversampled OCT Images Reconstruction

For proof-of-principle, the multilayered sponge-like phantom (Figure 18.C) was used for oversampled OCT images reconstruction. This phantom choice is determined mainly based on the reason that the deliberately prepared pores inside the phantom make the phantom more structural similar to the jawbone, comparing with our rest phantoms. The porous structure of the phantom can degrade the cross correlation coefficient between two successive A-scans. This structure enables us to analyze the inter-sample and intra-sample variations in the correlation coefficients at each lateral displacement caused due to the inhomogeneity of structural features in sample [62]. Besides, the pores in the images also enable us objective compare the reconstruction results in visual.

In image reconstruction, the images we use are unfiltered and corresponding filtered images discussed in section 5.3. Each image contains 1001 A-scans. Theoretically, the true assembled image width can be obtained from Equation (4.4) and is given as:

$$\text{Ture Reconstructed Image Width} = \frac{2 \times \text{Original Image Width}}{\zeta} \tag{4.32}$$

Where $\text{Original Image Width}$ is equal to 1001 in our case.

Figure 37 is one example of the rotational speed dependent downsampled images width. It is clear shown that the reconstructed accuracy (distance between the assembled image width and true reconstructed image width) for unfiltered image varies greatly than filtered images as the rotational speed increasing. This indicates that to avoid the uncertainty of reconstruction accuracy, the speckle should be better suppressed before image reconstruction.

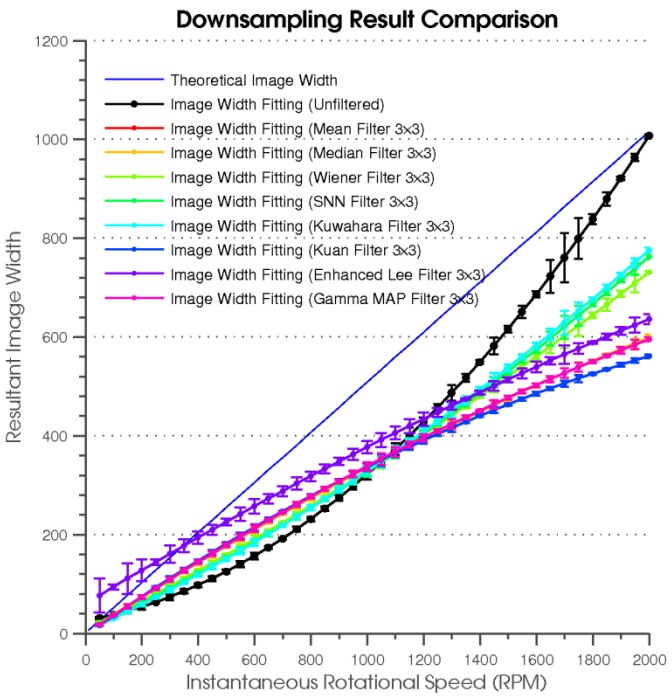

Figure 37. An example of assembled image width comparison. The despeckled images are filtered by corresponding digital filters with sliding window size of 3×3. The errorbars depict the standard error of mean (SEM).

Having a closer look at Figure 37, we find that the image width curves of all filtered images intersection with curve of unfiltered image almost at one point where the obtained image has a sampling ratio is almost half as large as the sliding window size of digital filters. The reconstruction accuracy of our method degrades when the number of correlated A-scan lines (numbers of A-scans obtained from conventional single lateral resolution volume) is not significantly larger than the denoising sliding window size. Under such circumstance, the digital filters not only reduce the speckle noises in the images but also increase the similarity between the consecutive uncorrelated A-scans. But in our method, we use the average downsampling threshold calculated by Equation (4.31), the made the selected threshold smaller than actual value. The number of A-scans the algorithm selected is less than the theoretical. Therefore, the assembled images become less accurate as the rotational speed increases.

We noticed that in Figure 37, some curves are overlapped, especially at the low rotation speed part. And it is also still hard to compare the reconstruction accuracy at different RPM. To aid visualization of the feasibility of our, we defined two new metrics for our downsampled images:

The first metric is the A-scan redundancy ratio (ARR), which measures the number of A-scans compared for each selected [62].

$$ARR = \frac{\text{Original Image Width}}{\text{Reconstructed Image Width}} \tag{4.33}$$

For an optimal downsampling algorithm, the ARR should have a value close to unity.

The second metric is distortion ratio (DR) defined as Equation (4.34). The DR is a value of percentage used to measure the degree of distortion of the assembled image after downsampling. A negative DR indicates the corresponding reconstructed image is over-downsampled (the measured object in the

assembled image is narrow than its physical size in lateral direction); where a positive DR represents the imaged objects have been stretched in lateral direction. For an optimal reconstruction algorithm, the DR value should be equal or close to zero. In our algorithm, the variation in DR values over the range of RPM provides us a powerful parameter to evaluate the robustness of the selected downsampling threshold (obtained from Equation (4.31)). The narrow range of DR variation, the higher assembly accuracy would be, and the downsampling threshold can be used in a wider range of RPM.

$$\mathrm{DR} = \frac{\text{Measured Reconstructed Image Width - Ture Reconstructed Image Width}}{\text{Ture Reconstructed Image Width}} \quad (4.34)$$

The sampling ratio of 2 was selected to calculate the corresponding downsampling thresholds (by Equation (4.31)) for image reconstruction. Figure 38 illustrates the variations in ARR and DR of different digital and different sliding window size. It is clearly seen that, in most instances, the assembled images are over-downsampled, especially when the rotational speed is relative high. Compared to the filtered images, the DR curve of unfiltered reconstructed images varies over a wider range than that of filtered images. This variation in DR can militate against the image reconstruction since the reconstruction accuracy cannot be significantly improved by simple modifying the threshold value to make the reconstruction less sensitive to the variation of rotational speed.

The experimental result illustrated in Figure 38 shows that the digital despeckling filters can improve the performance of our algorithm since they can reduce the speckle contrast (increase SNR) of OCT images. The DR curves of downsampled despeckled images look much smoother. And the RPM variation has relatively small influence on DR curves.

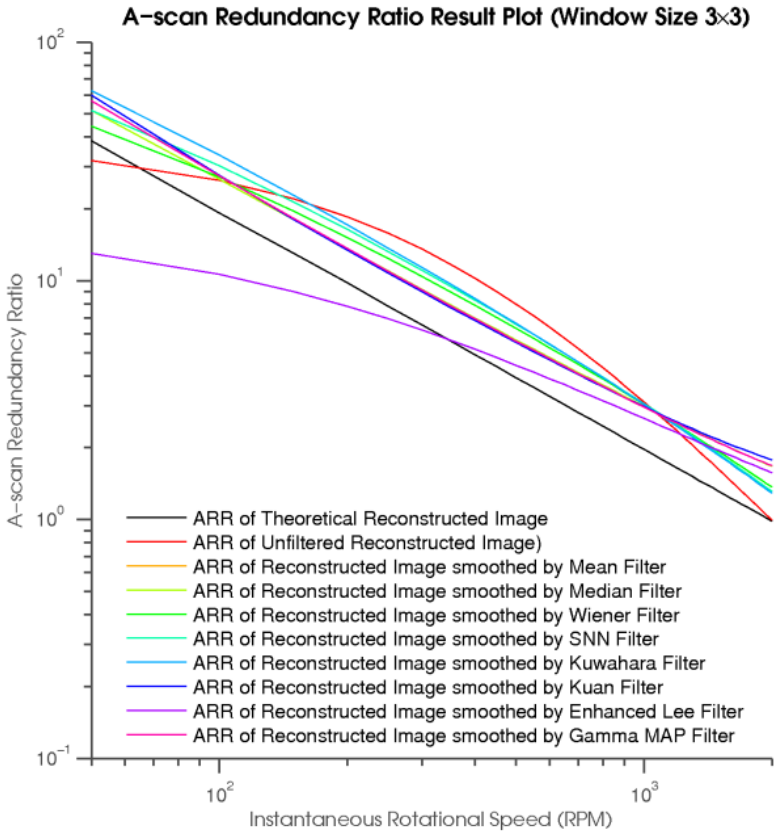

A. ARR of filters with window size 3×3

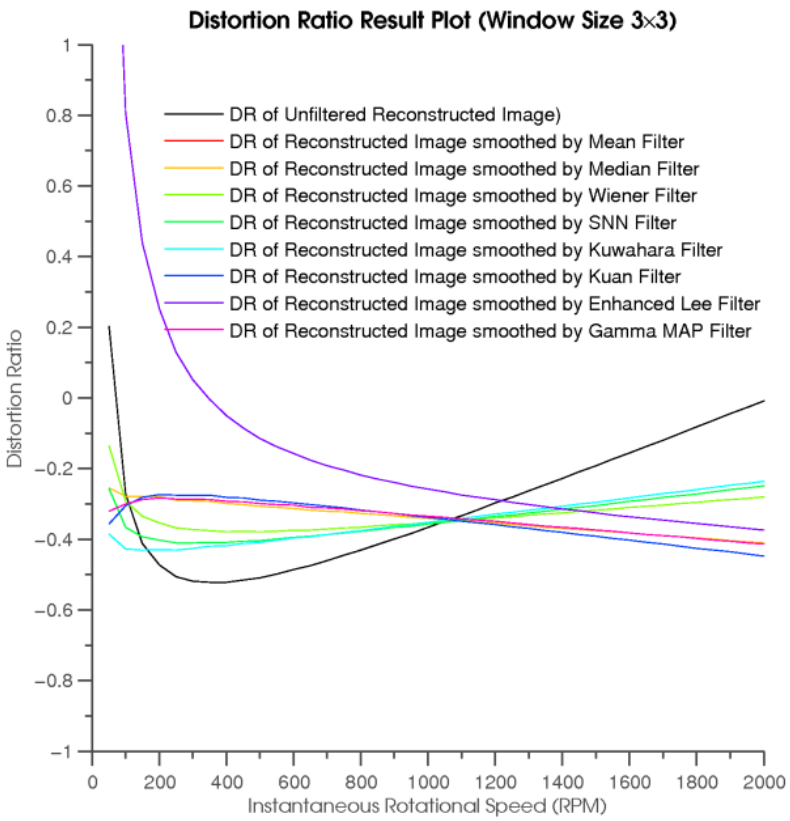

B. DR of filters with window size 3×3

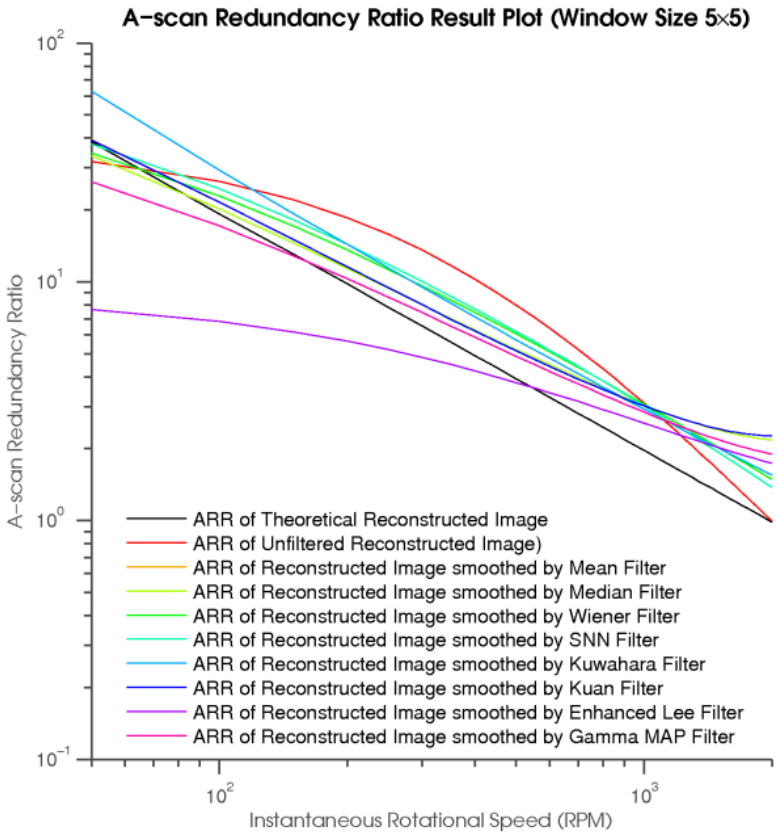

C. ARR of filters with window size 5×5

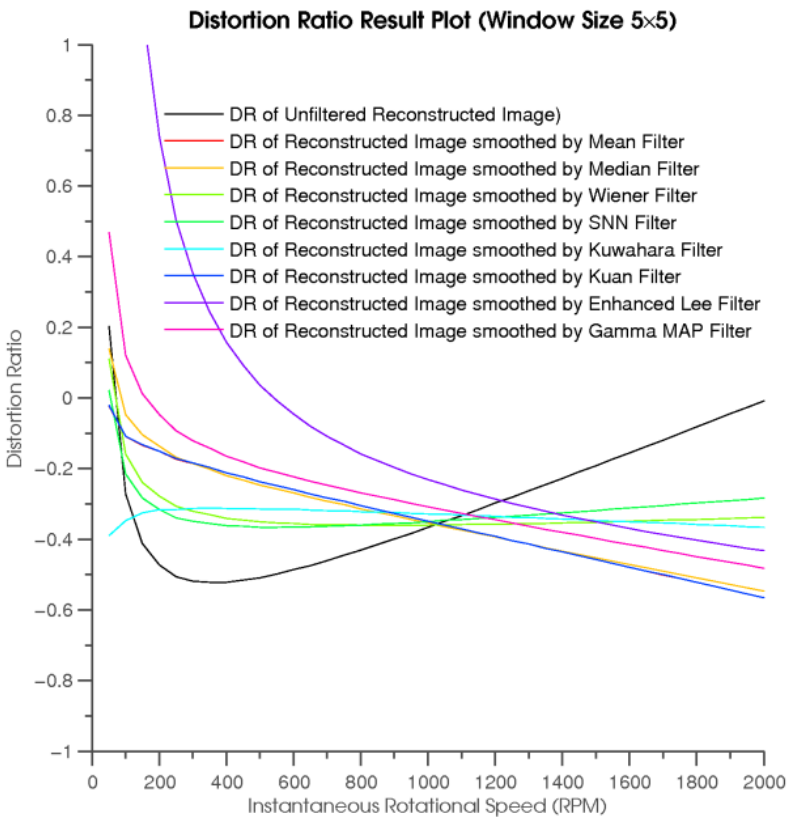

D. DR of filters with window size 5×5

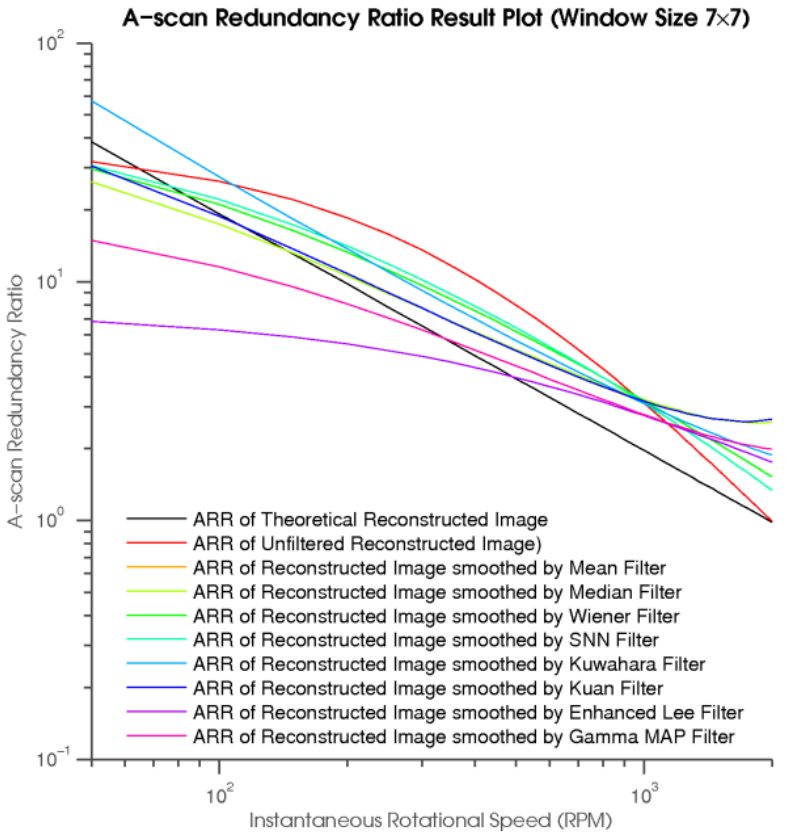

E. ARR of filters with window size 7×7

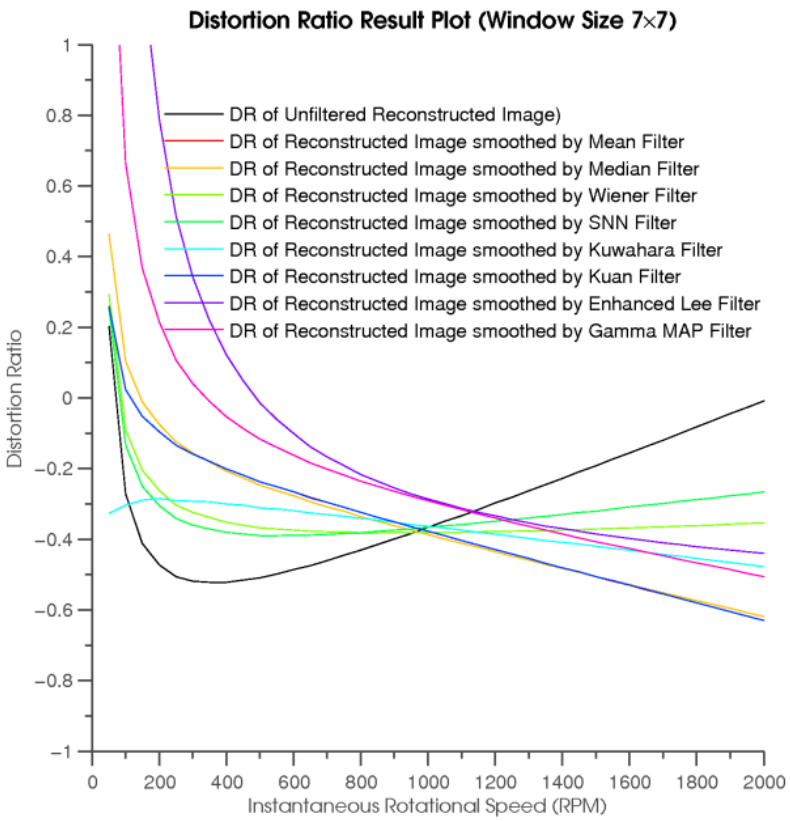

F. DR of filters with window size 7×7

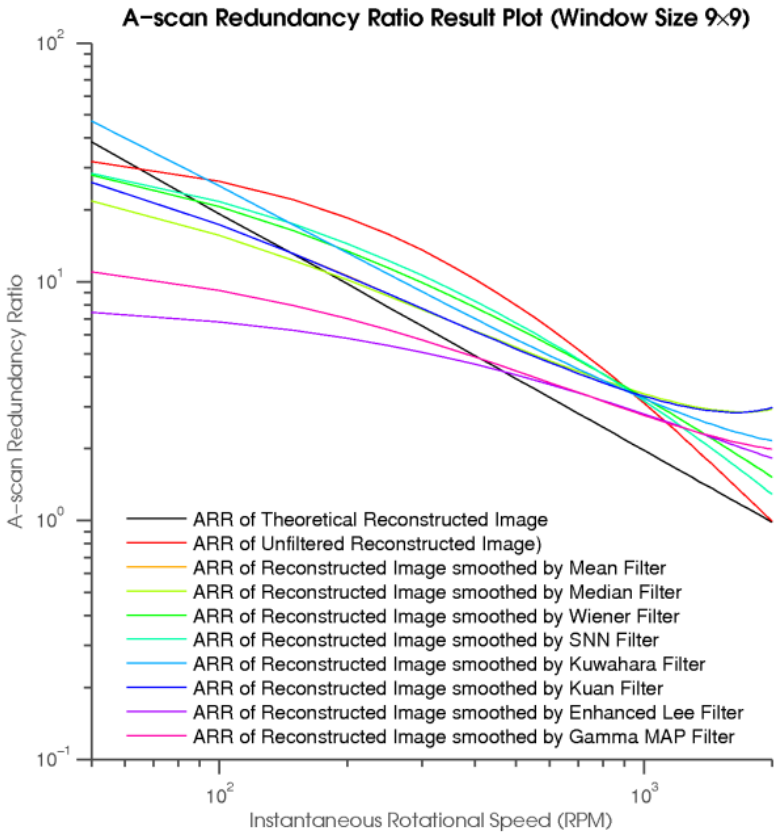

G. ARR of filters with window size 9×9

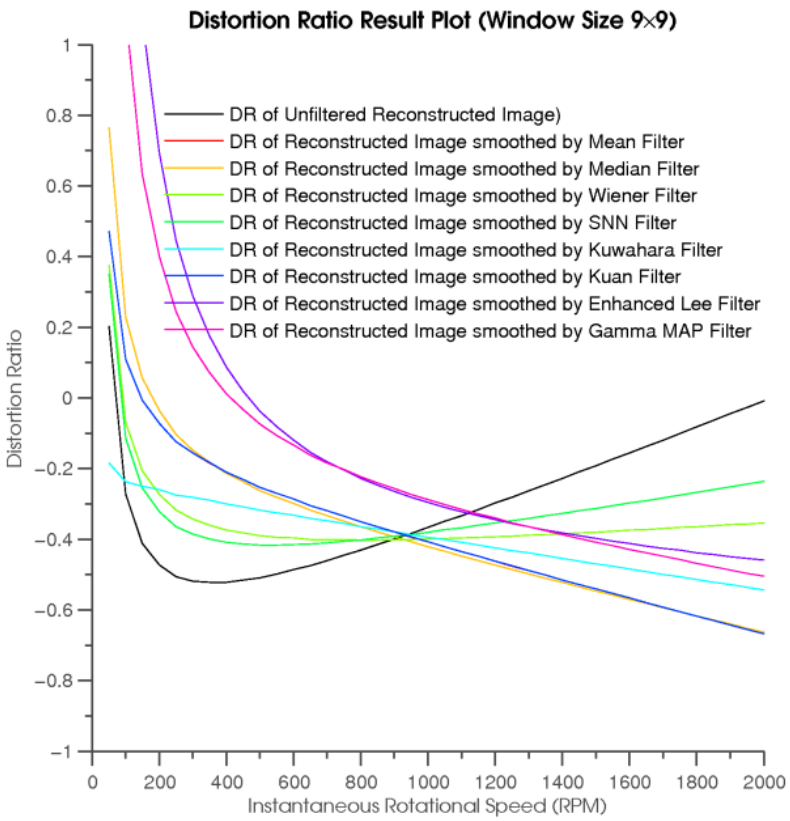

H. DR of filters with window size 9×9

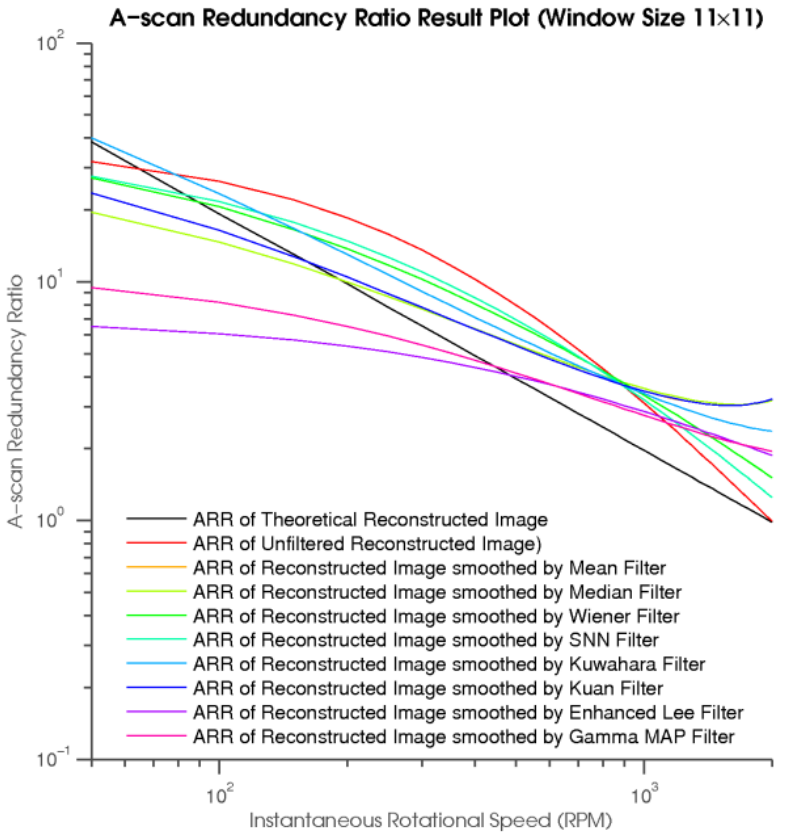

I. ARR of filters with window size 11×11

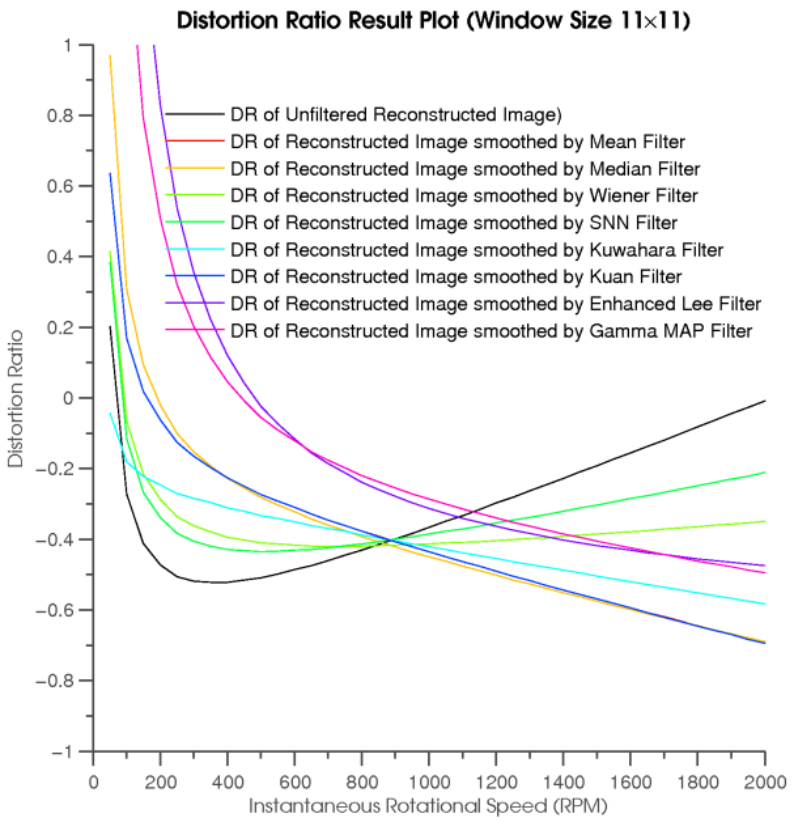

J. DR of filters with window size 11×11

Figure 38. Image reconstruction accuracy comparison. The average thresholds of RPM variation range from 50 to 2000 are selected for image reconstruction. In ARR graphs, the X-axis and Y-axis are displayed in logarithmic scale.

The reconstruction results for different digital despeckle filters are high consistent with despeckled image quality. This is because our reconstruction algorithm measures the differentiation of successive A-scans essentially. Although the digital filters can remove the influence of speckle noise to some extent, image features have also been blurred. Therefore, in our specific OCT system design, it requires a sophisticated despeckle filter that can not only suppress speckle noise but also preserve image features. By calling back to the result we have had in previous subsection 5.3. The adaptive Wiener filter is more suitable and is recommended to be applied before image reconstruction. In the discussion below, it will focus on the method how to find proper downsampling threshold for reconstruction accuracy improvement. This method is not only restricted to a certain filter, but should be considered as a global rule for any other filters when our reconstruction approach is applied.

Please notice, our algorithm failed to resample the images previously filtered by enhanced Lee filter or Gamma MAP filter, especially when the sampling ratio of the images are relatively high. The DR values of that downsampled images are remarkable larger than other images. By reviewed the despeckled images by both these two filters (Appendix A), we found these two filters had created some undesired bright pixel clusters in some areas. This strange result arises because the enhanced Lee filter and Gamma MAP filter are designed to suppress speckle noise based on homogeneity features. At the relative low RPM region, due to the high sampling ratio of the image, the speckle noises are replicated and appear as a high homogeneous area. These two filters have no ability to properly distinguish such noise, which leads to artificial pixel clusters. This also explains why these two filters got low scores in

the despeckling comparison. To improve the reconstruction accuracy of images filtered by these two filters, some speckle reduction techniques in hardware aspect (such as polarization diversity and frequency compounding) before digital signal processing.

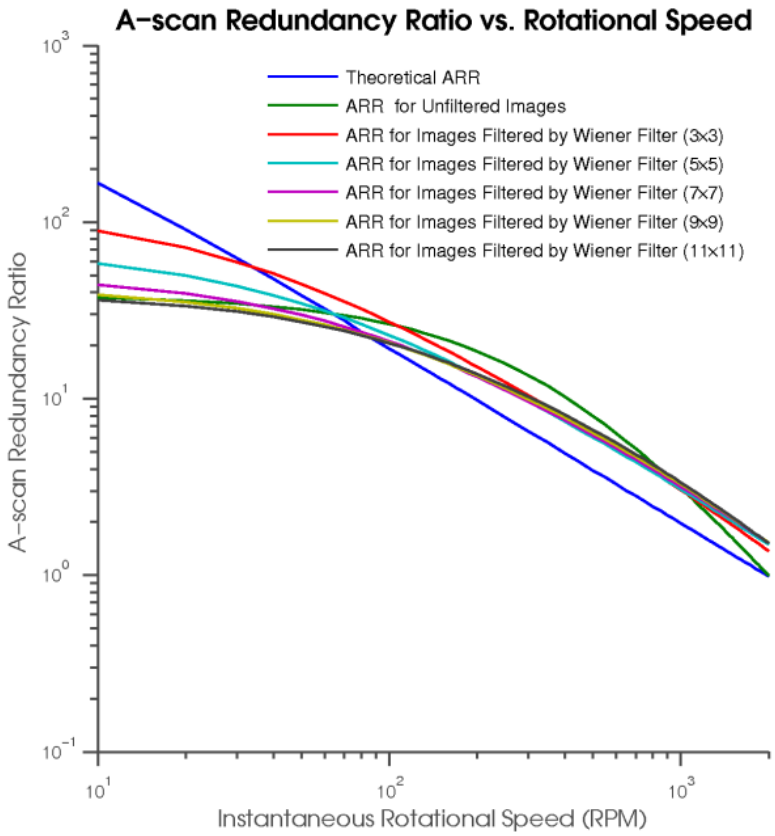

A. ARR vs. rotational speed

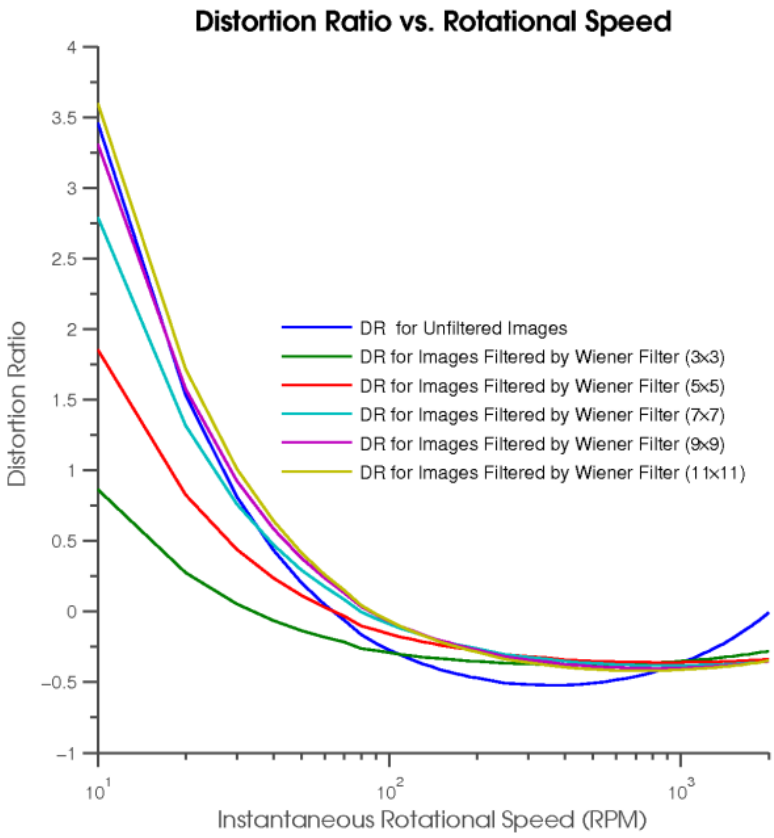

B. DR vs. rotational speed

Figure 39. Image reconstruction accuracy for images filtered by adaptive Wiener filters with averaged threshold.

Figure 39 shows the assembly accuracy of images filtered by adaptive Wiener filters. The ARR curves in Figure 39.A shows that the ARR values are larger than the theoretical in most conditions. This indicates that the selected downsampling threshold is too small. This reconstruction error is caused mainly because we define the downsampling threshold using Equation (4.31). As discussed in the beginning of this subsection, the digital filter's sliding window size can change the cross correlation coefficient between the successive A-scans. When the sliding window size is large than the number of A-scans OCT obtained from a conventional lateral resolution volume, the despeckling operation will increase the structural similarity of the uncorrelated A-scans. As a consequence, the calculated downsampling thresholds (obtained by Equation (4.30)) of low sampling ratio images are slightly larger than the thresholds obtained from high sampling ratio images. However, in our approach, images are assembled using the average value of downsampling thresholds of different rotational speeds. Therefore, the downsampling threshold should be actively modified to make the algorithm more robust to variation in rotational speed.

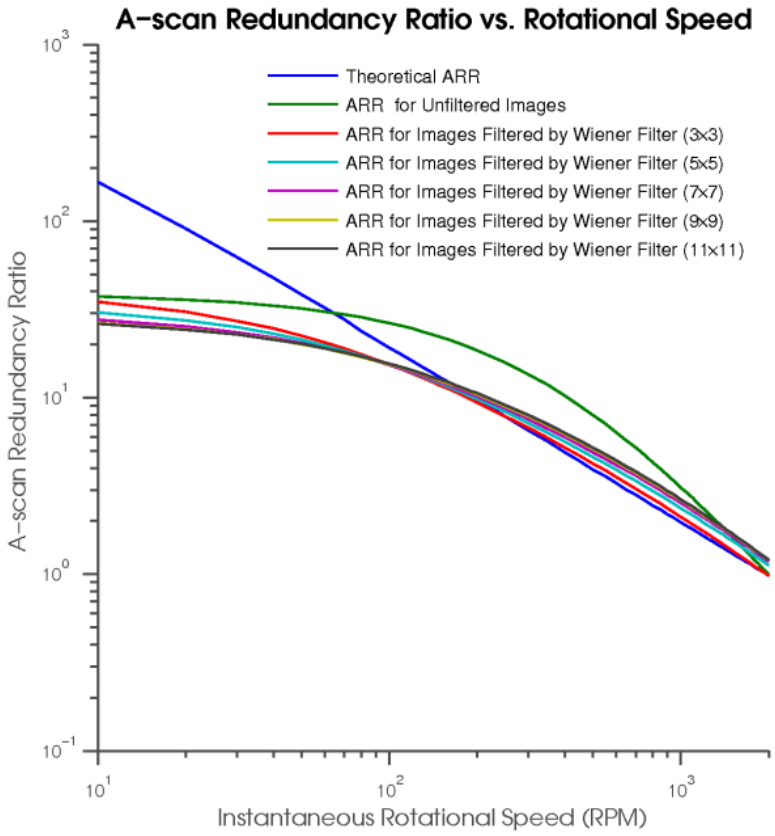

A. ARR vs. rotational speed

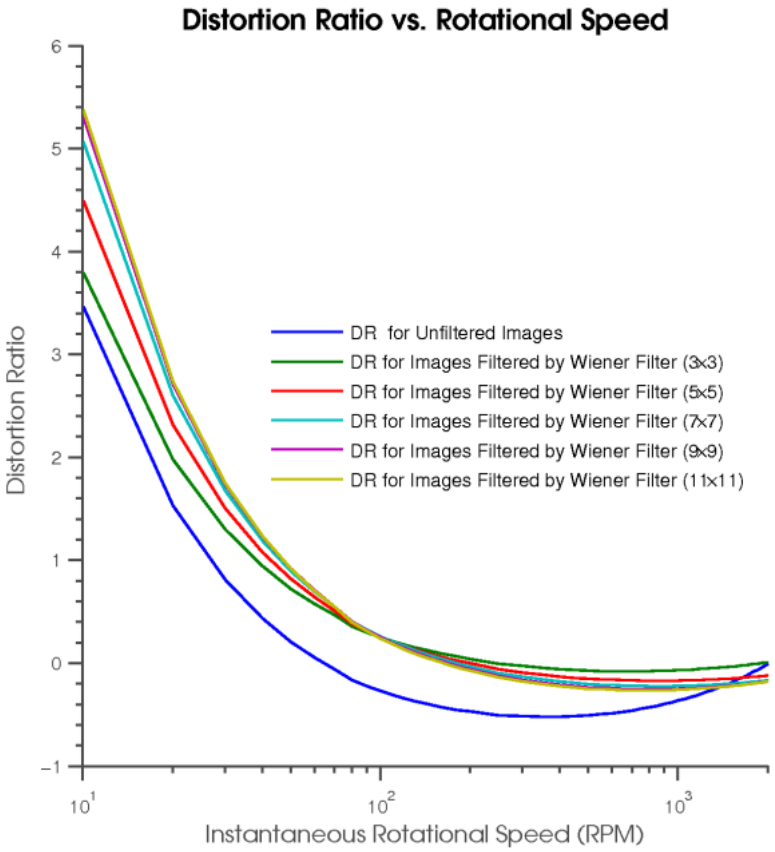

B. DR vs. rotational speed

Figure 40. Image reconstruction accuracy for images filtered by adaptive Wiener filters with modified downsampling threshold. The small errors for larger Wiener filters are kept with the intention of preventing overlapping

Figure 40 shows the reconstruction results after properly increasing the downsampling threshold value. Comparing with the plots in Figure 39, the ARR and DR curves are more close to the theoretical ARR line and zero, respectively, when the rotational speed is larger than 100 RPM. Please notice, in Figure 40, the reconstruction results of assembled images filtered by larger Wiener filters seems not as good as that despeckled by smaller Wiener filters. This doesn't mean that images filtered by larger digital filters cannot be reconstructed accurately by our algorithm. These mismatches can be eliminated by increasing corresponding downsampling thresholds.

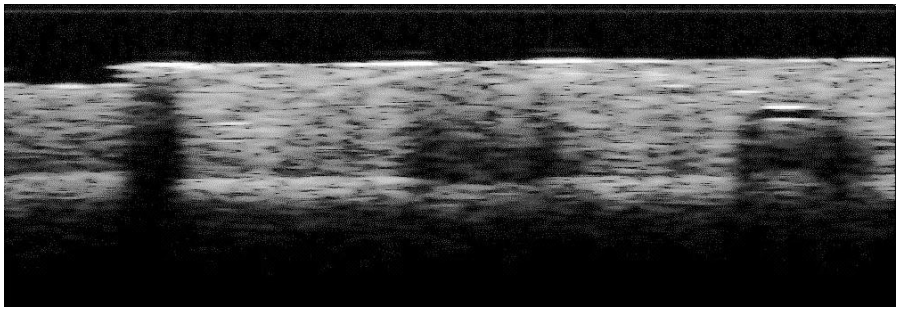

A. OCT image filtered by 5×5 adaptive Wiener filter

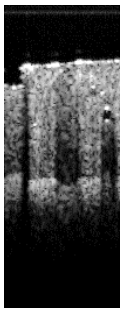

B. Reconstructed OCT Image with averaged threshold

C. Reconstructed OCT Image with modified threshold

Figure 41. Image reconstruction for a silicone-based tissue phantom with titanium dioxide (TiO_2) scattering particles. Image A is the original oversampled OCT image, which is extracted from optical phantom at rotational speed 350 RPM. B shows the assembled image using the averaged overall threshold; C, assembled image using modified downsampling threshold.

Figure 41 shows one reconstruction example. Figure 41.A displays the overlapped OCT image obtained at 350 RPM. Its oversampled ratio (ζ) equals to 11.2. The air bubble on the right side of the image is expanded in transverse direction. Figure 41.B shows the assembled image using dowsampling threshold of 0.969. The algorithm selected 131 A-scans from the oversampled image (Figure 41.A). The ARR and DR of the assembled image are 7.7 and -0.264, respectively. The assembled image in Figure 41.C was downsampled using modified threshold (0.979). It consists of 181 A-scans. The ARR and DR of the downsampled image are 5.53 and 0.0169, respectively. The corresponding sampling ratio (ζ) is approximately equal to 2.04. We can consider the oversampled image was perfectly reconstructed.

Besides, in experiments, we also noticed that the infrared dispersion would do great damage to the reconstruction result. OCT uses broadband light source. The different frequency waves have different refractive coefficients in any material and leads to a group delay. The measured intensity of the reflected light altered, especially the incidence angle of the light is sufficient large. The dispersion creates bright and homogeneous areas in obtained images (Figure 42.A), in which A-scans have a higher cross correlation coefficient than usual. As a consequence, the assembled image has a narrow width and objects in it behave as if they were compressed. Therefore, some algorithms should be designed to compensate for the dispersion effect.

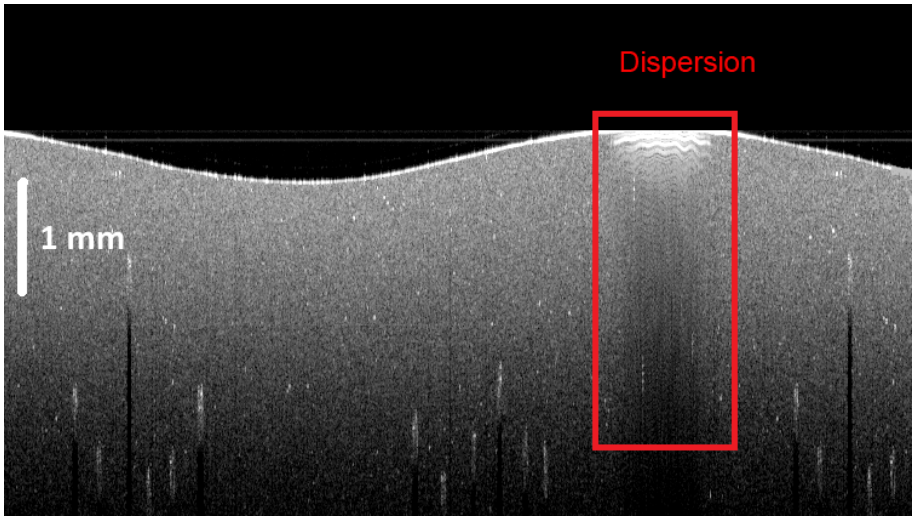

A. An OCT image contains an obvious dispersion region

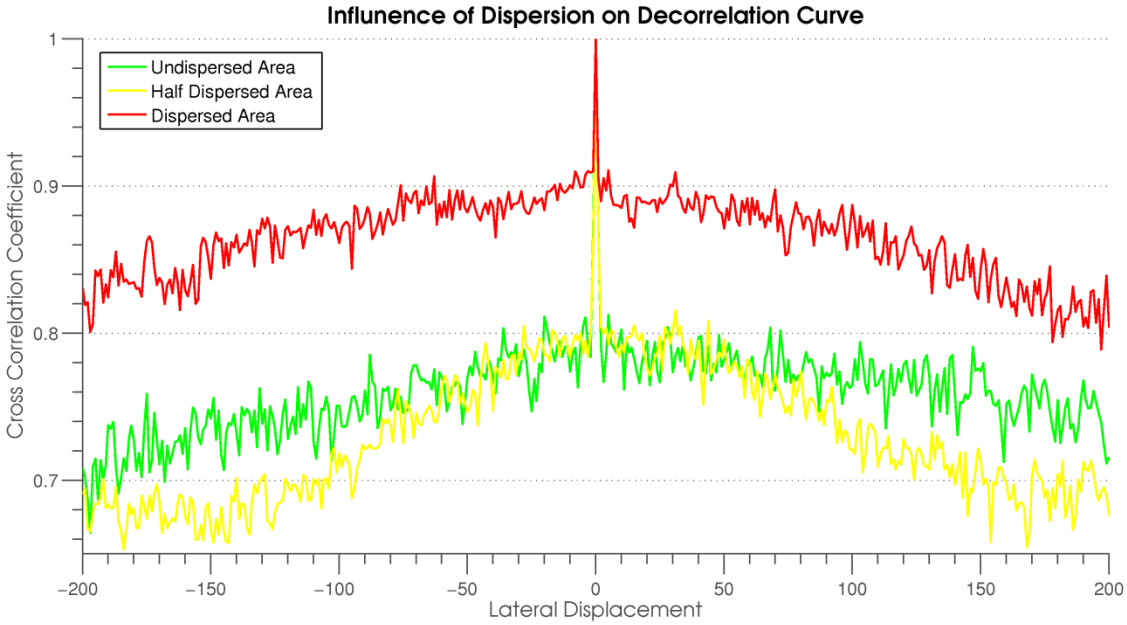

B. Decorrelation curves for undispersed and dispersed area.

Figure 42. Influence of dispersion on OCT decorrelation curve. In A, the light dispersion induced artifacts are highlighted by red box. To quantitatively analysis the effect of the light dispersion on decorrelation curves, several A-scans are selected in image A in the regions undispersed area, half dispersed area (the selected A-scan or its neighbors are within the dispersed area) and dispersed area. Their corresponding decorrelation curves are plotted in B. The data was taken from a silicone based phantom with titanium dioxide (TiO_2) power.

5.5 Short Discussion

In this chapter, some silicone-based optical phantoms were created for OCT image acquisition. OCT images with various sampling ratios were filtered by different digital filters for speckle noise suppression and image reconstruction. After taking many factors into consideration, we consider the 3×3 adaptive Wiener filter is particular suitable for our specific OCT application. Our experimental results of image reconstruction indicate that our modified cross-correlation based image reconstruction algorithm is capable of handling oversampled images with varying sampling ratio. The results also show that there is a strong connection between despeckle result and our image reconstruction algorithm. For a good assembly result, the speckle suppression technique should not only suppress the influence of speckle on OCT image, but also preserve the image features.

However, our reconstruction resamples OCT images are sensitive to the type of probing sample since there exists some inter-sample and intra-sample variations in the correlation coefficients at displacement. In the following chapter, experiments will be conducted to real animal jawbone. Results of such research will be presented and discussed to draw the final conclusions.

CHAPTER 6

RESULTS OF ANIMAL SAMPLES TESTING

6.1 Introduction

Jawbone is a complex organ that consists of lots of different types of cells that make the jaw not as homogeneous as the silicone phantoms we used. To verify the results that are proposed in Chapter 5, measurements will be tested on the real animal jawbone. The obtained results will be analyzed and presented. The feasibility of using the silicone phantoms instead of animal tissues in our future researches will be discussed.

6.2 OCT Images and Analysis

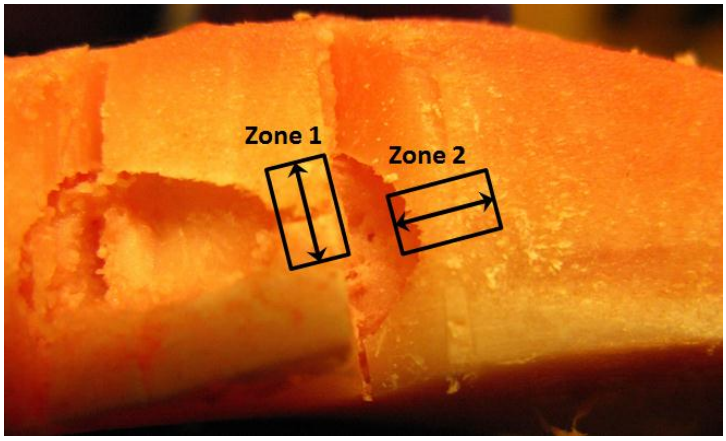

A. Incisions in the bottom of the mandibular bone

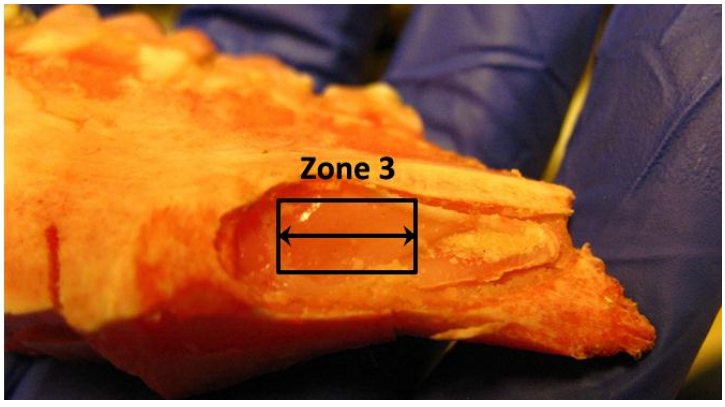

B. Cross sectional view of neurovascular bundle

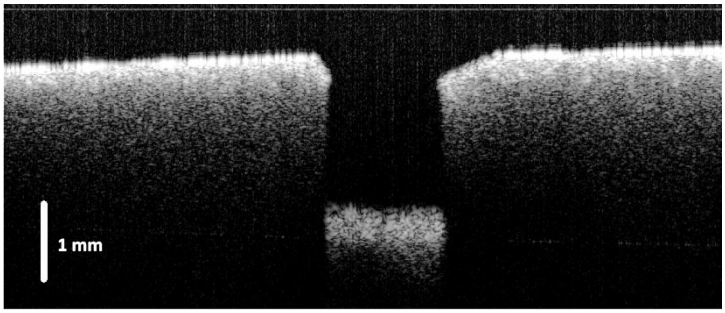

C. OCT image of zone 1

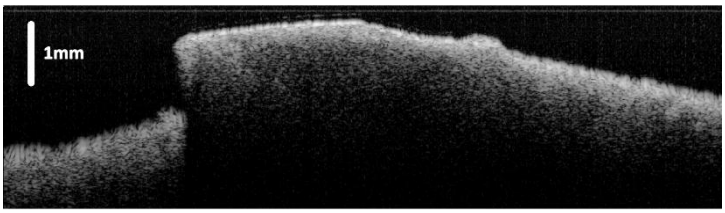

D. OCT image of zone 2

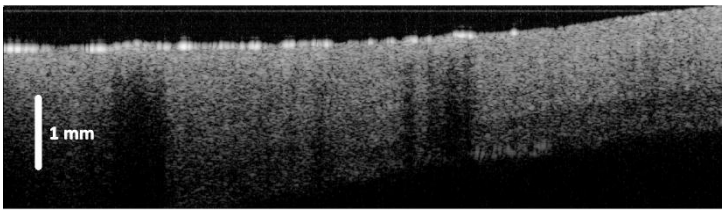

E. OCT image of zone 3

Figure 43. OCT images of interested areas in the mandibular bone. The boxes outlines the regions we interested and imaged. The arrows inside the boxes depict the direction of the lateral scanning of OCT measurement.

Figure 43 shows the OCT images obtained from the interested zones of the pig's jawbone. Figure 43.A and B are zoom-ined views of the mandibular bone. The OCT image of the interested region zone 1 labeled in Figure 43.A is presented in Figure 43.C. This figure contains two different tissues. The two higher parts at both side of the image are cortical bones. The middle low part is the neurovascular bundle. In this image, the neurovascular bundle looks very similar to the cortical bone in visual. However, it appears that bone surface has a large reflection coefficient.

In Figure 43.B, the wedge-shape incision has been made in cortical bone and its bottom was very close to the neurovascular bundle. Theoretically speaking, the obtained OCT image from such region should show cortical bone, trabecular bone and neurovascular bundle. But unfortunately, the results shown in Figure 43.D are not good. We cannot observe any trabecular bone in the right part of Figure 43.D (left low part is neurovascular bundle). This is because, in micro, both these two types of bones are composed of the same structural elements. They have almost same optical properties.

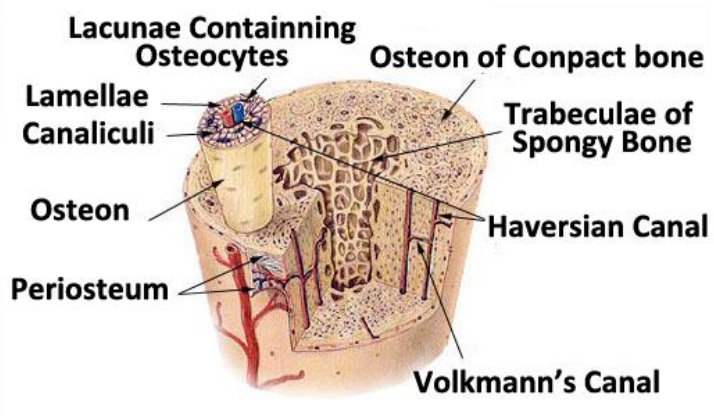

Figure 44. Microstructure of compact and spongy bone. The osteon is the basic structural unit of compact bone and it consists of lamellae, which surround the Haversian canal. The trabecula is the chief structural element in the trabecular bone. Trabeculae are most often characterized as rod or plate like structures (Image adaptive from [75])

The major difference between cortical bone and spongy bone is found on 1st and 2nd bone structural level [76]. In 1st bone structural level, the cortical bone is characterized by osteons (shown in Figure 44); whereas in spongy bone, it consists of trabeculae (shown in Figure 44). But both these two basic tissue elements have a size about few hundred microns. Bone tissues have very high scattering coefficients. The imaging depth of bone tissues for our system is very short (about 0.5 mm). This short penetration depth cannot provide us with enough information to classify different bones. And OCT is incapable of distinguish the different basic structures in the 2nd bone structural level, since the size range of these structures locates in the range from 1 μm to 20 μm. This size approximately equals to or beyond the resolutions (axial resolution: 10 μm and effective lateral resolution: 5 μm) of our OCT system.

Level	Cortical Bone		Spongy Bone	
	Structure	Size Range	Structure	Size Range
0	Solid Material	> 3000 μm	Solid Material	> 3000 μm
1	Secondary osteons Primary osteons Plexiform Interstitial bone	100 to 300 μm	Secondary trabeculae Primary trabeculae Trabecular Packets	75 to 200 μm
2	Lamellae Lacunae Cement lines	3 to 20 μm	Lamellae Cement lines Canaliculi	1 to 20 μm
3	Collagen-mineral Composite	0.06 to 0.6 μm	Collagen-mineral composite	0.06 to 0.4 μm

Table 7. Microstructure of cortical bone and spongy bone. (Data from [76])

The porous structure of the trabecular bone offers a good approach for bone classification in OCT. In Figure 45 A and B, two types of bones are separated probed by OCT. They show that the OCT has enough ability to detection the small pores inside the spongy bone. However, in Figure 43.D the porous structure was not visualized. This is probably because the pores of the spongy bone close to the surface have been smoothed or filled down in the process of incision preparation. And the short imaging depth

of OCT system also limits the possibility of detecting pores in the deeper part.

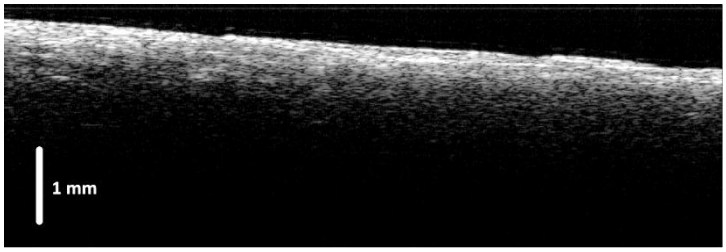

A. OCT image of cortical bone

B. OCT image of trabecular bone

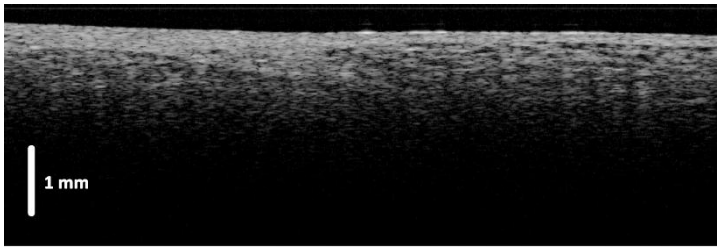

C. OCT image of neurovascular bundle

Figure 45. OCT images of different types of bones and neurovascular bundle.

Figure 43.E is the OCT image of the transverse plane of the neurovascular bundle. It shows that the image depth of nerves or blood vessels is relative longer than that in bone tissues (Figure 43 A&B). This means that the nerves or blood vessels have relative low optical properties than that of bone tissues. This result appears to contradict earlier conclusion we obtained from Figure 43.C. This disagreement is probably caused by the high light scattered soft membrane wrapped around the nerves or blood vessels, since the top layer (soft membrane) in Figure 45.C has larger pixel intensity than that of the second layer (nerves and blood vessels).

Given the current data we obtained from pig jawbone, it seems to be very difficult to distinguish different bone tissues from soft tissues using OCT since they have nearly similar features in OCT images in visual. Although we found that the scattering coefficient of the nerve fiber is smaller than the bone tissues, the intensity decay and speckle noise in OCT images make the tissues segmentation very complex. The most feasible approach to solve the question is to detect the pore structure of the spongy bone. This unique structure of the trabecular bone can be used to differentiate different bones rather.

Results shown in Figure 43 & Figure 45 also prove the conclusion we discussed in section 2.5. Due to the high scattering coefficients of the bone tissues and neurovascular bundle, the OCT imaging depth of our obtained images are limited in less than 1 mm. The available OCT system is unable to provide sufficient imaging depth for OCT image guided safety dental implant. Therefore, it is recommended to use a powerful laser source in future research and OCT integrated dental drill system design

6.3 Results of Image Reconstruction and Discussion

In previous chapter, we have verified our reconstruction approach by comparison with the ARR and DR parameters of different digital filters and found that the images filtered by adaptive filter, SNN filter and Kuwahara filter can give the best image assembly results. Therefore, our discussion will focus on these three filters and result for these most promising filters will be given.

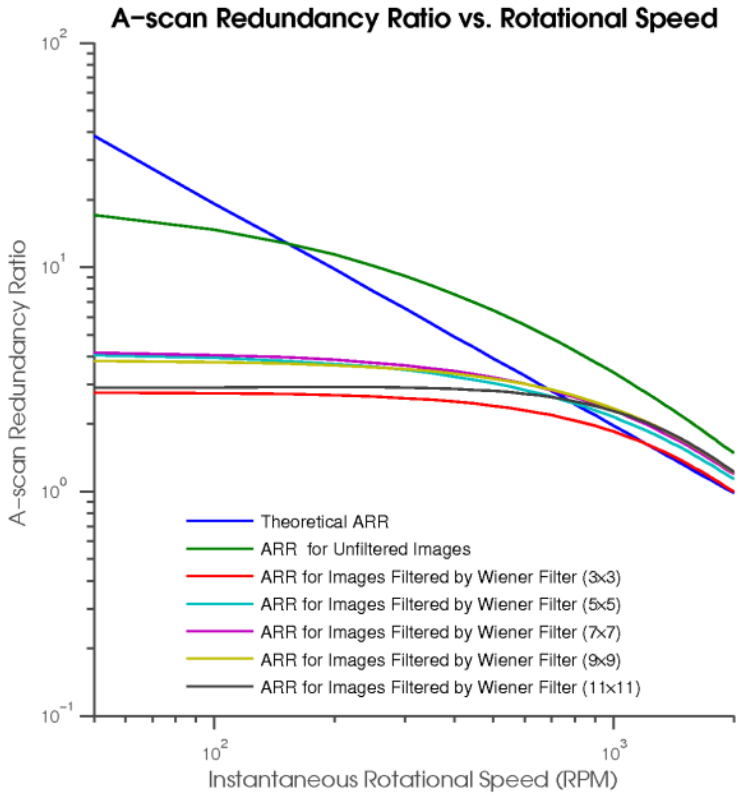

A. ARR of adaptive Wiener filters

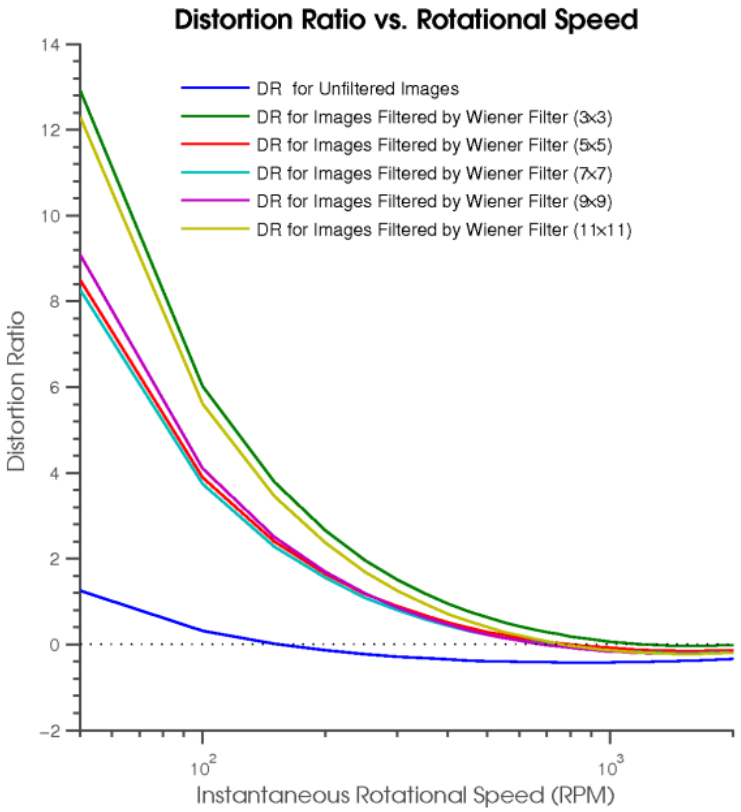

B. DR of adaptive Wiener filters

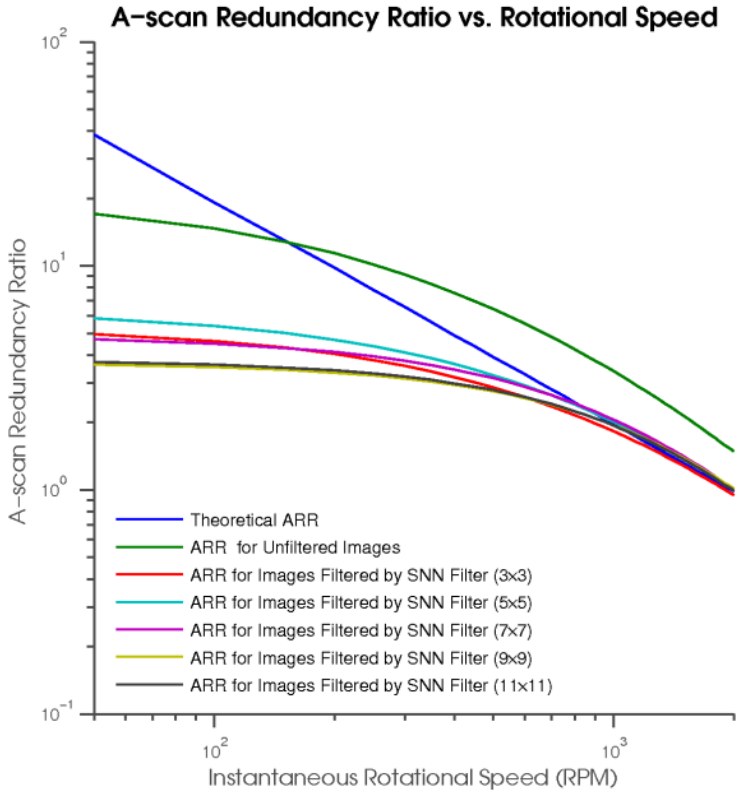

C. ARR of SNN filters

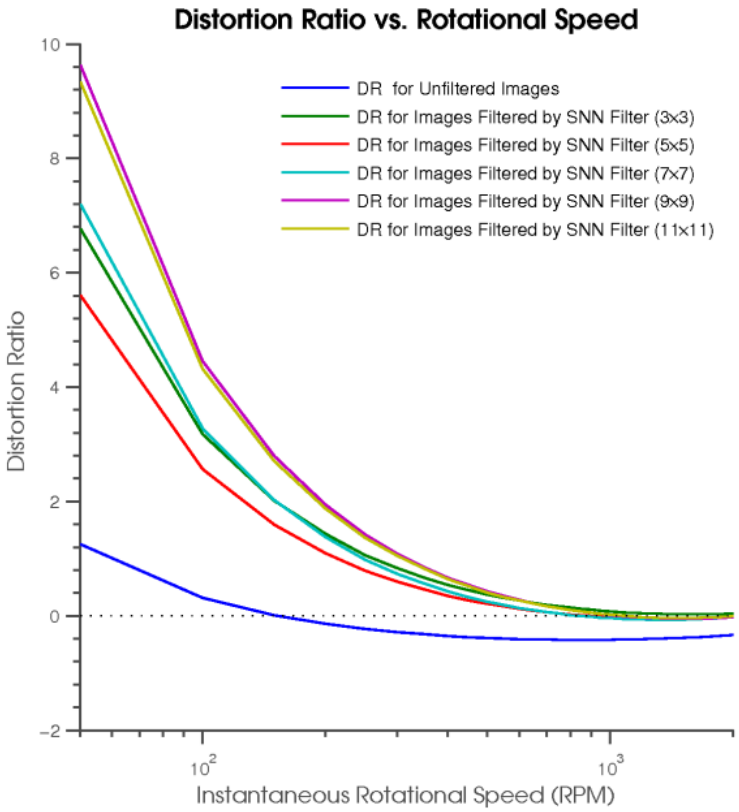

D. DR of SNN filters

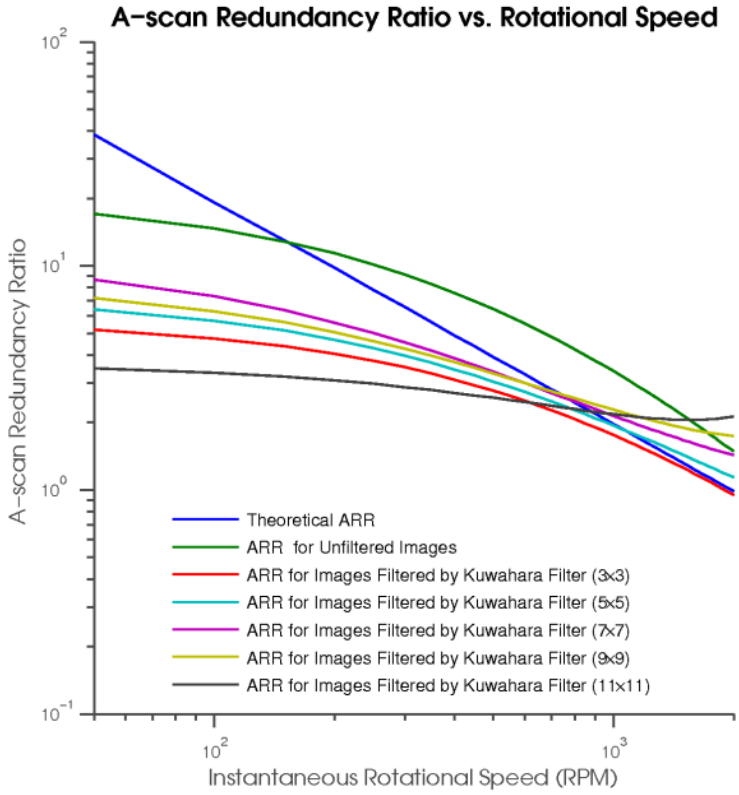

E. ARR of Kuwahara filters

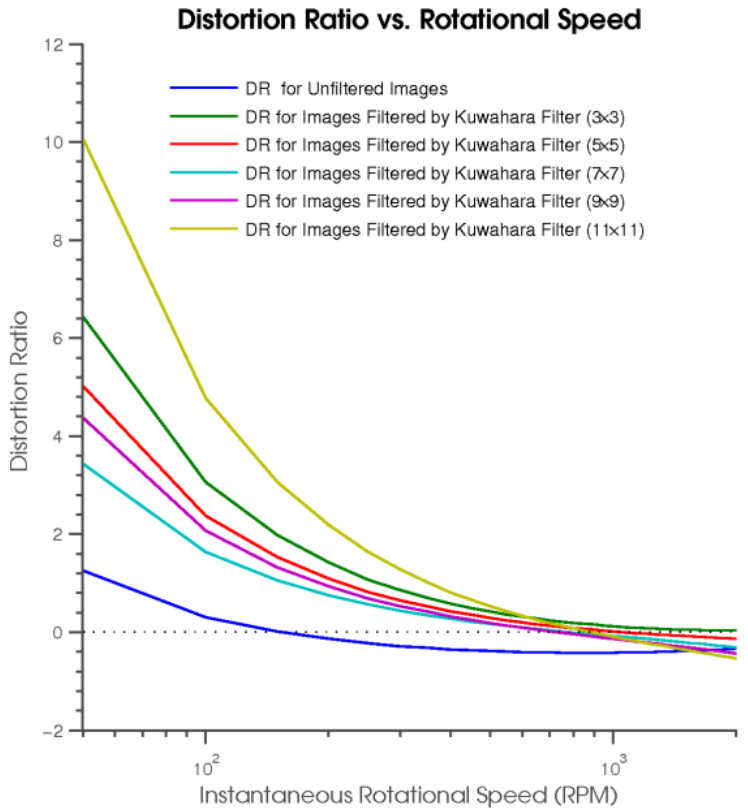

F. DR of Kuwahara filters

Figure 46. Image assembly accuracy results from pig bone tissues.

Figure 46 shows the reconstruction parameters, using different filters (downsampling threshold have been optimized for good reconstruction result). The plots in Figure 46 clearly indicate that our reconstruction algorithm perform relatively well in the OCT bone tissue image reconstruction. Especially for the images filtered by SNN filter, the ARR and DR curves are very close to theoretical ARR line and the zero reference line (no image distortion).

In Figure 46, we also noticed that, in the real animal tissues, the ARR (or DR) curves have naarower accurate reconstruction range than that we obtained from optical phantoms (Figure 38). This is probably because the scatterers in these two samples have quite different size. In our silicone-based optical phantoms, the scattering coefficients are controlled by the concentration of mixed titanium dioxide (TiO_2) particles. The mean radius of TiO_2 Power is about 50 nm with an unknown size distribution [9]. However, in the bone tissues, the collagen fibers are the primary scatterers. The average length of collagen fibers reaches the same order of magnitude as OCT's axial and lateral resolution. These large scatterers change the speckle noise pattern [19] and increase the cross correlation between successive A-scans.

We may summarize that for the high scattering tissues, the agreement RPM range becomes narrow. To accurately reconstruct OCT images of high scattering samples, it is necessary to limit the drill bit speed to a certain range based on the ARR or DR curve of the particular sample. For example, if we have a DR curve have similar trend as DR curve shown in Figure 46.B. For an accurate image reconstruction, the drill speed should be kept at least 800 RPM. However, this probably requires additional sensors or components and will increase the complexity and cost of the system.

6.4 Short Discussion

In this chapter, the experiments were conducted on pig's jawbone. The collected images were processed by speckle reduction and reconstruction algorithms mentioned in previous chapters. The results from real animal jawbone agreed with the results we presented in chapter 6. The conclusion about speckle noise reduction and the ability of our cross correlation based image reconstruction algorithm were verified. This also shows that the silicone elastomer-based optical phantoms are practically suit for our future researches. It can be considered as a substitute for jawbone in OCT experiments.

CHAPTER 7

CONCLUSIONS AND FUTURE WORKS

In this chapter the master project is concluded briefly and some suggestions for future researches and system design are provided

7.1 Conclusions

This master thesis carries out three studies revolving around the image processing for OCT images. This study begins with a background knowledge introduction. The procedures of dental implants and the complications caused by dental drilling are introduced. In the following parts, the principles behind OCT and human jawbone structure have been discussed. Then the speckle noise reduction filters, the image assessment algorithm and the cross-correlation based oversampled image reconstruction method are studied before our results analysis to provide background knowledge. In the following chapters, the OCT images from silicone elastomer-based tissue phantoms and pig jawbone are presented, analyzed and discussed.

The speckle noise is an inherent noise that contaminates all OCT image. In this master project, we tried to handle it by applying digital filters. Our results (in Appendix B) suggest that there is a tradeoff between speckle noise reduction and image feature persevering. The more speckle noise suppressed, the more image features will be lost. To compare the performance of different filters in speckle reduction and structure preservation, a weighted figure of metric (Equation (4.26)) was defined. The comparison results indicate that adaptive Wiener filter, the symmetric nearest neighbor (SNN) filter and Kuwahara filter can sufficiently suppress the speckle noise and increase the image quality while still preserving the image features.

The OCT images we will acquire are distorted because of the variation in dental drilling speed. To compensate the distortion, the modified cross correlation based method was posed. The experiments on tissue phantoms and pig jawbone demonstrate that our approach can assemble oversampled images with acceptable reconstruction accuracy. And our algorithm is simple enough that can enable image reconstruction to be done in real-time. But the problem with our approach is the image assembly result depends on the selected downsampling threshold. This value changes with the type of the probing samples, especially for the samples have high scattering properties. To precisely reconstruct oversampled images, the threshold needs to be adjusted dynamically. Some tissue classification algorithms could be used to improve the performance of our algorithm. Our results show that the images filtered by adaptive Wiener filter, the symmetric nearest neighbor (SNN) filter and Kuwahara filter can be reconstructed accurately. This finding indicates that there is a strong connection between the speckle noise suppression method and our image reconstruction algorithm. The reconstruction accuracy of our method relies on the structure features in OCT images.

To sum up, the adaptive Wiener filter is recommended since it gives a comprehensive result in our research. The images filtered by adaptive Wiener filter not only give a good result in speckle reduction

and OCT feature preservation, but also show a good accuracy in image reconstruction. And the structure of adaptive Wiener filter is simple and can be performed in real-time.

7.2 Recommendations

Although the OCT imaging system has been used in dentistry to image both teeth and gums at very high resolution, there are very few the publications about researches or experiments made for measuring the optical properties of human jawbone and its affiliated tissues. OCT imaging system is a very complicated system, it measure cross sectional structures of sample heavily rely on the optical properties of the probing samples. Human jaw consists of lots of different tissues. The optical properties of such tissues vary greatly depending on age, sex, race, pathological changes and many other factors. In order to image reconstruction and segmentation accuracies for our designing OCT integrated dental drill system, many experiments should be made for understanding the optical properties of different dental tissues in details before performing digital image processing.

In previous chapters, we also discussed the shortages of the current OCT systems that maybe they are unable to provide sufficient imaging depth for dental drilling safety. In our work, the imaging depth in real pig jawbone is less than 1 mm since the OCT system we used has only 10 mW output light power in sample arm. The maximal permissible light exposure is determined by safety standards. For most commercial OCT systems, this maximal power is limited to a relative low value to ensure ophthalmic and dermatologic exam safety (ANSI Z1361) [20]. Although there is no systematic or accepted standards that govern the safe exposure of dental tissues, in teeth whitening the laser source usually have an output power of few hundred micro Watt. Therefore, it is recommended in our future work to properly increase the OCT laser source output power. This increase can do no harm or very few damages to the health tissues in the vicinity of the drill bit. It is also recommended to use some laser splitters with different split ratios (such as 70/30) instead of the typical 50/50 splitter. They will help in increasing the imaging depth without changing or buying an expensive high output power laser source. Besides, the light source with longer wavelength (for instance 1600 nm) can also be tested. But the wavelength should not excess 1800 nm, since water absorption will increase notably [77].

About the tissues recognition, the final results are not as good as we expected. Different bone tissues are identical and show nearly same features in out obtained OCT images. Currently, the segmentation method is only based on structure difference, the porous structure in particular. It is recommended in the future researches to segment OCT images using machine-learning techniques (such as artificial neural networks, support vector machines or Hidden Markov model).

At last, it is recommended for future research to use real human jawbone for testing because that will help in obtaining more accurate results.

References

[1] R. Nagel, *Cure tooth decay: remineralize cavities and repair your teeth naturally with good food*: Golden Child Publishing 2010.

[2] Copyright © 2011 NIDCR. *Tooth Loss in Adults and Seniors*. Available: http://www.nidcr.nih.gov/DataStatistics/FindDataByTopic/ToothLoss/ToothLossAdults20to64 http://www.nidcr.nih.gov/DataStatistics/FindDataByTopic/ToothLoss/ToothLossSeniors65andOlder.

[3] Copyright © 2011 P. Dutta. *Dental implants at the university dental and implant centre*. Available: http://www.universitydental.co.uk/articles/treatments/Implants.html.

[4] A. Jokstad, "Common complications with implants and implant prostheses," *Evidence-Based Dentistry,* vol. 5 (3), pp. 70-71, 2004.

[5] J. G. Charles, B. Guillermo, R. Kitichai, and Y. K. K. Joseph, "Clinical complications with implants and implant prostheses," *The Journal of Prosthetic Dentistry,* vol. 90 (2), pp. 121-132, 2003.

[6] L. G. Ellies, "The incidence of altered sensation of the mental nerve after mandibular implant placement," *Journal of Oral and Maxillofacial Surgery,* vol. 57 (12), pp. 1410-1412, 1999.

[7] Copyright © 2011 M. Shohat. *Dental implants*. Available: http://www.scoop.it/t/dental-implants.

[8] E. Margallo Balbas, P. A. Wieringa, P. J. French, R. A. Lee, and P. Breedveld, "Surgical drill system and surgical drill bit to be used therein," the Netherlands, 2007.

[9] D. M. de Bruin, R. H. Bremmer, V. M. Kodach, R. de Kinkelder, J. van Marle, T. G. van Leeuwen, and D. J. Faber, "Optical phantoms of varying geometry based on thin building blocks with controlled optical properties," *Journal of Biomedical Optics,* vol. 15 (2), pp. 025001-025010, 2010.

[10] Copyright © 2011 F. Gaillard. *Photo of the mandible demonstrating the frequency of mandibular fractures by location*. Available: http://en.wikipedia.org/wiki/File:Mandbular_fractures.png#filelinks.

[11] G. Greenstein and D. Tarnow, "The mental foramen and nerve: Clinical and anatomical factors related to dental implant placement: A literature review," *Journal of Periodontology,* vol. 77 (12), pp. 1933-1943, 2006.

[12] D. V. Kuzmanovic, A. G. T. Payne, J. A. Kieser, and G. J. Dias, "Anterior loop of the mental nerve: a morphological and radiographic study," *Clinical Oral Implants Research,* vol. 14 (4), pp. 464-471, 2003.

[13] G. Juodzbalys, H.-L. Wang, and G. Sabalys, "Anatomy of mandibular vital structures. Part I: Mandibular canal and inferior alveolar neurovascular bundle in relation with dental implantology," *Journal of Oral & Maxillofacial Research,* vol. 1 (1), p. e2, 2010.

[14] G. Juodzbalys, H.-L. Wang, and G. Sabalys, "Anatomy of mandibular vital structures. Part II: Mandibular incisive canal, mental foramen and associated neurovascular bundles in relation with dental implantology," *Journal of Oral & Maxillofacial Research,* vol. 1 (1), p. e3, 2010.

[15] B. Sahin, H. S. Ozkan, and M. Gorgu, "An anatomical variation of mental nerve and foramen in a trauma patient," *International Journal of Anatomical Variations,* vol. 3 pp. 165-166, 2010.

[16] Copyright © 2011 DRosenbach. *Mandibular incisive canal highlighted*. Available: http://en.wikipedia.org/wiki/File:Mandibular_Incisive_Canal_Highlighted.jpg.

[17] B. Colston, U. Sathyam, L. DaSilva, M. Everett, P. Stroeve, and L. Otis, "Dental OCT," *Optics Express,* vol. 3 (6), pp. 230-238, 1998.

[18] A. N. Bashkatov, E. A. Genina, V. I. Kochubey, and V. V. Tuchin, "Optical properties of human cranial bone in the spectral range from 800 to 2000 nm," In: proceeding, pp. 616310-616311, 2006.

[19] J. M. Schmitt, S. H. Xiang, and K. M. Yung, "Speckle in optical coherence tomography," *Journal of Biomedical Optics,* vol. 4 (1), pp. 95-105, 1999.

[20] B. E. Bouma and G. J. Tearney, *Handbook of optical coherence tomography*, 1st ed. NewYork: Informa Healthcare, 2002.

[21] Copyright © 2011 D. Sampson. *Introduction to optical coherence tomography (OCT)* Available: http://obel.ee.uwa.edu.au/research/oct/intro/.

[22] D. Huang, E. A. Swanson, C. P. Lin, J. S. Schuman, W. G. Stinson, W. Chang, M. R. Hee, T. Flotte, K. Gregory, C. A. Puliafito, and J. G. Fujimoto, "Optical coherence tomography," *Science,* vol. 254 (5035), pp. 1178-1181, Nov 22 1991.

[23] P. H. Tomlins and R. K. Wang, "Theory, developments and applications of optical coherence tomography," *Journal of Physics D: Applied Physics,* vol. 38 (15), p. 2519, 2005.

[24] Copyright © 2011 G. Popescu. *Low-coherence interferometry*. Available: light.ece.illinois.edu/ECE460/PDF/LCI.pdf.

[25] A. F. Fercher, C. K. Hitzenberger, G. Kamp, and S. Y. El-Zaiat, "Measurement of intraocular distances by backscattering spectral interferometry," *Optics Communications,* vol. 117 (1-2), pp. 43-48, 1995.

[26] M. Choma, M. Sarunic, C. Yang, and J. Izatt, "Sensitivity advantage of swept source and Fourier domain optical coherence tomography," *Opt. Express,* vol. 11 (18), pp. 2183-2189, 2003.

[27] Copyright © 2011 M. V. Sarunic. *Fourier domain OCT*. Available: http://borg.ensc.sfu.ca/FDOCT.htm.

[28] A. F. Fercher, W. Drexler, C. K. Hitzenberger, and T. Lasser, "Optical coherence tomography - principles and applications," *Reports on Progress in Physics,* vol. 66 (2), pp. 239-303, 2003.

[29] Z. Yaqoob, J. Wu, and C. Yang, "Spectral domain optical coherence tomography: a better OCT imaging strategy," *BioTechniques,* vol. 39 (6), pp. S6-s13, 2005.

[30] S.-W. Lee, H.-W. Jeong, B.-M. Kim, Y.-C. Ahn, W. Jung, and z. Chen, "Optimization for axial resolution, depth range, and sensitivity of spectral domain sptical coherence tomography at 1.3 µm," *Journal of the Korean Physical Society,* vol. 55 (6), pp. 2354-2360, 2009.

[31] A. Maheshwari, M. Choma, and J. Izatt, "Heterodyne swept-source optical coherence tomography for complete complex conjugate ambiguity removal," *Journal of Biomedical Optics,* vol. 10 (6), 2005.

[32] Copyright © 2011 Wikipedia. *Convolution illustrated: longitudinal (XZ) central slice of a 3D image acquired by a fluorescence microscope*. Available: http://en.wikipedia.org/wiki/File:Convolution_Illustrated_eng.png.

[33] Y. Wang, J. Nelson, Z. Chen, B. Reiser, R. Chuck, and R. Windeler, "Optimal wavelength for ultrahigh-resolution optical coherence tomography," *Opt. Express,* vol. 11 (12), pp. 1411-1417, 2003.

[34] Y. Chen, D. M. de Bruin, C. Kerbage, and J. F. de Boer, "Spectrally balanced detection for optical frequency domain imaging," *Opt. Express,* vol. 15 (25), pp. 16390-16399, 2007.

[35] R. Leitgeb, C. Hitzenberger, and A. Fercher, "Performance of fourier domain vs. time domain optical coherence tomography," *Opt. Express,* vol. 11 (8), pp. 889-894, 2003.

[36] A. G. Podoleanu, "Unbalanced versus balanced operation in an optical coherence tomography system," *Applied Optics,* vol. 39 (1), pp. 173-182, 2000.

[37] S. Yun, G. Tearney, B. Bouma, B. Park, and J. de Boer, "High-speed spectral-domain optical coherence tomography at 1.3 um wavelength," *Opt. Express,* vol. 11 (26), pp. 3598-3604, 2003.

[38] F. A. Jenkins and H. E. White, *Fundamentals of optics*: McGraw-Hill, 2001.

[39] B. C. Wilson and S. L. Jacques, "Optical reflectance and transmittance of tissues: principles and applications," *IEEE Journal of Quantum Electronics,* vol. 26 (12), pp. 2186-2199, 1990.

[40] D. Fried, R. E. Glena, J. D. B. Featherstone, and W. Seka, "Nature of light scattering in dental enamel and dentin at visible and near-infrared wavelengths," *Applied Optics,* vol. 34 (7), pp. 1278-1285, 1995.

[41] X. Wang, "Estimation of effective scatterer size and number density in near-infrared tomography " Doctor of Philosophy, Department of Physics and Astronomy, DARTMOUTH COLLEGE, Hanover, New Hampshire, 2007.

[42] Copyright © 2011 S. L. Jacques and S. A. Prahl. *Reduced scattering coefficient* Available: http://omlc.ogi.edu/classroom/ece532/class3/musp.html.

[43] Copyright © 2011 M. E. Anderson. *A beginner's guide to speckle*. Available: http://dukemil.bme.duke.edu/Ultrasound/k-space/node5.html.

[44] E. A. Peter and et al., "Advanced modelling of optical coherence tomography systems," *Physics in Medicine and Biology,* vol. 49 (7), p. 1307, 2004.

[45] F. Gasca, L. Ramrath, G. Huettmann, and A. Schweikard, "Automated segmentation of tissue structures in optical coherence tomography data," *Journal of Biomedical Optics,* vol. 14 (3), pp. 034046-034021, 2009.

[46] D. D. Royston, R. S. Poston, and S. A. Prahl, "Optical Properties of Scattering and Absorbing Materials Used in the Development of Optical Phantoms at 1064 nm," *J. Biomedical Optics,* vol. 1 pp. 110-116, 1996.

[47] W. Georges and et al., "An optical phantom with tissue-like properties in the visible for use in PDT and fluorescence spectroscopy," *Physics in Medicine and Biology,* vol. 42 (7), p. 1415, 1997.

[48] R. J. Cooper, R. Eames, J. Brunker, L. C. Enfield, A. P. Gibson, and J. C. Hebden, "A tissue equivalent phantom for simultaneous near-infrared optical tomography and EEG," *Biomed. Opt. Express,* vol. 1 (2), pp. 425-430, 2010.

[49] R. Srinivasan, D. Kumar, and M. Singh, "Optical tissue-equivalent phantoms for medical imaging," *Trends in Biomaterials and Artificial Organs,* vol. 15 (2), pp. 42-47, 2002.

[50] S. T. Flock, S. L. Jacques, B. C. Wilson, W. M. Star, and M. J. C. van Gemert, "Optical properties of intralipid: A phantom medium for light propagation studies," *Lasers in Surgery and Medicine,* vol. 12 (5), pp. 510-519, 1992.

[51] Copyright © 2011 S. Prahl. *Optical phantoms*. Available: http://www.bme.ogi.edu/~prahl/projects/phantoms.html.

[52] W. F. Seka, J. D. Featherstone, S. F. Borzillary, and S. F. Borzillary, "Light deposition in dental

hard tissue and simulated thermal response," (0022-0345 (Print)), 19950714 DCOM-19950714 1995.

[53] W. F. Cheong, S. A. Prahl, and A. J. Welch, "A review of the optical properties of biological tissues," *IEEE Journal of Quantum Electronics,* vol. 26 (12), pp. 2166-2185, 1990.

[54] V. M. Kodach, J. Kalkman, D. J. Faber, and T. G. van Leeuwen, "Quantitative comparison of the OCT imaging depth at 1300 nm and 1600 nm," *Biomed. Opt. Express,* vol. 1 (1), pp. 176-185, 2010.

[55] Copyright © 2011 D. Corning. *Sylgard® 184 solicone elastomer kit*. Available: http://www.dowcorning.com/applications/search/products/Details.aspx?prod=01064291&type=PROD.

[56] A. Ozcan, A. Bilenca, A. E. Desjardins, B. E. Bouma, and G. J. Tearney, "Speckle reduction in optical coherence tomography images using digital filtering," *J. Opt. Soc. Am. A,* vol. 24 (7), pp. 1901-1910, 2007.

[57] P. Puvanathasan and K. Bizheva, "Speckle noise reduction algorithm for optical coherence tomography based on interval type II fuzzy set," *Optics Express,* vol. 15 (24), pp. 15747-15758, 2007.

[58] K. Su Cheol and H. Seung Hong, "A speckle reduction filter using wavelet-based methods for medical imaging application," In: proceeding of *Engineering in Medicine and Biology Society, 2001. Proceedings of the 23rd Annual International Conference of the IEEE*, pp. 2480-2483 vol.2483, 2001.

[59] D. C. Adler, T. H. Ko, and J. G. Fujimoto, "Speckle reduction in optical coherence tomography images by use of a spatially adaptive wavelet filter," *Opt. Lett.,* vol. 29 (24), pp. 2878-2880, 2004.

[60] H. M. Salinas and D. C. Fernandez, "Comparison of PDE-based nonlinear diffusion approaches for image enhancement and denoising in optical coherence tomography," *IEEE Trans Med Imaging.,* vol. 26 (6), pp. 761-771., 2007.

[61] A. Wong, A. Mishra, K. Bizheva, and D. A. Clausi, "General Bayesian estimation for speckle noise reduction in optical coherence tomography retinal imagery," *Opt. Express,* vol. 18 (8), pp. 8338-8352, 2010.

[62] A. Ahmad, S. G. Adie, E. J. Chaney, U. Sharma, and S. A. Boppart, "Cross-correlation-based image acquisition technique for manually-scanned optical coherence tomography," *Opt. Express,* vol. 17 (10), pp. 8125-8136, 2009.

[63] F. Jin, P. Fieguth, L. Winger, and E. Jernigan, "Adaptive Wiener filtering of noisy images and image sequences," In: proceeding of *Image Processing, 2003. ICIP 2003. Proceedings. 2003 International Conference on*, pp. III-349-352 vol.342, 2003.

[64] M. Kuwahara, K. Hachimura, S. Eiho, and M. Kinoshita, "Digital processing of biomedical images," ed, 1976, pp. 187-203, 1976.

[65] Copyright © 2011 *Kuwahara filter*. Available: http://www.incx.nec.co.jp/imap-vision/library/wouter/kuwahara.html.

[66] D. Harwood, M. Subbarao, H. Hakalahti, and L. S. Davis, "A new class of edge-preserving smoothing filters," *Pattern Recogn. Lett.,* vol. 6 (3), pp. 155-162, 1987.

[67] D. T. Kuan, A. A. Sawchuk, T. C. Strand, and P. Chavel, "Adaptive noise smoothing filter for images with signal-dependent noise," *Pattern Analysis and Machine Intelligence, IEEE Transactions on,* vol. PAMI-7 (2), pp. 165-177, 1985.

[68] S. Zhenghao and K. B. Fung, "A comparison of digital speckle filters," In: proceeding of *Geoscience and Remote Sensing Symposium, 1994. IGARSS '94. Surface and Atmospheric Remote Sensing: Technologies, Data Analysis and Interpretation., International*, pp. 2129-2133 vol.2124, 1994.

[69] A. Lopes, E. Nezry, R. Touzi, and H. Laur, "Maximum a posteriori speckle filtering and first order texture models in SAR images," In: proceeding of *Geoscience and Remote Sensing Symposium, 1990. IGARSS '90. 'Remote Sensing Science for the Nineties'., 10th Annual International*, pp. 2409-2412, 1990.

[70] Copyright © 2011 R. Fisher, S. Perkins, A. Walker, and E. Wolfart. *Median filter*. Available: http://homepages.inf.ed.ac.uk/rbf/HIPR2/median.htm.

[71] A. Lopes, E. Nezry, R. Touzi, and H. Laur, "Structure detection and statistical adaptive speckle filtering in SAR images," *International Journal of Remote Sensing,* vol. 14 (9), pp. 1735 - 1758, 1993.

[72] A. Lopes, R. Touzi, and E. Nezry, "Adaptive speckle filters and scene heterogeneity," *Geoscience and Remote Sensing, IEEE Transactions on,* vol. 28 (6), pp. 992-1000, 1990.

[73] R. Vanithamani and G. Umamaheswari, "Performance analysis of filters for speckle reduction in medical ultrasound images " *International Journal of Computer Applications,* vol. 12 (6), pp. 23-27, 2010.

[74] Z. Wang, A. C. Bovik, H. R. Sheikh, and E. P. Simoncelli, "Image quality assessment: From error visibility to structural similarity," *Image Processing, IEEE Transactions on,* vol. 13 (4), pp. 600-612, 2004.

[75] Copyright © 2011 *Compact Bone & Spongy (Cancellous Bone)*. Available: http://training.seer.cancer.gov/anatomy/skeletal/tissue.html.

[76] Copyright © 2011 *Bone Structure*. Available: http://www.engin.umich.edu/class/bme456/bonestructure/bonestructure.htm.

[77] C. L. Darling, G. D. Huynh, and D. Fried, *Light scattering properties of natural and artificially demineralized dental enamel at 1310 nm* vol. 11: SPIE, 2006.

Appendix A

Filtered OCT images

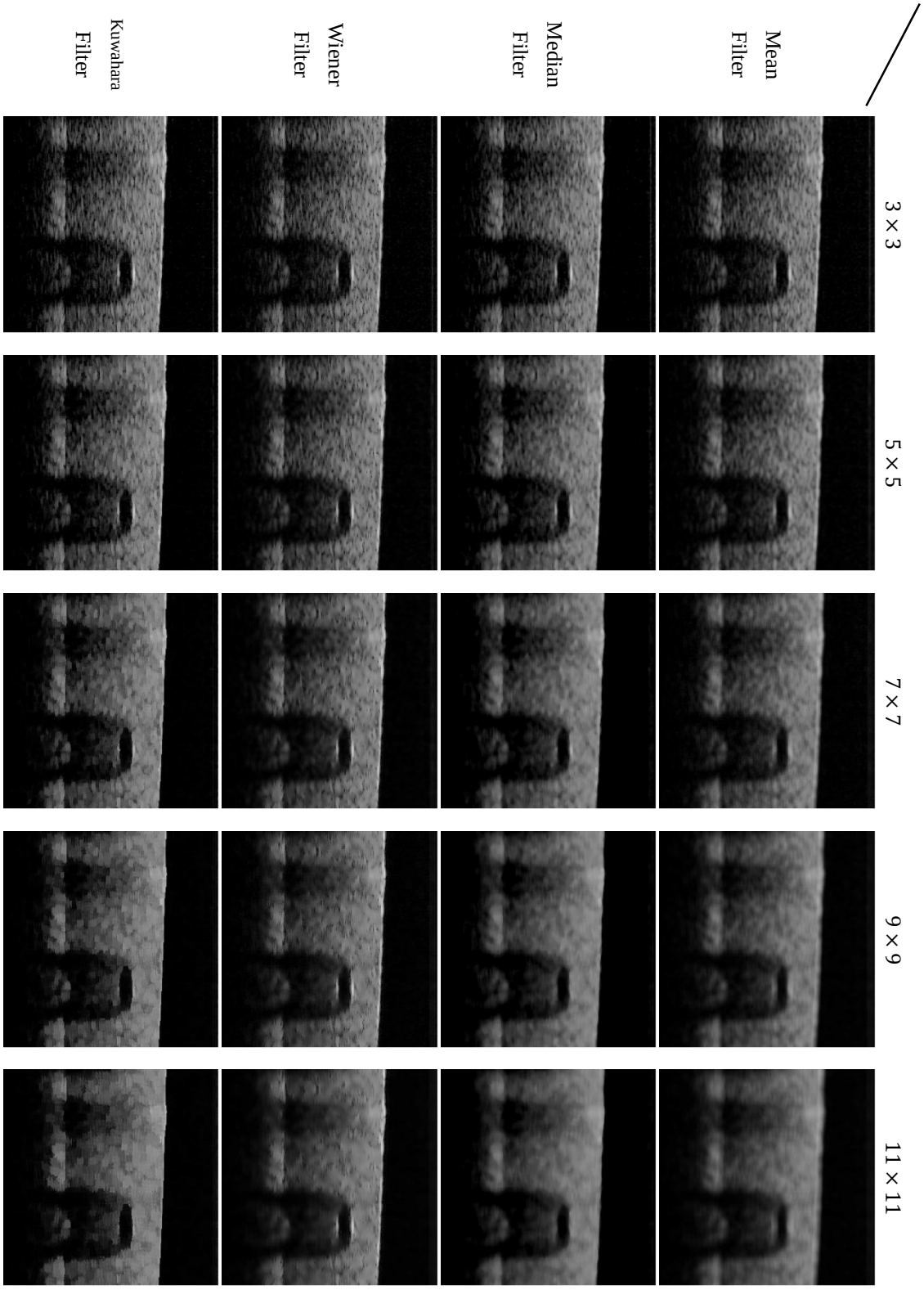

SNN filter
Kuan filter
Enhanced Lee filter
Gamma MAP filter
3 × 3
5 × 5
7 × 7
9 × 9
11 × 11

Appendix B

Image Quality Assessments for optical phantom

A. Equivalent Number of Looks (ENL) Comparison

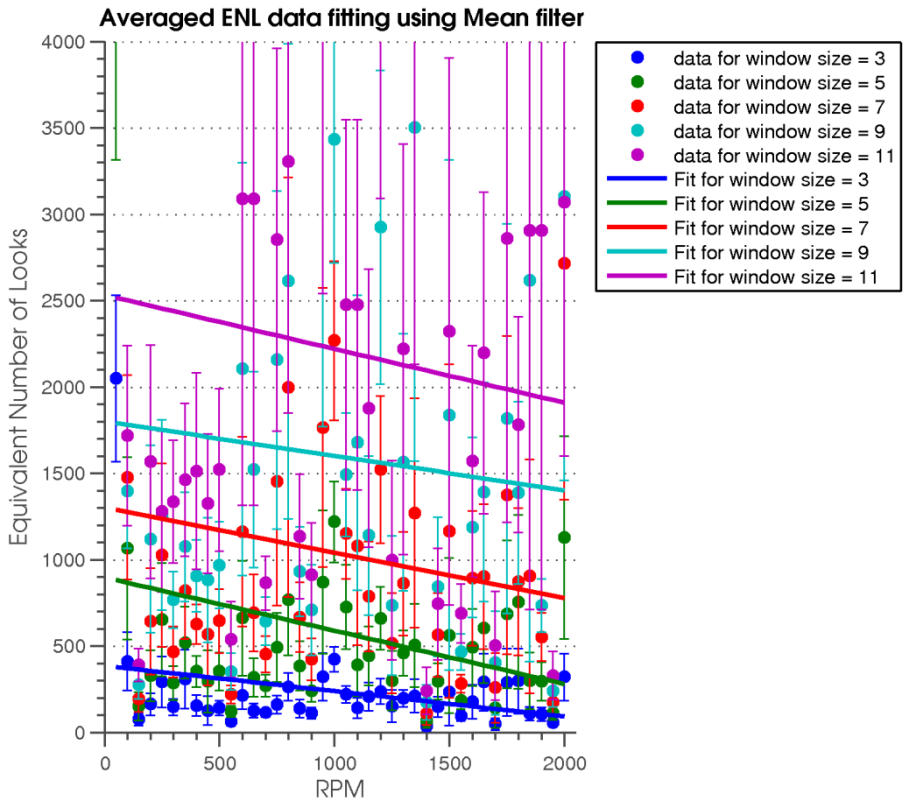

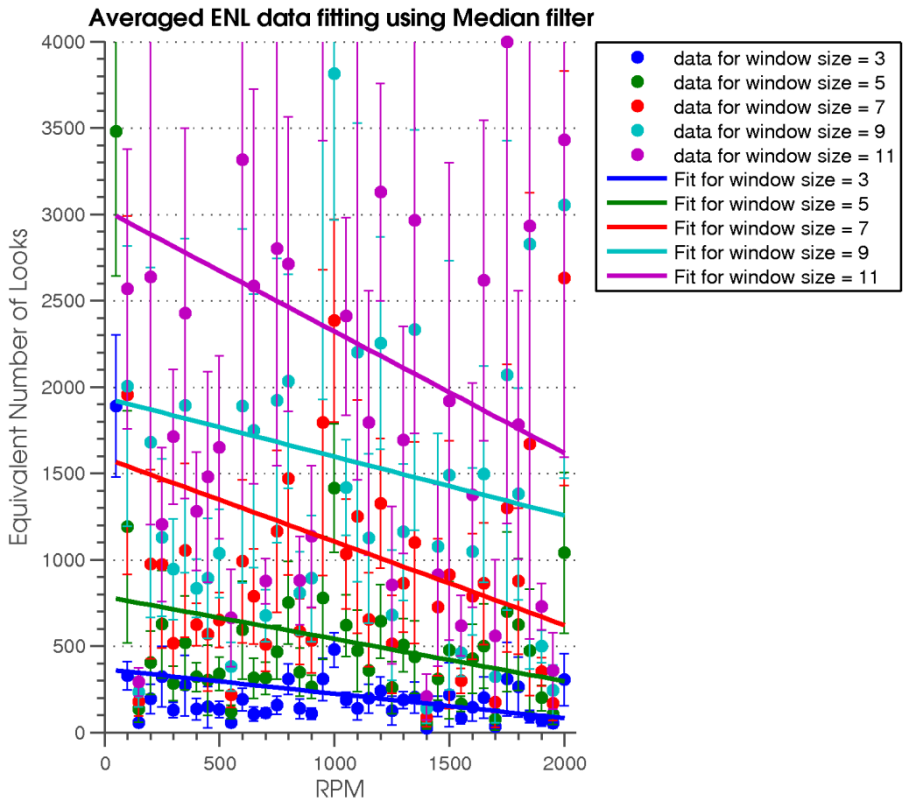
Averaged ENL data fitting using Median filter
Equivalent Number of Looks
RPM
0
500
1000
1500
2000
2500
3000
3500
4000
data for window size = 3
data for window size = 5
data for window size = 7
data for window size = 9
data for window size = 11
Fit for window size = 3
Fit for window size = 5
Fit for window size = 7
Fit for window size = 9
Fit for window size = 11

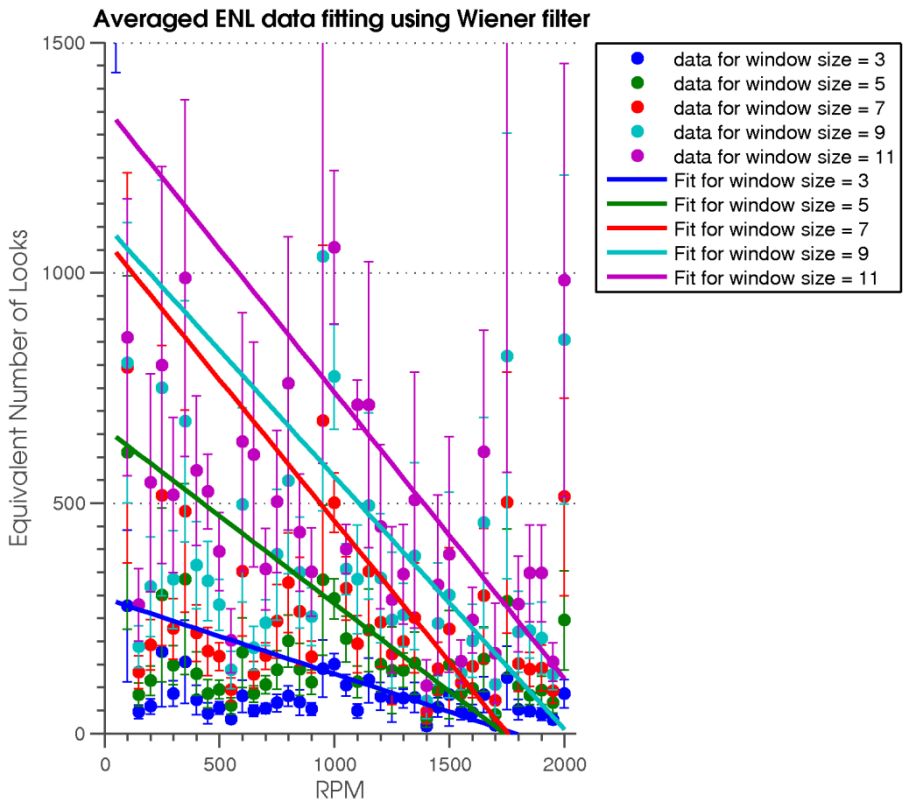
Averaged ENL data fitting using Wiener filter
Equivalent Number of Looks
RPM
0
500
1000
1500
2000
data for window size = 3
data for window size = 5
data for window size = 7
data for window size = 9
data for window size = 11
Fit for window size = 3
Fit for window size = 5
Fit for window size = 7
Fit for window size = 9
Fit for window size = 11

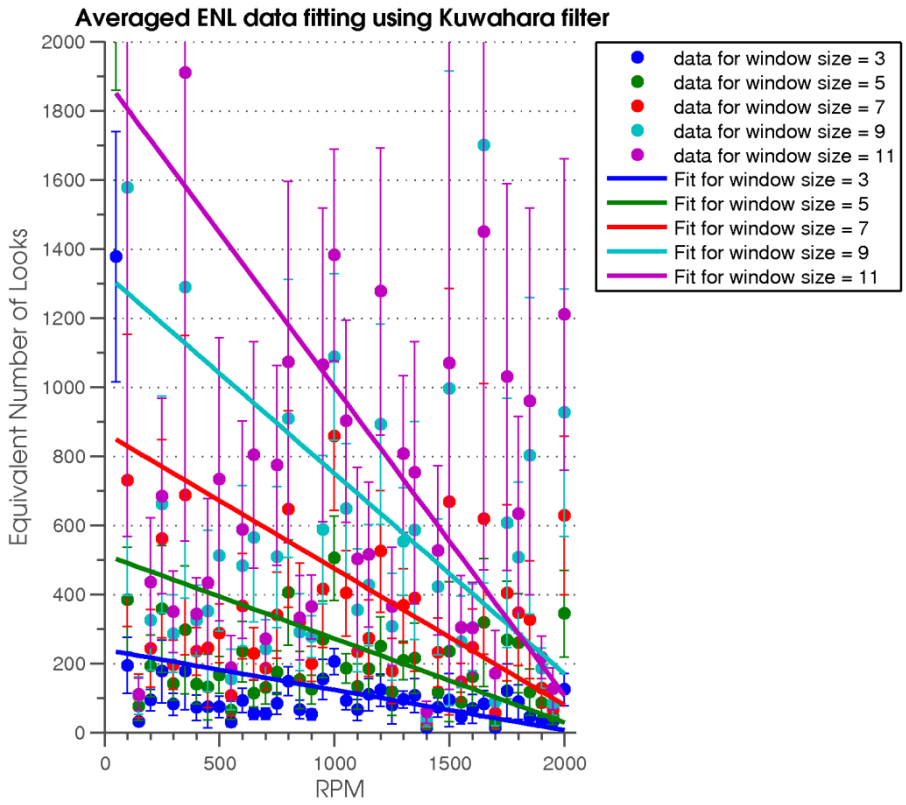
Averaged ENL data fitting using Kuwahara filter
Equivalent Number of Looks
RPM
0
200
400
600
800
1000
1200
1400
1600
1800
2000
0
500
1000
1500
2000
data for window size = 3
data for window size = 5
data for window size = 7
data for window size = 9
data for window size = 11
Fit for window size = 3
Fit for window size = 5
Fit for window size = 7
Fit for window size = 9
Fit for window size = 11

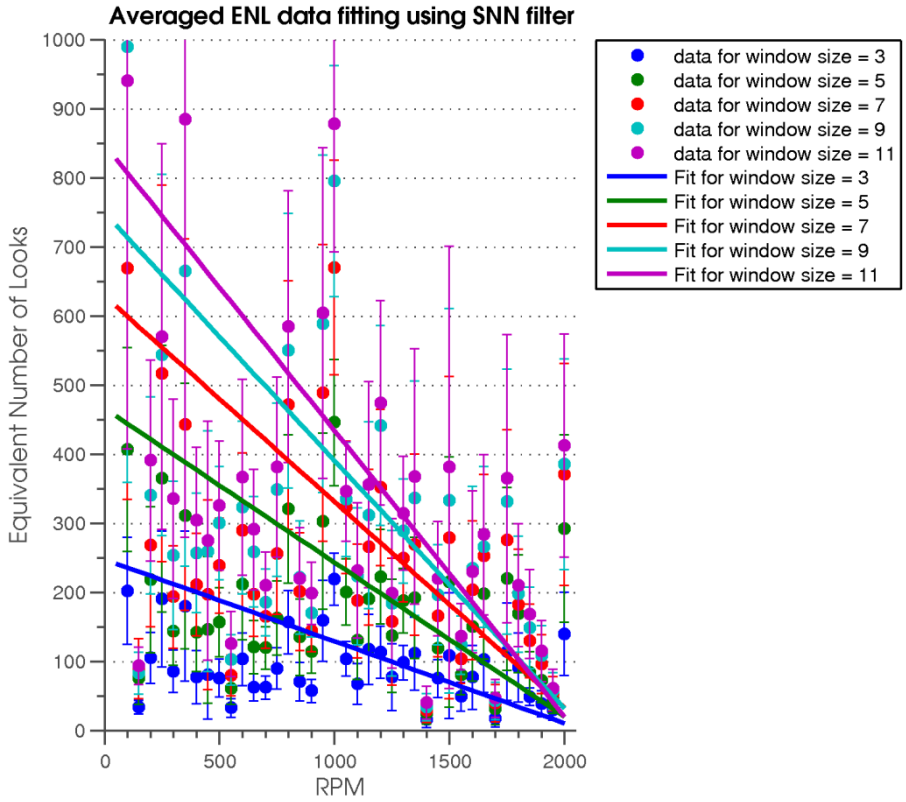
Averaged ENL data fitting using SNN filter
Equivalent Number of Looks
RPM
0
100
200
300
400
500
600
700
800
900
1000
0
500
1000
1500
2000
data for window size = 3
data for window size = 5
data for window size = 7
data for window size = 9
data for window size = 11
Fit for window size = 3
Fit for window size = 5
Fit for window size = 7
Fit for window size = 9
Fit for window size = 11

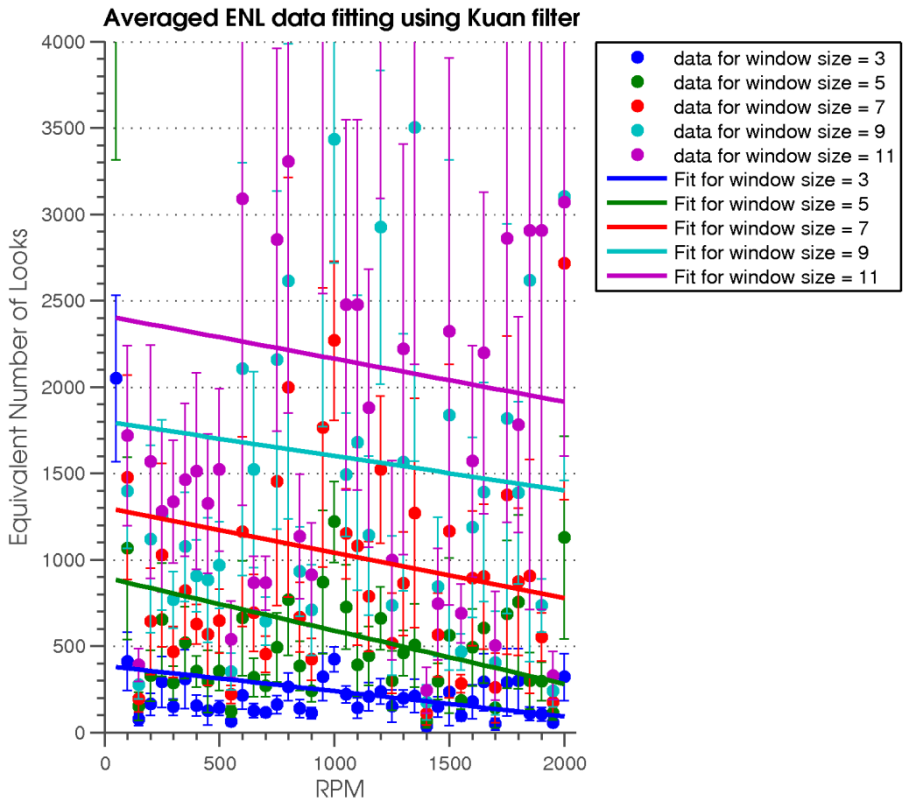
Averaged ENL data fitting using Kuan filter
Equivalent Number of Looks
RPM
0
500
1000
1500
2000
2500
3000
3500
4000
data for window size = 3
data for window size = 5
data for window size = 7
data for window size = 9
data for window size = 11
Fit for window size = 3
Fit for window size = 5
Fit for window size = 7
Fit for window size = 9
Fit for window size = 11

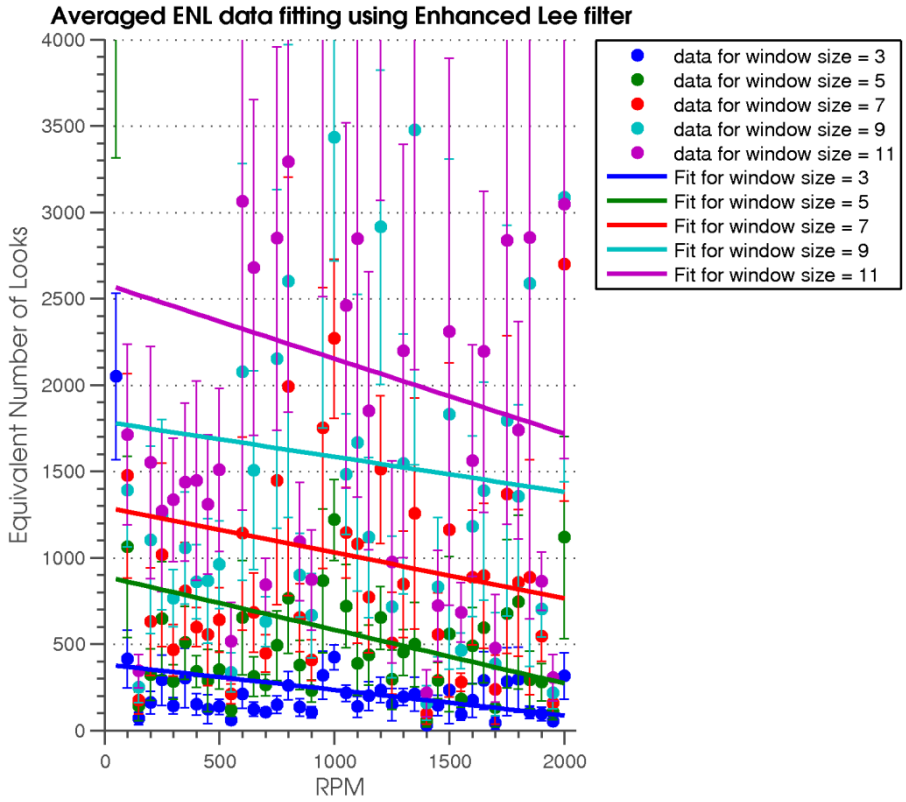
Averaged ENL data fitting using Enhanced Lee filter
Equivalent Number of Looks
RPM
0
500
1000
1500
2000
2500
3000
3500
4000
data for window size = 3
data for window size = 5
data for window size = 7
data for window size = 9
data for window size = 11
Fit for window size = 3
Fit for window size = 5
Fit for window size = 7
Fit for window size = 9
Fit for window size = 11

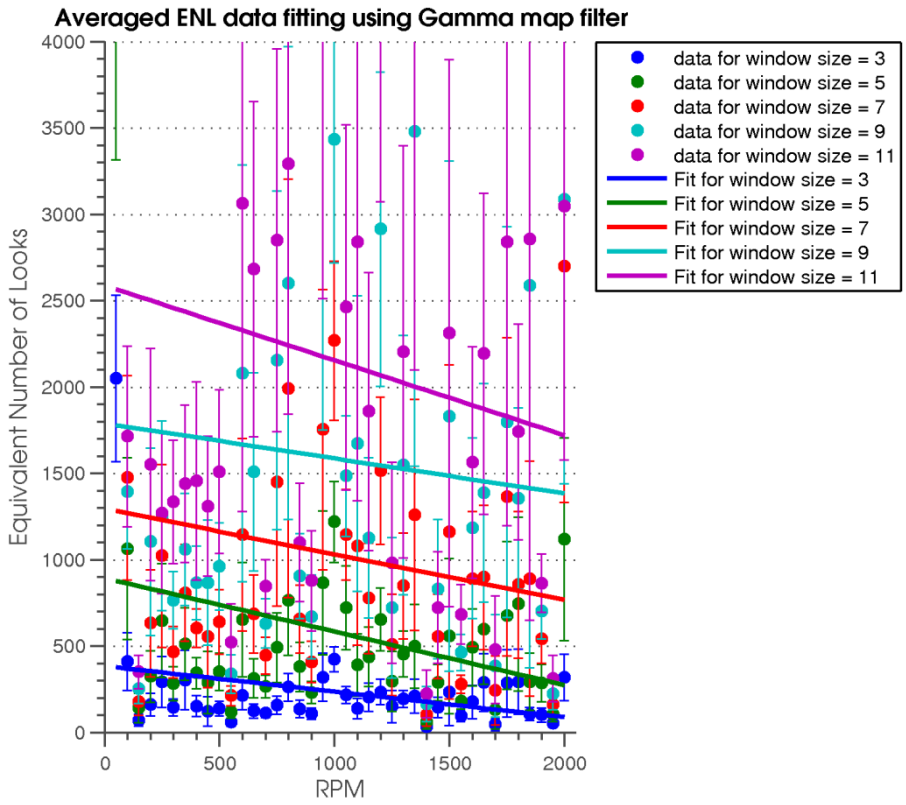

B. Contrast-to-Noise Ratio (CNR) Comparison

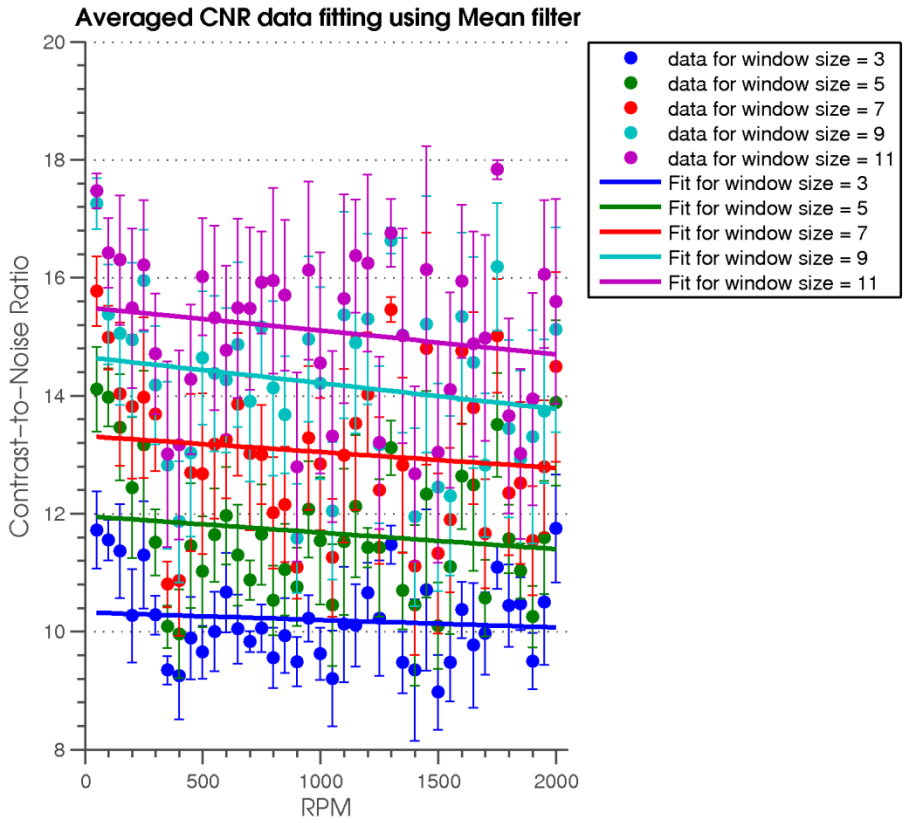

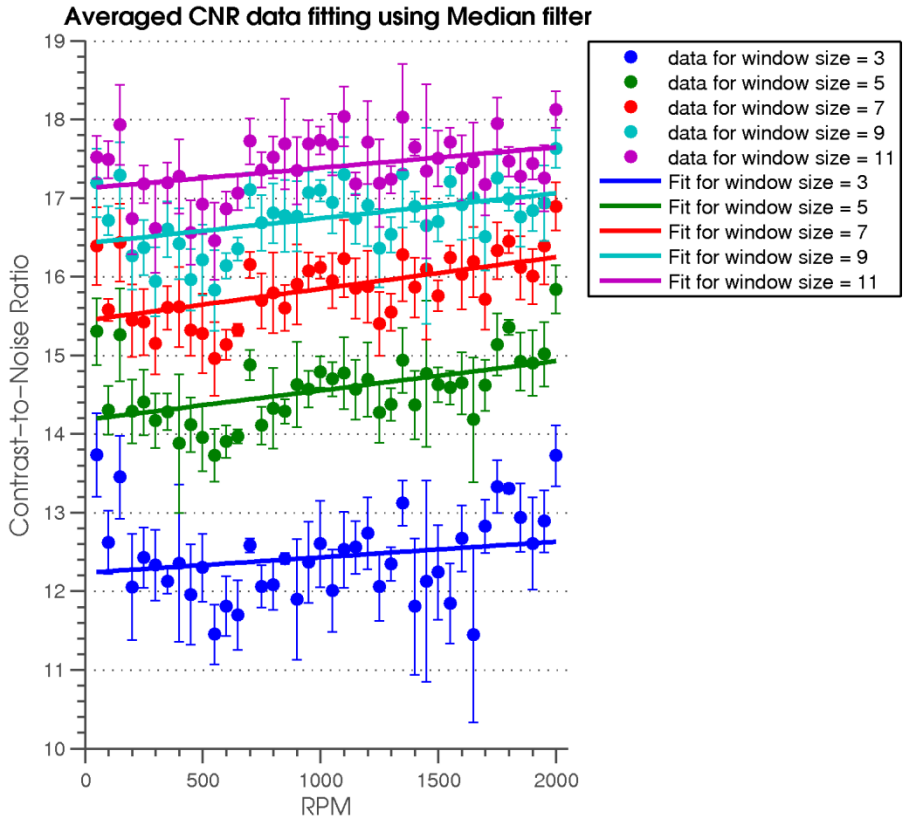
Averaged CNR data fitting using Median filter
Contrast-to-Noise Ratio
RPM
data for window size = 3
data for window size = 5
data for window size = 7
data for window size = 9
data for window size = 11
Fit for window size = 3
Fit for window size = 5
Fit for window size = 7
Fit for window size = 9
Fit for window size = 11

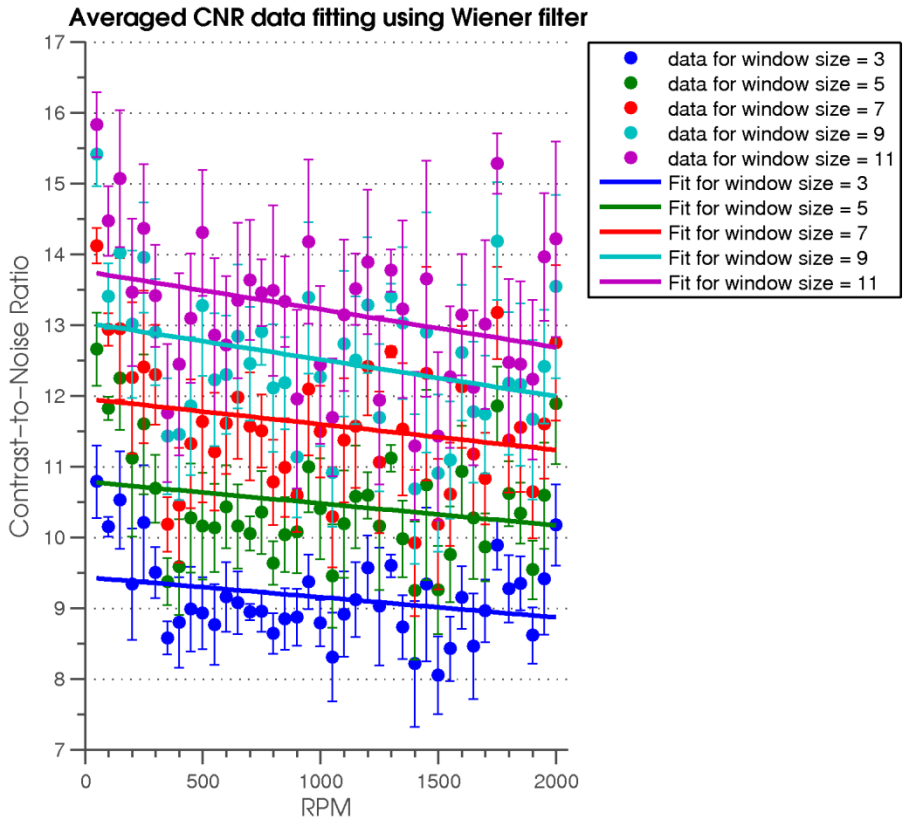
Averaged CNR data fitting using Wiener filter
Contrast-to-Noise Ratio
RPM
data for window size = 3
data for window size = 5
data for window size = 7
data for window size = 9
data for window size = 11
Fit for window size = 3
Fit for window size = 5
Fit for window size = 7
Fit for window size = 9
Fit for window size = 11

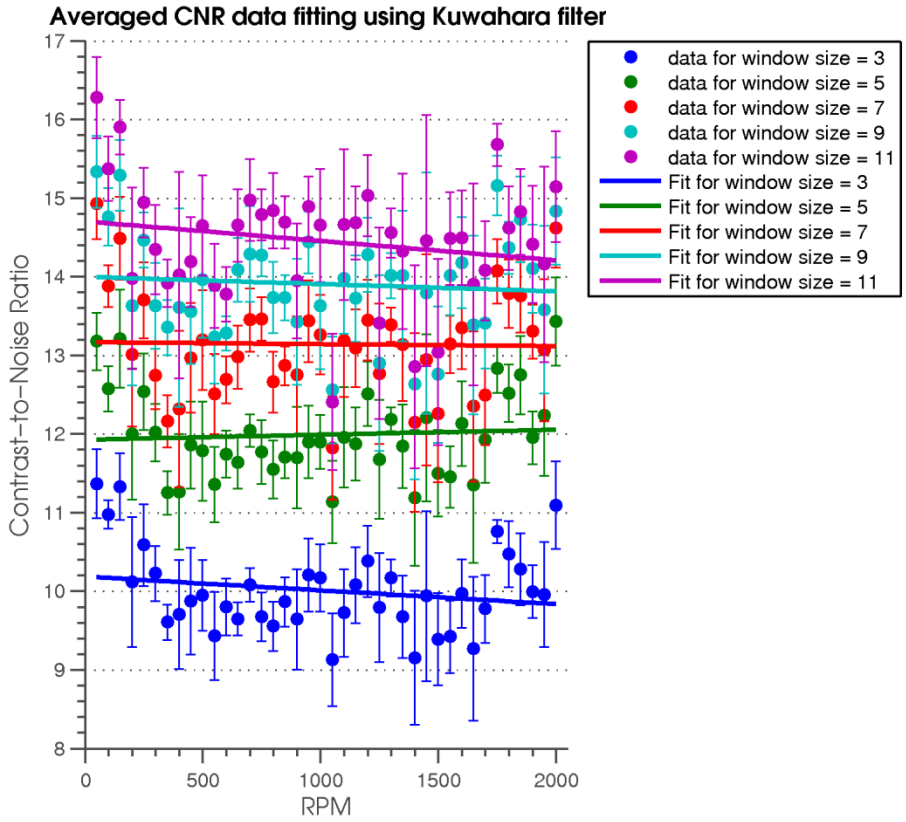
Averaged CNR data fitting using Kuwahara filter
Contrast-to-Noise Ratio
RPM
data for window size = 3
data for window size = 5
data for window size = 7
data for window size = 9
data for window size = 11
Fit for window size = 3
Fit for window size = 5
Fit for window size = 7
Fit for window size = 9
Fit for window size = 11

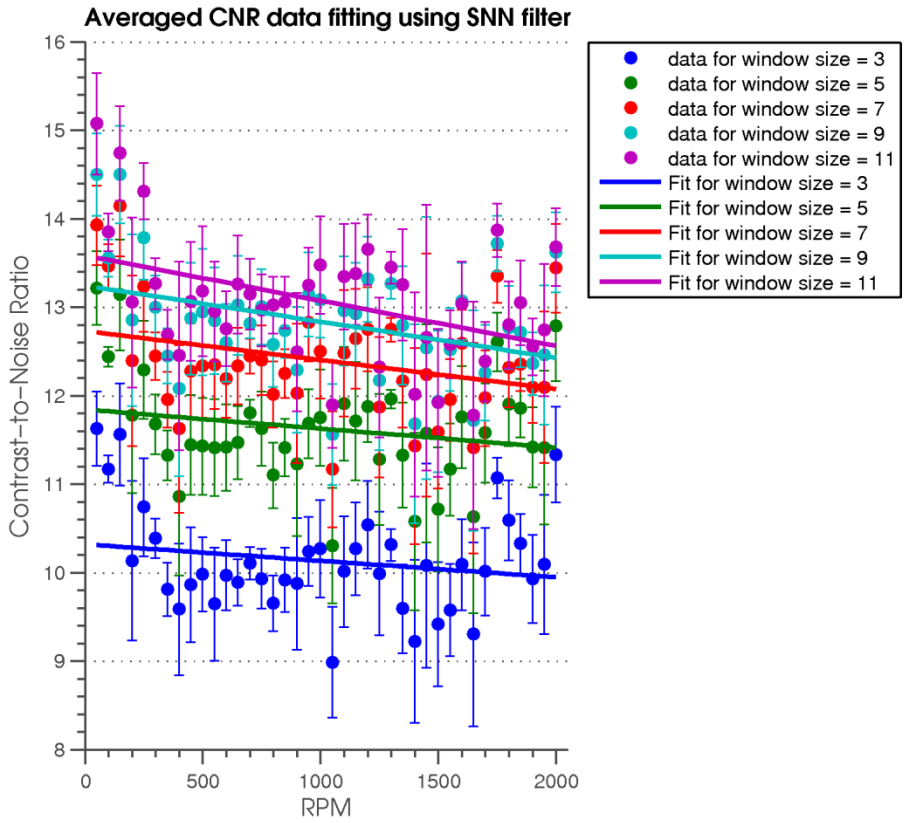
Averaged CNR data fitting using SNN filter
Contrast-to-Noise Ratio
RPM
data for window size = 3
data for window size = 5
data for window size = 7
data for window size = 9
data for window size = 11
Fit for window size = 3
Fit for window size = 5
Fit for window size = 7
Fit for window size = 9
Fit for window size = 11

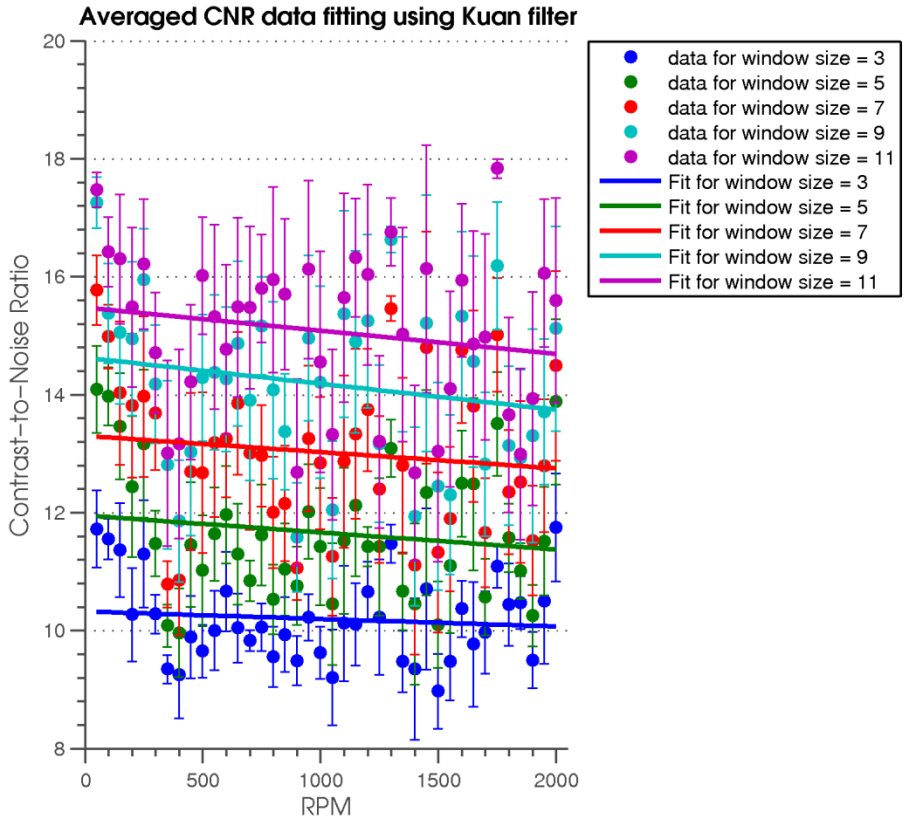
Averaged CNR data fitting using Kuan filter
Contrast-to-Noise Ratio
RPM
20
18
16
14
12
10
8
0
500
1000
1500
2000
data for window size = 3
data for window size = 5
data for window size = 7
data for window size = 9
data for window size = 11
Fit for window size = 3
Fit for window size = 5
Fit for window size = 7
Fit for window size = 9
Fit for window size = 11

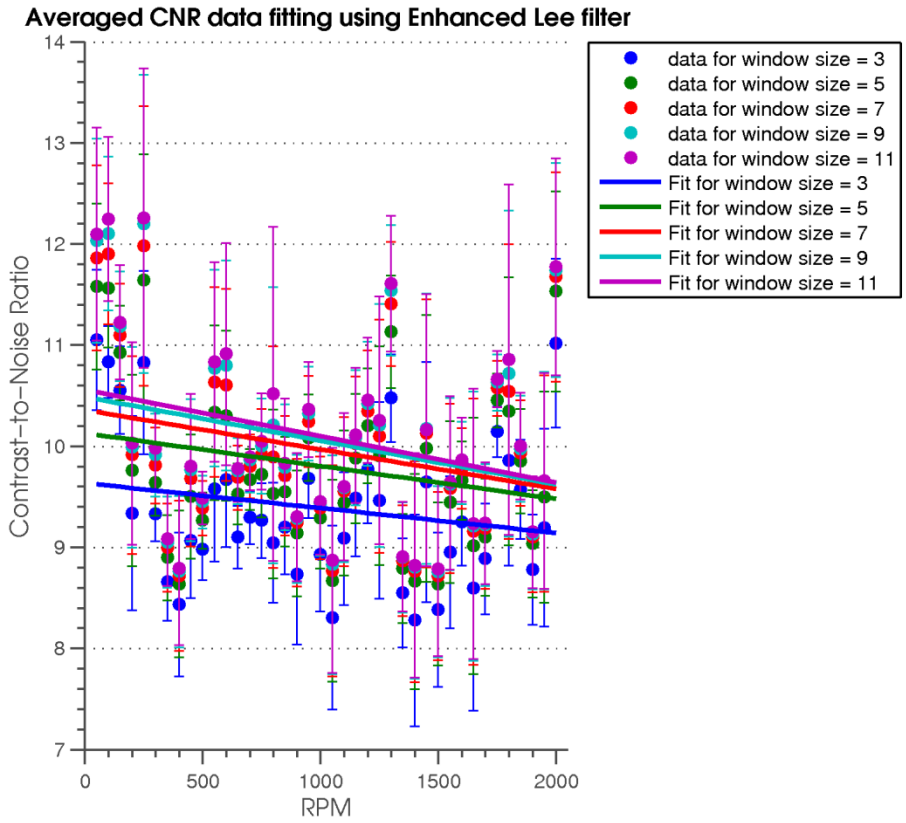
Averaged CNR data fitting using Enhanced Lee filter
Contrast-to-Noise Ratio
RPM
14
13
12
11
10
9
8
7
0
500
1000
1500
2000
data for window size = 3
data for window size = 5
data for window size = 7
data for window size = 9
data for window size = 11
Fit for window size = 3
Fit for window size = 5
Fit for window size = 7
Fit for window size = 9
Fit for window size = 11

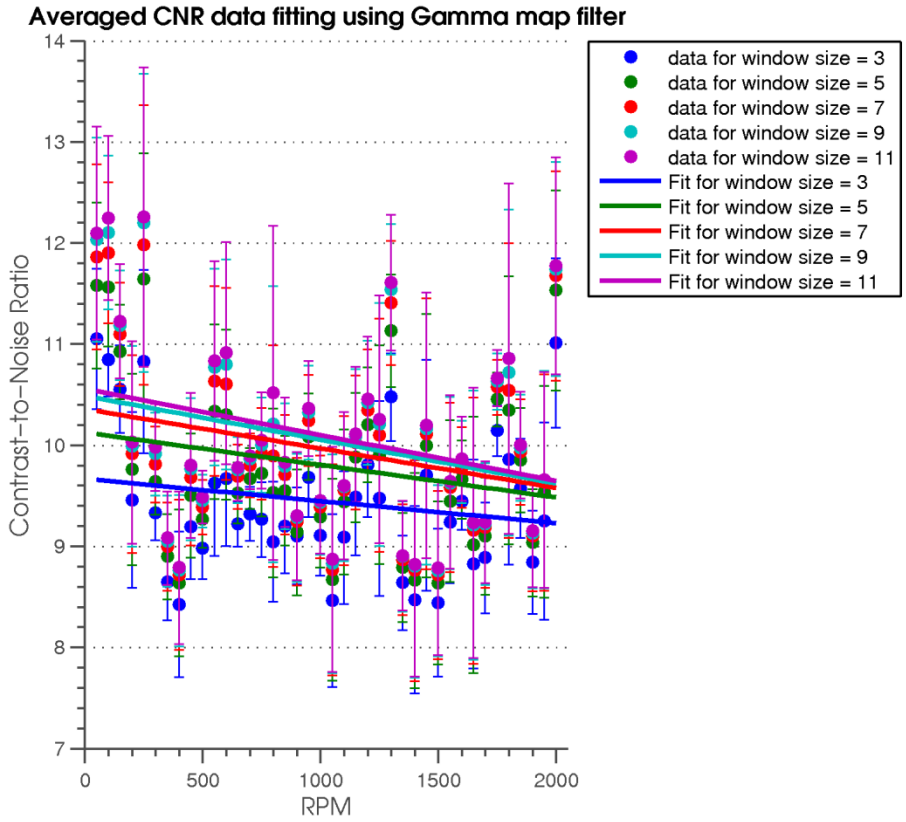

C. Edge Preserver Factor (EPF) Comparison

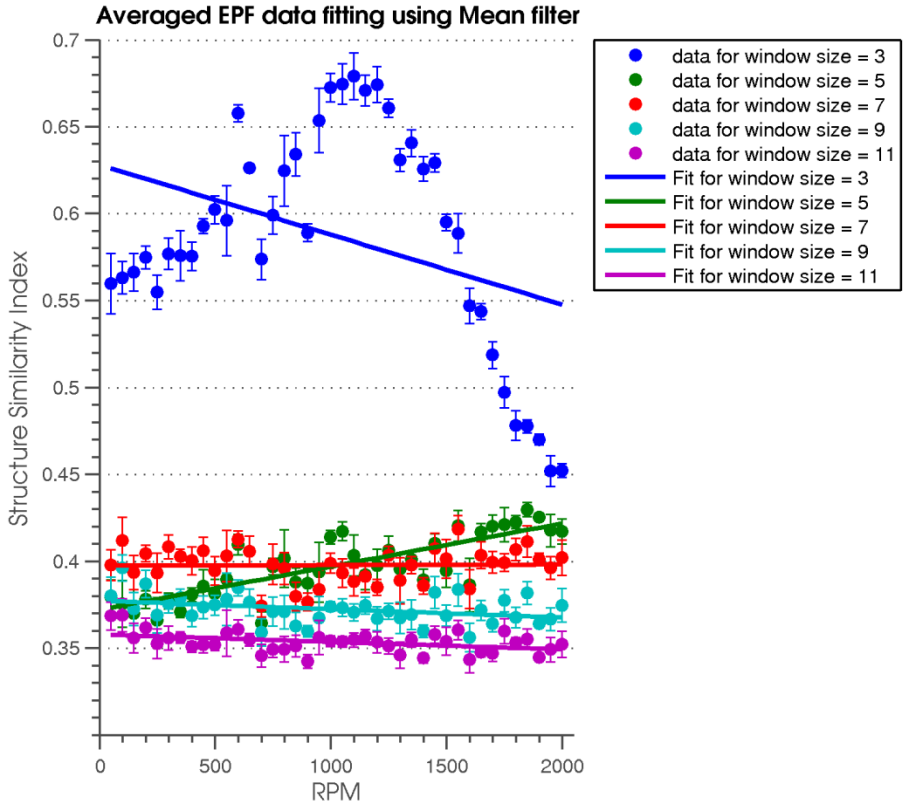

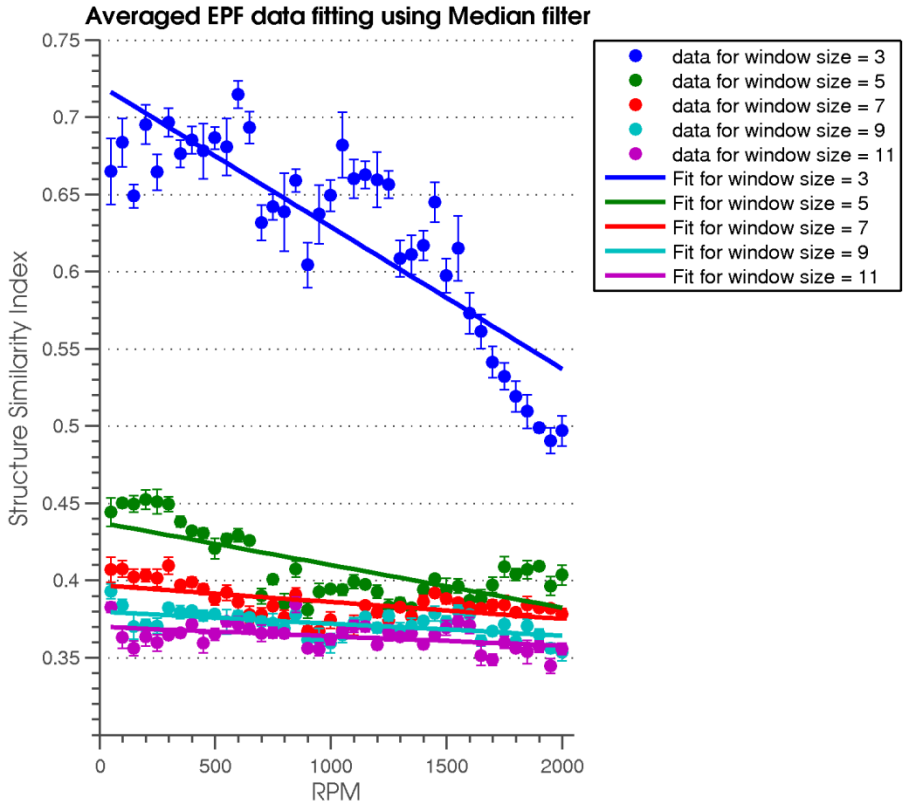
Averaged EPF data fitting using Median filter
Structure Similarity Index
RPM
0.75
0.7
0.65
0.6
0.55
0.5
0.45
0.4
0.35
0
500
1000
1500
2000
data for window size = 3
data for window size = 5
data for window size = 7
data for window size = 9
data for window size = 11
Fit for window size = 3
Fit for window size = 5
Fit for window size = 7
Fit for window size = 9
Fit for window size = 11

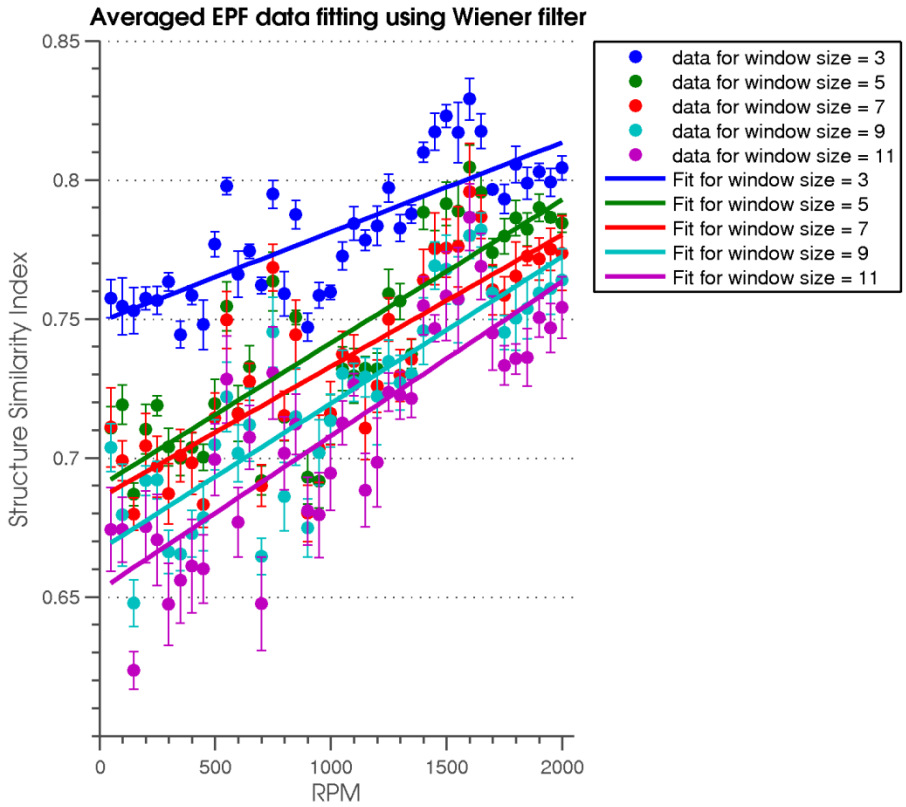
Averaged EPF data fitting using Wiener filter
Structure Similarity Index
RPM
0.85
0.8
0.75
0.7
0.65
0
500
1000
1500
2000
data for window size = 3
data for window size = 5
data for window size = 7
data for window size = 9
data for window size = 11
Fit for window size = 3
Fit for window size = 5
Fit for window size = 7
Fit for window size = 9
Fit for window size = 11

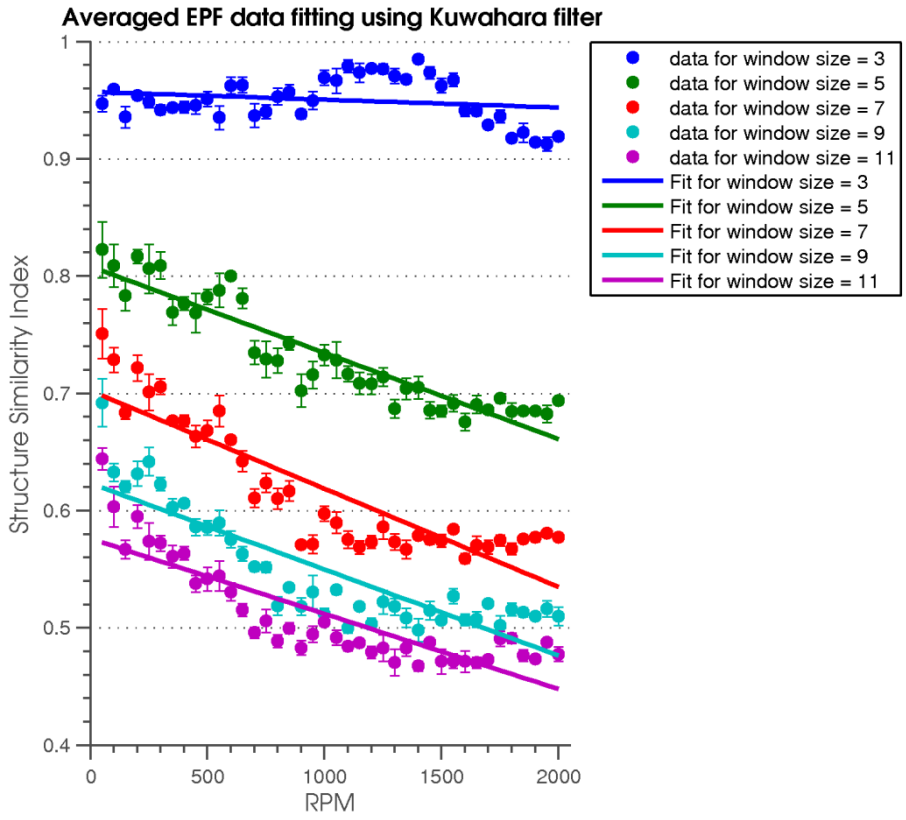
Averaged EPF data fitting using Kuwahara filter
Structure Similarity Index
RPM
data for window size = 3
data for window size = 5
data for window size = 7
data for window size = 9
data for window size = 11
Fit for window size = 3
Fit for window size = 5
Fit for window size = 7
Fit for window size = 9
Fit for window size = 11

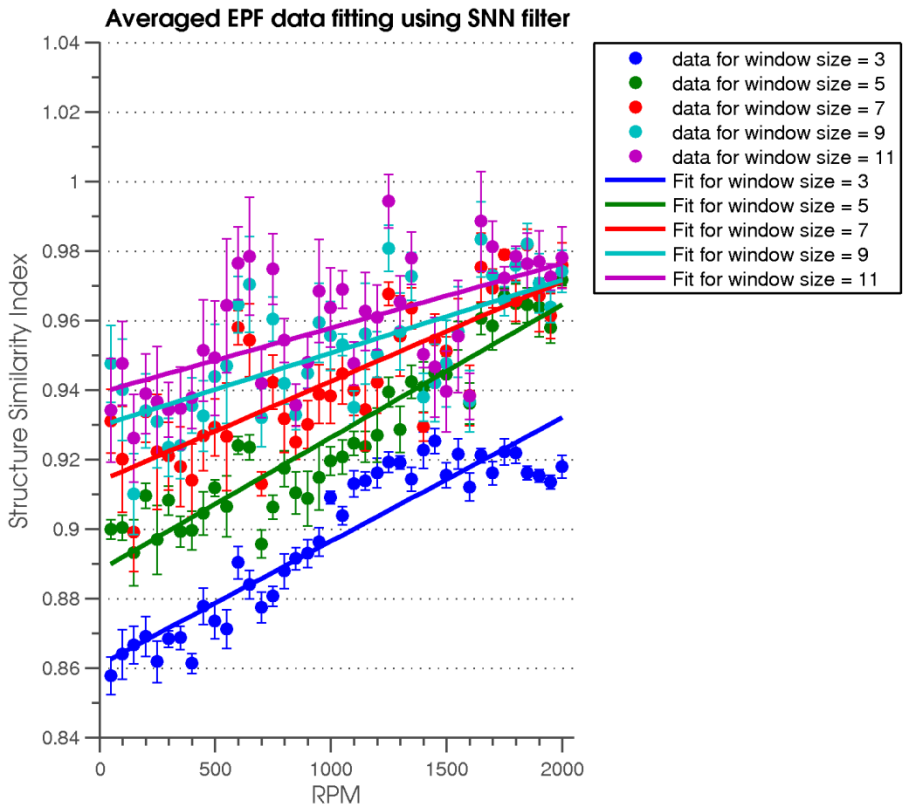
Averaged EPF data fitting using SNN filter
Structure Similarity Index
RPM
data for window size = 3
data for window size = 5
data for window size = 7
data for window size = 9
data for window size = 11
Fit for window size = 3
Fit for window size = 5
Fit for window size = 7
Fit for window size = 9
Fit for window size = 11

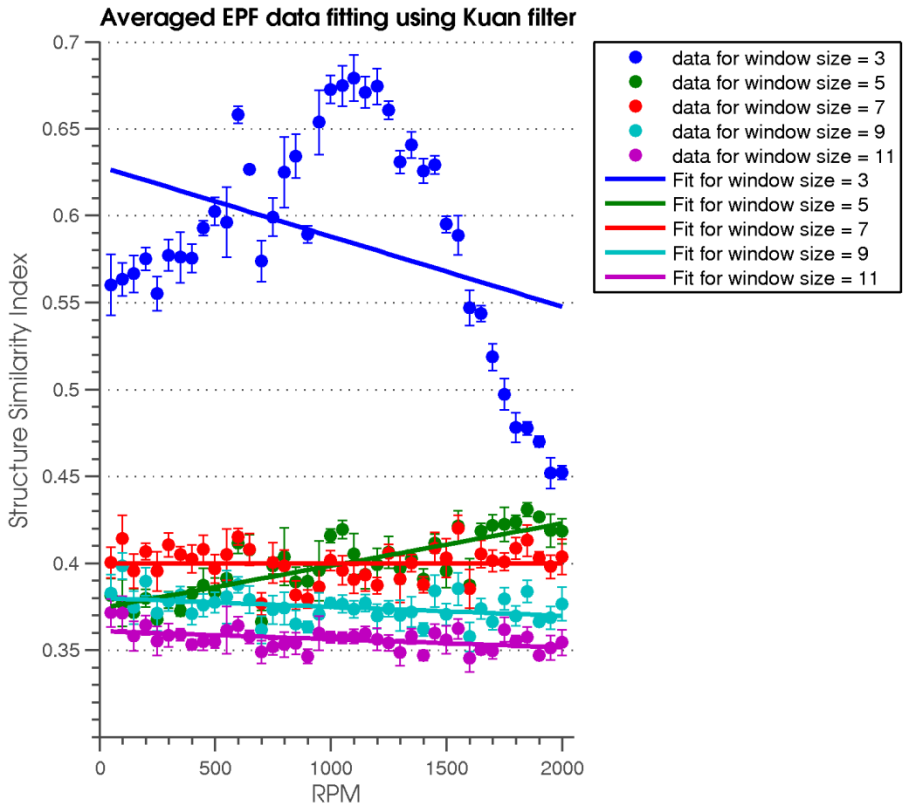
Averaged EPF data fitting using Kuan filter
Structure Similarity Index
RPM
0.7
0.65
0.6
0.55
0.5
0.45
0.4
0.35
0
500
1000
1500
2000
data for window size = 3
data for window size = 5
data for window size = 7
data for window size = 9
data for window size = 11
Fit for window size = 3
Fit for window size = 5
Fit for window size = 7
Fit for window size = 9
Fit for window size = 11

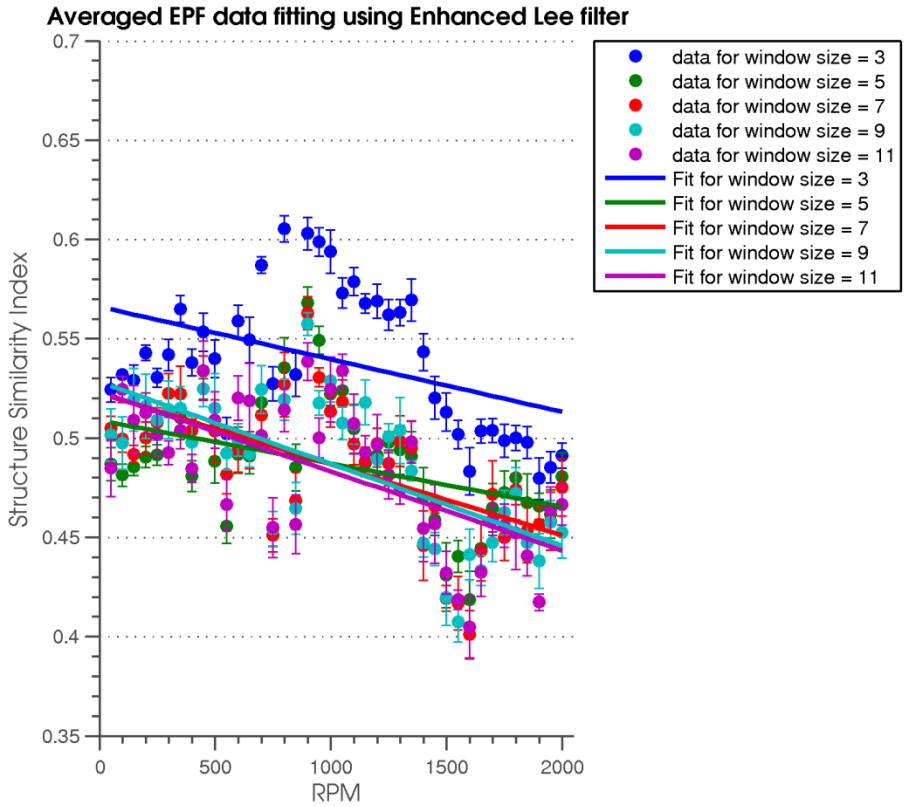
Averaged EPF data fitting using Enhanced Lee filter
Structure Similarity Index
RPM
0.7
0.65
0.6
0.55
0.5
0.45
0.4
0.35
0
500
1000
1500
2000
data for window size = 3
data for window size = 5
data for window size = 7
data for window size = 9
data for window size = 11
Fit for window size = 3
Fit for window size = 5
Fit for window size = 7
Fit for window size = 9
Fit for window size = 11

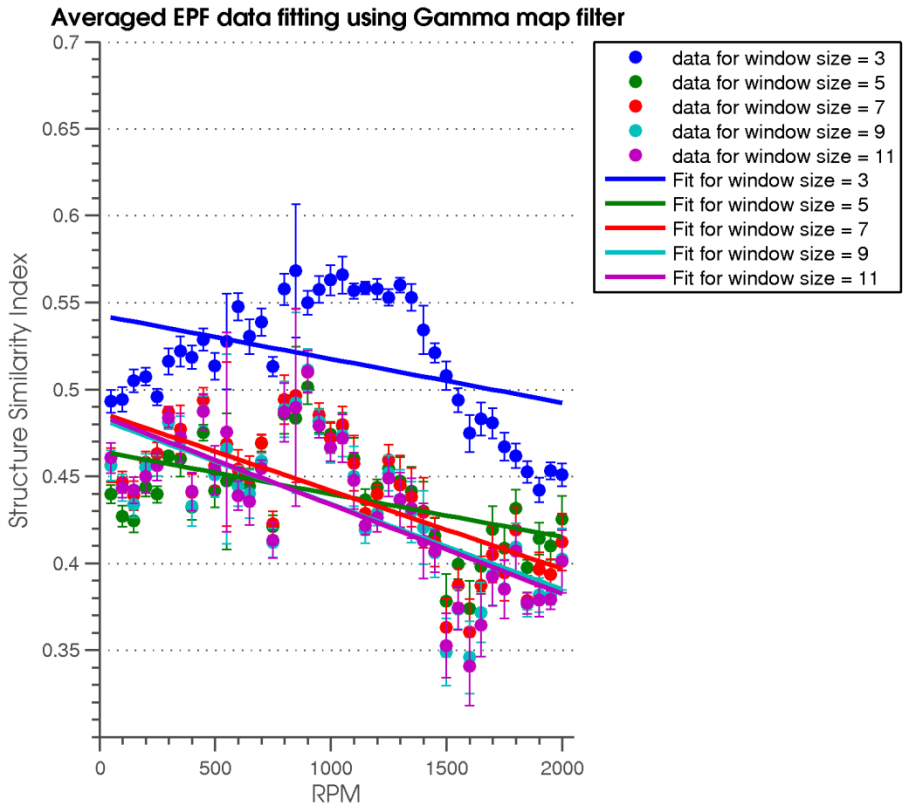

D. Structure Similarity Index (SSIM) Comparison

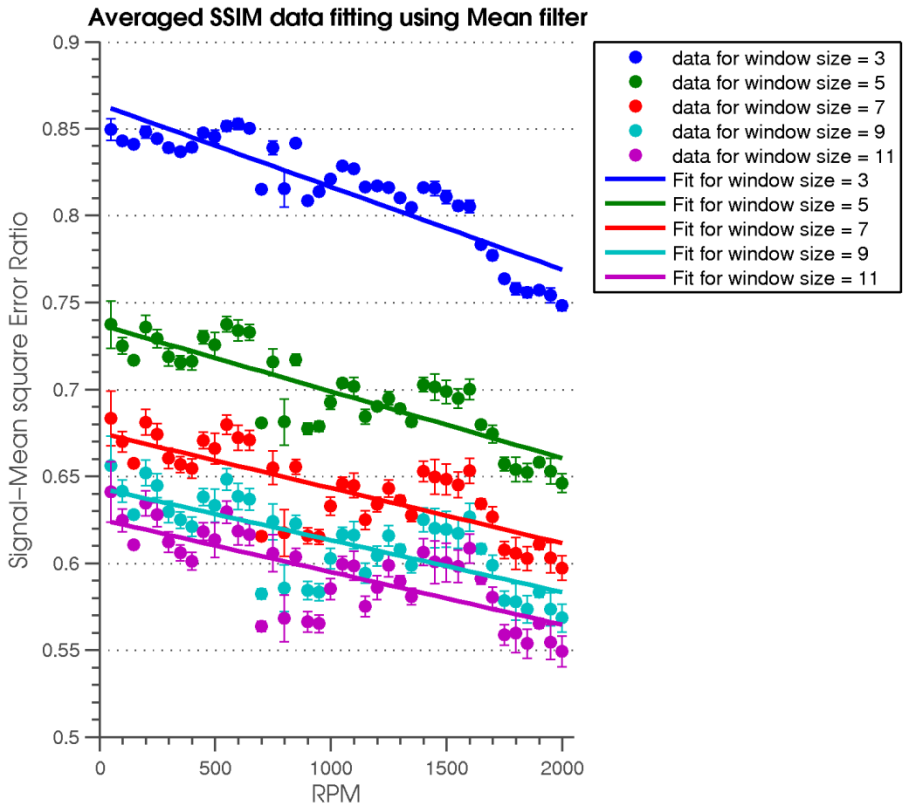

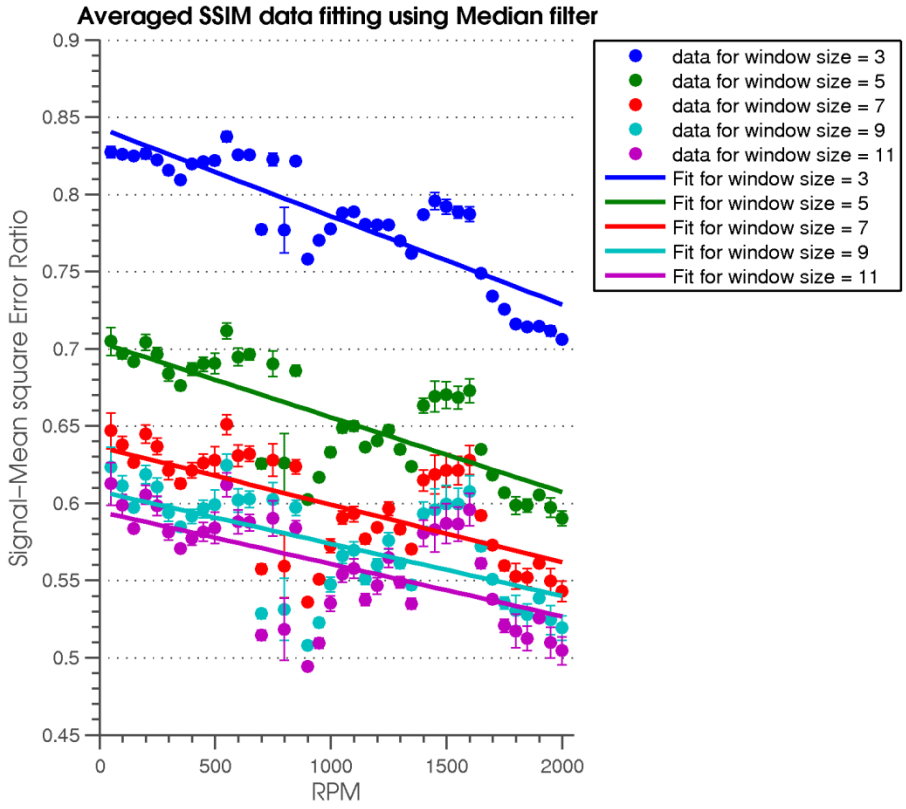
Averaged SSIM data fitting using Median filter
Signal–Mean square Error Ratio
RPM
0.9
0.85
0.8
0.75
0.7
0.65
0.6
0.55
0.5
0.45
0
500
1000
1500
2000
data for window size = 3
data for window size = 5
data for window size = 7
data for window size = 9
data for window size = 11
Fit for window size = 3
Fit for window size = 5
Fit for window size = 7
Fit for window size = 9
Fit for window size = 11

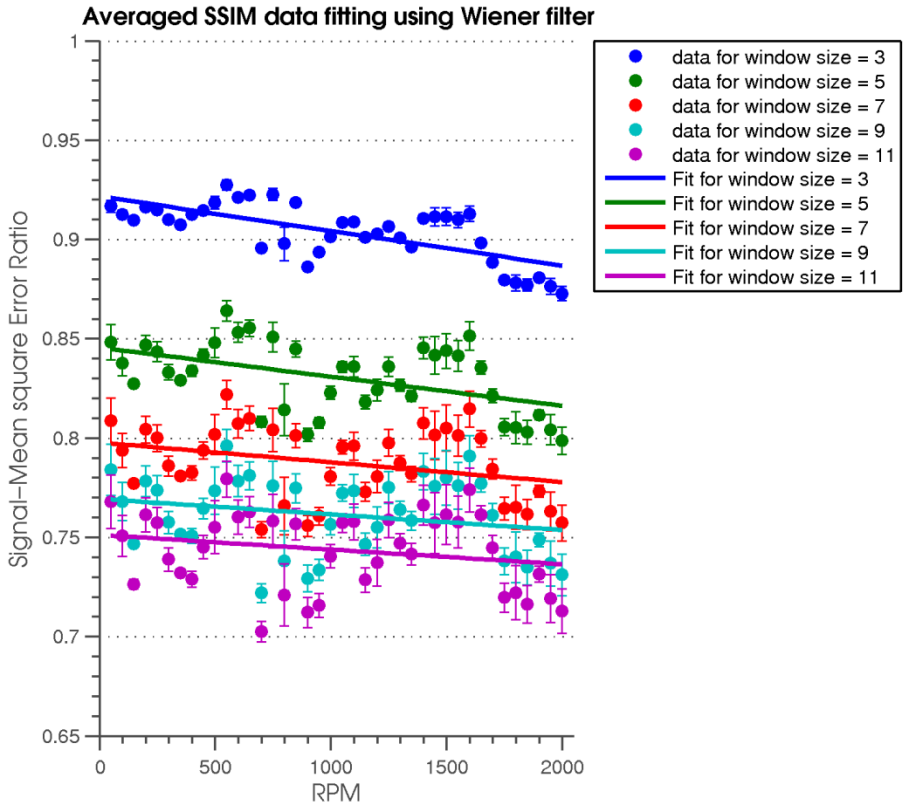
Averaged SSIM data fitting using Wiener filter
Signal–Mean square Error Ratio
RPM
1
0.95
0.9
0.85
0.8
0.75
0.7
0.65
0
500
1000
1500
2000
data for window size = 3
data for window size = 5
data for window size = 7
data for window size = 9
data for window size = 11
Fit for window size = 3
Fit for window size = 5
Fit for window size = 7
Fit for window size = 9
Fit for window size = 11

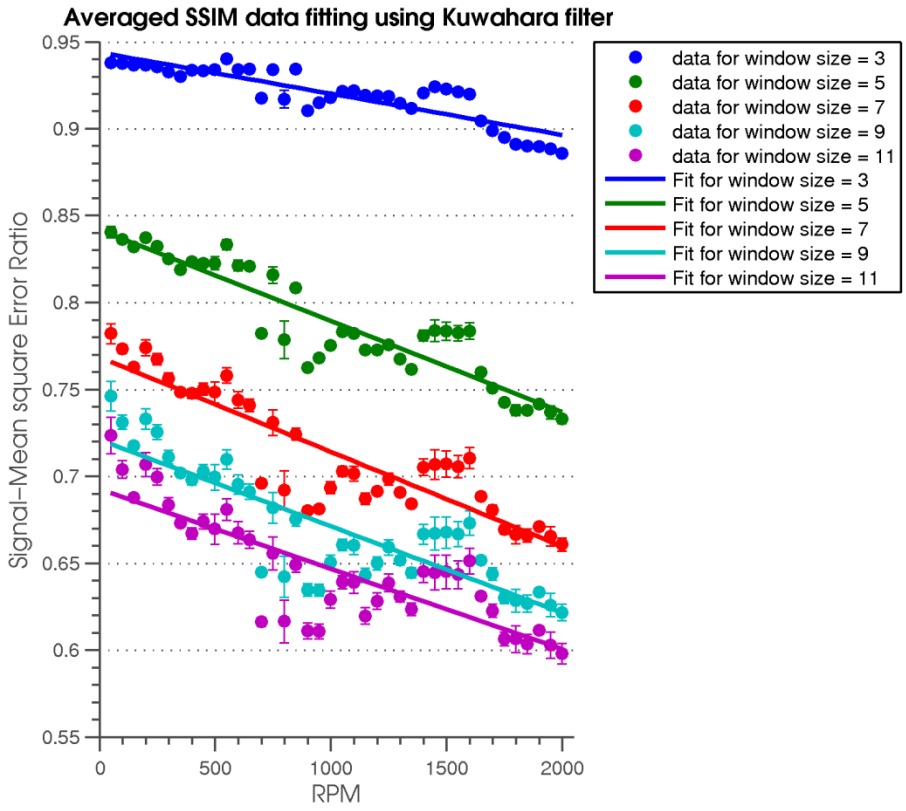
Averaged SSIM data fitting using Kuwahara filter
Signal–Mean square Error Ratio
RPM
0.95
0.9
0.85
0.8
0.75
0.7
0.65
0.6
0.55
0
500
1000
1500
2000
data for window size = 3
data for window size = 5
data for window size = 7
data for window size = 9
data for window size = 11
Fit for window size = 3
Fit for window size = 5
Fit for window size = 7
Fit for window size = 9
Fit for window size = 11

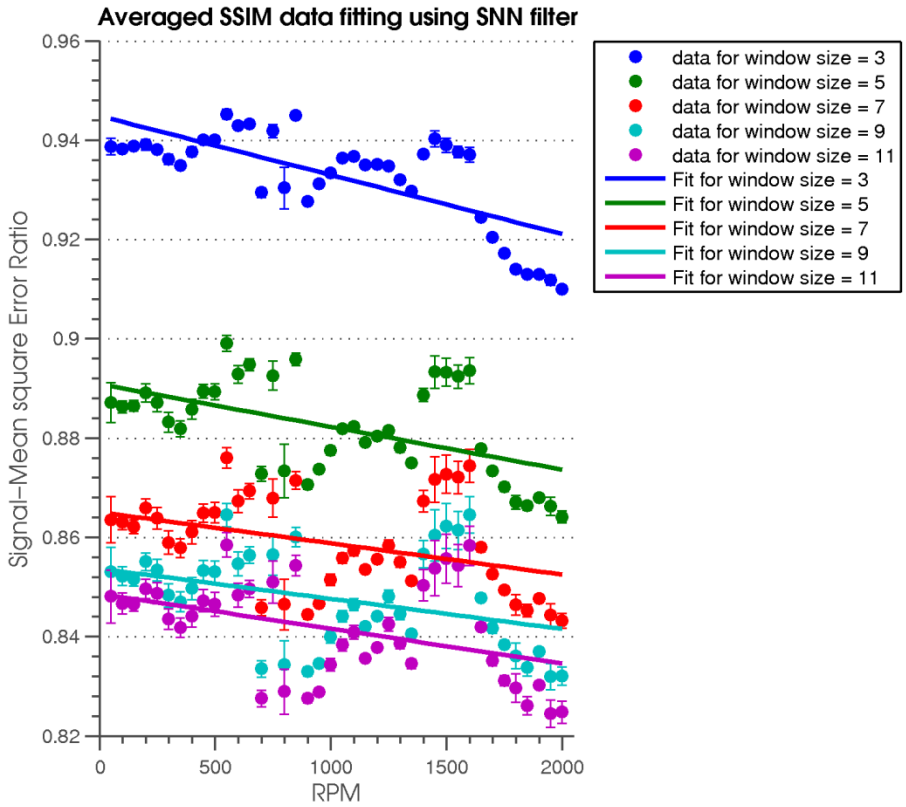
Averaged SSIM data fitting using SNN filter
Signal–Mean square Error Ratio
RPM
0.96
0.94
0.92
0.9
0.88
0.86
0.84
0.82
0
500
1000
1500
2000
data for window size = 3
data for window size = 5
data for window size = 7
data for window size = 9
data for window size = 11
Fit for window size = 3
Fit for window size = 5
Fit for window size = 7
Fit for window size = 9
Fit for window size = 11

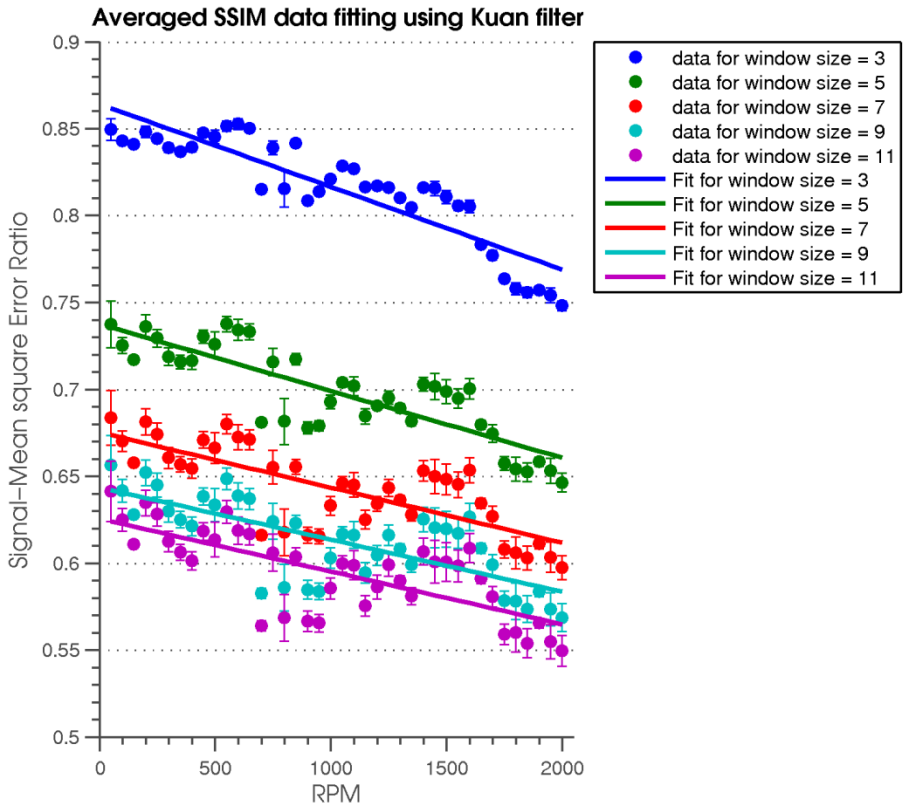
Averaged SSIM data fitting using Kuan filter
Signal–Mean square Error Ratio
RPM
0.9
0.85
0.8
0.75
0.7
0.65
0.6
0.55
0.5
0
500
1000
1500
2000
data for window size = 3
data for window size = 5
data for window size = 7
data for window size = 9
data for window size = 11
Fit for window size = 3
Fit for window size = 5
Fit for window size = 7
Fit for window size = 9
Fit for window size = 11

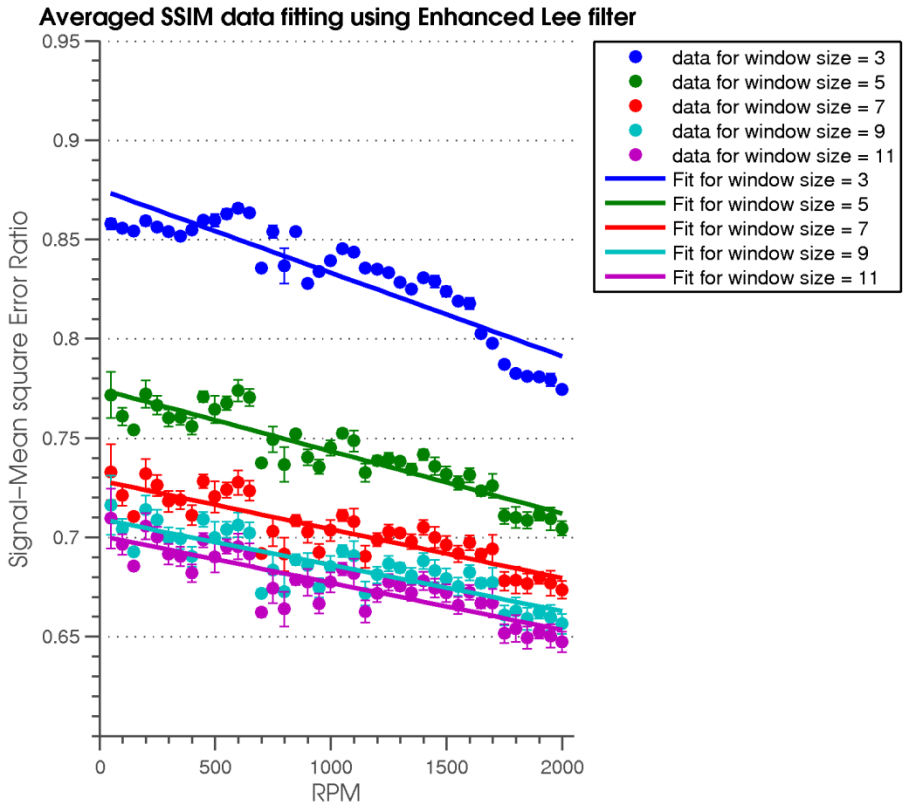
Averaged SSIM data fitting using Enhanced Lee filter
Signal–Mean square Error Ratio
RPM
0.95
0.9
0.85
0.8
0.75
0.7
0.65
0
500
1000
1500
2000
data for window size = 3
data for window size = 5
data for window size = 7
data for window size = 9
data for window size = 11
Fit for window size = 3
Fit for window size = 5
Fit for window size = 7
Fit for window size = 9
Fit for window size = 11

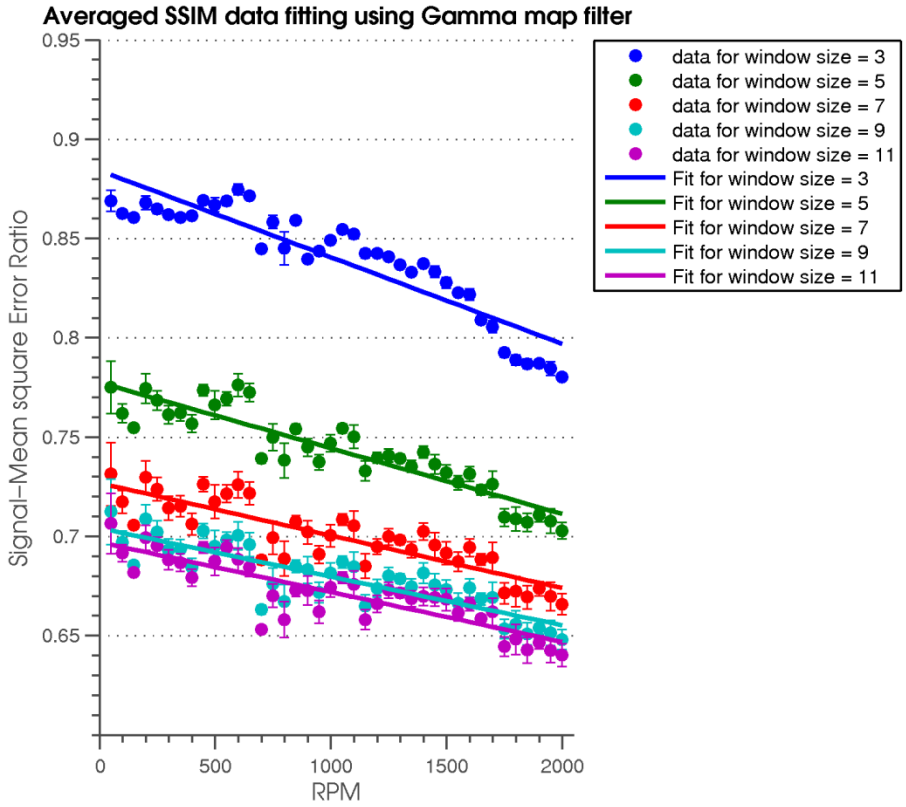

E. Signal-to-Noise Ratio (SNR) Comparison

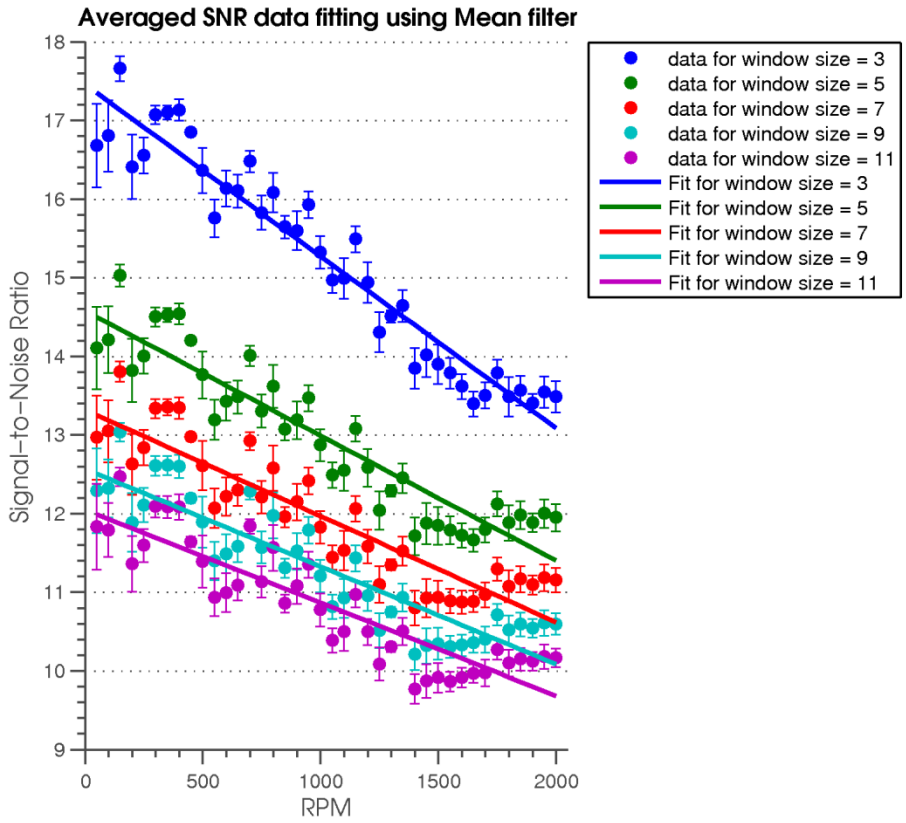

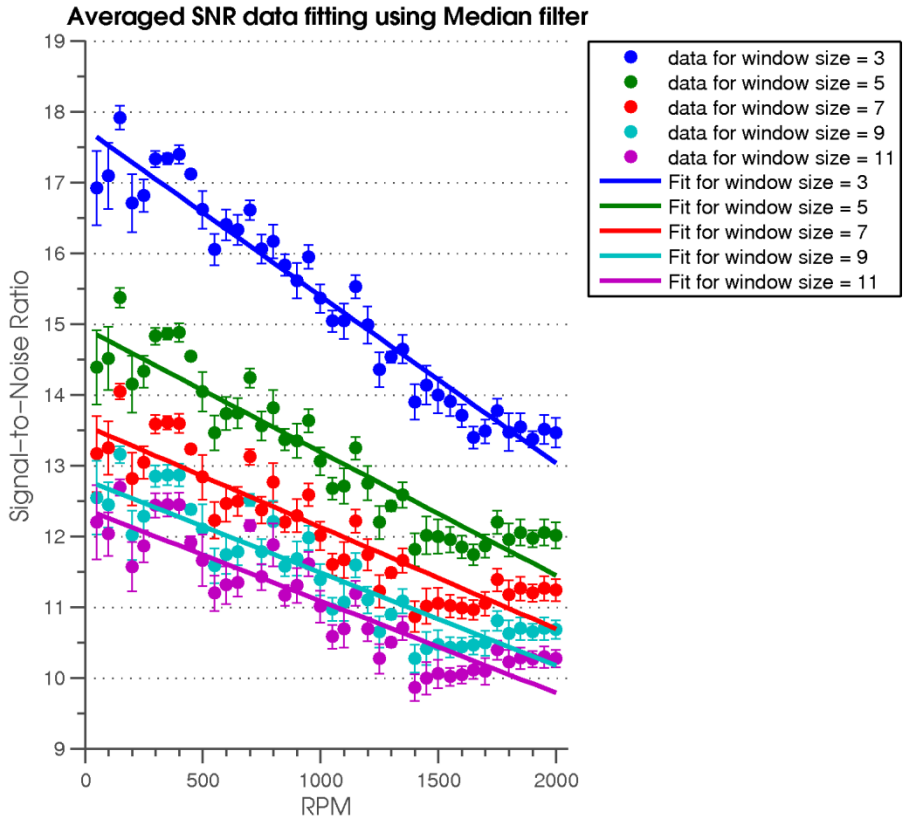
Averaged SNR data fitting using Median filter
Signal-to-Noise Ratio
RPM
data for window size = 3
data for window size = 5
data for window size = 7
data for window size = 9
data for window size = 11
Fit for window size = 3
Fit for window size = 5
Fit for window size = 7
Fit for window size = 9
Fit for window size = 11

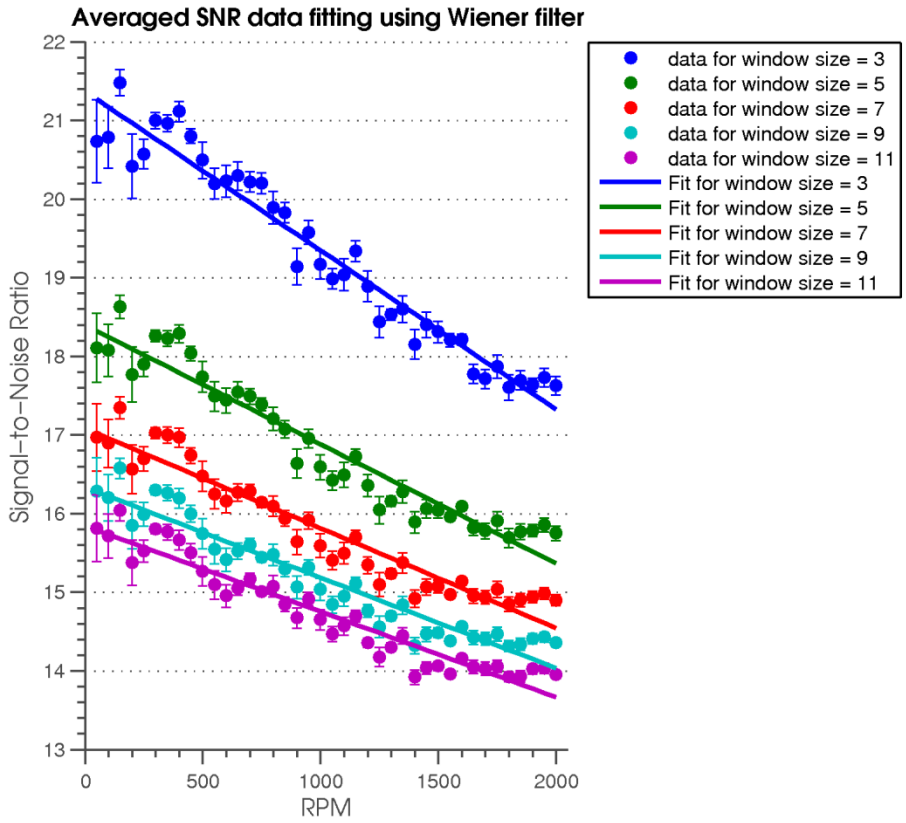
Averaged SNR data fitting using Wiener filter
Signal-to-Noise Ratio
RPM
data for window size = 3
data for window size = 5
data for window size = 7
data for window size = 9
data for window size = 11
Fit for window size = 3
Fit for window size = 5
Fit for window size = 7
Fit for window size = 9
Fit for window size = 11

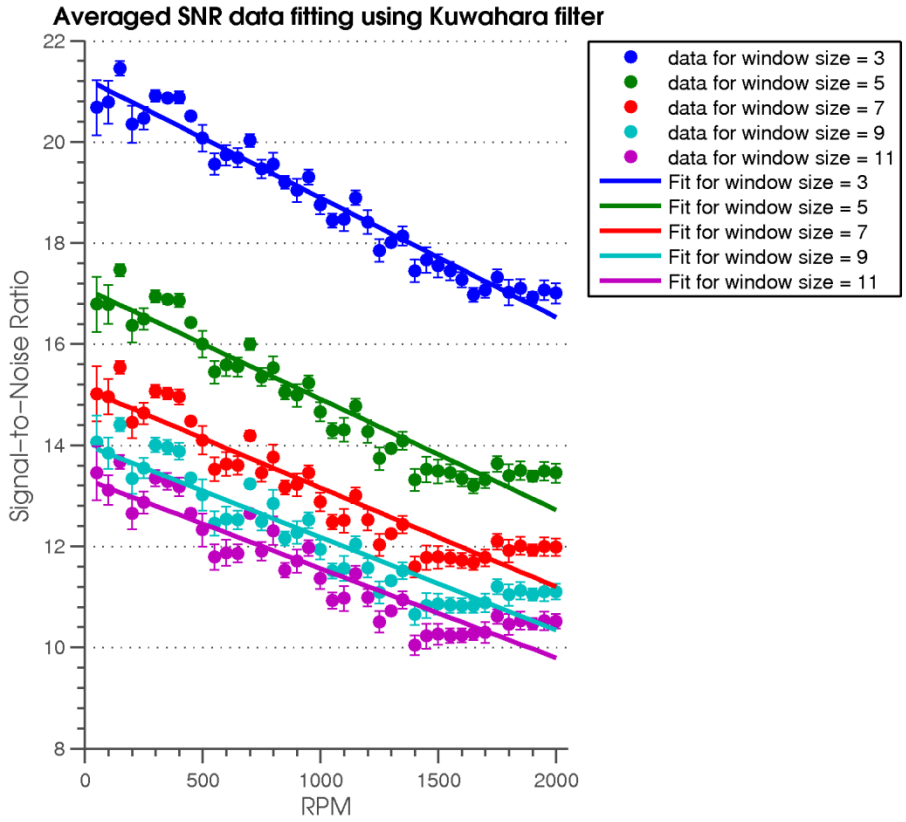
Averaged SNR data fitting using Kuwahara filter
Signal-to-Noise Ratio
RPM
22
20
18
16
14
12
10
8
0
500
1000
1500
2000
data for window size = 3
data for window size = 5
data for window size = 7
data for window size = 9
data for window size = 11
Fit for window size = 3
Fit for window size = 5
Fit for window size = 7
Fit for window size = 9
Fit for window size = 11

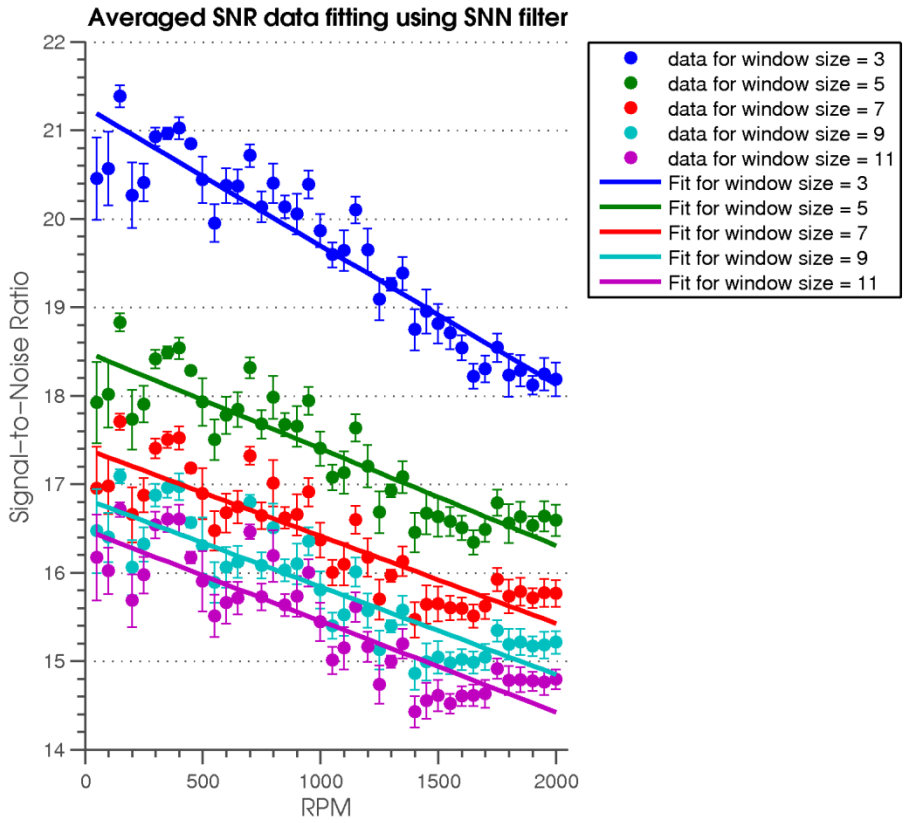
Averaged SNR data fitting using SNN filter
Signal-to-Noise Ratio
RPM
22
21
20
19
18
17
16
15
14
0
500
1000
1500
2000
data for window size = 3
data for window size = 5
data for window size = 7
data for window size = 9
data for window size = 11
Fit for window size = 3
Fit for window size = 5
Fit for window size = 7
Fit for window size = 9
Fit for window size = 11

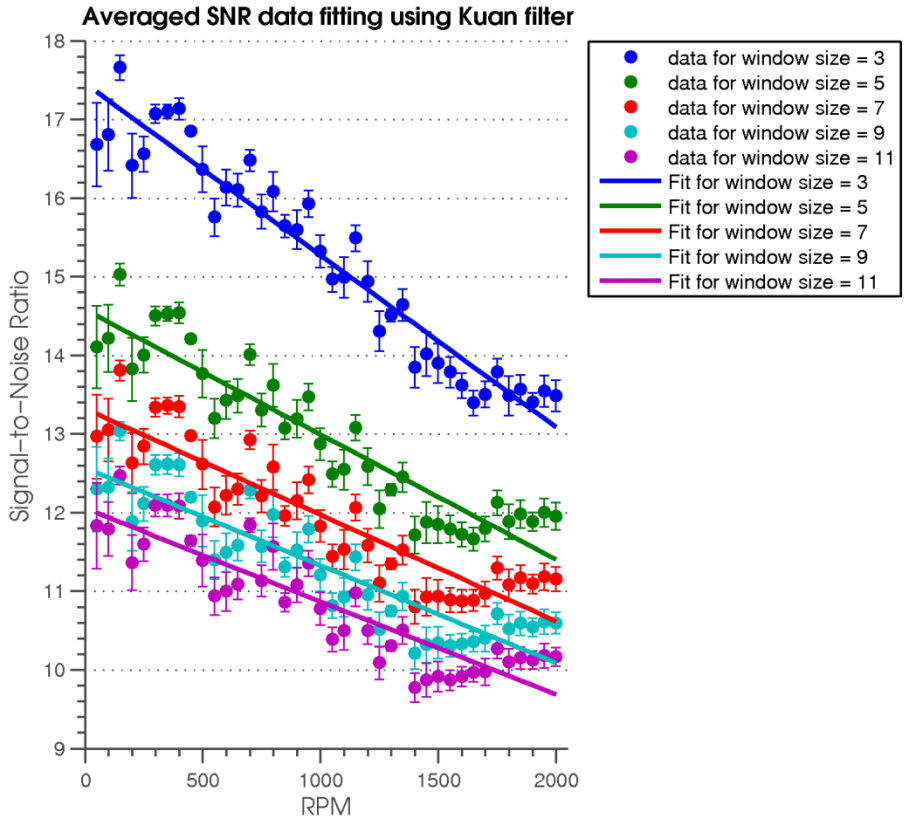
Averaged SNR data fitting using Kuan filter
Signal-to-Noise Ratio
RPM
data for window size = 3
data for window size = 5
data for window size = 7
data for window size = 9
data for window size = 11
Fit for window size = 3
Fit for window size = 5
Fit for window size = 7
Fit for window size = 9
Fit for window size = 11

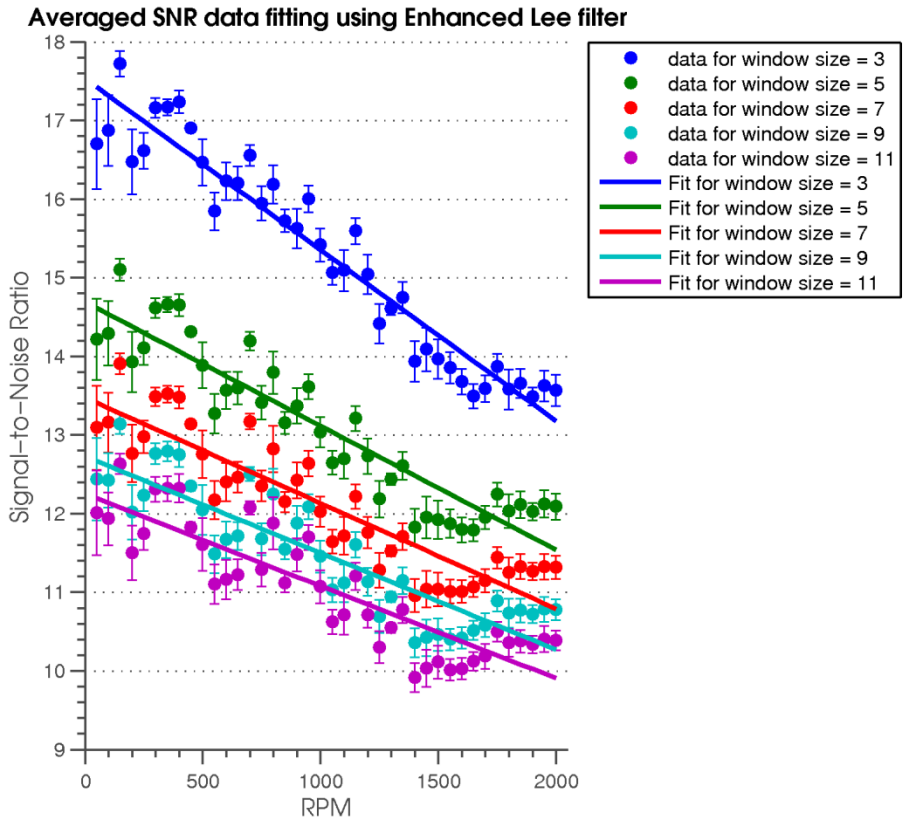
Averaged SNR data fitting using Enhanced Lee filter
Signal-to-Noise Ratio
RPM
data for window size = 3
data for window size = 5
data for window size = 7
data for window size = 9
data for window size = 11
Fit for window size = 3
Fit for window size = 5
Fit for window size = 7
Fit for window size = 9
Fit for window size = 11

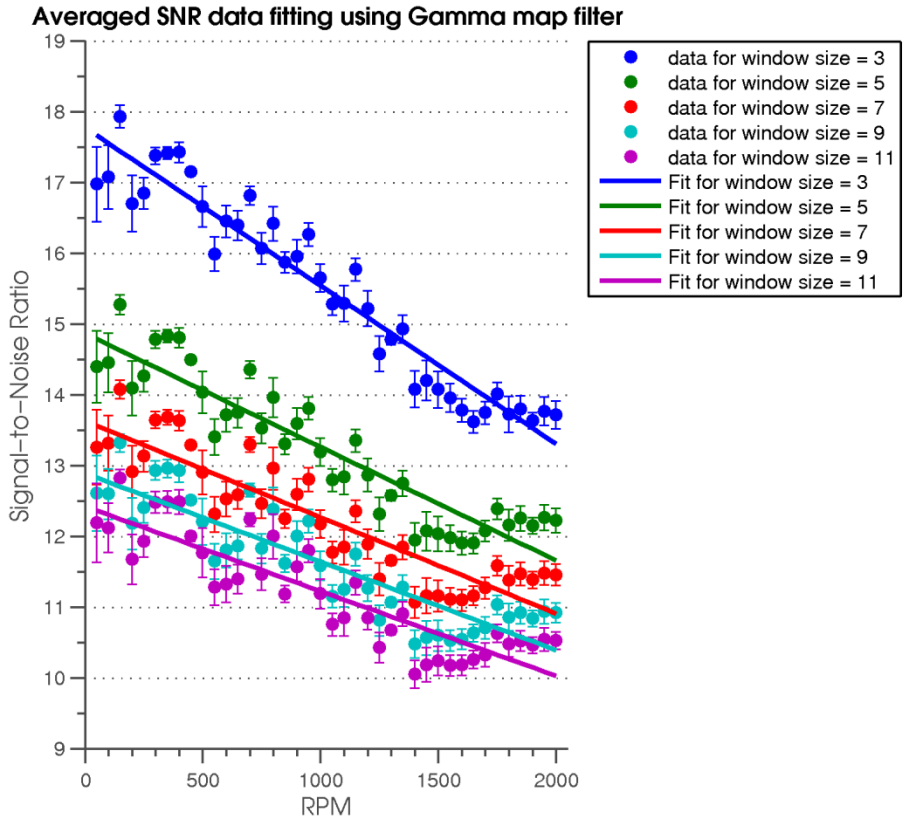

F. Peak Signal-to-Noise Ratio (PSNR) Comparison

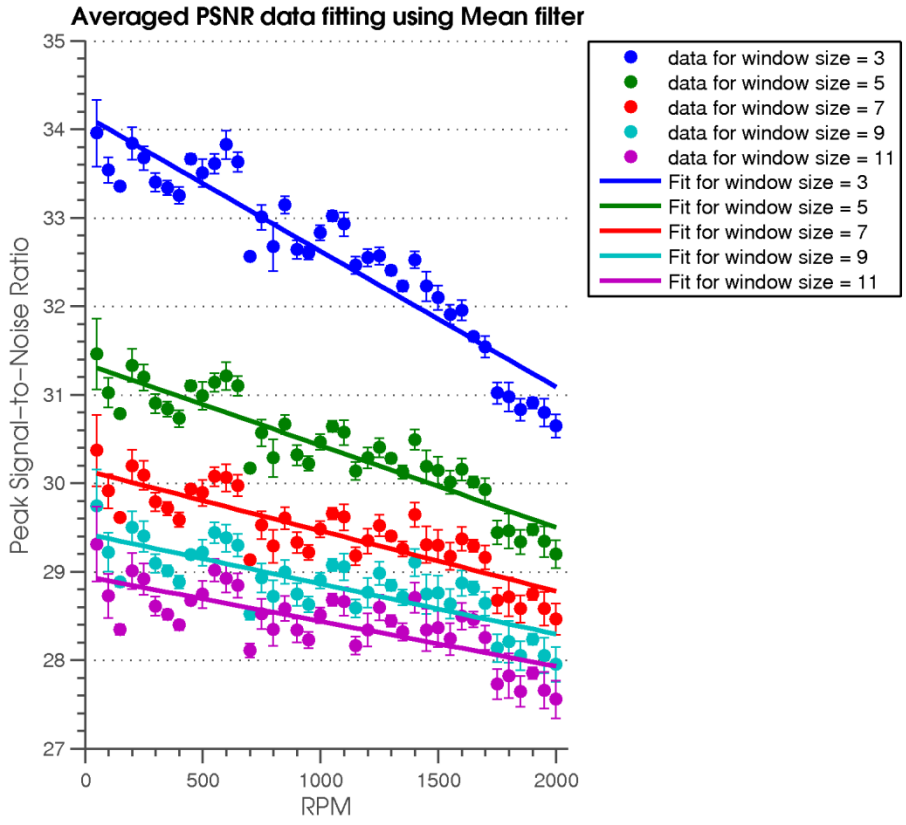

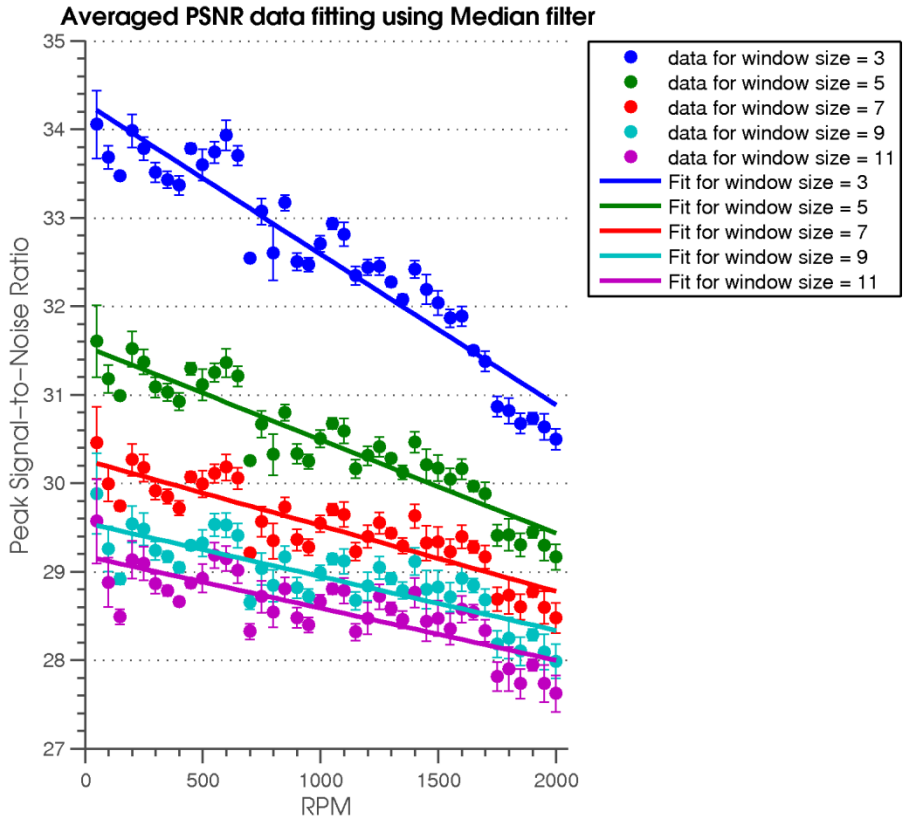
Averaged PSNR data fitting using Median filter
Peak Signal-to-Noise Ratio
RPM
35
34
33
32
31
30
29
28
27
0
500
1000
1500
2000
data for window size = 3
data for window size = 5
data for window size = 7
data for window size = 9
data for window size = 11
Fit for window size = 3
Fit for window size = 5
Fit for window size = 7
Fit for window size = 9
Fit for window size = 11

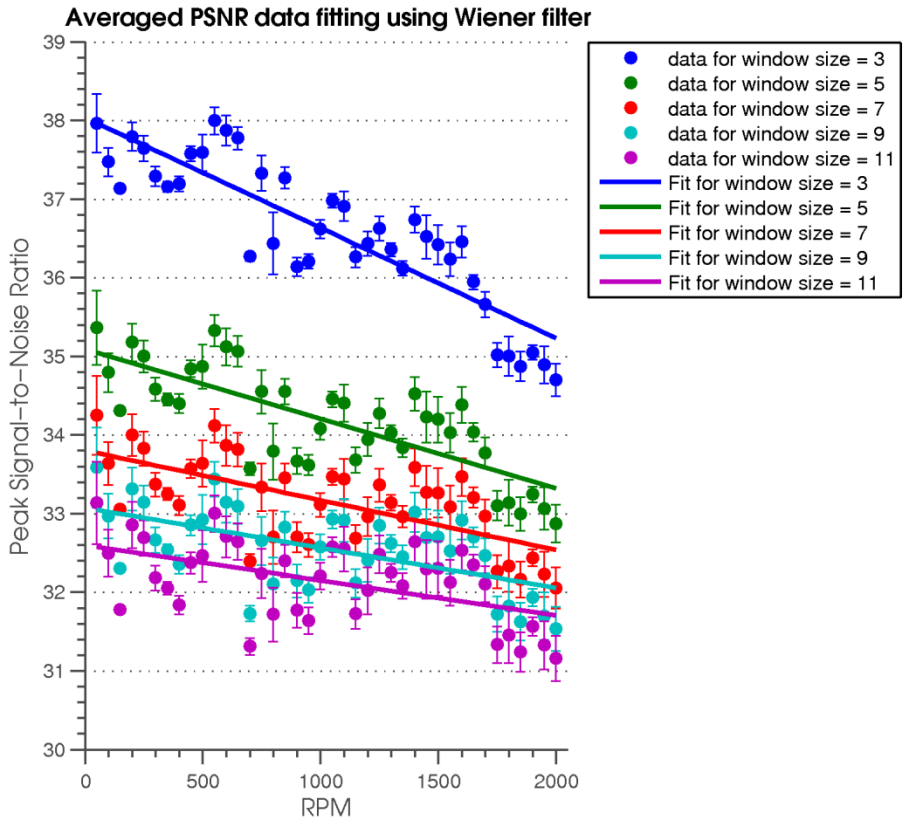
Averaged PSNR data fitting using Wiener filter
Peak Signal-to-Noise Ratio
RPM
39
38
37
36
35
34
33
32
31
30
0
500
1000
1500
2000
data for window size = 3
data for window size = 5
data for window size = 7
data for window size = 9
data for window size = 11
Fit for window size = 3
Fit for window size = 5
Fit for window size = 7
Fit for window size = 9
Fit for window size = 11

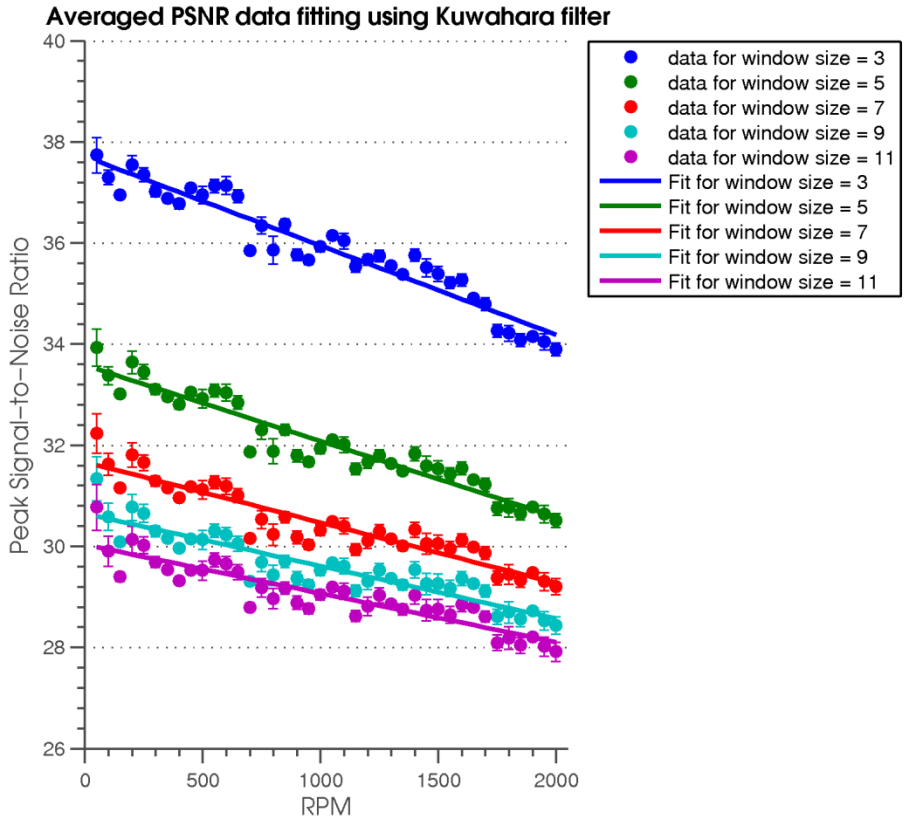
Averaged PSNR data fitting using Kuwahara filter
Peak Signal-to-Noise Ratio
RPM
40
38
36
34
32
30
28
26
0
500
1000
1500
2000
data for window size = 3
data for window size = 5
data for window size = 7
data for window size = 9
data for window size = 11
Fit for window size = 3
Fit for window size = 5
Fit for window size = 7
Fit for window size = 9
Fit for window size = 11

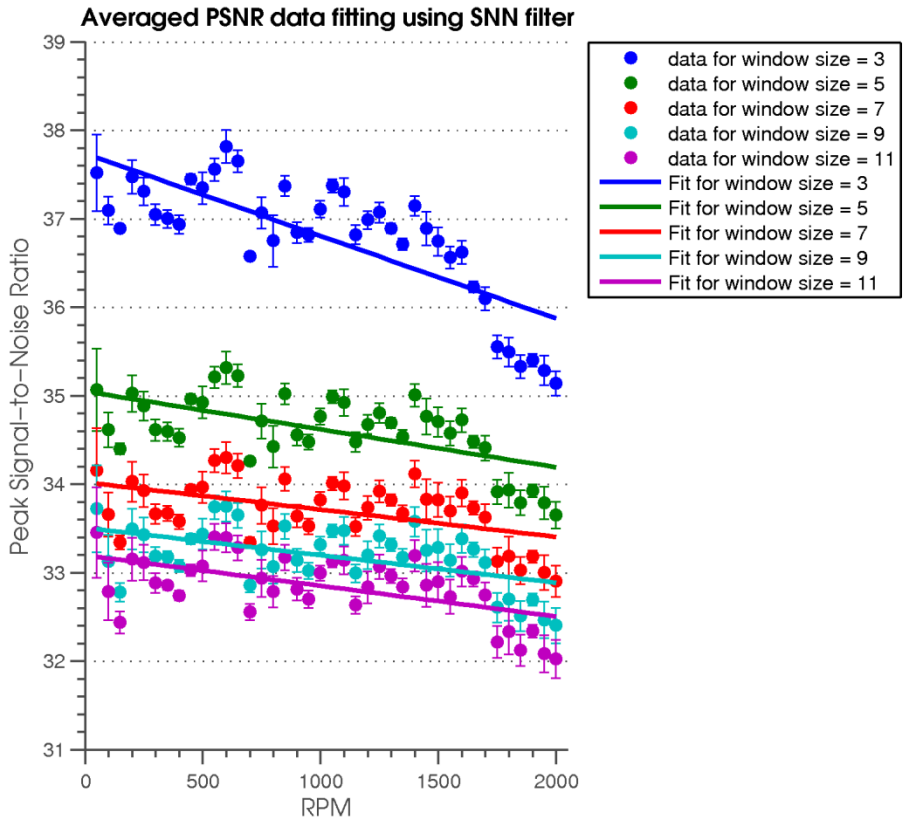
Averaged PSNR data fitting using SNN filter
Peak Signal-to-Noise Ratio
RPM
39
38
37
36
35
34
33
32
31
0
500
1000
1500
2000
data for window size = 3
data for window size = 5
data for window size = 7
data for window size = 9
data for window size = 11
Fit for window size = 3
Fit for window size = 5
Fit for window size = 7
Fit for window size = 9
Fit for window size = 11

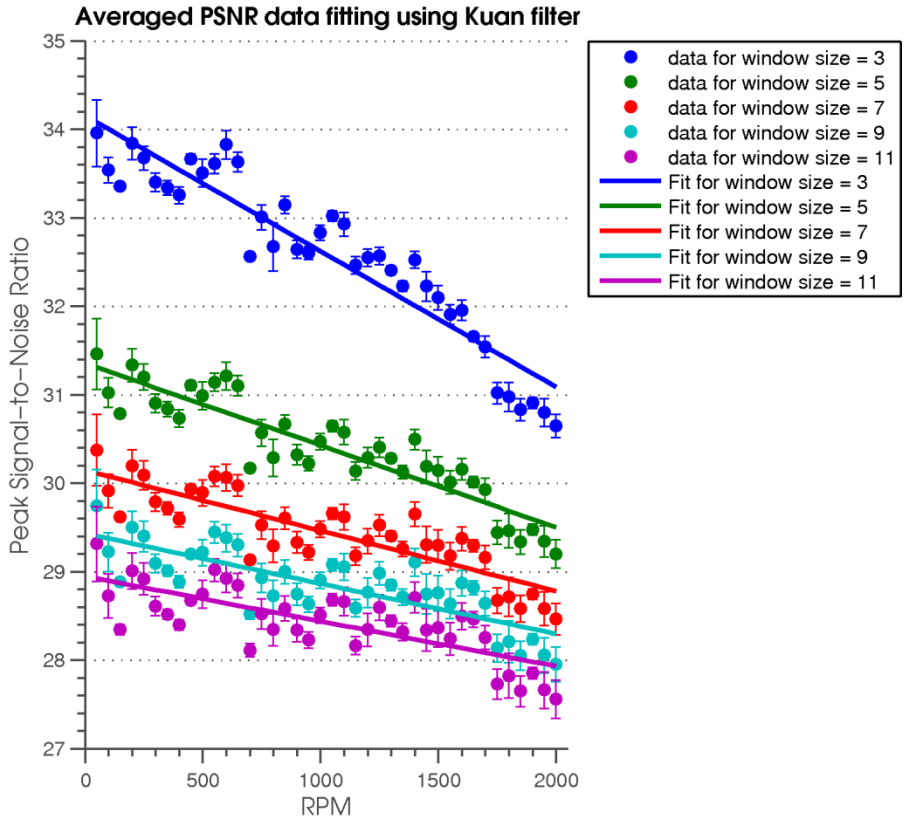
Averaged PSNR data fitting using Kuan filter
Peak Signal-to-Noise Ratio
RPM
35
34
33
32
31
30
29
28
27
0
500
1000
1500
2000
data for window size = 3
data for window size = 5
data for window size = 7
data for window size = 9
data for window size = 11
Fit for window size = 3
Fit for window size = 5
Fit for window size = 7
Fit for window size = 9
Fit for window size = 11

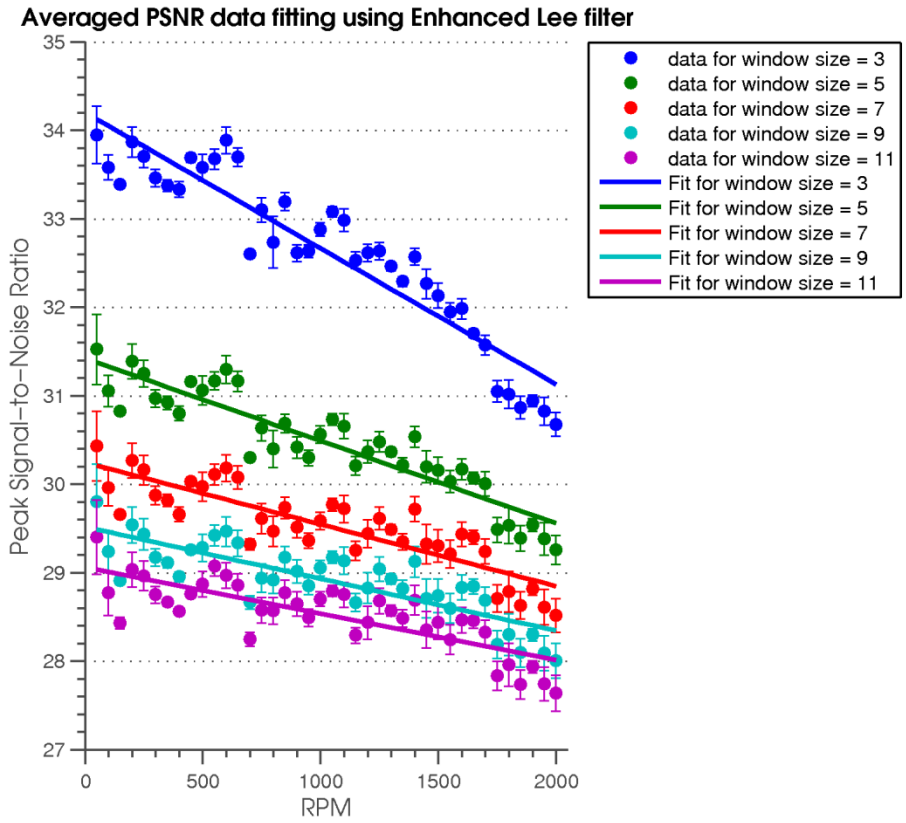
Averaged PSNR data fitting using Enhanced Lee filter
Peak Signal-to-Noise Ratio
RPM
35
34
33
32
31
30
29
28
27
0
500
1000
1500
2000
data for window size = 3
data for window size = 5
data for window size = 7
data for window size = 9
data for window size = 11
Fit for window size = 3
Fit for window size = 5
Fit for window size = 7
Fit for window size = 9
Fit for window size = 11

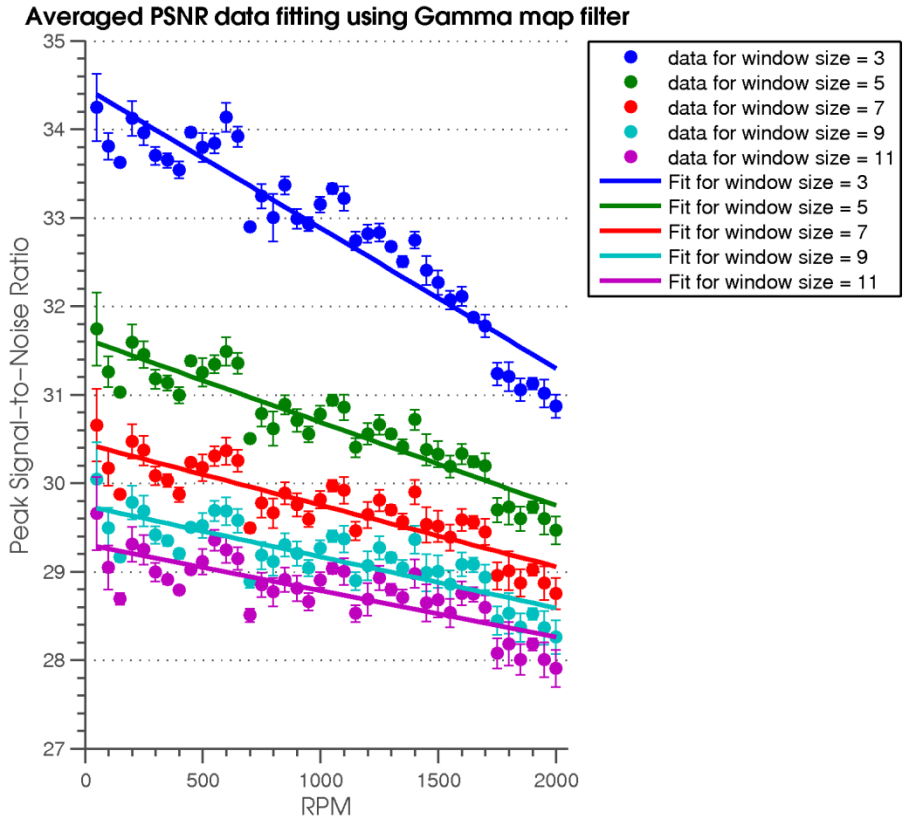

G. Signal-to-Mean Square Error (S/MSE) Comparison

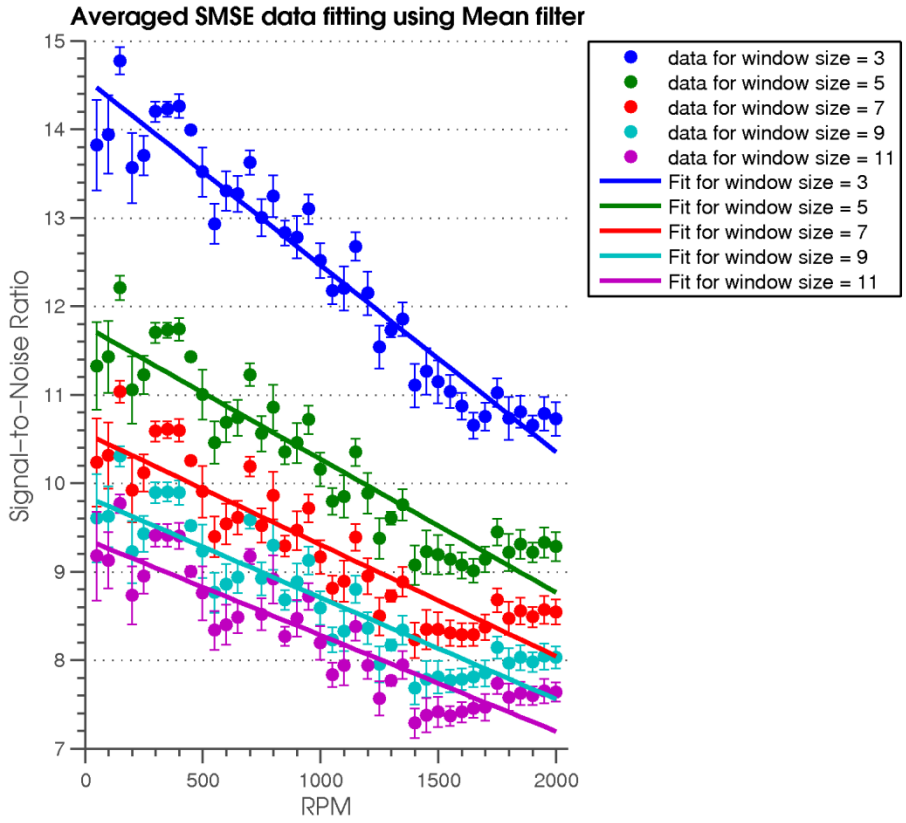

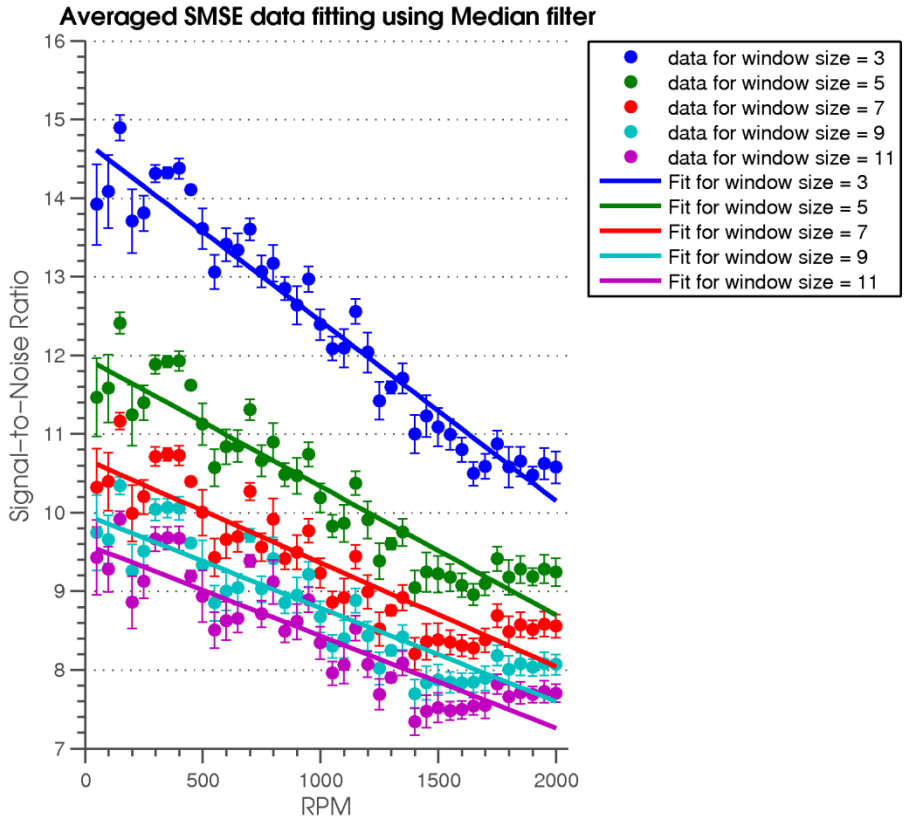
Averaged SMSE data fitting using Median filter
Signal-to-Noise Ratio
RPM
16
15
14
13
12
11
10
9
8
7
0
500
1000
1500
2000
data for window size = 3
data for window size = 5
data for window size = 7
data for window size = 9
data for window size = 11
Fit for window size = 3
Fit for window size = 5
Fit for window size = 7
Fit for window size = 9
Fit for window size = 11

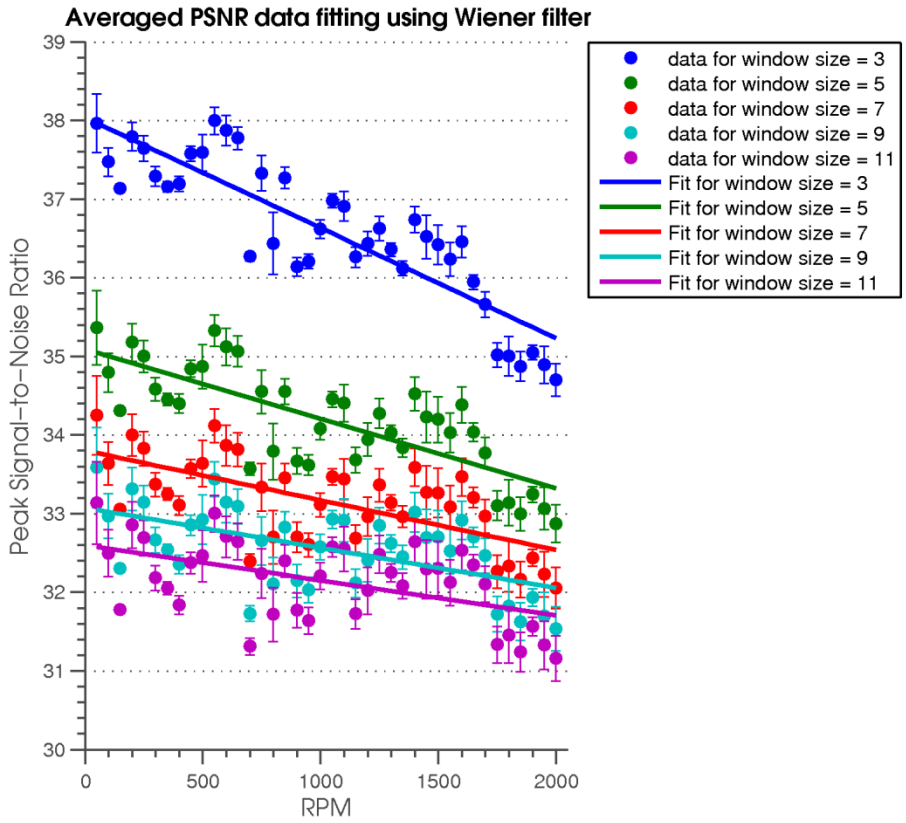
Averaged PSNR data fitting using Wiener filter
Peak Signal-to-Noise Ratio
RPM
39
38
37
36
35
34
33
32
31
30
0
500
1000
1500
2000
data for window size = 3
data for window size = 5
data for window size = 7
data for window size = 9
data for window size = 11
Fit for window size = 3
Fit for window size = 5
Fit for window size = 7
Fit for window size = 9
Fit for window size = 11

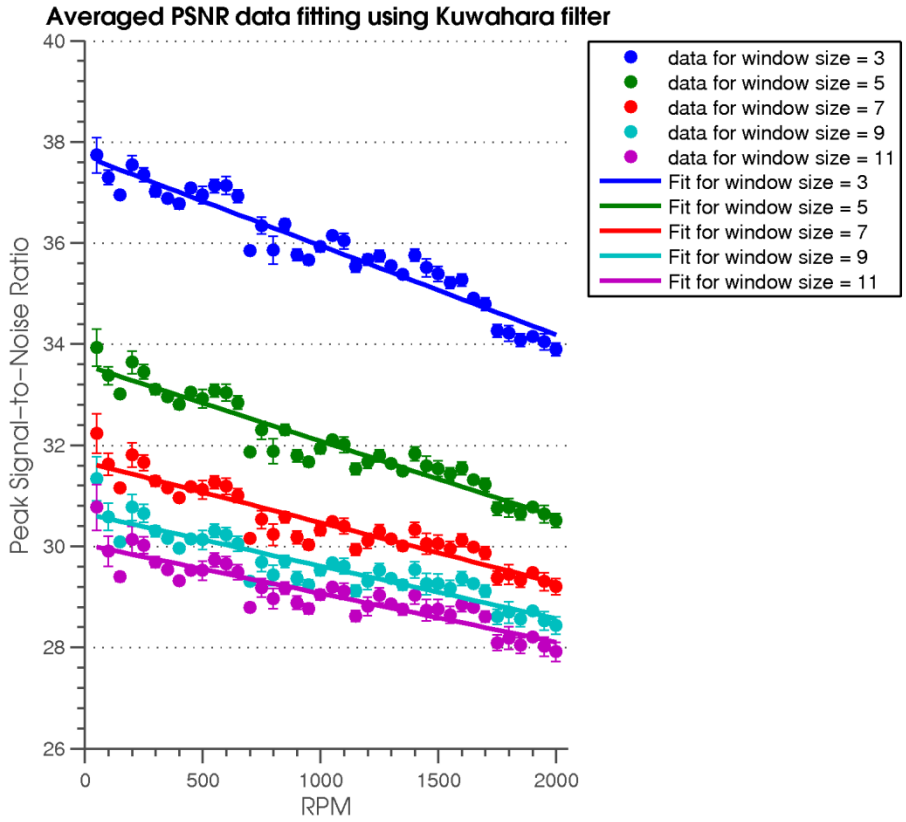
Averaged PSNR data fitting using Kuwahara filter
Peak Signal-to-Noise Ratio
RPM
40
38
36
34
32
30
28
26
0
500
1000
1500
2000
data for window size = 3
data for window size = 5
data for window size = 7
data for window size = 9
data for window size = 11
Fit for window size = 3
Fit for window size = 5
Fit for window size = 7
Fit for window size = 9
Fit for window size = 11

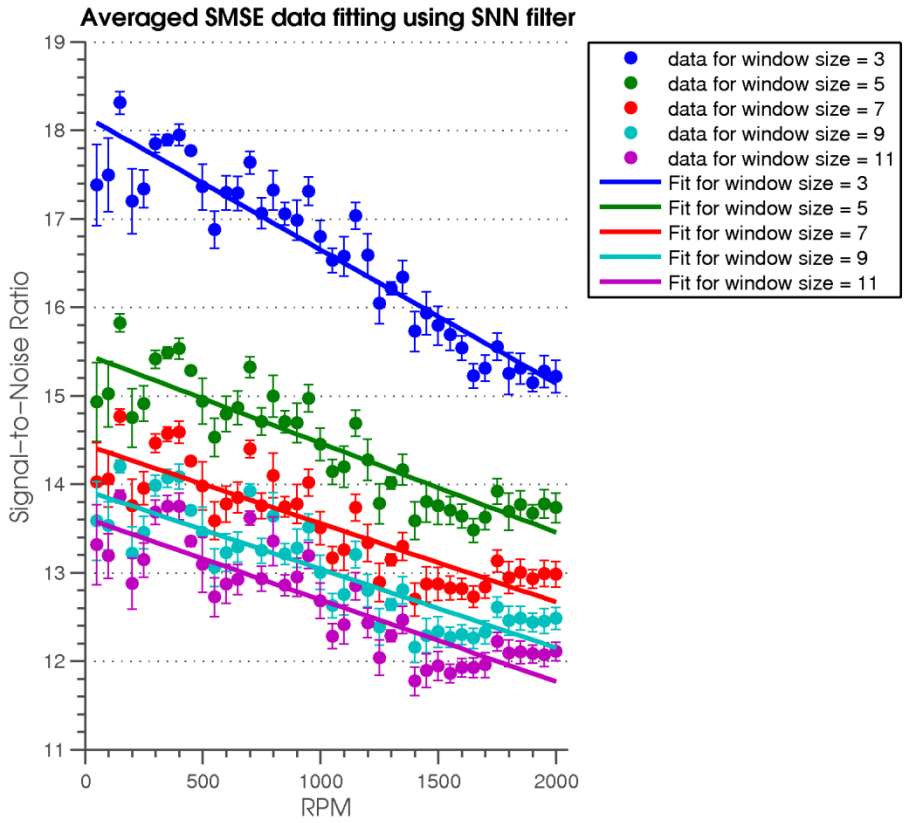
Averaged SMSE data fitting using SNN filter
Signal-to-Noise Ratio
RPM
19
18
17
16
15
14
13
12
11
0
500
1000
1500
2000
data for window size = 3
data for window size = 5
data for window size = 7
data for window size = 9
data for window size = 11
Fit for window size = 3
Fit for window size = 5
Fit for window size = 7
Fit for window size = 9
Fit for window size = 11

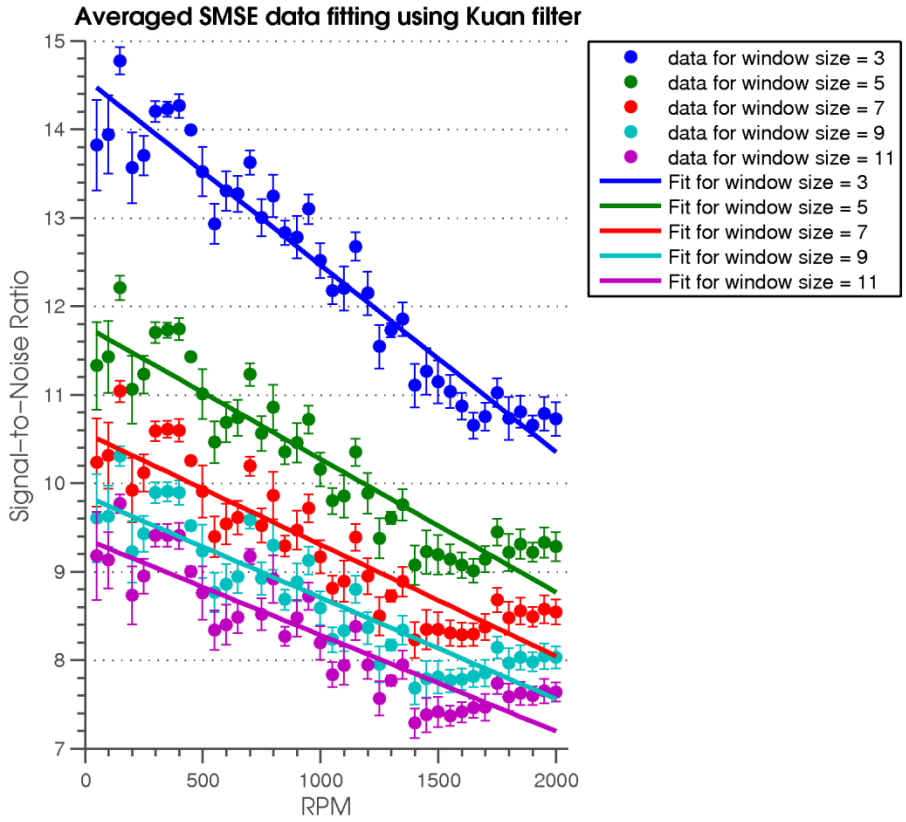
Averaged SMSE data fitting using Kuan filter
Signal-to-Noise Ratio
RPM
15
14
13
12
11
10
9
8
7
0
500
1000
1500
2000
data for window size = 3
data for window size = 5
data for window size = 7
data for window size = 9
data for window size = 11
Fit for window size = 3
Fit for window size = 5
Fit for window size = 7
Fit for window size = 9
Fit for window size = 11

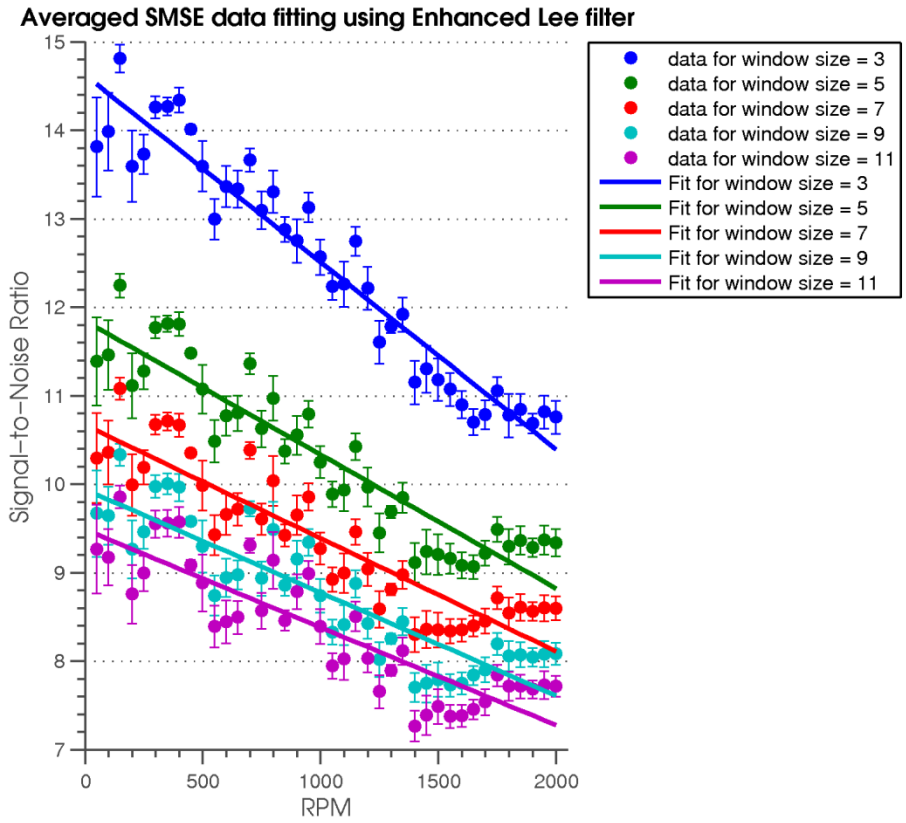
Averaged SMSE data fitting using Enhanced Lee filter
Signal-to-Noise Ratio
RPM
15
14
13
12
11
10
9
8
7
0
500
1000
1500
2000
data for window size = 3
data for window size = 5
data for window size = 7
data for window size = 9
data for window size = 11
Fit for window size = 3
Fit for window size = 5
Fit for window size = 7
Fit for window size = 9
Fit for window size = 11

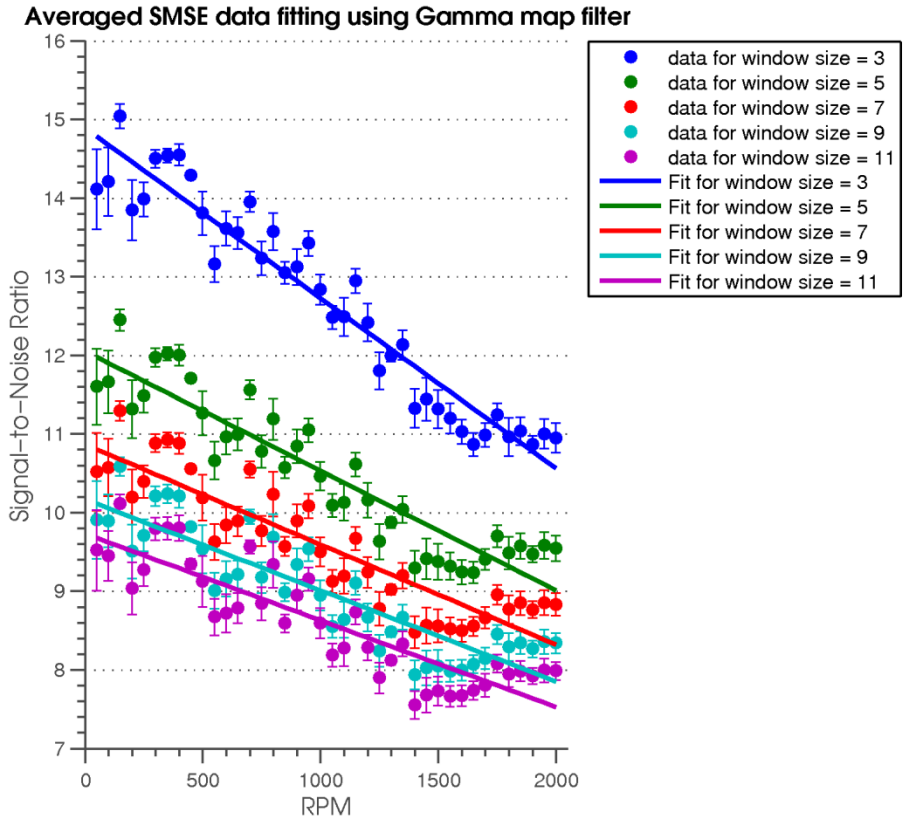

H. Root Mean Square Error (RMSE) Comparison

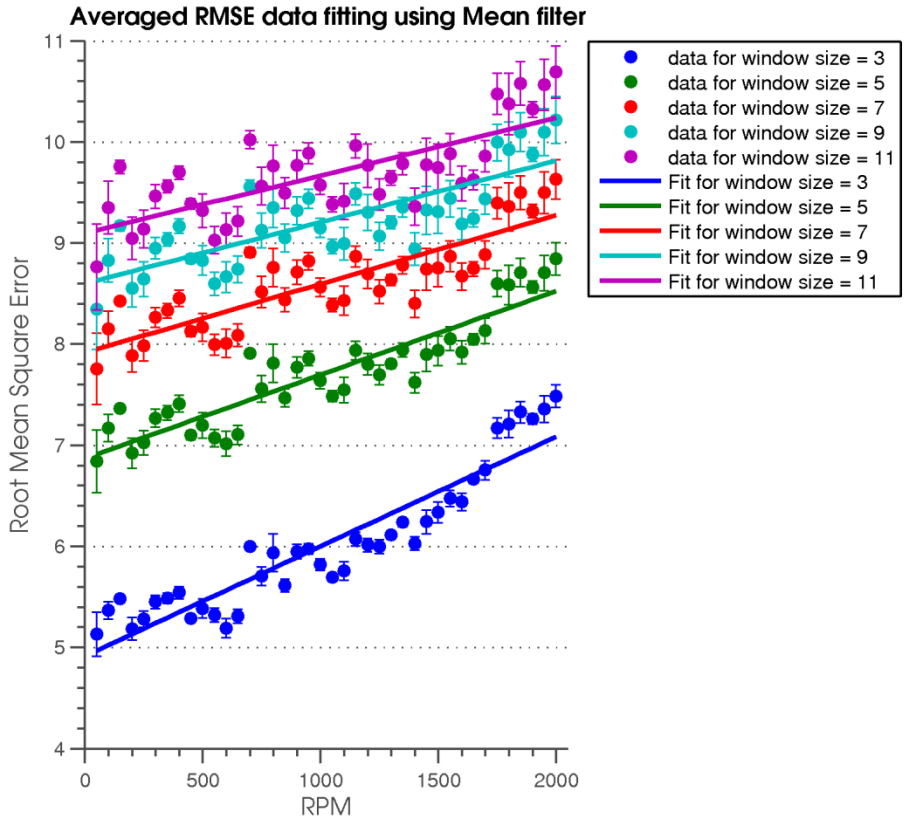

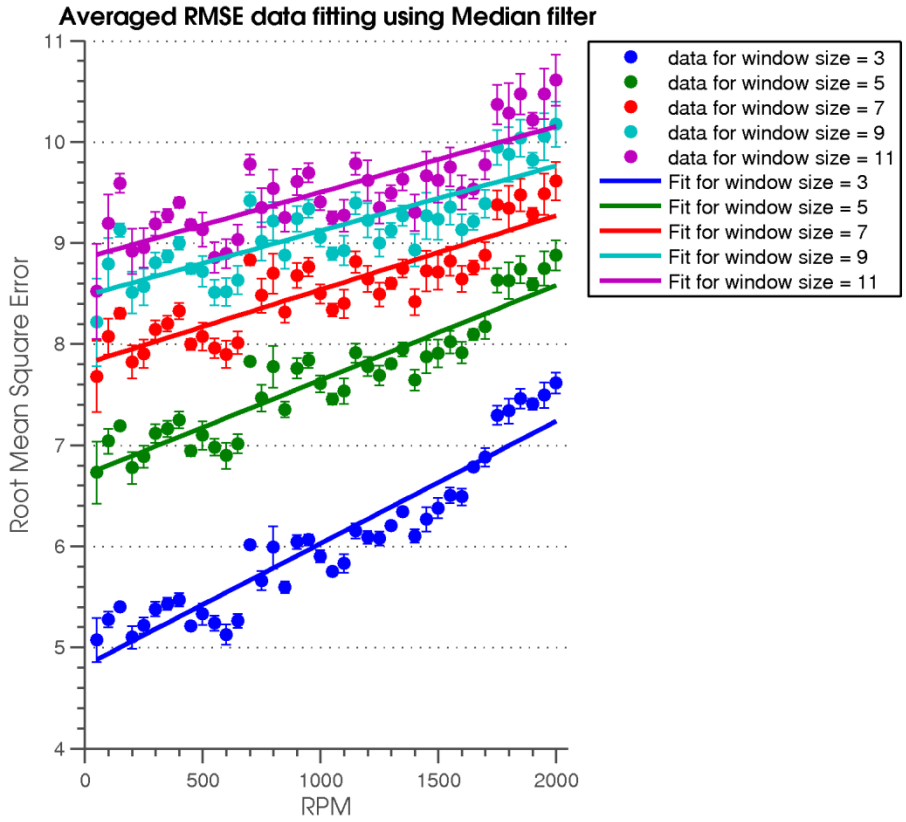
Averaged RMSE data fitting using Median filter
Root Mean Square Error
RPM
data for window size = 3
data for window size = 5
data for window size = 7
data for window size = 9
data for window size = 11
Fit for window size = 3
Fit for window size = 5
Fit for window size = 7
Fit for window size = 9
Fit for window size = 11

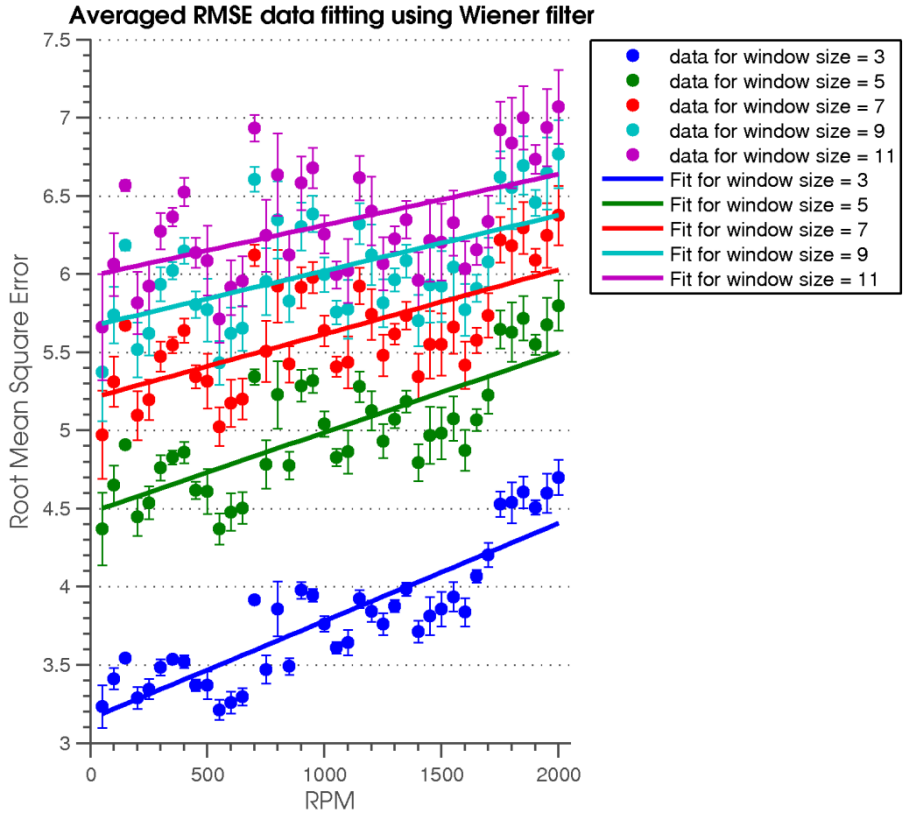
Averaged RMSE data fitting using Wiener filter
Root Mean Square Error
RPM
data for window size = 3
data for window size = 5
data for window size = 7
data for window size = 9
data for window size = 11
Fit for window size = 3
Fit for window size = 5
Fit for window size = 7
Fit for window size = 9
Fit for window size = 11

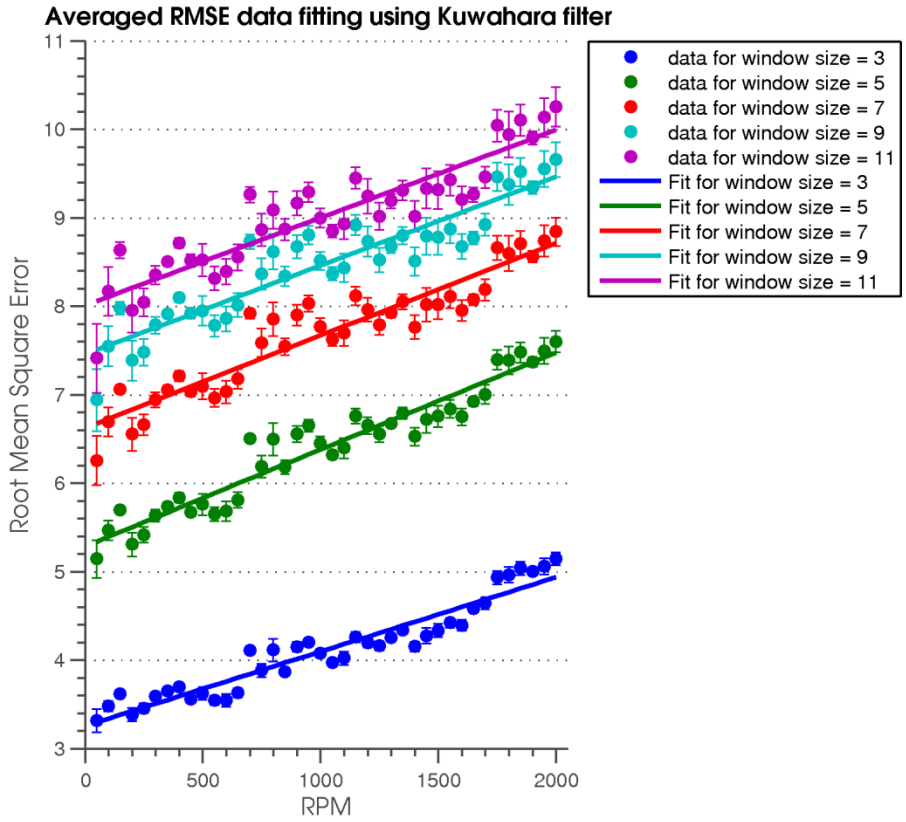
Averaged RMSE data fitting using Kuwahara filter
Root Mean Square Error
RPM
data for window size = 3
data for window size = 5
data for window size = 7
data for window size = 9
data for window size = 11
Fit for window size = 3
Fit for window size = 5
Fit for window size = 7
Fit for window size = 9
Fit for window size = 11

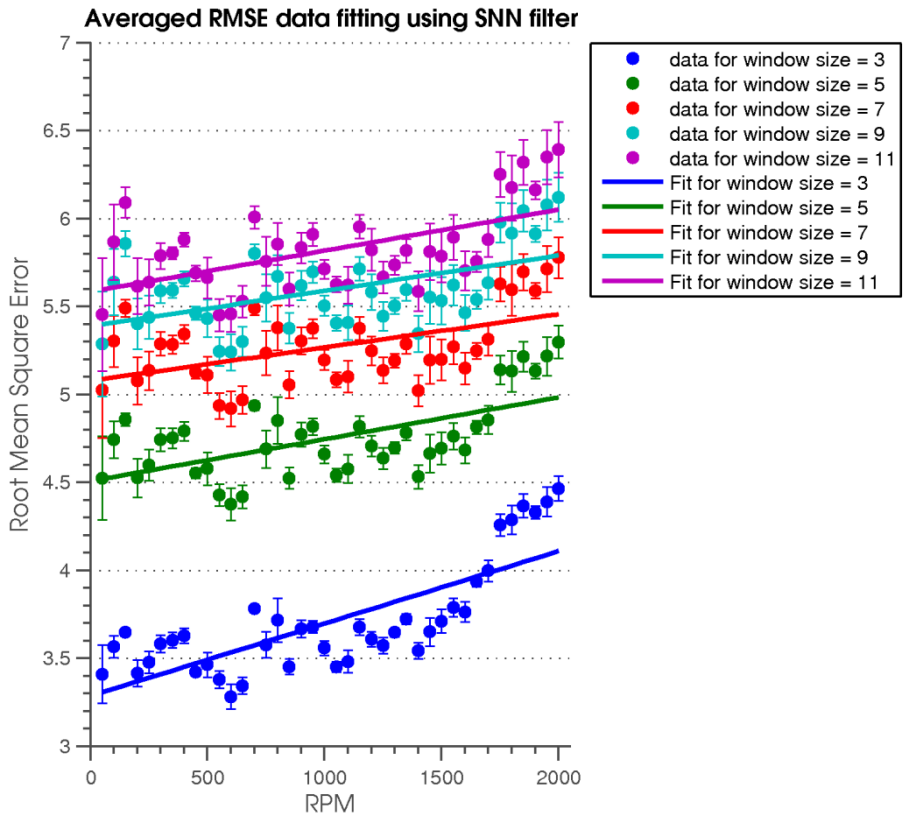
Averaged RMSE data fitting using SNN filter
Root Mean Square Error
RPM
data for window size = 3
data for window size = 5
data for window size = 7
data for window size = 9
data for window size = 11
Fit for window size = 3
Fit for window size = 5
Fit for window size = 7
Fit for window size = 9
Fit for window size = 11

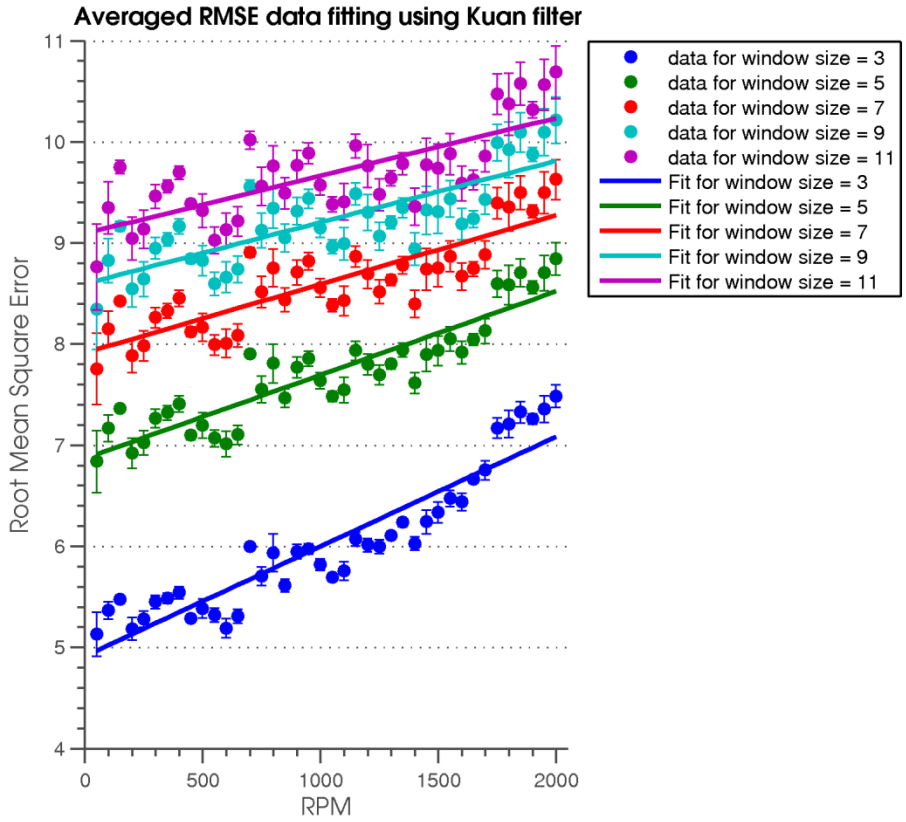
Averaged RMSE data fitting using Kuan filter
Root Mean Square Error
RPM
data for window size = 3
data for window size = 5
data for window size = 7
data for window size = 9
data for window size = 11
Fit for window size = 3
Fit for window size = 5
Fit for window size = 7
Fit for window size = 9
Fit for window size = 11

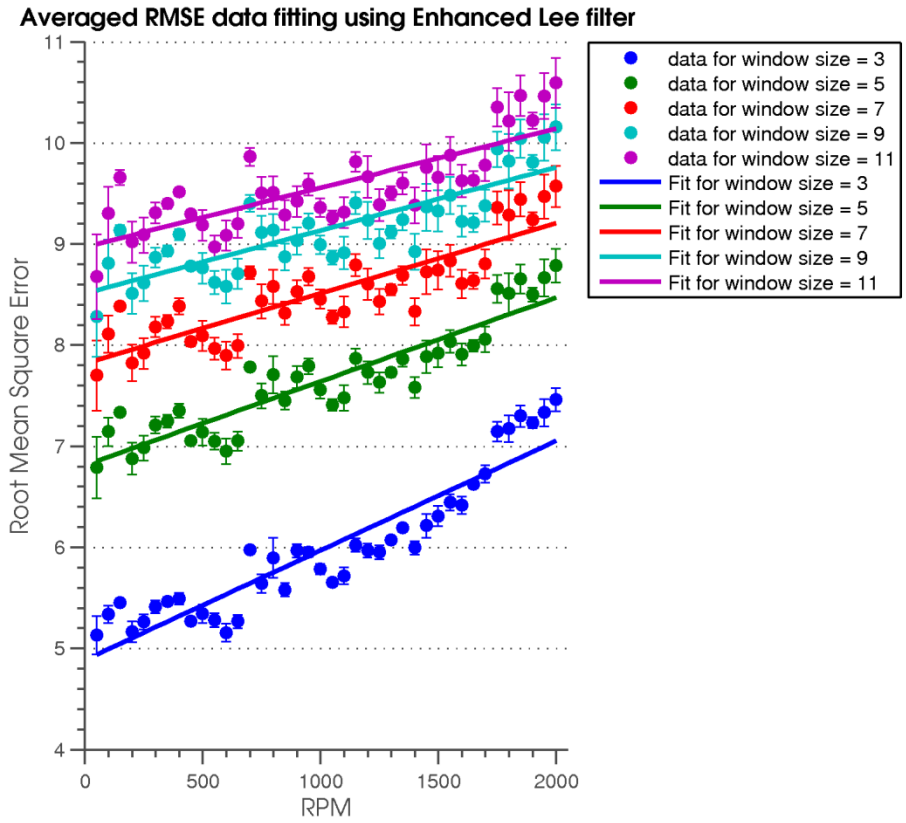
Averaged RMSE data fitting using Enhanced Lee filter
Root Mean Square Error
RPM
data for window size = 3
data for window size = 5
data for window size = 7
data for window size = 9
data for window size = 11
Fit for window size = 3
Fit for window size = 5
Fit for window size = 7
Fit for window size = 9
Fit for window size = 11

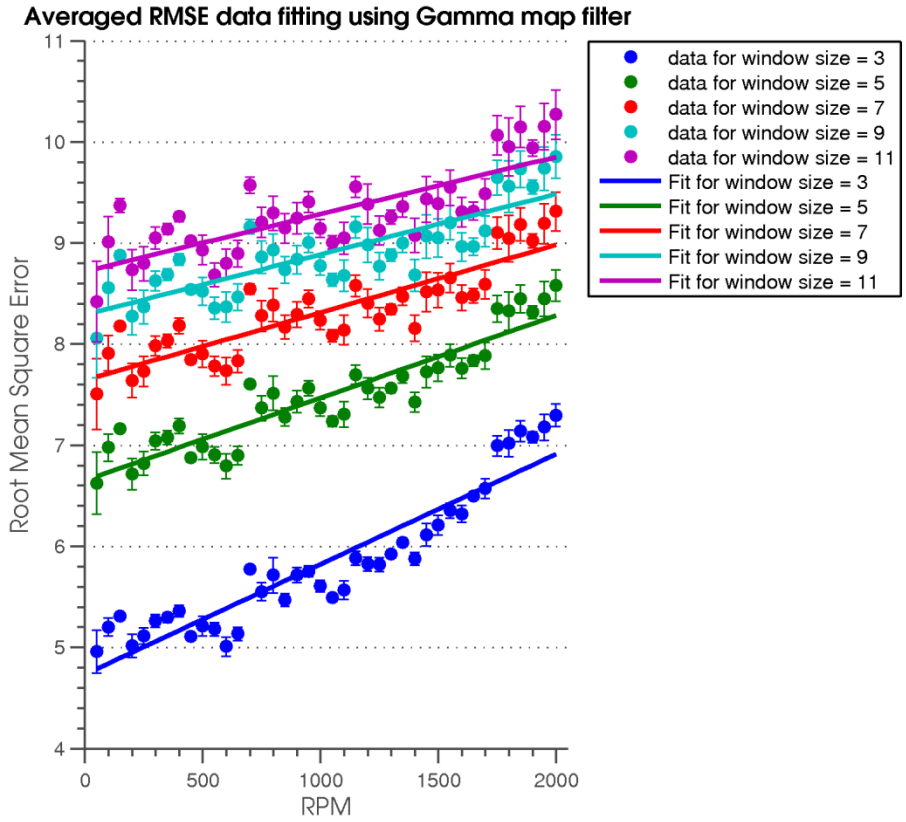
Averaged RMSE data fitting using Gamma map filter
Root Mean Square Error
RPM
11
10
9
8
7
6
5
4
0
500
1000
1500
2000
data for window size = 3
data for window size = 5
data for window size = 7
data for window size = 9
data for window size = 11
Fit for window size = 3
Fit for window size = 5
Fit for window size = 7
Fit for window size = 9
Fit for window size = 11

Appendix C

Result of Image Quality Assessment

Metrics			Mean filter					Median filter					Adaptive Wiener Filter					Kuwahara filter				
Weights			3	5	7	9	11	3	5	7	9	11	3	5	7	9	11	3	5	7	9	11
ENL	2	Original	400	900	1300	1800	2500	400	800	1600	1950	3000	300	700	1100	1150	1900	250	550	900	1350	1900
		Normalized	0.055	0.236	0.382	0.564	0.818	0.055	0.2	0.491	0.618	1	0.018	0.164	0.309	0.327	0.6	0	0.109	0.236	0.4	0.6
		Weighted	0.109	0.473	0.764	1.127	1.636	0.109	0.4	0.982	1.236	2	0.036	0.327	0.618	0.655	1.2	0	0.218	0.473	0.8	1.2
CNR	2	Original	10.4	12	13.8	14.5	15.6	12.7	14.8	16.1	16.8	17.6	9.5	10.8	12	13.1	13.8	10.2	12	13.2	14	14.8
		Normalized	0.111	0.309	0.531	0.617	0.753	0.395	0.654	0.815	0.901	1	0	0.16	0.309	0.444	0.531	0.086	0.309	0.457	0.556	0.654
		Weighted	0.222	0.617	1.062	1.235	1.506	0.79	1.309	1.63	1.802	2	0	0.321	0.617	0.889	1.062	0.173	0.617	0.914	1.111	1.309
EPF	2	Original	0.63	0.42	0.4	0.38	0.36	0.72	0.44	0.4	0.38	0.37	0.81	0.79	0.77	0.76	0.75	0.96	0.81	0.7	0.62	0.58
		Normalized	0.439	0.098	0.065	0.033	0	0.585	0.13	0.065	0.033	0.016	0.732	0.699	0.667	0.65	0.634	0.976	0.732	0.553	0.423	0.358
		Weighted	0.878	0.195	0.13	0.065	0	1.171	0.26	0.13	0.065	0.033	1.463	1.398	1.333	1.301	1.268	1.951	1.463	1.106	0.846	0.715
SSIM	2	Original	0.87	0.74	0.675	0.645	0.635	0.85	0.71	0.64	0.31	0.6	0.925	0.85	0.8	0.77	0.75	0.945	0.84	0.77	0.72	0.69
		Normalized	0.882	0.677	0.575	0.528	0.512	0.85	0.63	0.52	0	0.457	0.969	0.85	0.772	0.724	0.693	1	0.835	0.724	0.646	0.598
		Weighted	1.764	1.354	1.15	1.055	1.024	1.701	1.26	1.039	0	0.913	1.937	1.701	1.543	1.449	1.386	2	1.669	1.449	1.291	1.197
SNR	1	Original	17.4	14.6	13.4	12.6	12	17.8	15	13.6	12.8	12.5	21.4	18.4	17	16.4	16.8	21.2	17.2	15.2	14.1	13.3
		Normalized	0.574	0.277	0.149	0.064	0	0.617	0.319	0.17	0.085	0.053	1	0.681	0.532	0.468	0.511	0.979	0.553	0.34	0.223	0.138
		Weighted	0.574	0.277	0.149	0.064	0	0.617	0.319	0.17	0.085	0.053	1	0.681	0.532	0.468	0.511	0.979	0.553	0.34	0.223	0.138
PSNR	1	Original	34.2	31.4	30.2	29.5	29	34.3	31.6	30.3	29.6	29.2	38.1	35.1	33.8	33.1	32.6	37.8	33.6	31.8	30.8	30.1
		Normalized	0.571	0.264	0.132	0.055	0	0.582	0.286	0.143	0.066	0.022	1	0.67	0.527	0.451	0.396	0.967	0.505	0.308	0.198	0.121
		Weighted	0.571	0.264	0.132	0.055	0	0.582	0.286	0.143	0.066	0.022	1	0.67	0.527	0.451	0.396	0.967	0.505	0.308	0.198	0.121
S/MSE	1	Original	14.8	11.8	10.5	9.8	9.4	14.7	12	10.7	10	9.8	18.5	15.5	14.2	13.5	13	18.2	14	12.2	13.2	10.4
		Normalized	0.593	0.264	0.121	0.044	0	0.582	0.286	0.143	0.066	0.044	1	0.67	0.527	0.451	0.396	0.967	0.505	0.308	0.418	0.11
		Weighted	0.593	0.264	0.121	0.044	0	0.582	0.286	0.143	0.066	0.044	1	0.67	0.527	0.451	0.396	0.967	0.505	0.308	0.418	0.11
RMSE	1	Original	7.1	8.4	9	9.6	10.2	7.2	8.5	9.1	9.8	10.2	4.4	5.4	6.1	6.3	6.7	4.9	7.5	8.6	9.5	10
		Normalized	0.475	0.689	0.787	0.885	0.984	0.492	0.705	0.803	0.918	0.984	0.033	0.197	0.311	0.344	0.41	0.115	0.541	0.721	0.869	0.951
		Weighted	0.475	0.689	0.787	0.885	0.984	0.492	0.705	0.803	0.918	0.984	0.033	0.197	0.311	0.344	0.41	0.115	0.541	0.721	0.869	0.951
		Complement	0.525	0.311	0.213	0.115	0.016	0.508	0.295	0.197	0.082	0.016	0.967	0.803	0.689	0.656	0.59	0.885	0.459	0.279	0.131	0.049
Figure of merit			5.237	3.755	3.72	3.759	4.183	6.061	4.414	4.434	3.403	5.081	7.404	6.572	6.387	6.318	6.808	7.922	5.991	5.175	5.018	4.839
Order			14	30	31	29	24	12	23	22	40	17	4	9	10	11	8	2	13	16	18	21

Metrics			SNN filter					Kuan filter					Enhanced Lee filter					Gamma Map filter				
Weights			3	5	7	9	11	3	5	7	9	11	3	5	7	9	11	3	5	7	9	11
ENL	2	Original	250	500	650	800	900	400	800	1300	1800	1900	400	900	1300	1800	2600	400	900	1300	1800	2600
		Normalized	0	0.091	0.145	0.2	0.236	0.055	0.2	0.382	0.564	0.6	0.055	0.236	0.382	0.564	0.855	0.055	0.236	0.382	0.564	0.855
		Weighted	0	0.182	0.291	0.4	0.473	0.109	0.4	0.764	1.127	1.2	0.109	0.473	0.764	1.127	1.709	0.109	0.473	0.764	1.127	1.709
CNR	2	Original	10.3	11.8	12.8	13.2	13.6	10.4	12	13.3	14.7	15.5	9.6	10.15	10.3	10.45	10.5	9.7	10.2	10.4	10.5	10.6
		Normalized	0.099	0.284	0.407	0.457	0.506	0.111	0.309	0.469	0.642	0.741	0.012	0.08	0.099	0.117	0.123	0.025	0.086	0.111	0.123	0.136
		Weighted	0.198	0.568	0.815	0.914	1.012	0.222	0.617	0.938	1.284	1.481	0.025	0.16	0.198	0.235	0.247	0.049	0.173	0.222	0.247	0.272
EPF	2	Original	0.93	0.96	0.97	0.97	0.975	0.63	0.42	0.4	0.38	0.36	0.57	0.52	0.525	0.53	0.525	0.545	0.46	0.488	0.487	0.486
		Normalized	0.927	0.976	0.992	0.992	1	0.439	0.098	0.065	0.033	0	0.341	0.26	0.268	0.276	0.268	0.301	0.163	0.208	0.207	0.205
		Weighted	1.854	1.951	1.984	1.984	2	0.878	0.195	0.13	0.065	0	0.683	0.52	0.537	0.553	0.537	0.602	0.325	0.416	0.413	0.41
SSIM	2	Original	0.945	0.884	0.864	0.852	0.848	0.865	0.74	0.68	0.645	0.635	0.88	0.775	0.73	0.71	0.7	0.89	0.78	0.73	0.71	0.7
		Normalized	1	0.904	0.872	0.854	0.847	0.874	0.677	0.583	0.528	0.512	0.898	0.732	0.661	0.63	0.614	0.913	0.74	0.661	0.63	0.614
		Weighted	2	1.808	1.745	1.707	1.694	1.748	1.354	1.165	1.055	1.024	1.795	1.465	1.323	1.26	1.228	1.827	1.48	1.323	1.26	1.228
SNR	1	Original	21.3	18.5	17.4	17.9	16.5	17.4	14.6	13.4	12.6	12.1	17.5	14.8	13.5	12.8	12.2	17.8	15	14.8	13	12.5
		Normalized	0.989	0.691	0.574	0.628	0.479	0.574	0.277	0.149	0.064	0.011	0.585	0.298	0.16	0.085	0.021	0.617	0.319	0.298	0.106	0.053
		Weighted	0.989	0.691	0.574	0.628	0.479	0.574	0.277	0.149	0.064	0.011	0.585	0.298	0.16	0.085	0.021	0.617	0.319	0.298	0.106	0.053
PSNR	1	Original	37.8	35.1	34	33.5	33.2	34.2	31.4	30.2	29.4	29	34.2	31.4	30.2	29.5	29.1	34.5	31.6	30.5	29.7	29.4
		Normalized	0.967	0.67	0.549	0.495	0.462	0.571	0.264	0.132	0.044	0	0.571	0.264	0.132	0.055	0.011	0.604	0.286	0.165	0.077	0.044
		Weighted	0.967	0.67	0.549	0.495	0.462	0.571	0.264	0.132	0.044	0	0.571	0.264	0.132	0.055	0.011	0.604	0.286	0.165	0.077	0.044
S/MSE	1	Original	18.2	15.5	14.5	14	13.6	14.6	11.8	10.6	9.9	9.4	14.6	12.9	10.6	10	9.5	15	12.1	10.9	10.2	9.8
		Normalized	0.967	0.67	0.56	0.505	0.462	0.571	0.264	0.132	0.055	0	0.571	0.385	0.132	0.066	0.011	0.615	0.297	0.165	0.088	0.044
		Weighted	0.967	0.67	0.56	0.505	0.462	0.571	0.264	0.132	0.055	0	0.571	0.385	0.132	0.066	0.011	0.615	0.297	0.165	0.088	0.044
RMSE	1	Original	4.2	5	5.3	5.6	6.1	7.1	8.5	9.3	9.8	10.3	7.1	8.5	9.3	9.7	10.2	6.8	8.4	9	9.5	9.9
		Normalized	0	0.131	0.18	0.23	0.311	0.475	0.705	0.836	0.918	1	0.475	0.705	0.836	0.902	0.984	0.426	0.689	0.787	0.869	0.934
		Weighted	0	0.131	0.18	0.23	0.311	0.475	0.705	0.836	0.918	1	0.475	0.705	0.836	0.902	0.984	0.426	0.689	0.787	0.869	0.934
		Complement	1	0.869	0.82	0.77	0.689	0.525	0.295	0.164	0.082	0	0.525	0.295	0.164	0.098	0.016	0.574	0.311	0.213	0.131	0.066
Figure of merit			7.975	7.41	7.338	7.403	7.27	5.199	3.666	3.574	3.776	3.716	4.865	3.859	3.408	3.479	3.781	4.997	3.664	3.566	3.449	3.825
Order			1	3	6	5	7	15	33	35	28	32	20	25	39	37	27	19	34	36	38	26